Vibration Control using Shunted Piezoelectric and Electromagnetic Transducers

Sam Behrens
M.Eng. (Elec.)
B.E. (Mech.)

A thesis submitted in fulfilment of the requirements for the degree of

Doctor of Philosophy

School of Electrical Engineering and Computer Science

The University of Newcastle
Callaghan, N.S.W. 2308
Australia

May 2004

The UNIVERSITY of NEWCASTLE
AUSTRALIA

I LOOK AHEAD

To my parents
Rick and Sally Behrens

Declaration

I hereby certify that the work embodied in this thesis is the result of original research and has not been submitted for a higher degree to any other University or Institution.

Sam Behrens
May 2004

Abstract

Mechanical structures encounter vibration in response to environmental conditions and dynamic loads. In most circumstances, vibration contributes to mechanical fatigue which can eventually lead to catastrophic failure. Consequently, vibration control is a necessity for prolonging the operational life of structures.

Piezoelectric and electromagnetic transducers have been used for control of vibration for many years. They normally sense mechanical vibration and generate an opposing vibration through another piezoelectric and electromagnetic transducer. This is usually referred to as active feedback vibration control.

Another vibration control strategy senses and actuates simultaneously through an appropriately designed electrical impedance which is connected to the terminals of a single transducer. This technique requires no additional sensor, has improved robustness and stability, and a similar feedback structure compared to active feedback vibration control.

The objective of this thesis is to develop new vibration control techniques by expanding on both the previously mentioned strategies.

The first part of this thesis considers connecting an electrical impedance to a piezoelectric transducer to control vibration. This part reinforces that this vibration control strategy can be modelled as a variation of active feedback vibration control whereby the impedance parameterises the effective controller. A series of new vibration controllers are then presented.

Applying the knowledge gained in the first part of this thesis, the second part considers replacing the piezoelectric transducer with an electromagnetic transducer. Although the underlying dynamics and physical properties of the transducers are different, the feedback structures are remarkably similar to that of active feedback vibration control. A number of new vibration control strategies are proposed for a variety of mechanical systems.

Throughout the thesis, theoretical ideas and concepts are experimentally compared and validated on simple mechanical apparatuses to evaluate their vibration control performance.

Acknowledgments

Exploring the area of vibration control requires a large amount of technical and capital infrastructure. I would therefore like to extend my personal gratitude to the Laboratory for Dynamics and Control of Smart Structures, University of Newcastle, and the sometimes forgotten Australian tax payer for supporting me.

Also, I would like to acknowledge and sincerely thank my supervisor, Dr. S. O. Reza Moheimani, for his direction and support throughout the course of my Ph.D. research, and my colleague, Dr. Andrew J. Fleming, for his assistance and knowledge of electronics, control theory and theoretical analysis. My thanks to Mr. Dominik Niederberger and Mr. Ben Vautier for their theoretical and technical suggestions. Mr. Ian Powell, Mr. Roy Murcott and Mr. Russell Hicks from the university technical staff were also an important resource for design and construction of electronic instruments and mechanical apparatuses.

My sincere thanks to my good friends Andrew, Marco, Wade and Scott for their contributions and understanding.

Contents

Chapter 1

Introduction

Vibration is defined as the *to* and *fro* of an object, such as a clock pendulum. Mechanical structures encounter vibration in response to environmental and operating conditions. Sometimes vibration is desired, as in the case of the vibrating string on a musical instrument. Often it is unwanted, as in the case of the wing on an aircraft, because contributes to *fatigue* which leads to catastrophic failure of the mechanical structure. Consequently, vibration control is essential for the optimal performance and safety of many applications.

1.1 Present Vibration Control Techniques

A typical vibration control scenario is shown in Figure 1.1, whereby a mechanical structure, in the form of a bridge, is disturbed by a wind disturbance force f. By minimising the vibration, or energy of the system, this effectively increases the life and integrity of the structure. For the bridge, it may be desirable to minimise the velocity at point ν on the structure as this effectively reduces the energy of the system. Minimising strain, acceleration or displacement may be advantageous depending on the application.

At present, there are four vibration control fields: (1) passive, (2) active feedback, (3) self-sensing and (4) shunt.

Passive vibration control consists of two main strategies; viscoelastic materials (or viscoelastic damping) and tuned vibration absorbers. Viscoelastic materials, normally rubber, induce damping through the natural damping properties of the material. Tuned vibration absorbers are a simple mass-spring-damper system that is tuned to the required control performance.

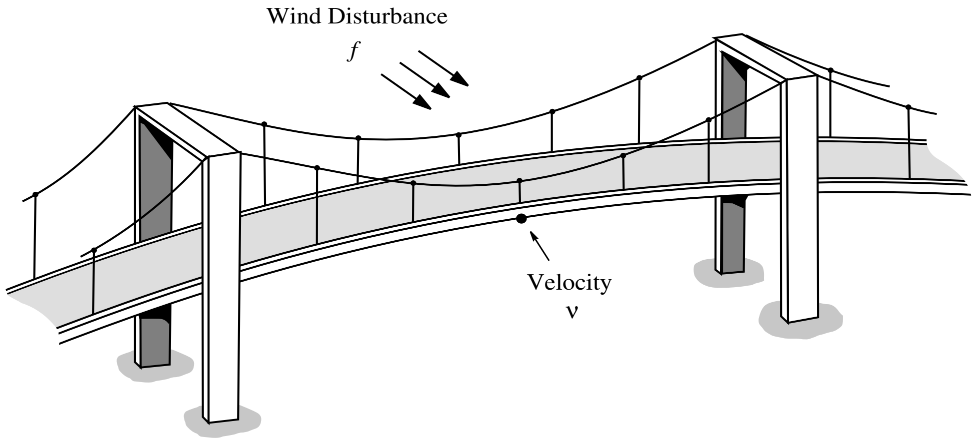

Figure 1.1: Typical vibration control scenario.

See reference [31] for more details on passive vibration control.

Active feedback vibration control requires the use of sensors and actuators. Vibration is sensed using an accelerometer, a strain gauge or piezoelectric transducer. An actuator voltage V_a is derived to counteract the sensed measurement. This is a typical regulator control problem, as shown in Figure 1.2, where P is the plant, K is the controller, w is the applied disturbance, z is the performance output and y is the sensed output. For example, consider Figure 1.1 where ν is the velocity performance signal and f is the spatial disturbance. The measured output y would typically be obtained from an additional transducer. The controller K is designed to minimise the relationship from applied disturbance f (or w) to the performance variable ν (or z). Active feedback control difficulties are due, in the most part, to the intrinsic nature of the plant P. These systems contain a large number of lightly damped resonant modes which create major challenges in modelling and control design. Additionally, environmental factors alter the resonance frequencies, compromising the stability margins and restricting the performance. Examples of active feedback control can be found in references [45, 46, 49, 75].

Self-sensing or sensori-actuation vibration control was established by Dosch, Inman and Garcia [31] where a single transducer could amalgamate both functions of sensing and actuating. By deducting the capacitive voltage drop from the applied terminal voltage, an estimation of the internal piezoelectric strain voltage can be achieved through a bridge circuit. The reconstructed strain voltage can be employed as an active feedback sensor effectively eliminating the need for an additional transducer for actuation. A similar rate-of-strain estimation

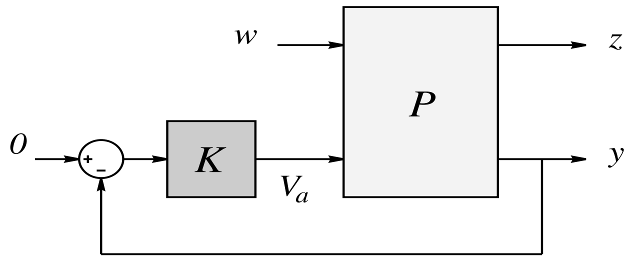

Figure 1.2: Typical regulator control problem.

technique is also offered in [7]. Although piezoelectric self-sensing techniques are subject to the typical problems linked to active feedback control schemes, an added benefit is gained. The transfer function from an applied actuator voltage to the sensed strain is in effect *collocated* [78]. In certain controller classes, collocation achieves closed-loop stability, robustness and generally reduces the complexity of the design process [78]. Piezoelectric self-sensing methodology estimation is highly reliant on the transducer capacitance value. If the sensing capacitance in the bridge circuit is not perfectly balanced to the transducer capacitance, it can result in strain estimation errors. If an erroneous estimate is used within a feedback control loop, such uncertainty may severely effect performance and/or cause instability. In addition, the sensing circuit may detune due to variations to temperature, load and age of the piezoelectric transducer. An attempt to address the problems of capacitance sensitivity can be found in [2, 24, 107]. In spite of the related problems, a number of applications have appeared throughout the literature [5, 16, 50, 72, 104].

Shunt control requires the connection of an electrical impedance to the terminals of a transducer with the aim to control vibration. Electrical impedance designs include resistors [41, 48], inductive networks [14, 15, 41, 48, 56, 112, 113, 114, 117], switched networks [26, 29, 92], negative capacitors [10, 11, 115] and active impedances [39]. These methodologies will be fully discussed in greater detail in Chapter 2. Shunt control has a number of advantages, when compared to active feedback control schemes, as most configurations do not require a parametric model of the plant. Therefore, this simplifies the implementation and tuning process. Shunt controllers, like self-sensing controllers, are also perfectly *collocated* [78] and require no additional feedback sensors. In some circumstances, shunt controllers may not require high voltage electronic amplifiers which are needed for active feedback control schemes [41, 48].

This thesis is focused on shunt control, but for the sake of completeness, other vibration control strategies may be cited.

1.2 Problem Statement and Motivation

Mechanical structures encounter vibration in response to environmental and operating conditions. Sometimes these vibrations are desired, as in the case of the vibrating string on a musical instrument. Often they are unwanted, for instance the wing on an aircraft, where vibration can lead to the catastrophic failure of the structure. Consequently, control of vibration is a necessity in many applications to prolong their structural life.

Vibration control has the potential to be successfully applied to an array of applications ranging from simple consumer items to advanced industrial uses to increase operational performance and/or personal safety.

Vibration control innovations in consumer items such as snow skis, snowboards, mountain bikes, tennis and squash rackets are currently being assessed [16, 54, 67]. Performance benefits include improved power, comfort, control and operation [16, 54, 67].

Many commercial computer drives, digital-video-disk (DVD) and compact-disk (CD) drives incorporate vibration control systems. By controlling the mechanical vibration of the read/write head, the seek-time is decreased, hence the data rate can be improved [44].

The control of aerospace vibration is also the focus of a significant research effort. During certain modes of flight, buffeting loads on aerospace structures can result in high levels of vibration. Such vibration can lead to mechanical fatigue, a smaller flight envelope and reduction of lift performance of the aircraft [97]. Other examples of aerospace vibration control can be found in references [5, 50, 58, 72, 111].

Additional vibration control opportunities include: suppression of acoustic radiation from underwater submersibles [118], launch vehicle acoustic noise mitigation [30, 90], acoustic transmission reduction panels [71, 96], active antenna structures [45], nano-positioning systems [27], underwater sonar [101], car suspension systems [73], vibration isolation platforms [95], control of enclosed-sound fields [55], magnetic levitation [19, 108], magnetic bearings [87], micro-electro-mechanical-systems (MEMS) devices [6] and Stewart platforms [28].

1.3 Thesis Overview and Contributions

In this thesis, shunt control is defined as the attachment of an electrical impedance to the terminals of an electromechanical transducer, either piezoelectric or electromagnetic, in order

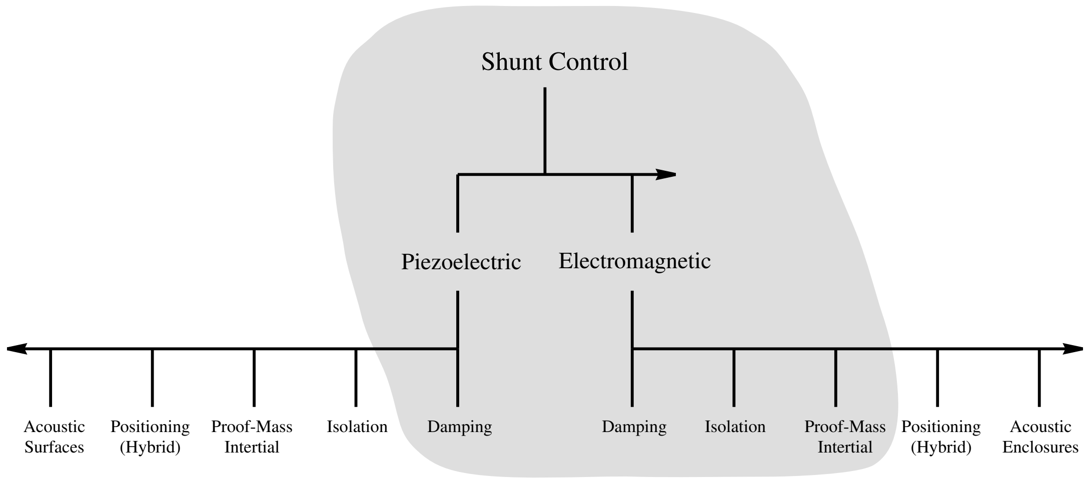

Figure 1.3: Summary of shunt vibration control. Shaded region indicates research areas covered within this thesis.

to control vibration. At present, there are two very distinct fields of shunt control; piezoelectric and electromagnetic, as illustrated in Figure 1.3. The thesis illustrates that both these control strategies compliment each other. Therefore, the following work will be presented in two unique parts.

Part I will concentrate on piezoelectric shunt control while Part II will focus on electromagnetic shunt control. The shaded region of Figure 1.3 indicates work addressed in this thesis. Topics not shaded will not be dealt with as, for the most part, they are still under conceptual development.

Part I contains two chapters: 2) Piezoelectric Shunt Damping, and 3) Multivariable Piezoelectric Shunt Damping.

Chapter 2 begins with a review of piezoelectric transducers and present piezoelectric shunt control strategies. It is then followed by the development of several new piezoelectric shunt controllers. The material in this chapter was presented in the conference papers [C7, C9, C10, C11, C12, C13 and C14] and subsequently the journal papers [J3, J5, J6 and J8]. See proceeding section, Section 1.3.1, for conference and journal paper details.

Chapter 3 follows on from Chapter 2 by extending the explored concepts to shunt control using multiple piezoelectric transducers. Concepts presented in this chapter were published in the journal paper [J4].

Part II contains three chapters: 4) Electromagnetic Shunt Damping, 5) Electromagnetic Shunt Isolation, and 6) Proof-Mass Inertial Vibration Control.

Chapter 4 introduces electromagnetic transducers and builds on Part I by developing the concept of electromagnetic shunt control. This chapter also develops three novel electromagnetic shunt controllers. This chapter was presented in the conference papers [C1, C2, C4, C5 and C6] and journal papers [J1 and J2].

In Chapter 5 an electromagnetic shunt control is applied to a simple mechanical isolation system. Several different electromagnetic shunt controllers were developed and explored for this scenario. Some material in this chapter was presented in the conference paper [C3].

Chapter 6 applies electromagnetic shunt control and its associated controller to a simple proof-mass inertial system. Chapter 6 is based on the journal paper [JR1].

All of the above control strategies will be validated on experimental apparatuses.

The thesis is concluded in Chapter 7, with a discussion and suggests future research opportunities for shunt control.

1.3.1 Publications

Outcomes throughout the course of this research have included nine international journal papers and fourteen international conference papers. Details are listed below.

Journal Papers

[J1] *Synthesis and Implementation of Sensor-Less Active Shunt Controllers for Electromagnetically Actuated Systems.*
A. J. Fleming, S. O. R. Moheimani, S. Behrens
IEEE Transactions on Control Systems Technology
March 2005, Volume 13, Number 2, Pages 246-261

[J2] *Passive Vibration Control via Electromagnetic Shunt Damping.*
S. Behrens, A. J. Fleming, S. O. R. Moheimani
IEEE/ASME Transactions on Mechatronics
February 2005, Volume 10, Number 1, Pages 118-122

[J3] *Multi-mode Piezoelectric Shunt Damping with a Highly Resonant Impedance.*
S. O. R. Moheimani, S. Behrens
IEEE Transactions on Control Systems Technology
May 2004, Volume 12, Number 3, Pages 484-491

[J4] *Dynamics, Control and Stability of Multivariable Piezoelectric Shunts.*
S. O. R. Moheimani, A. J. Fleming, S. Behrens
IEEE/ASME Transactions on Mechatronics
March 2004, Volume 9, Number 1, Pages 87-99

[J5] *Multiple Mode Current Flowing Passive Piezoelectric Shunt Controller.*
S. Behrens, S. O. R. Moheimani, A. J. Fleming
ASME Journal of Sound and Vibration
October 2003, Volume 266, Number 5, Pages 929-942

[J6] *On the Feedback Structure of Wideband Piezoelectric Shunt Damping Systems.*
S. O. R. Moheimani, A. J. Fleming, S. Behrens
IOP Smart Materials and Structures
January 2003, Volume 12, Pages 49-56

[J7] *Reducing the Inductance Requirements of Piezoelectric Shunt Damping Systems.*
A. J. Fleming, S. Behrens, S. O. R. Moheimani
IOP Smart Materials and Structures
January 2003, Volume 12, Pages 57-64

[J8] *A Highly Resonant Controller for Multi-mode Piezoelectric Shunt Damping.*
S. O. R. Moheimani, A. J. Fleming, S. Behrens
IEE Electronics Letters
December 2001, Volume 37, Number 25, Pages 1505-1506

Journal Papers in Review

[JR1] *Proof-mass Inertial Vibration Control using a Shunted Electromagnetic Transducer*
A. J. Fleming, S. Behrens, S. O. R. Moheimani
IEEE/ASME Transactions on Mechatronics
Submitted December 2003

[JR2] *Adaptive Electromagnetic Shunt Dampening*
D. Niederberger, S. Behrens, A. J. Fleming, S. O. R. Moheimani, M. Morari
IEEE/ASME Transactions on Mechatronics
Submitted November 2003

Conference Proceedings

[C1] *Control Orientated Synthesis of Electromagnetic Shunt Impedances for Vibration Control.*
S. Behrens, A. J. Fleming, S. O. R. Moheimani
IFAC Mechatronics 2003
December 2004, Manly, NSW, Australia

[C2] *Negative Inductor-Resistor for Electromagnetic Shunt Damping.*
S. Behrens, A. J. Fleming, S. O. R. Moheimani
IFAC Mechatronics 2003
December 2004, Manly, NSW, Australia

[C3] *Vibration Isolation Using a Shunted Electromagnetic Transducer.*
S. Behrens, A. J. Fleming, S. O. R. Moheimani
SPIE Smart Structures and Materials 2004: Damping and Isolation
March 2004, San Diego, California, USA

[C4] *Active LQR and H_2 Shunt Control of Electromagnetic Transducers.*
A. J. Fleming, S. Behrens, S. O. R. Moheimani
IEEE Conference on Decision and Control
December 2003, Maui, Hawaii, USA

[C5] *Electromagnetic Shunt Damping.*
S. Behrens, A. J. Fleming, S. O. R. Moheimani
IEEE/ASME International Conference on Advanced Intelligent Mechatronics
July 2003, Kobe, Japan

[C6] *Electrodynamic Vibration Suppression.*
S. Behrens, A. J. Fleming, S. O. R. Moheimani
SPIE Smart Structures and Materials 2003: Damping and Isolation
March 2003, San Diego, California, USA

[C7] *Robust Piezoelectric Passive Shunt Dampener.*
A. J. Fleming, S. Behrens, S. O. R. Moheimani
SPIE Smart Structures and Materials 2003: Damping and Isolation
March 2003, San Diego, California, USA

[C8] *An Autonomous Piezoelectric Shunt Damping System.*
A. J. Fleming, S. Behrens, S. O. R. Moheimani
SPIE Smart Structures and Materials 2003: Damping and Isolation
March 2003, San Diego, California, USA

[C9] *Dynamics and Stability of Wideband Vibration Absorbers with Multiple Piezoelectric Transducers.*
S. O. R. Moheimani, S. Behrens, A. J. Fleming
IFAC Mechatronics 2002
December 2002, Berkeley, California, USA

[C10] *Series-Parallel Impedance Structure for Piezoelectric Vibration Damping.*
S. Behrens, A. J. Fleming, S. O. R. Moheimani
SPIE Smart Materials, Nano- and Micro-Smart Systems
December 2002, Melbourne, Victoria, Australia

[C11] *Multiple Mode Passive Piezoelectric Shunt Dampener.*
S. Behrens, S. O. R. Moheimani, A. J. Fleming
IFAC Mechatronics 2002
December 2002, Berkeley, California, USA

[C12] *Multi-mode Piezoelectric Shunt Damping with a Highly Resonant Impedance.*
S. O. R. Moheimani, S. Behrens
IEEE Conference on Control Applications
September 2002, Glasgow, Scotland

[C13] *On the Feedback Structure of Wideband Piezoelectric Shunt Damping Systems.*
S. O. R. Moheimani, A. J. Fleming, S. Behrens
IFAC World Congress 2002
July 2002, Barcelona, Spain

[C14] *Current Flowing Multiple Mode Piezoelectric Shunt Dampener.*
S. Behrens, A. J. Fleming, S. O. R. Moheimani
SPIE Smart Structures and Materials 2002: Damping and Isolation
March 2002, San Diego, California, USA

Part I

Piezoelectric Shunt Control

Chapter 2

Piezoelectric Shunt Damping

By attaching a piezoelectric transducer to a mechanical structure and shunting the terminals of the transducer with appropriate designed electrical impedance, vibration control can be mitigated. This technique is commonly referred to piezoelectric shunt damping.

This chapter starts with a brief introduction to piezoelectric transducers and current piezoelectric shunt damping techniques. A model for a piezoelectric shunt damping is then developed to aid in the design of four new vibration controllers. The developed model, and controllers, are then verified experimentally on three piezoelectric laminated structures.

2.1 Piezoelectric Transducers

In 1880 Pierre and Jacques Curie discovered and published the piezoelectric effect while studying the formation of an electrical charge on the surface of certain naturally occurring crystals under mechanical stress. Further research revealed the opposite effect when they applied an electrical charge to the crystal, a volume deformation was noted.

Quartz, topaz and Rochelle salt [18] are examples of naturally occurring materials which exhibit a weak piezoelectric effect. Progress in material development has allowed scientists to manufacture piezoelectric materials with characteristics that are better suited to piezoelectric transducers. The two most commonly used piezoelectric materials in transducer applications are lead-zirconium-titanate (PZT) and polyvinylidene-fluoride (PVDF). PZT is a stiff ceramic material that is regularly used for actuating applications due to its enhanced electromechanical coefficients. For sensing applications, the semi-crystalline polymer film

PVDF is frequently used because its malleable properties make it easier to cut and shape. However, for the same voltage PZT produces ~ 5 times more strain, is ~ 40 times more rigid and has a permittivity ~ 100 times greater than PVDF.

Recent developments suggest that single piezoelectric crystals [103] possess exceptional properties and are poised to revolutionise piezoelectric materials, as well as transducers [103]. Single piezoelectric crystals exhibit nearly 5 times the strain and 3 times the electromechanical coupling than conventional PZT materials.

Additional information about piezoelectric materials can be found in references [1, 3, 43, 62, 63, 64, 88].

2.1.1 Modelling a Piezoelectric Transducer

For vibration control, a thin sliver of piezoelectric material, normally PZT, is sandwiched between two conducting layers. This forms a piezoelectric transducer, as shown in Figure 2.1. The transducer is then glued to the surface or laminated within the mechanical structure using a strong adhesive materials.

Since piezoelectric transducers are multi-dimensional devices, as shown in Figure 2.1, the modelling the transducer is represented by

$$\begin{aligned} \varepsilon^i &= S^E_{ij}\sigma_j + d_{mi}E_m \\ D_m &= d_{mi}\sigma_i + \zeta_{ik}E_k, \end{aligned} \tag{2.1}$$

where $i, j = 1, 2, \ldots, 6$ and $m, k = 1, 2, 3$ represent the coordinate system for the transducer element [43]. Notations E, ε, D, σ, S^E, d and ξ correspond to the electrical field, strain, electrical displacement, stress, elastic compliant, piezoelectric coefficient and dielectric permittivity. A more detailed explanation can be found in [4, 10, 22, 43].

When a piezoelectric transducer is used as a sensor, the strain over the area covered by the transducer is proportional to the open-circuit voltage. When used as an acuator, an applied voltage results in a strain. Piezoelectric transducers behave electrically like a series capacitor and mechanically like a stiff spring [63]. It is common to model piezoelectric transducers as a series capacitor C_p and a strain dependent voltage source V_p, as shown in Figure 2.1 [31, 48, 110]. However, more complex models can be found in [3, 4, 10, 22, 43].

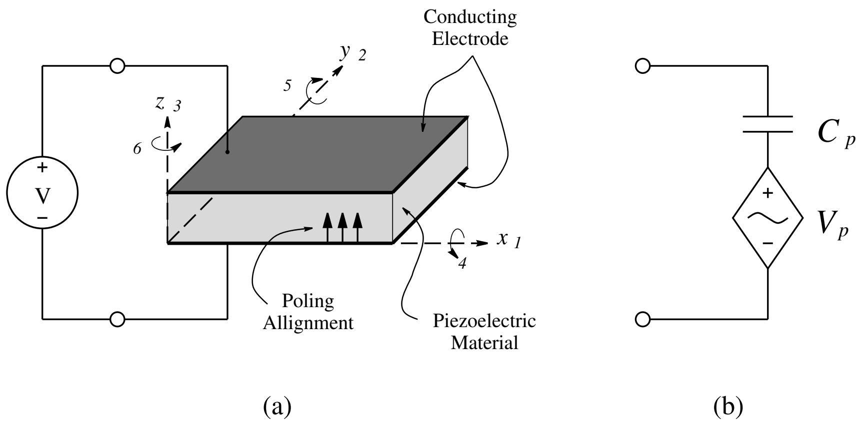

Figure 2.1: Piezoelectric transducer (a) and electrically equivalent model (b).

2.2 Review of Piezoelectric Shunt Damping

Piezoelectric shunt damping of mechanical structures is now an active area of research in which new applications are emerging. For some interesting applications, refer to [5, 16, 50, 72, 102, 104, 114] and references therein.

The first documented piezoelectric shunt damping technique was proposed by Forward [41]. Forward suggested that by shunting the terminals of a structurally laminated piezoelectric transducer with a resistor, he was able to experimentally demonstrate mechanical damping. Adding a resistor to the piezoelectric transducer is equivalent to viscoelastic dampener [51, 91]. With existing transducers, resistive impedance offers very little mechanical damping. This technique is equivalent to an extremely light viscoelastic dampener treatment [48]. Future transducers utilising high electromechanical coupling coefficients may be of greater use [103].

Initially appearing in reference [41], piezoelectric shunt damping is generally credited to Hagood *et al.* [48]. By placing a series inductor-resistor network across the terminals of the piezoelectric transducer, it was demonstrated that the amplitude of a single structural mode was dramatically reduced. Because of the piezoelectric transducer's intrinsic capacitance, the inductor-resistor network is tuned to a single structural mode. This technique is equivalent to a passive tuned mechanical absorber [51, 91], where the introduced dynamics by the shunt circuit act to effectively increase mechanical damping [48]. Reference [48] introduced a theoretical method for determining an optimal resistance value for the inductor-resistor network. The parallel circuit variation to [48] was later proposed by [112]. Although the two circuits, series and parallel, achieve comparable performance levels, the parallel network is less sensitive to sub-optimal resistance values [10, 12]. A more in-depth review of single-mode piezoelectric shunt damping can be found in reference [10].

Single-mode damping using many piezoelectric transducers and series/parallel inductor-resistor damping circuits can reduce multiple structural modes. However, bonding to or embedding multiple piezoelectric shunts onto/into the host structure may result in problems. The mechanical structure may be too small to accommodate all the transducers and/or the shunt circuits, and inclusion of many transducers may weaken the mechanical structure.

The methods suggested in references [41, 48, 112], although effective, can only be applied to one structural mode. However, following [48], a number of authors attempted to extend this technique to allow for passive damping of several modes. Reference [56] suggests parallel combinations of a series of inductor-resistor circuits with several series capacitor-inductor-resistor branches. The authors experimentally demonstrated the effectiveness of this specific structure in reducing vibrations due to two modes of a structure. However, this synthesis procedure is not straightforward, making it difficult to extend the application to more modes.

In references [113, 114, 117], the authors proposed the use of current-blocking circuits to separate inductor-resistor branches tuned to each resonance frequency. This method works well for a small number of modes. However, as the number of modes increases so does the complexity of the shunt circuit network, resulting in implementation difficulties. References [12, 35] show an effective method for determining the optimal resistance values for [113, 114, 117]. A more in-depth review can be found in reference [10].

More recently the current-flowing shunt controller was introduced in [14, 15], which is examined in greater detail later in the thesis. This technique follows on from the previous technique [113, 114, 117]. The idea is to introduce a current-flowing capacitor-inductor circuit into each inductor-resistor branch. The complexity of the electrical shunt proposed in [14, 15] is considerably less than that proposed in [113, 114, 117]. However, the freedom of choice of the capacitive, or alternatively the inductive elements, may complicate the design process.

The current-flowing circuit dual, or series-parallel circuit, is intended as a method for lowering inductive component values [13]. The series-parallel circuit will also be examined in greater detail in later sections.

So far, the multi-mode techniques presented are essentially variations of the original single-mode circuits. An innovative approach to designing piezoelectric shunt damping circuits or control orientated shunt controllers was presented by [84]. By casting the system as a feedback control problem, an effective controller can be designed and from this design the shunt impedance can be deducted. The passivity and therefore the stability of the shunted system can be guaranteed [84] under certain assumptions. This controller has comparable benefits to that of current-flowing and series-parallel circuits; low in order, easy to tune and suitable for modally dense systems. Both these circuit designs will also be examined in greater detail in Section 2.5.3.

Active shunt impedances cannot be implemented using passive elements such as capacitors, inductors and resistors [59]. For example, the negative capacitor shunt circuit [10, 11, 115, 118] is an elementary technique for broad-band piezoelectric shunt damping. Negative capacitor shunts are immune to structural variations due to operational and environmental conditions, but variations in the transducer dynamics will effect the control performance and stability. Overall observations from [10, 11, 115, 118] suggest active shunt impedances provide greater vibration suppression than passive shunts, but the system stability is not guaranteed.

In an effort to eliminate the need for simulated inductors, as required for the majority of passive shunt circuits [41, 48, 112], researchers have developed switched shunt or switched stiffness techniques [26]. Currently there are three types of shunts, where the piezoelectric transducer is in series with a switch [26] or a switch in series/parallel with a capacitor [29], a switch in series with a resistor [23] and a switch in series with an inductor [92]. For these techniques, determining the passive element (i.e. capacitor, resister or inductor) and/or the switching cycle for the switch is not straight forward. These techniques are only applicable to single-degree-of-freedom mechanical structures or mechanical structures with sinusoidal disturbances. However, the authors have tried to conjure some theory to these non-trivial problems.

Vibration control using shunt impedance could be considered as a standard regulator feedback control problem where the controller is cast as an impedance. This will be referred to as impedance synthesis [37, 39]. These techniques could include LQG, $\mathcal{H}_2$ and $\mathcal{H}_\infty$ controller designs to determine a suitable impedance. Reference [39] first proposed this technique and raised several interesting observations. Similar synthesis techniques will be presented in Part II of this thesis in the context of electromagnetic systems.

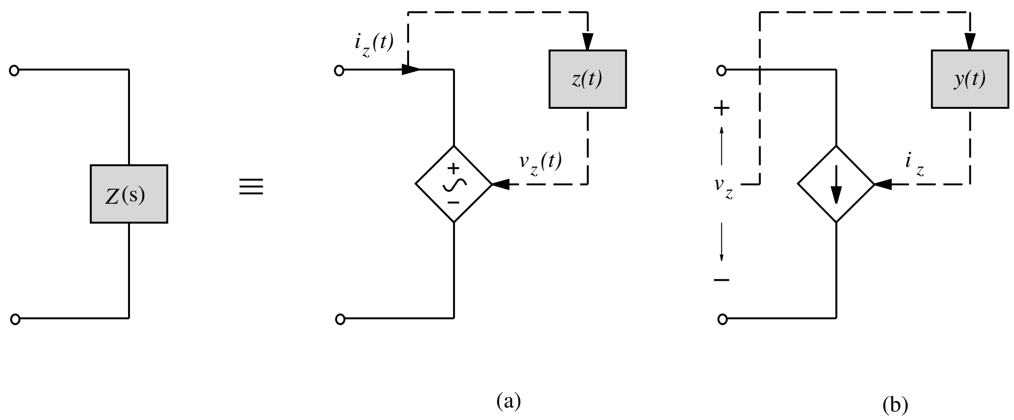

Figure 2.2: Arbitrary impedance $Z(s)$ implemented by a current-controlled-voltage-source (a) and voltage-controlled-current-source (b).

2.3 Review of Synthetic Impedance Device

The main difficulty associated with implementing piezoelectric shunt impedances is that they often require very large inductors in the order of thousands of Henries. Synthetic inductors constructed from opamps have been proposed as a possible solution [93]. However, if a large number of modes are to be controlled, such as the case for multi-mode shunts, the construction of the shunt circuit requires a considerable number of high voltage opamps. These circuits have numerous limitations. They are large in size, require an external power supply, are difficult to initially tune, are sensitive to temperature and have voltage limitations due to internal gains of the simulated inductor circuit.

To overcome the simulated inductance problems the synthetic admittance circuit was first proposed by [36]. This technique allowed for the implementation of an impedance, or admittance, shunt circuit in an efficient way. The author [36] demonstrated implementation of a series inductor-resistor shunt controller without the use of a synthetic inductor.

Recently a second generation of the synthetic admittance has been developed whereby the new technique has current or voltage feedback [40]. Consider a two-terminal device capable of implementing any arbitrary shunt impedance, as shown in Figure 2.2. An arbitrary impedance $Z(s)$ can be established at the terminals by either sensing a current i_z and applying a voltage v_z, or sensing a voltage v_z and applying a current i_z.

Referring to Figure 2.2 (a), the voltage $v_z(t)$ can be ascertained by sensing the current $i_z(t)$, i.e. $v_z(t) = f(i_z(t))$. That is, $v_z(t) = z(t)i_z(t)$ where $z(t)$ is the desired linear transfer function for the impedance. Alternatively, in the Laplace domain

$$V_z(s) = Z(s)I_z(s). \tag{2.2}$$

To implement the required impedance $Z(s)$, a current-controlled-voltage-source (CCVS) is used, as shown in Figure 2.3 (a). In Figure 2.3 (a), within the high frequency bandwidth of the control loop, the reference potential V_{ref} appears across the load, i.e. a unity gain voltage amplifier. The additional resistance and differential amplifier generate the current measurement V_R with gain R_s V/A.

Similarly for Figure 2.2 (b), the current $i_z(t)$ can be ascertained by sensing the voltage $v_z(t)$, i.e. $i_z(t) = f(v_z(t))$. That is, $i_z(t) = y(t)v_z(t)$ where $y(t)$ is the desired linear transfer function for the admittance i.e. $y(t) = \frac{1}{z(t)}$. In the Laplace domain,

$$I_z(s) = Y(s)V_z(s) = \frac{1}{Z(s)}V_z(s). \tag{2.3}$$

A voltage-controlled-current-source (VCCS) is required to implement an admittance $Y(s)$, as shown in Figure 2.3 (b). In Figure 2.3 (b), within the high frequency bandwidth of the control loop, the reference potential V_{ref} appears across the sensing impedance R_s, thus, the resulting current is described by $\frac{I_L(s)}{V_{ref}(s)} = \frac{1}{R_s}$.

Selecting the right configuration for implementing CCVS or VCCS will depend on the relative order of the desired impedance. Practical digital implementation of *improper* [68] transfer functions is not possible, therefore the correct selection should make the transfer function $Z(s)$ or $Y(s)$ proper [68].

A practical implementation of CCVS or VCCS is shown in Figure 2.4 [36, 40]. The device is capable of ± 200 V operation at a maximum DC current of ± 30 A. A dSpace 1104 based system is used to implement the required impedance $Z(s)$ or admittance $Y(s)$ transfer functions or filter, as shown in Figure 2.3. Further analysis and more detailed discussions of CCVS or VCCS can be found in reference [40].

Using synthetic inductors [93], a synthetic admittance circuit [36] or CCVS/VCCS [40], strictly speaking, will not be "passive" [68], as they will be made of "active" components, such as opamps, transistors and digital signal processors (DSPs). However, there are clear advantages in using such techniques. For example, CCVS/VCCS implementation replaces various virtual circuits such as virtual capacitors and inductors, negative impedance converters and transformers [59]. Additionally, only a single high-voltage opamp is required to provide close to an ideal implementation of any arbitrary shunt impedance.

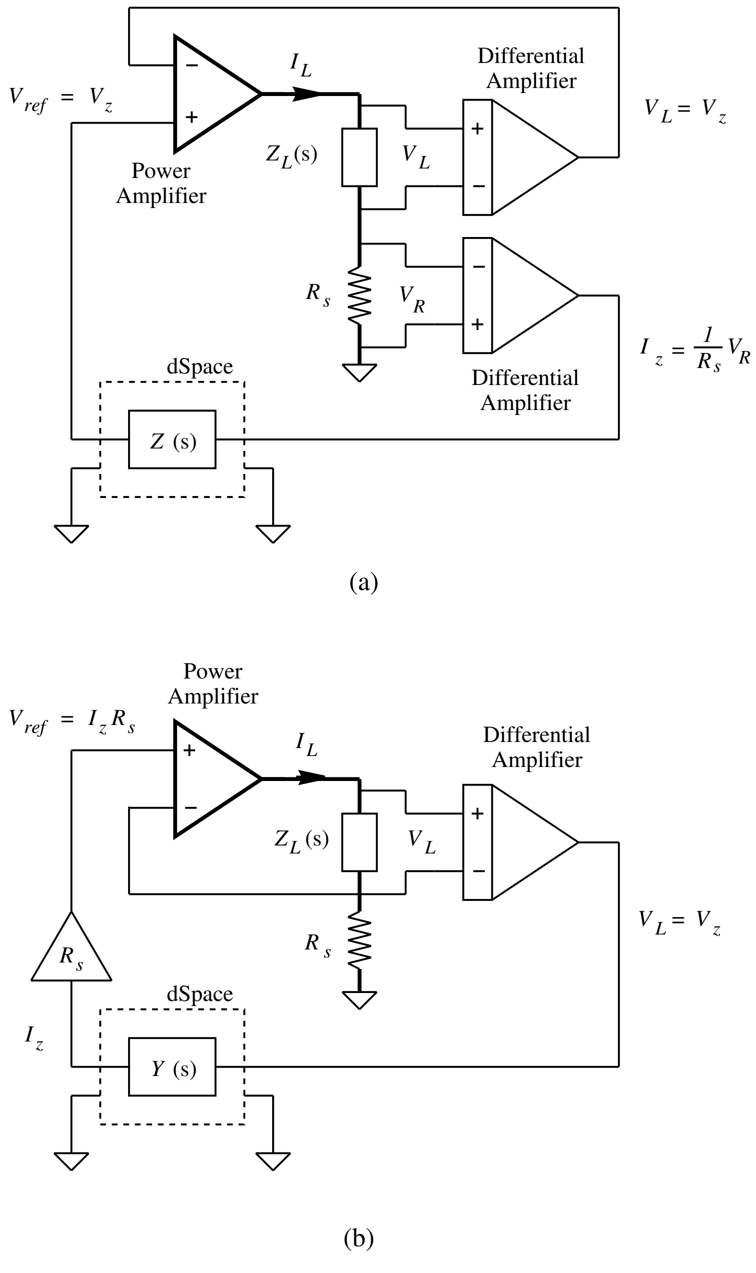

Figure 2.3: The simplified schematic of a differential voltage feedback amplifier (a) and current feedback amplifier (b). The load impedance $Z_L(s)$ represents piezoelectric transducer.

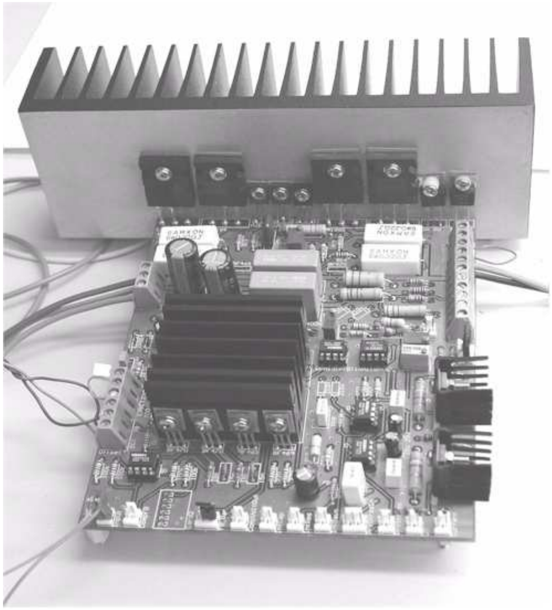

Figure 2.4: Practical implementation of a voltage amplifier with current instrumentation [36, 40].

2.4 Modelling a Mechanical System

This section will consider a method for modelling the presence of a shunt circuit attached to a piezoelectric laminate structure, as shown in Figure 2.5. The aim is to dampen vibration from two external disturbances. The first is a voltage disturbance V_a, as shown in Figure 2.5, and the second is a spatial force disturbance f.

From reference [10, 82], the following relationships are defined for small amplitude vibration:

$$G_{ad}(s) = \frac{d(s)}{V_a(s)} = \sum_{k=1}^{M} \frac{F_k \phi_k}{s^2 + 2\zeta_k \omega_k s + \omega_k^2} \tag{2.4}$$

and

$$G_{vv}(s) = \frac{V_p(s)}{V_z(s)} = \sum_{k=1}^{M} \frac{\alpha_k}{s^2 + 2\zeta_k \omega_k s + \omega_k^2}, \tag{2.5}$$

where F_k, ϕ_k and α_k represent the lumped modal and piezoelectric constants applicable to the k^{th} mode of vibration for some large finite number M. Additionally, $V_p(s)$ is the induced voltage within the piezoelectric transducer. For ease of modelling, the disturbance and shunted transducer are physically identical, poled in the same direction and are attached to the structure in a collocated fashion, hence $G_{av}(s) = \frac{V_p(s)}{V_a(s)} = G_{vv}(s)$. In reality, this assumption is rarely the case and should be disregarded.

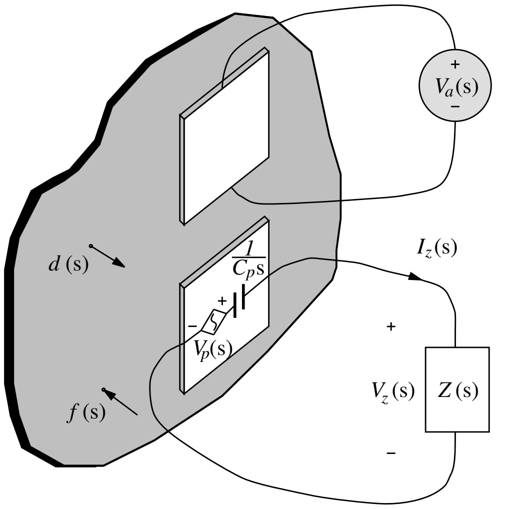

Figure 2.5: General piezoelectric laminated structure excited by a distributed force $f(s)$ and voltage $V_a(s)$ is applied to a disturbance patch. The resulting vibration $d(s)$ is suppressed by the presence of an electrical impedance $Z(s)$ connected to the piezoelectric transducer.

Modelling of the above transfer functions is usually either analytical, finite element analysis or system identification.

Analytical modelling requires mathematical models for structural dynamics and piezoelectric transducers [10, 43, 82]. In this case, the physical properties of the mechanical structure and the piezoelectric transducer are required. Initially, physical parameters are assumed and applied to building a model for the system. A set of experimental data is then obtained and used to optimise the model until it agrees with the data. Sometimes a non-linear optimisation technique is used to optimise the model parameters [10].

Finite element analysis (FEA) involves cutting a mechanical structure into several discrete elements or models, and by describing the behavior of each element a model for the overall system can be formulated. Normally, this technique develops high order models [25, 76]. As with the analytical modelling, FEA models are commonly tuned to the experimental data [33].

System identification is normally considered as a “black box” approach whereby experimental data is fed into an algorithm which outputs a model for the system. This technique does not require any prior knowledge i.e. does not require any mechanical structure or piezoelectric transducer parameters. System identification field is very diverse [77, 106]. However, from observations the frequency domain subspace system identification has proven extremely effective in identifying high order resonant systems [79, 80], as well as for the systems dealt with in this thesis. Van Overschee and De Moor algorithm [105] will be used throughout the thesis[1]. For more information refer to references [79, 80].

2.4.1 Modelling the Presence of Shunt Circuit

The derivation in the following section will reiterate the work presented in the author's Masters thesis [10]. For consistency, the same notations used in the Masters thesis will be applied to this thesis.

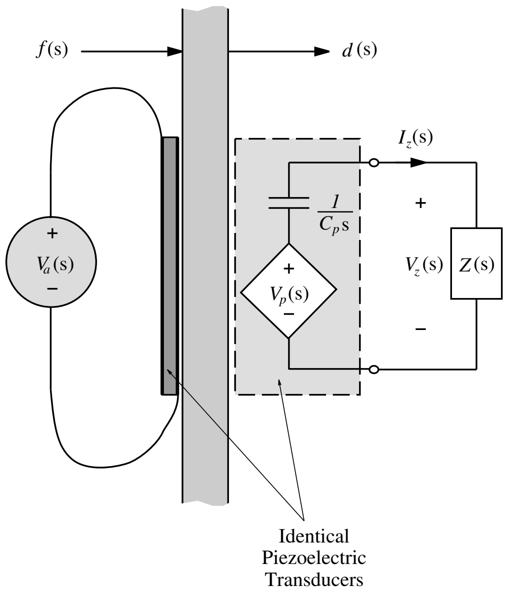

Figure 2.6: A mechanical structure disturbed by an applied actuator voltage $V_a(s)$ and force $f(s)$. Resulting vibration $d(s)$ suppressed by the presence of an elctrical impedance $Z(s)$ connected to a piezoelectric transducer.

Ohm's law states, in the Laplace domain, the following relationship between voltage and current is

$$V_z(s) = I_z(s)Z(s). \tag{2.6}$$

Referring to Figure 2.6, by applying Kirchhoff's voltage law, the following relationship can

[1]A Matlab implementation of this algorithum can be downloaded from http://routh.newcastle.edu.au

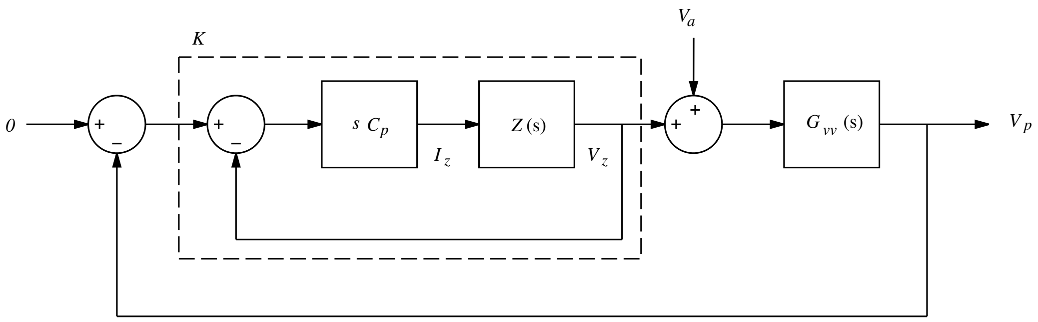

Figure 2.7: Piezoelectric shunt damping (strain) feedback control problem parameterised by $Z(s)$.

be obtained

$$V_z(s) = V_p(s) - \frac{1}{C_p s} I_z(s), \tag{2.7}$$

where C_p is the capacitance for the piezoelectric transducer. By substituting (2.6) into (2.7), the following is obtained

$$V_z(s) = \frac{Z(s)}{\frac{1}{C_p s} + Z(s)} V_p(s) = \frac{C_p s Z(s)}{1 + C_p s Z(s)} V_p(s). \tag{2.8}$$

From the principle of superposition [10, 43], the disturbance voltage $V_a(s)$ to transducer strain voltage $V_p(s)$ is

$$V_p(s) = G_{av}(s) V_a(s) - G_{vv}(s) V_z(s). \tag{2.9}$$

By adding (2.8) to (2.9) the following shunted composite system, or closed-loop system, can be obtained

$$\tilde{G}_{av} \triangleq \frac{V_p(s)}{V_a(s)} = \frac{G_{av}(s)}{1 + G_{vv}(s) K(s)}, \tag{2.10}$$

where the effective controller $K(s)$ is

$$\begin{aligned} K(s) &= \frac{Z(s)}{Z(s) + \frac{1}{C_p s}} \\ &= \frac{1}{1 + \frac{1}{C_p s} Y(s)}, \end{aligned} \tag{2.11}$$

and the admittance $Y(s)$ is equivalent to $\frac{1}{Z(s)}$. Now Equation (2.10) can be represented as a collocated feedback control problem where the effective controller is parameterised by the electrical shunt impedance $Z(s)$ or admittance $Y(s)$, as shown in Figures 2.7 and 2.8.

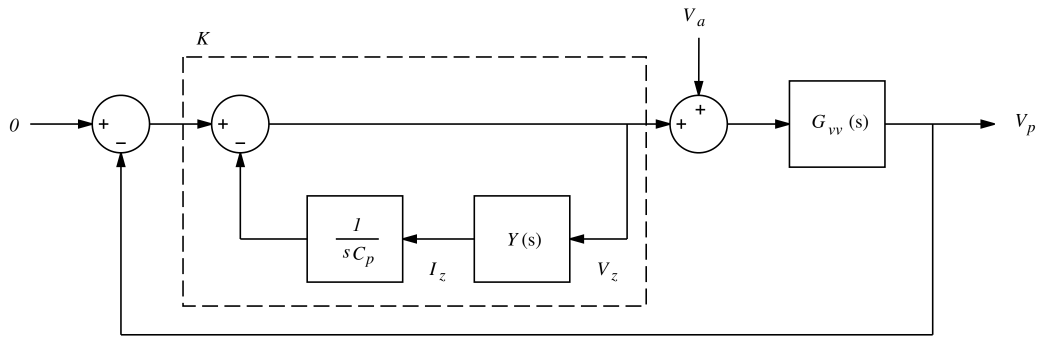

Figure 2.8: Piezoelectric shunt damping (strain) feedback control problem parameterised by $Y(s)$.

Alternatively, the closed-loop transfer function between disturbance voltage $V_a(s)$ to displacement $d(s)$ can also be derived in a similar fashion [10],

$$\tilde{G}_{ad} \triangleq \frac{d(s)}{V_a(s)} = \frac{G_{ad}(s)}{1 + G_{vv}(s)K(s)}. \tag{2.12}$$

By considering the principle of superposition, the disturbance force $f(s)$ can be included [10],

$$V_p(s) = \frac{G_{av}(s)}{1 + G_{vv}(s)K(s)} V_a(s) + \frac{G_{fv}(s)}{1 + G_{vv}(s)K(s)} f(s) \tag{2.13}$$

and

$$d(s) = \frac{G_{ad}(s)}{1 + G_{vv}(s)K(s)} V_a(s) + \frac{G_{fd}(s)}{1 + G_{vv}(s)K(s)} f(s), \tag{2.14}$$

where $G_{fd}(s) = \frac{d(s)}{f(s)}$ is the transfer function from an applied force $f(s)$ to the displacement $d(s)$ and $G_{fv}(s) = \frac{V_p(s)}{f(s)}$ is the applied force $f(s)$ to the transducer strain voltage $V_p(s)$. Further analysis and interpretation can be found in references [10, 84].

2.5 Proposed Shunt Controllers

In this section, four new shunt control techniques for piezoelectric shunt damping will be developed and presented.

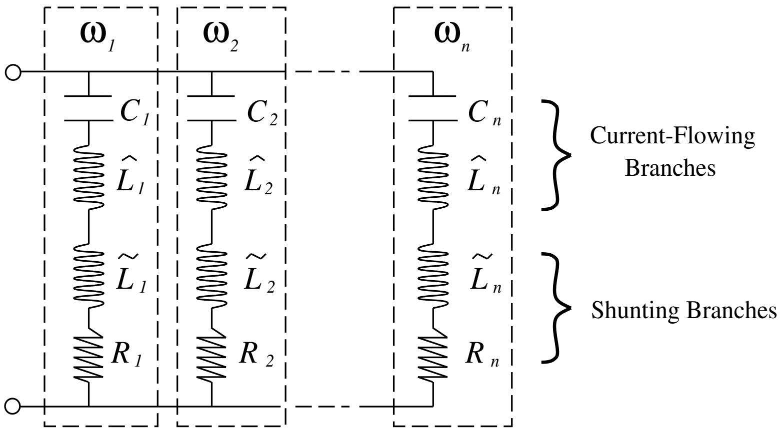

Figure 2.9: Proposed current-flowing multiple mode shunt circuit.

2.5.1 Current-Flowing Shunt Controller

The current-flowing shunt is similar in nature to the current-blocking circuit [113], as described in Section 2.2. Instead of preventing the current from flowing at a specific frequency ω_i $(i = 1, 2, 3, \ldots, n)$, current flow is allowed. This is achieved by using a series capacitor-inductor circuit $C_i - \hat{L}_i$, shown in Figure 2.9. The series, $C_i - \hat{L}_i$, is tuned to the structural resonance frequency ω_i. The series capacitor-inductor circuit, $C_i - \hat{L}_i$, appears to be a short-circuit at ω_i and approximately open-circuit for all other frequencies. The shunting branch $\tilde{L}_i - C_p$ is also tuned to ω_i, when C_p is the capacitance of the piezoelectric transducer. Therefore, each circuit branch $C_i - \hat{L}_i - \tilde{L}_i - R_i$ is functional at its own frequency ω_i, but is approximately open-circuit at all other frequencies. Notice that some level of interaction between modes that are closely spaced is expected. However, for modes that are widely spaced, this interaction will be minimal.

Example: Current-Flowing Shunt Controller for Two Modes

To illustrate the proposed shunt circuit, consider the two mode case shown in Figure 2.10, at mode frequencies ω_1 and ω_2. The first branch of the shunt circuit, with shunt inductor $\tilde{L}_1 = 1/(\omega_1^2 C_p)$ and R_1, is inserted with a current-flowing circuit consisting of a series capacitor-inductor circuit $C_1 - \hat{L}_1$, the electrical impedance is designed to approach a short-circuit at the branch frequency of ω_1, as indicated with ω_1 in Figure 2.10. This is done by selecting C_1 and $\hat{L}_1$ so that the resonance frequency is at $\omega_1 = 1/\sqrt{C_1 \hat{L}_1}$, which is a fundamental characteristic of any resonant capacitor-inductor circuit. The current-flowing circuit in the second branch also uses a resonant circuit when the electrical impedance approaches a short-circuit at the second structural frequency of ω_2 by selecting C_2 and $\hat{L}_2$, such as $\omega_2 = 1/\sqrt{C_2\hat{L}_2}$. When the two branches are connected together and presented to the piezoelectric shunting layer terminals, each branch acts independently for its respective modes. That is, the first branch is designed to introduce damping at ω_1 while not disturbing the second branch that is approximately open-circuit at ω_1, i.e. the impedance is very large. The same reason applies for the second branch.

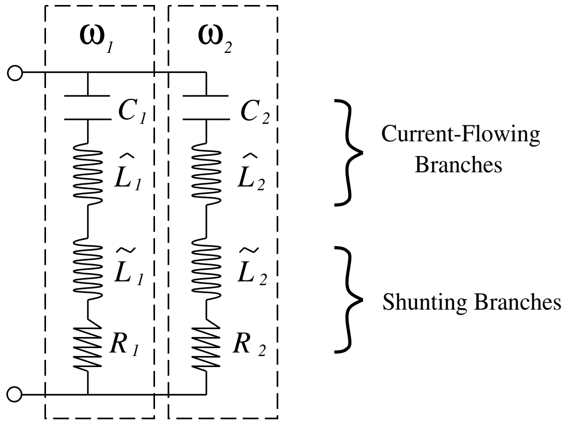

Figure 2.10: Proposed two mode current-flowing shunt circuit.

Generalised Current-Flowing Shunt Controller

The generalised case for n structural modes is

$$\tilde{L}_1 = \frac{1}{\omega_1^2 C_p}, \quad \cdots \quad, \tilde{L}_n = \frac{1}{\omega_n^2 C_p} \quad , \tag{2.15}$$

where $\tilde{L}_i$ is tuned into piezoelectric capacitance C_p. Frequencies ω_i are the mode frequencies to be passively controlled assuming that $\omega_1 < \omega_2 < \ldots < \omega_n$. The relationship for $\hat{L}_i$ current-flowing branches is

$$\hat{L}_1 = \frac{1}{\omega_1^2 C_1}, \quad \cdots \quad, \hat{L}_n = \frac{1}{\omega_n^2 C_n}. \tag{2.16}$$

By combining the series inductor values together e.g. $L_i = \tilde{L}_i + \hat{L}_i$,

$$L_1 = \frac{C_p + C_1}{\omega_1^2 C_1 C_p}, \quad \cdots \quad, L_n = \tilde{L}_n + \hat{L}_n = \frac{C_p + C_n}{\omega_n^2 C_n C_p}, \tag{2.17}$$

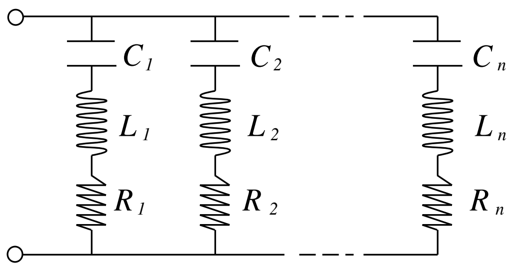

Figure 2.11: Proposed modified current-flowing multiple mode shunt circuit.

the total impedance for each shunting branch $Z_i(s)$ has been simplified. Therefore, the *modified* current-flowing shunt, shown in Figure 2.11, has one less passive element in each shunting branch. The proposed modified controller, shown in Figure 2.11, resembles the circuit of Holkamp [56]. However, there are significant differences between the two approaches.

One distinction is that the shunt circuit proposed in [56] includes only one resistor-inductor circuit for the first mode, while in this approach a capacitor-inductor-resistor circuit is used to shunt each mode. Furthermore, the methodology proposed here for determining the capacitive and inductive elements is very different to that suggested in [56]. By following the above procedure, capacitors and inductors for each parallel branch of the circuit can be determined in a very straightforward manner. This is in contrast to the methodology proposed in [56] that requires the solution to a non-trivial optimisation problem.

The total shunt branch impedance $Z_i(s)$, is

$$Z_1(s) = \frac{s^2 + \frac{R_1}{L_1}s + \frac{1}{L_1C_1}}{\frac{1}{L_1}s}, \quad \cdots \quad, Z_n(s) = \frac{s^2 + \frac{R_n}{L_n}s + \frac{1}{L_nC_n}}{\frac{1}{L_n}s}, \tag{2.18}$$

or the admittance $Y_i(s) = \frac{1}{Z_i(s)}$ is

$$Y_1(s) = \frac{\frac{1}{L_1}s}{s^2 + \frac{R_1}{L_1}s + \frac{1}{L_1C_1}}, \quad \cdots \quad, Y_n(s) = \frac{\frac{1}{L_n}s}{s^2 + \frac{R_n}{L_n}s + \frac{1}{L_nC_n}}. \tag{2.19}$$

By adding the shunt branches together, the total shunt admittance is derived as

$$Y(s) = \sum_{i=1}^{n} Y_i(s) = \sum_{i=1}^{n} \frac{\frac{1}{L_i}s}{s^2 + \frac{R_i}{L_i}s + \frac{1}{L_iC_i}}. \tag{2.20}$$

Now the feedback controller (2.11) can be determined as

$$K(s) = \frac{1}{1 + \frac{1}{C_p s}Y(s)}. \tag{2.21}$$

Using (2.20), it can be shown that the effective feedback controller is

$$K(s) = \frac{1}{1 + \sum\limits_{i=1}^{n} \frac{\frac{1}{L_i C_p}}{s^2 + \frac{R_i}{L_i} s + \frac{1}{L_i C_i}}} \tag{2.22}$$

or alternatively,

$$K(s) = \frac{\prod\limits_{i=1}^{n} \left(s^2 + \frac{R_i}{L_i} s + \frac{1}{L_i C_i} \right)}{\prod\limits_{i=1}^{n} \left(s^2 + \frac{R_i}{L_i} s + \frac{1}{L_i C_i} \right) + \sum\limits_{i=1}^{n} \frac{1}{L_i C_p} \prod\limits_{l=1, l \neq i}^{n} \left(s^2 + \frac{R_l}{L_l} s + \frac{1}{L_l C_l} \right)}. \tag{2.23}$$

Notice that the controller has a highly resonant structure and it applies a high gain at each target host structure resonance frequency. Viewing the shunted system in this manner has the advantage that the residual effects of each mode on other modes can be determined in a straightforward manner. It can be observed that as long as the controlled modes are reasonably spaced, this "residual effect" will be minimal. However, if two modes are very close, this effect can not be ignored and may degrade the performance of the shunted system at those specific resonance frequencies.

2.5.2 Series-Parallel Shunt Controller

In this section, a new multiple mode piezoelectric shunt damping structure is presented. The series-parallel impedance structure contains significantly smaller inductors than other resonant shunt techniques [14, 114].

Consider the series-parallel impedance structure shown in Figure 2.12 (a). Each parallel network $C_i - L_{h_i} - L_{b_i} - R_i$ contains two sub-networks, a current-blocking network $C_i - L_{h_i}$ and a parallel single mode shunt damping network $L_{b_i} - R_i$. As in reference [112] for a specific mode with resonance frequency ω_i, both the current-blocking and shunt damping networks $C_i - L_{h_i}$ and $L_{b_i} - C_p$, are tuned to ω_i. Note that C_p is the piezoelectric transducer capacitance.

The operation is described fairly simply. At a specific structural resonance ω_i, the current-blocking networks when tuned to that specific mode has an extremely large impedance. All other adjacent current-blocking networks, when tuned to the remaining structural resonance frequencies, have a low impedance at ω_i. Thus, a voltage applied at the terminals results in a current that flows freely through the detuned low impedance current-blocking networks and through the shunt damping networks connected in parallel to the current-blocking network

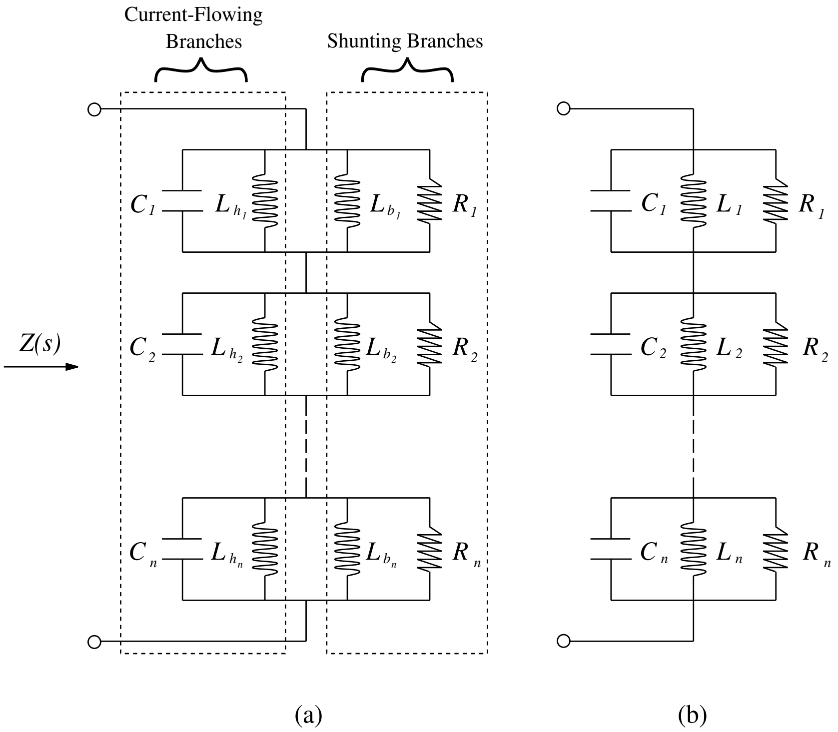

Figure 2.12: Series-parallel impedance structure (a) and simplified circuit (b).

tuned to ω_i. This way the circuit is decoupled so that each damping network $L_{b_i} - R_i - C_p$ can be tuned individually to the target resonance frequency. At a structural resonance ω_i, the overall impedance is approximately equivalent to $L_{b_i} - R_i$, that is, a series combination L_{b_i} with R_i.

In its simplest form, as described above, the series-parallel impedance structure contains fewer components than traditional current-blocking networks [112]. The circuit is little more than the parallel dual of so-called current-blocking techniques [14], as described in the previous section. Benefits arise from a suitable choice in the arbitrary capacitances C_i. The recommended capacitance value is 10 to 20 times larger than the piezoelectric capacitance. In this case, the current-blocking inductors will be significantly smaller than the damping inductors. As shown in Figure 2.12 (b), the circuit can be simplified by combining the parallel current-blocking and damping inductors.

When the current-blocking and damping inductors are tuned to the resonance frequencies ω_i, i.e.

$$L_{h_i} = \frac{1}{\omega_i^2 C_i} \quad \text{for all} \quad i = \{1, 2, 3, ..., n\} \tag{2.24}$$

and

$$L_{b_i} = \frac{1}{\omega_i^2 C_p} \quad \text{for all} \quad i = \{1, 2, 3, ..., n\}, \tag{2.25}$$

the effective inductance resulting from the parallel connection of (2.24) and (2.25) is

$$L_i = \left(\frac{L_{b_i} L_{h_i}}{L_{b_i} + L_{h_i}} \right) \quad \text{for all} \quad i = \{1, 2, 3, ..., n\}. \tag{2.26}$$

As C_i has been chosen significantly larger than C_p, there is a dramatic reduction in required inductance value. The impedance of the modified series-parallel controller, as shown in Figure 2.12 (b), is

$$Z(s) = \sum_{i=1}^{n} \frac{\frac{1}{C_i} s}{s^2 + \frac{1}{R_i C_i} s + \frac{1}{L_i C_i}}. \tag{2.27}$$

2.5.3 Resonant Shunt Controllers

As shown in Section 2.2, a number of impedance structures have been suggested. This includes the single-mode shunt damping impedance proposed in [41, 48, 112] and several modifications of this technique to allow for multi-mode shunt damping [56, 113, 114]. This section proposed a new class of admittances suitable for multi-mode piezoelectric shunt damping. Furthermore, stability and robustness properties for this class of admittances were analysed and studied.

In Section 2.4.1, piezoelectric shunt damping is equivalent to a feedback control problem with a specific feedback structure, as shown in Figures 2.7 and 2.8[2]. This understanding of the underlying feedback structure can be interpreted as from the existing results in the literature in a meaningful way. Furthermore, new contributions may be made to the field in the form of generating new classes of high-performance shunt damping impedance structures.

Notice that in Figure 2.8, the closed-loop transfer function from the disturbance input $V_a(s)$ to $d(s)$ can be written as

$$\tilde{G}_{ad}(s) \triangleq \frac{d(s)}{V_a(s)} = \frac{G_{ad}(s)}{1 + K(s) G_{vv}(s)} \tag{2.28}$$

where

$$K(s) = \frac{1}{1 + \frac{1}{C_p s} Y(s)}. \tag{2.29}$$

Now the role of the shunting admittance $Y(s)$ is to move the closed-loop poles of the system deeper into the left half plane, i.e. to add more damping to each mode. Therefore, an effective

[2]This observation was first made in reference [10].

admittance structure for this purpose is [84]

$$Y(s) = \frac{C_p s \sum_{i=1}^{N} \frac{\alpha_i \omega_i^2}{s^2+2d_i\omega_i s+\omega_i^2}}{1 - \sum_{i=1}^{N} \frac{\alpha_i \omega_i^2}{s^2+2d_i\omega_i s+\omega_i^2}}, \tag{2.30}$$

where $\alpha_i \geq 0$ and $d_i > 0$ for $i = 1, 2, \ldots, N$, and

$$\sum_{i=1}^{N} \alpha_i = 1. \tag{2.31}$$

An immediate choice for $\alpha_i = \frac{1}{N}$ for $i = 1, 2, \ldots, N$. This will ensure that the condition in (2.31) is satisfied. It is straightforward to verify that for the admittance structure defined in (2.30), the effective controller expression in (2.29) will be

$$K(s) = 1 - \sum_{i=1}^{N} \frac{\alpha_i \omega_i^2}{s^2 + 2d_i\omega_i s + \omega_i^2}. \tag{2.32}$$

This then can be shown to be equivalent to

$$K(s) = \sum_{i=1}^{N} \frac{\alpha_i s(s + 2d_i\omega_i)}{s^2 + 2d_i\omega_i s + \omega_i^2}. \tag{2.33}$$

It should be possible to imagine why this specific structure may be quite effective in reducing unwanted vibrations of the base structure. Flexible structures are inherently highly resonant systems whose dynamics consist of a large number of very lightly damped modes. The admittance suggested in (2.30), once shunted to the piezoelectric transducer with the piezoelectric capacitance of C_p, will result in an equivalent feedback control problem where the controller $K(s)$ is defined in (2.33). It can be observed that this controller has a highly resonant structure dictated by the damping factors $d_1, \ldots, d_N$. The controller applies a high gain at each specific resonance frequency. This is done by applying a very narrow bandpass filter around each resonance frequency of the base structure.

To see the connection with earlier work if $N = 1$, then the controller may be tuned to one specific resonance frequency, say ω_ℓ. In this case, it can be shown that

$$Y(s) = \frac{\omega_\ell^2 C_p}{s + 2d_\ell\omega_\ell}.$$

Hence, $Y(s)$ effectively represents the series connection of a resistor $R = \frac{2d_\ell}{\omega_\ell C_p}$ with an inductor $L = \frac{1}{\omega_\ell^2 C_p}$ shunted across the piezoelectric transducer terminals. This is the original single-mode shunt damping circuit proposed by Hagood and von Flotow [48]. Based on this observation, it may be argued that $Y(s)$ in (2.30) effectively generates a phase and gain relationship around each resonant frequency that is similar to the generated by an inductor-resistor $(L - R)$ circuit tuned to that specific resonant frequency.

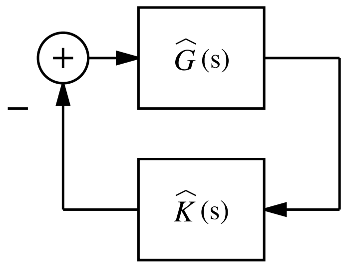

Figure 2.13: Equivalent system for study of closed-loop stability.

Closed-loop Stability In this section, the stability properties of the proposed shunting impedance is studied. By inspection, it can be verified that the closed-loop stability of the shunted system is equivalent to the stability of the feedback connection in Figure 2.13 with

$$\begin{aligned}\hat{G}(s) &= sG_{vv}(s)\\ &= \sum_{i=1}^{M} \frac{\gamma_i s}{s^2 + 2\zeta_i\omega_i s + \omega_i^2}\end{aligned} \tag{2.34}$$

and

$$\hat{K}(s) = \sum_{i=1}^{N} \frac{\alpha_i(s + 2d_i\omega_i)}{s^2 + 2d_i\omega_i s + \omega_i^2}.$$

The proof of closed-loop stability is rather straightforward and is based on the observation that $\hat{K}(s)$ is a strictly positive real (SPR) transfer function, i.e. $\hat{K}$ is stable and $\hat{K}(j\omega) + \hat{K}(-j\omega) > 0$ for all $\omega \in \mathbf{R}$, and $\hat{G}(s)$ is a positive real (PR) transfer function, i.e. $\hat{G}$ is stable and $\hat{G}(j\omega) + \hat{G}(-j\omega) \geq 0$ for all $\omega \in \mathbf{R}$. The feedback connection of two SISO systems, where one is a SPR and the other is a PR transfer function, is stable with a guaranteed gain margin of infinity, refer to Chapter 10 of [70]. Therefore, the admittance suggested in (2.30) results in a closed-loop system that is constant with favourable stability margins [84]. Alternatively, using the root-loci or Bode diagram to determine the stability for the system can also be considered. Since, the stability of system has already been proven earlier it is pointless expanding the stability proof. However, using the root-loci or Bode diagram to prove the closed-loop stability is open to further examination.

It should be noted that (2.34) with M arbitrarily large, i.e. $M \gg N$, is a reasonable finite-dimensional approximation of (2.5). For further explanation, refer to reference [60]. In addition, ζ_i must be positive, i.e. $\zeta_i > 0$. That is, the mechanical system does not include negative damping i.e. a self-excited system.

Properties of the Proposed Admittance and Implementation Issues The ultimate goal is to implement the admittance $Y(s)$ digitally using the synthetic admittance circuit proposed in Section 2.3. For this to be achievable in an efficient way, $Y(s)$ must satisfy a number of conditions. It should be at least proper, and preferably strictly proper with a bandwidth that is not excessively larger than that of the highest in-bandwidth mode of the base structure that is to be controlled. In this section, the structure of the proposed admittance is studied and will show that it satisfies all the above conditions.

The stability of $Y(s)$ is studied first. This can be verified by observation that the Nyquist plot of

$$\sum_{i=1}^{M} \frac{\alpha_i \omega_i^2}{s^2 + 2d_i\omega_i s + \omega_i^2} \tag{2.35}$$

with $M \gg N$ will never cross the critical point, $-1 + j0$. This along with the feedback structure of $Y(s)$ in Equation (2.30), establishes the stability of the admittance $Y(s)$.

Next, the admittance $Y(s)$ can be written as

$$\begin{aligned} Y(s) &= \frac{\sum_{i=1}^{N} \frac{C_p \alpha_i \omega_i^2 s}{s^2+2d_i\omega_i s+\omega_i^2}}{\sum_{i=1}^{N} \frac{\alpha_i s(s+2d_i\omega_i)}{s^2+2d_i\omega_i s+\omega_i^2}} \\ &= \frac{H(s)}{J(s)}. \end{aligned}$$

Now it can be verified that the numerator transfer function, $H(s)$, is a positive real transfer function, which means

$$-\frac{\pi}{2} \leq \angle H(s) \leq \frac{\pi}{2}.$$

Furthermore, it can be verified that

$$0 < \angle J(s) < \pi.$$

The conclusion may be made

$$-\frac{\pi}{2} < \angle Y(s) < \frac{\pi}{2},$$

which means that $Y(s)$ is a strictly positive real transfer function, i.e. the Nyquist plot of $Y(s)$ is confined to the right half of the complex plane. The implication of this observation is that $Y(s)$ is indeed possible using purely passive circuit components, i.e. resistors, inductors and capacitors [84]. Such a circuit may be realised by observing that $Y(s)$ can be written as

$$Y(s) = \frac{C_p \sum_{i=1}^{N} \alpha_i \omega_i^2 \prod_{\ell=1,\ell\neq i}^{N}(s^2 + 2d_\ell\omega_\ell s + \omega_\ell^2)}{\sum_{i=1}^{N} \alpha_i (s + 2d_i\omega_i) \prod_{\ell=1,\ell\neq i}^{N}(s^2 + 2d_\ell\omega_\ell s + \omega_\ell^2)}. \tag{2.36}$$

Robustness Issues An interesting property of the admittance proposed in (2.30) is its robustness. To make this clearer, under (2.30) the closed-loop system is stable with a gain margin of infinity. Therefore, the spill-over effect due to the existence of out-of-bandwidth modes will not destabilise the closed-loop system. As a matter of fact, the spill-over effect will be minimal since the admittance, and hence the resulting equivalent controller $K(s)$ in (2.33), has a highly resonant nature.

The structure of the admittance $Y(s)$ is such that if the resonant frequencies $\omega_1, \ldots, \omega_N$ are slightly different from the actual resonance frequencies of the base structure, closed-loop stability is guaranteed. This is a favourable property as these resonance frequencies are known to change with environmental conditions and dynamic loading.

A particularly important robustness feature of the proposed admittance structure is that it maintains closed-loop stability even if the value of the piezoelectric capacitance in (2.30) is estimated incorrectly. A proof of this claim follows.

Assume that the actual value of the piezoelectric capacitance is C_p, while the estimate of $\bar{C}_p$ is $\bar{C}_p = \eta C_p$. Therefore, the admittance expression in (2.30) should be modified to

$$Y(s) = \frac{\bar{C}_p s \sum_{i=1}^{N} \frac{\alpha_i \omega_i^2}{s^2 + 2d_i\omega_i s + \omega_i^2}}{1 - \sum_{i=1}^{N} \frac{\alpha_i \omega_i^2}{s^2 + 2d_i\omega_i s + \omega_i^2}}.$$

Arguing along similar lines in Section 2.5.3, the stability of the resulting closed-loop system is equivalent to the stability of the system $G_{vv}(s)$ with

$$\hat{G}(s) = sG_{vv}(s)$$

and

$$\hat{K}(s) = \frac{\frac{1}{s}}{1 + \frac{\eta}{s}\tilde{Y}(s)},$$

where

$$\tilde{Y}(s) = \frac{1}{C_p} Y(s).$$

Now, that $Y(s)$ is a strictly positive, real transfer function that has already been established. Therefore, strict positive realness of $\tilde{Y}(s)$ follows immediately. Thus, it can be proved that $\hat{K}(s)$ is stable and that $\hat{K}(j\omega) + \hat{K}(-j\omega) > 0$ for all $\omega \in \mathbf{R}$. So, $\hat{K}(s)$ is itself a strictly positive real system. Given that $\hat{G}(s)$ is a positive real system, the closed-loop system is stable for any $\eta > 0$ [84] and may be concluded. Although the closed-loop system will not be destabilised, the performance of the system may severely deteriorate as η deviates from one.

Optimal Tuning of the Admittance The structure of the admittance in (2.30) guarantees closed-loop stability of the system. In order to achieve good performance, appropriate values for the damping parameters $d_1, d_2, \ldots, d_N$ need to be determined. This may be done by seeking a solution to the following optimisation problem:

$$d_1^*, d_2^*, \ldots, d_N^* = \arg\min \|\tilde{G}_{ad}(s)\|_2. \tag{2.37}$$

This is a non-convex optimisation problem that could have many local minima. Typically, a gradient descent technique could be used to solve the problem. In doing so, an initial starting point would need to be chosen to start the optimisation process. Given that for all positive $d_1, d_2, \ldots, d_N$ the closed-loop system is stable and any positive value may be considered acceptable. However, considering the structure of the system, it may be possible to find a set of damping ratios reasonably close to a minima.

The transfer function $G_{vv}(s)$ in (2.5) is a high order system of very lightly damped resonant modes. Depending on the geometry of the structure, these modes may be reasonably far away from one another. Given the highly localised nature of $Y(s)$, it may be a reasonable assumption to consider the effect of each individual bandpass section of the admittance on the specific mode of the base structure. Doing so would mean searching for a value of the damping ratio that would place the closed-loop poles of the system as deep into the left half of the complex plane as possible. A repeat of this procedure for every single mode that is to be controlled may result in a good starting point for the optimisation problem (2.37).

Additional Resonant Shunt Controller Another impedance structure that results in a favorable closed-loop performance can be constructed by choosing the following for an effective controller: K

$$K(s) = \sum_{i=1}^{N} \frac{\alpha_i s^2}{s^2 + 2d_i\omega_i s + \omega_i^2}, \tag{2.38}$$

where $\alpha_i \geq 0$ for $i = 1, 2, ..., N$ and

$$\sum_{i=1}^{N} \alpha_i = 1. \tag{2.39}$$

Also, the admittance transfer function that has to be implemented is

$$\begin{aligned} Y(s) &= \frac{C_p s \sum_{i=1}^{N} \frac{\alpha_i\left(2d_i\omega_i s + \omega_i^2\right)}{s^2+2d_i\omega_i s+\omega_i^2}}{1 - \sum_{i=1}^{N} \frac{\alpha_i\left(2d_i\omega_i s + \omega_i^2\right)}{s^2+2d_i\omega_i s+\omega_i^2}} \\ &= \frac{C_p \sum_{i=1}^{N} \alpha_i \left(2d_i\omega_i s + \omega_i^2\right) \Pi_{l=1, i\neq l}^{N} \left(s^2 + 2d_l\omega_l s + \omega_l^2\right)}{\sum_{i=1}^{N} (\alpha_i s)\, \Pi_{l=1, i\neq l}^{N} \left(s^2 + 2d_l\omega_l s + \omega_l^2\right)}. \end{aligned} \tag{2.40}$$

By using the same techniques illustrated above, similar stability, implementation, robustness and optimal results can be obtained.

2.5.4 Robust Passive Shunt Controller

In the previous section, Section 2.5.3, piezoelectric shunt damping showed that it can be viewed as a feedback control problem of a specific structure. Using this underlying structure, an impedance $Y(s)$ that moves the damped poles of the shunted system deeper into the left-half plane can be designed, i.e. to add more damping.

Two effective admittances for this purpose were developed, as shown in Section 2.5.3. They are

$$Y_1(s) = \frac{C_p s \sum_{i=1}^{N} \frac{\alpha_i \omega_i^2}{s^2 + 2\hat{d}_i \hat{\omega}_i s + \hat{\omega}_i^2}}{1 - \sum_{i=1}^{N} \frac{\alpha_i \omega_i^2}{s^2 + 2d_i \omega_i s + \omega_i^2}} = \frac{C_p \sum_{i=1}^{N} \left(\alpha_i \omega_i^2\right) \Pi_{l=1, i \neq l}^{N} \left(s^2 + 2d_l \omega_l s + \omega_l^2\right)}{\sum_{i=1}^{N} \left(s + 2d_i \omega_i\right) \Pi_{l=1, i \neq l}^{N} \left(s^2 + 2d_l \omega_l s + \omega_l^2\right)} \tag{2.41}$$

and

$$Y_2(s) = \frac{C_p s \sum_{i=1}^{N} \frac{\alpha_i \left(2d_i \omega_i s + \omega_i^2\right)}{s^2 + 2d_i \omega_i s + \omega_i^2}}{1 - \sum_{i=1}^{N} \frac{\alpha_i \left(2d_i \omega_i s + \omega_i^2\right)}{s^2 + 2d_i \omega_i s + \omega_i^2}} = \frac{C_p \sum_{i=1}^{N} \alpha_i \left(2d_i \omega_i s + \omega_i^2\right) \Pi_{l=1, i \neq l}^{N} \left(s^2 + 2d_l \omega_l s + \omega_l^2\right)}{\sum_{i=1}^{N} \left(\alpha_i s\right) \Pi_{l=1, i \neq l}^{N} \left(s^2 + 2d_l \omega_l s + \omega_l^2\right)}, \tag{2.42}$$

where ω_i is the specified frequencies and the damping parameter d_i must satisfy $d_i > 0$ for $i = 1, 2, 3, \ldots, N$. Also for passivity, the following condition must be satisfied:

$$\sum_{i=1}^{N} \alpha_i = 1 \text{ and } \alpha_i > 0. \tag{2.43}$$

An immediate choice for α_i is

$$\alpha_i = \frac{1}{N} \text{ for } i = 1, 2, 3, \ldots, N.$$

It is straightforward to verify that for the impedances $Y_1(s)$ and $Y_2(s)$, the effective controllers $K(s)$ in Equation (2.11) will be

$$K_1(s) = \sum_{i=1}^{N} \frac{\alpha_i s \left(s + 2d_i \omega_i\right)}{s^2 + 2d_i \omega_i s + \omega_i^2} \tag{2.44}$$

and

$$K_2(s) = \sum_{i=1}^{N} \frac{\alpha_i s^2}{s^2 + 2d_i \omega_i s + \omega_i^2}. \tag{2.45}$$

Normally for the proposed impedances (2.41) and (2.42), the frequencies $\hat{\omega}_i$ are equal to the structural resonance frequencies ω_i, i.e. $\omega_i = \hat{\omega}_i$. For the proposed robust passive piezoelectric shunt controller, additional controllers are placed above and below ω_i. That is,

$$\omega_i = \{\hat{\omega}_{i,-M}, \ldots, \hat{\omega}_{i,-2}, \hat{\omega}_{i,-1}, \hat{\omega}_{i,0}, \hat{\omega}_{i,1}, \hat{\omega}_{i,2}, \ldots, \hat{\omega}_{i,M}\} \qquad i\epsilon\{1 \cdots N\},$$

where $\hat{\omega}_{i,0}$ is equivalent to the specific frequencies, i.e. $\omega_i = \hat{\omega}_{i,0}$, assuming that

$$\hat{\omega}_{i,-M} < \ldots < \hat{\omega}_{i,-2} < \hat{\omega}_{i,-1} < \hat{\omega}_{i,0} < \hat{\omega}_{i,1} < \hat{\omega}_{i,2} < \ldots < \hat{\omega}_{i,M} \qquad i\epsilon\{1 \cdots N\}$$

and

$$\hat{\omega}_{1,x} < \ldots < \hat{\omega}_{i,x_N} \qquad x_1, \ldots, x_N \epsilon\{-M \cdots M\}.$$

Therefore, the new damping vector is described as

$$d_i = \{\hat{d}_{i,-M}, \ldots, \hat{d}_{i,-2}, \hat{d}_{i,-1}, \hat{d}_{i,0}, \hat{d}_{i,1}, \hat{d}_{i,2}, \ldots, \hat{d}_{i,M}\} \qquad i\epsilon\{1 \cdots N\},$$

and

$$\{\hat{d}_{i,-M}, \ldots, \hat{d}_{i,-2}, \hat{d}_{i,-1}, \hat{d}_{i,0}, \hat{d}_{i,1}, \hat{d}_{i,2}, \ldots, \hat{d}_{i,M}\} > 0 \qquad i\epsilon\{1 \cdots N\}.$$

The two new impedances have the following structures:

$$Y_1(s) = \frac{C_p s \sum_{i=1}^{N} \Phi_1}{1 - \sum_{i=1}^{N} \Phi_1}, \tag{2.46}$$

$$\Phi_1 = \left(\sum_{j=-M}^{-1} \frac{\alpha_{i,j}\hat{\omega}_{i,j}^2}{s^2 + 2\hat{d}_{i,j}\hat{\omega}_{i,j}s + \hat{\omega}_{i,j}^2} + \frac{\alpha_{i,0}\hat{\omega}_{i,0}^2}{s^2 + 2\hat{d}_{i,0}\hat{\omega}_{i,0}s + \hat{\omega}_{i,0}^2} + \sum_{j=1}^{M} \frac{\alpha_{i,j}\hat{\omega}_{i,j}^2}{s^2 + 2\hat{d}_{i,j}\hat{\omega}_{i,j}s + \hat{\omega}_{i,j}^2} \right)$$

and

$$Y_2(s) = \frac{C_p s \sum_{i=1}^{N} \Phi_2}{1 - \sum_{i=1}^{N} \Phi_2}, \tag{2.47}$$

$$\Phi_2 = \left(\sum_{j=-M}^{-1} \frac{\alpha_{i,j}\left(2\hat{d}_{i,j}\hat{\omega}_{i,j}s + \hat{\omega}_{i,j}^2\right)}{s^2 + 2\hat{d}_{i,j}\hat{\omega}_{i,j}s + \hat{\omega}_{i,j}^2} + \frac{\alpha_{i,0}\left(2\hat{d}_{i,0}\hat{\omega}_{i,0}s + \hat{\omega}_{i,0}^2\right)}{s^2 + 2\hat{d}_{i,0}\hat{\omega}_{i,0}s + \hat{\omega}_{i,0}^2} + \sum_{j=1}^{M} \frac{\alpha_{i,j}\left(2\hat{d}_{i,j}\hat{\omega}_{i,j}s + \hat{\omega}_{i,j}^2\right)}{s^2 + 2\hat{d}_{i,j}\hat{\omega}_{i,j}s + \hat{\omega}_{i,j}^2} \right),$$

where the modified condition $\sum_{i=1}^{N}\sum_{i=-M}^{M} \alpha_{i,j} = 1$ and $\alpha_{i,j} > 0$ must be satisfied by both Equations (2.46) and (2.47).

It can be observed that the proposed robust passive piezoelectric shunt controller has the order $2M + 1$ for each i^{th} mode. The overall impedance or controller order is $N(2M + 1)$. Therefore, the effective controllers $K_1(s)$ and/or $K_2(s)$ are equivalent to

$$K_1(s) = \sum_{i=1}^{N} \left(\sum_{j=-M}^{-1} \frac{\alpha_{i,j}s\left(s + 2\hat{d}_{i,j}\hat{\omega}_{i,j}\right)}{s^2 + 2\hat{d}_{i,j}\hat{\omega}_{i,j}s + \hat{\omega}_{i,j}^2} + \frac{\alpha_{i,0}s\left(s + 2\hat{d}_{i,0}\hat{\omega}_{i,0}\right)}{s^2 + 2\hat{d}_{i,0}\hat{\omega}_{i,0}s + \hat{\omega}_{i,0}^2} + \sum_{j=1}^{M} \frac{\alpha_{i,j}s\left(s + 2\hat{d}_{i,j}\hat{\omega}_{i,j}\right)}{s^2 + 2\hat{d}_{i,j}\hat{\omega}_{i,j}s + \hat{\omega}_{i,j}^2} \right) \tag{2.48}$$

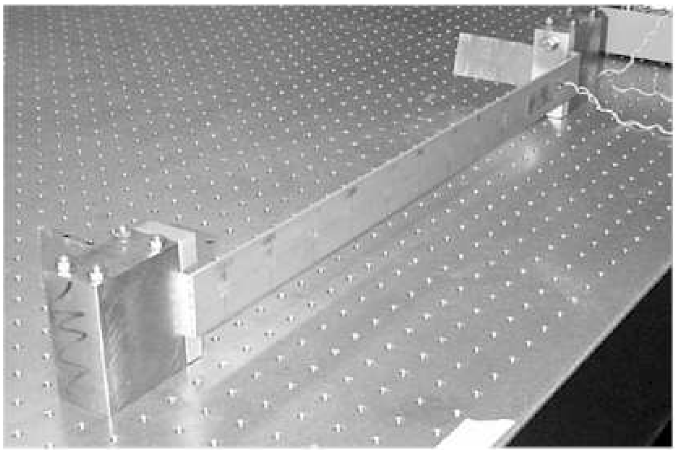

Figure 2.14: Piezoelectric laminated simply supported beam apparatus [10].

and/or

$$K_2(s) = \sum_{i=1}^{N} \left(\sum_{j=-M}^{-1} \frac{\alpha_{i,j} s^2}{s^2 + 2\hat{d}_{i,j}\hat{\omega}_{i,j} s + \hat{\omega}_{i,j}^2} + \frac{\alpha_{i,0} s^2}{s^2 + 2\hat{d}_{i,0}\hat{\omega}_{i,0} s + \hat{\omega}_{i,0}^2} + \sum_{j=1}^{M} \frac{\alpha_{i,j} s^2}{s^2 + 2\hat{d}_{i,j}\hat{\omega}_{i,j} s + \hat{\omega}_{i,j}^2} \right). \tag{2.49}$$

2.6 Experimental Verification

In this section, the proposed control schemes will be validated experimentally on three piezoelectric laminated resonant structures: a simply supported beam, a simply supported plate and a cantilever beam.

2.6.1 Piezoelectric Experimental Apparatuses

Photographs of the three piezoelectric laminate structures are shown in Figures 2.14, 2.15 and 2.16. For all structures, two piezoelectric patches are bonded to the surface in a collocated fashion using a strong adhesive material. On each structure, a piezoelectric patch will be used as an actuator to generate a disturbance, and another as a shunting layer, as shown in Figure 2.17.

The experimental simply supported beam apparatus, as shown in Figure 2.14, consists of a uniform aluminium beam with a rectangular cross section. The beam parameters are given

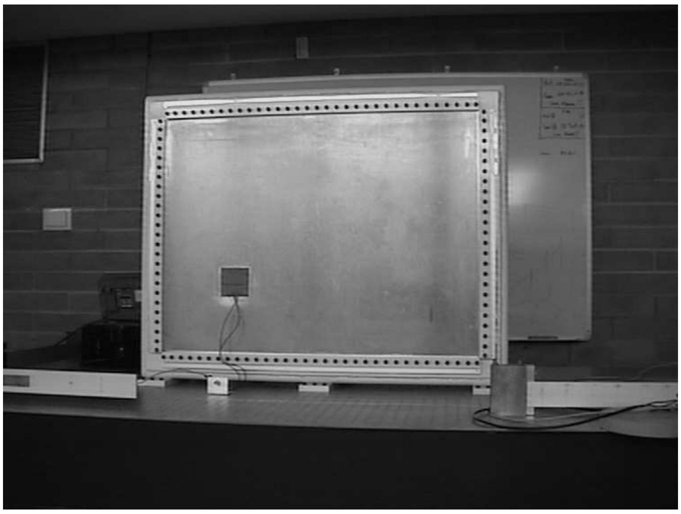

Figure 2.15: Piezoelectric laminated simply supported plate apparatus.

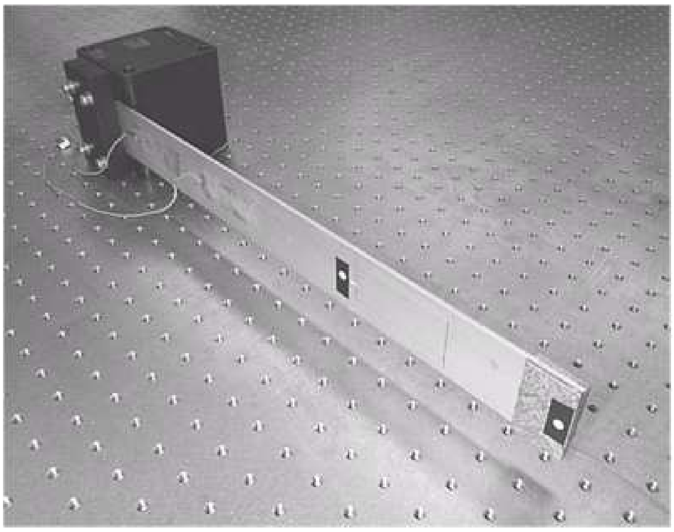

Figure 2.16: Piezoelectric laminated cantilever apparatus.

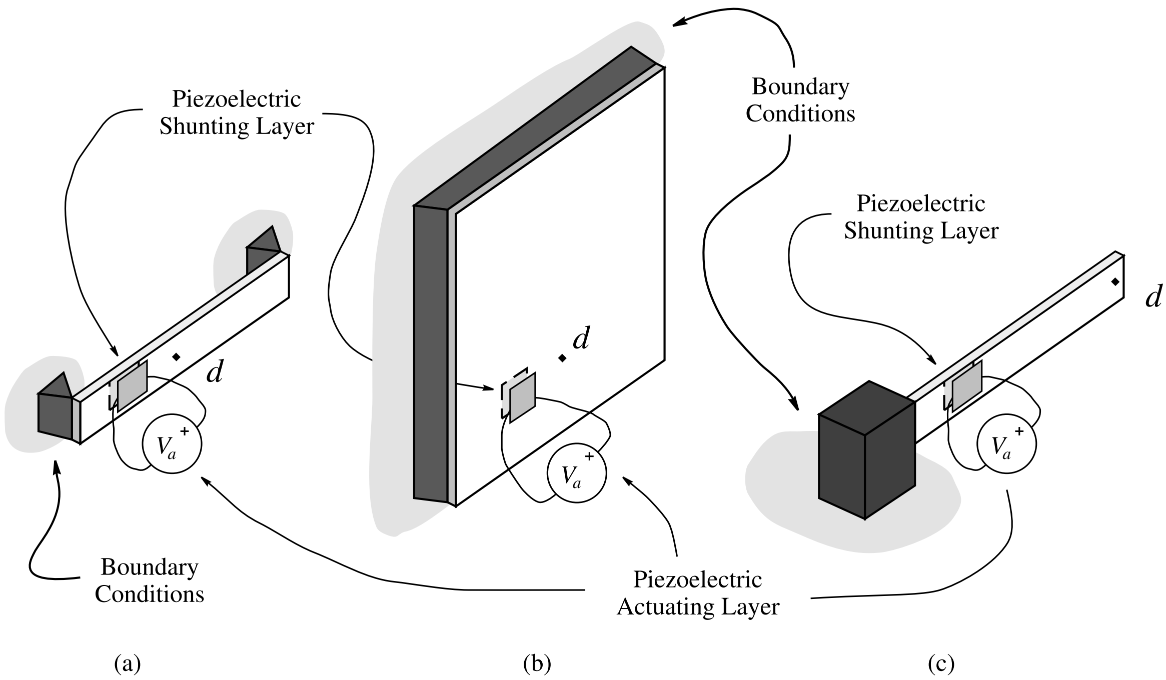

Figure 2.17: Experimental piezoelectric laminated structures: simply supported beam (a), simply supported plate (b) and cantilever beam (c). Note V_a is the applied disturbance actuator voltage and d is the displacement at some point on the structure.

in Table 2.1. A pair of identical piezoelectric ceramic patches are attached symmetrically to either side of the beam structure at 0.05 m from one of the pinned boundary conditions, with reference to Figure 2.17. The piezoceramic elements used on the experimental structure are PIC151[3] lead-zirconium-titanate (PZT) patches. The physical parameters for the PIC151 piezoelectric ceramic patches are given in Table 2.2. For a detailed description of the simply supported beam apparatus, please refer to reference [10].

The experimental plate is of uniform thickness and pinned at all edges. Two PIC151 piezoelectric ceramic patches are attached symmetrically to either side of the plate surface in a collocated manner, as shown in Figure 2.17. Dimensions of the plate and physical properties of the piezoelectric layers are summarised in Tables 2.3 and 2.4 respectively. For a more detailed description of the experimental plate apparatus, please refer to [52].

The cantilever beam apparatus consists of a uniform aluminium bar with a rectangular cross section, clamped at one end. A small mass M is attached to the free end of the structure. Two PIC151 piezoelectric ceramic patches are attached to the surface using a strong adhesive material. Dimensions of the cantilever structure and physical properties of the piezoelectric layers are summarised in Tables 2.5 and 2.6 respectively.

When observing the dynamics of a structure, it is common practice to consider the transfer function between the displacement at some point on the structure and the disturbance actuator voltage applied to the actuating patch $G_{ad}(s)$. Another important transfer function is the dynamics between the shunting piezoelectric voltage (assuming $Z(s) = \infty$) and the actuator voltage. Since the shunting layer voltage and actuating voltage are collocated, as shown in Figure 2.17, $G_{vv}(s)$ can be directly measured, i.e. $G_{vv}(s) = G_{av}(s)$.

For the resonant structures, the energy of the system needs to be experimentally minimised. This can be achieved by minimising the transfer function $G_{ad}(s)$, i.e. the disturbance actuator voltage $V_a(s)$ to the displacement at a point on the structure $d(s)$, as this effectively reduces the vibration.

To verify the presence of an attached piezoelectric shunted transducer, a theoretical model is needed for the transfer functions $G_{vv}(s)$ and $G_{ad}(s)$. Therefore, a model for the plant will consist of one input and two outputs (SIMO system). That is

$$\begin{bmatrix} V_p(s) \\ d(s) \end{bmatrix} = G_p(s)\ V_a(s), \tag{2.50}$$

[3]These patches are manufactured by Polytec PI Ceramics.

Parameter	Symbol	Unit
Length	L	0.6 m
Width	w_b	0.05 m
Thickness	h_b	0.003 m
Young's modulus	E_b	65×10^9 N/m^2
Mass / unit area	ρ	2650 kg/m^2

Table 2.1: Simply supported beam parameters.

where the open-loop plant transfer function matrix $G_p(s)$ is

$$G_p(s) = \begin{bmatrix} G_{vv}(s) \\ G_{ad}(s) \end{bmatrix},$$

or $G_p(s) \in \mathbb{C}^{2\times1}$. Note s is equivalent to $j\omega$.

Employing a Polytec PSV-300 laser scanning vibrometer and a Hewlett Packard 35670A spectrum analyser, the experimental transfer functions $G_{ad}(s)$ and $G_{vv}(s)$ were measured. The experimental transfer functions for all three piezoelectric laminated structures are shown in Figures 2.18, 2.19 and 2.20. Using the subspace based system identification technique, as described in Section 2.4, models were obtained for each experimental apparatus. The identified model transfer functions are also shown in Figures 2.18, 2.19 and 2.20. Overall, the identified models were found to be a good representation, in the bandwidth of interest, for the piezoelectric experimental apparatuses.

2.6.2 Shunt Controllers

In this section, the proposed controller designs can now be experimental validated.

Current-Flowing Shunt Controller

The proposed control scheme will be validated experimentally on two resonant structures; the simply supported beam and the simply supported plate.

Parameter	**Symbol**	**Unit**
Location x-direction	x_1	$0.05\ m$
Length	l_p	$0.0699\ m$
Thickness	h_p	$0.25 \times 10^{-3}\ m$
Capacitance	C_p	$105.77 \times 10^{-9}\ F$
Young's modulus	E_p	$62 \times 10^{9}\ N/m^2$
Strain constant	d_{31}	$-210 \times 10^{-12}\ m/V$
Electromechanical coupling factor	k_{31}	0.340
Stress constant / voltage coefficient	g_{31}	$-11.5 \times 10^{-3}\ Vm/N$

Table 2.2: Simply supported beam piezoelectric transducer parameters.

Parameter	**Symbol**	**Unit**
Length	L_x	$0.8\ m$
Length	L_y	$0.6\ m$
Thickness	h	$0.004\ m$
Young's modulus	E	$65 \times 10^{9}\ N/m^2$
Poisson's ratio	ν	0.3
Mass / unit area	ρ	$10.6\ kg/m^2$

Table 2.3: Simply supported plate parameters.

Parameter	Symbol	Unit
Location x-direction	x_1	$0.1536\ m$
Location y-direction	y_1	$0.1418\ m$
Length	$L_{px}\ L_{py}$	$0.0724\ m$
Thickness	h_p	$0.0025\ m$
Capacitance	C_p	$67.9 \times 10^{-9}\ F$
Young's modulus	E_p	$62 \times 10^{9}\ N/m^2$
Poisson's ratio	ν_p	0.3
Strain constant	d_{31}	$-320 \times 10^{-12}\ m/V$
Electromechanical coupling factor	k_{31}	0.44
Stress constant / voltage coefficient	g_{31}	$-9.5 \times 10^{-3}\ V\ m/N$

Table 2.4: Simply supported plate piezoelectric transducer parameters.

Parameter	Symbol	Unit
Length	L	$0.450\ m$
Width	w	$0.050\ m$
Thickness	h	$0.003\ m$
Young's modulus	E	$65 \times 10^{9}\ N/m^2$
Mass / unit area	ρ	$7.2\ Kg/m^2$
Mass	M	$0.2\ Kg$

Table 2.5: Cantilever beam parameters.

Parameter	Symbol	Unit
Piezoelectric actuator location	x_1	0.130 m
Piezoelectric shunt location	x_1	0.130 m
Length	l_p	0.075 m
Width	w_p	0.025 m
Thickness	h_p	0.0025 m
Capacitance	C_p	104×10^{-9} F
Young's modulus	E_p	62×10^{9} N/m^2
Strain constant	d_{31}	-320×10^{-12} m/V
Electromechanical coupling factor	k_{31}	0.44
Stress constant / voltage coefficient	g_{31}	-9.5×10^{-3} $V\ m/N$

Table 2.6: Cantilever piezoelectric transducer parameters.

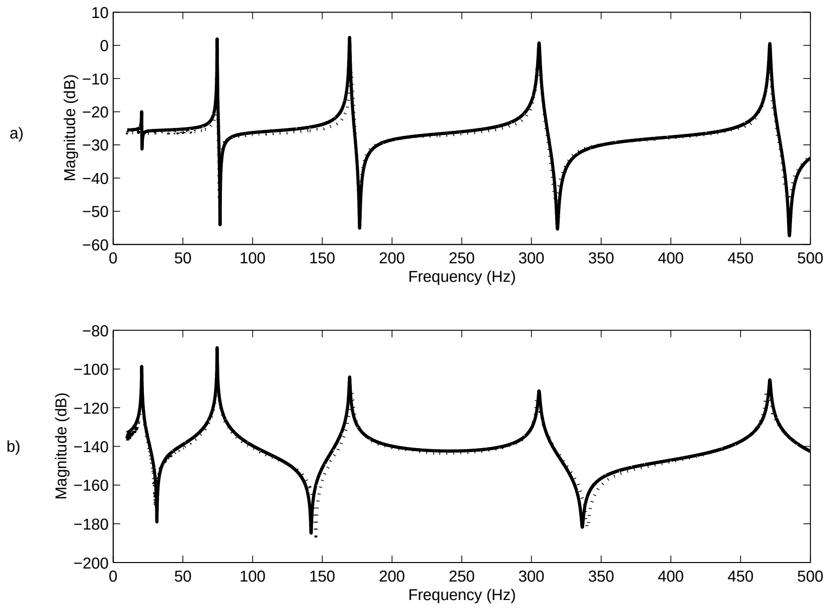

Figure 2.18: Simply supported beam frequency response of $|G_{vv}(s)|$ (a) and $|G_{ad}(s)|$(b), for the piezoelectric laminated simply supported beam structure. Experimental data ($\cdots$) and model obtained using subspace based system identification (—).

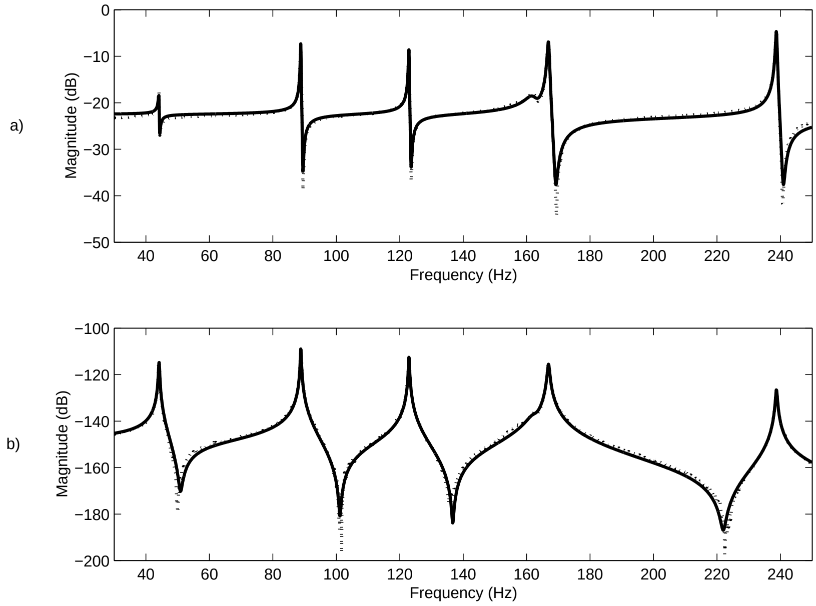

Figure 2.19: Frequency response of $|G_{vv}(s)|$ (a) and $|G_{ad}(s)|$ (b), for piezoelectric laminated plate bounded structure. Experimental data $(\cdots)$ and model obtained using subspace based system identification (—).

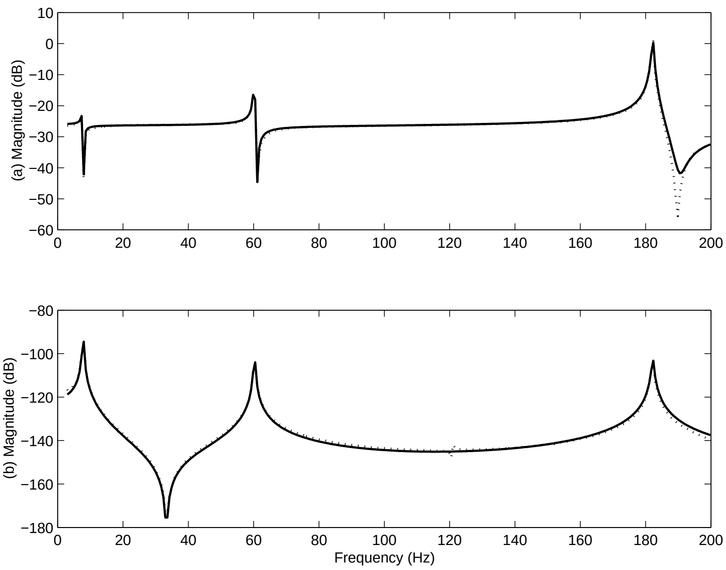

Figure 2.20: Frequency response of $|G_{vv}(s)|$ (a) and $|G_{ad}(s)|$ (b). Experimental data $(\cdots)$ and identified model (—).

Mode	Value (Hz)
ω_2	76
ω_3	173
ω_4	306
ω_5	472

Table 2.7: Experimental resonant frequencies for the simply supported beam.

Simply Supported Beam From Figure 2.18, the resonant modes of the laminated structure can be obtained. The resonance frequencies for the structure are shown in Table 2.7. The $2nd$, $3rd$, $4th$ and $5th$ structural modes were chosen due to their highly resonant nature. The 1^{st} mode was neglected due to the reduced control authority.

Assuming the capacitance values C_2 ,C_3, C_4 and C_5 to be 10 nF and the experimentally measured piezoelectric shunt capacitance C_p is 105.77 nF, the required inductance values can be calculated using Equation (2.17), as shown in Table 2.8.

In order to find the appropriate shunt resistance R_i, an optimisation approach can be used. An optimisation technique was proposed in [12], where the $\mathcal{H}_2$ norm of the controlled system is minimised. Optimal shunt resistance values obtained using this optimisation technique are displayed in Table 2.7.

Simulated results for $|G_{ad}(s)|$ and $\left|\tilde{G}_{ad}(s)\right|$, the shunted transfer function from the disturbance voltage to displacement, show that the resonance amplitudes have been considerably dampened, as shown in Figure 2.21. Table 2.9 summarises the simulated amplitude reductions for the $2nd$, $3rd$, $4th$ and $5th$ modes.

Using a synthetic impedance, as described in Section 2.3, with the required current-flowing shunt impedance, the frequency response of the shunted structure can be measured using the laser scanning vibrometer. Figure 2.22 shows the experimentally measured displacement responses for $|G_{ad}(s)|$ and $\left|\tilde{G}_{ad}(s)\right|$. The experimental resonant amplitudes were successfully reduced, as summarised in Table 2.9.

Simply Supported Plate Considering Figure 2.19, the resonance frequencies of the simply supported plate structure can be obtained, as shown in Table 2.10. The $1st$, $2nd$, $3rd$, $5th$

Symbol	Unit (H)
L_2	480.0
L_3	92.6
L_4	29.6
L_5	12.4

Symbol	Unit (Ω)
R_2	1423
R_3	1212
R_4	913
R_5	798

Table 2.8: Circuit parameters for the simply supported beam.

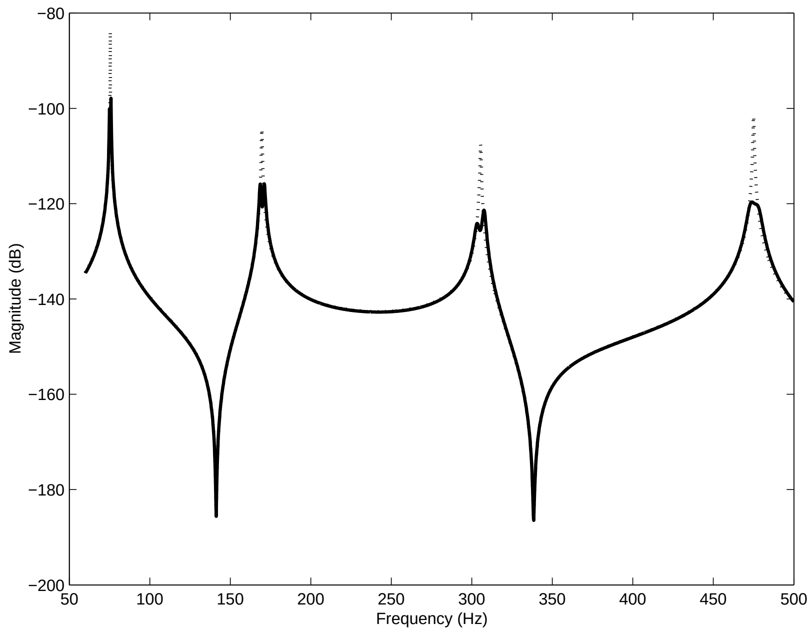

Figure 2.21: Simulated beam frequency response. $|G_{ad}(s)|$ undamped response $(\cdots)$ and $\left|\tilde{G}_{ad}(s)\right|$ damped response (—).

Mode	Simulated (dB)	Experimental (dB)
2	14.5	13.5
3	8.2	7.8
4	14.1	13.8
5	16.4	15.8

Table 2.9: Amplitude reduction for the simply supported beam.

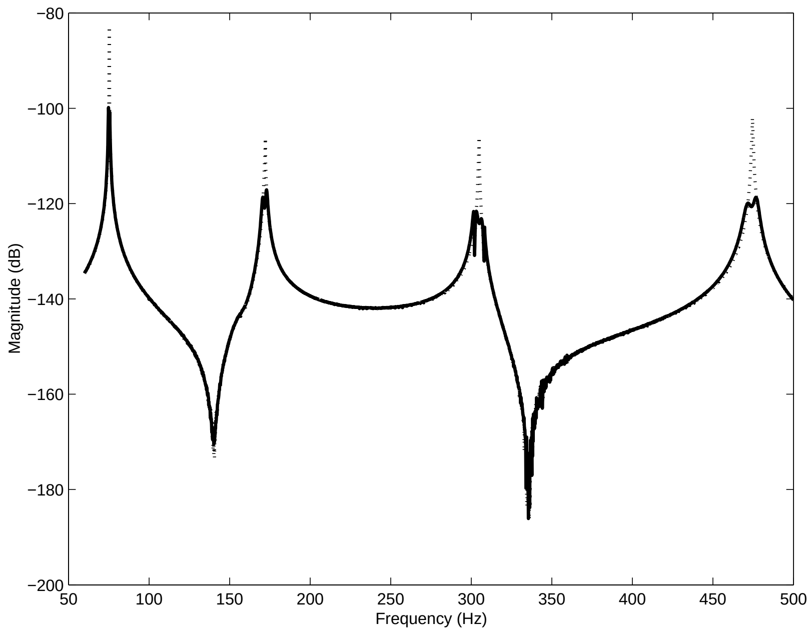

Figure 2.22: Experimental beam frequency response. $|G_{ad}(s)|$ undamped response $(\cdots)$ and $\left|\tilde{G}_{ad}(s)\right|$ damped response (—).

and $6th$ structural modes were chosen due to their high resonant amplitudes. The $4th$ mode was neglected due to the reduced control authority and its proximity to the $5th$ mode.

Setting C_1, C_2 ,C_3, C_5 and C_6 to be 7 nF, and C_p equal to 67.9 nF, the required inductance values can be calculated, as shown in Table 2.11. The already mentioned $\mathcal{H}_2$ norm optimisation strategy is employed to determine the required resistance values which are tabulated in Table 2.11.

Simulated results for $|G_{ad}(s)|$ and $\left|\tilde{G}_{ad}(s)\right|$ show that the structural amplitudes of the resonant structure have been dampened, as shown in Figure 2.23 and Table 2.12.

Using the synthetic impedance, as described in Section 2.3, and the laser scanning vibrometer, $|G_{ad}(s)|$ and $\left|\tilde{G}_{ad}(s)\right|$ can be measured. The frequency response for the experimental undamped and damped systems are shown in Figure 2.24. Experimental results, shown in Figure 2.24, demonstrate that the structural modes of the bounded structure have been considerably damped. The experimental resonant amplitudes were successfully reduced, as shown in Table 2.12.

Mode	**Unit** (Hz)
ω_1	44.85
ω_2	90.2
ω_3	124.2
ω_4	161.6
ω_5	167.6
ω_6	237.2

Table 2.10: Experimental resonant frequencies for the plate bounded structure.

Symbol	**Unit** (H)
L_1	1986.3
L_2	491.1
L_3	259.2
L_5	142.2
L_6	71.1

Symbol	**Unit** (Ω)
R_1	2498.2
R_2	1858.3
R_3	1272.6
R_5	1641.5
R_6	1400.1

Table 2.11: Circuit parameters for the plate bounded structure.

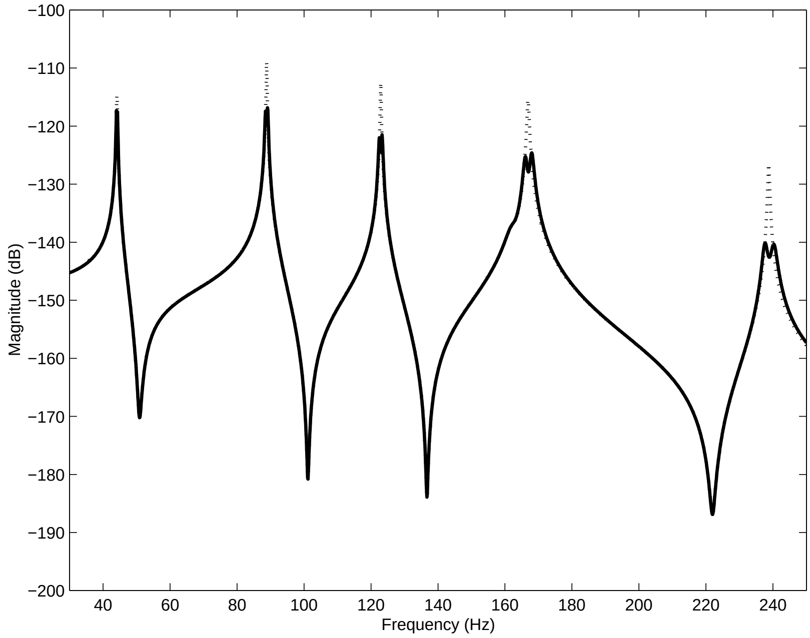

Figure 2.23: Simulated plate frequency response. $|G_{ad}(s)|$ undamped response $(\cdots)$ and $\left|\tilde{G}_{ad}(s)\right|$ damped response (—).

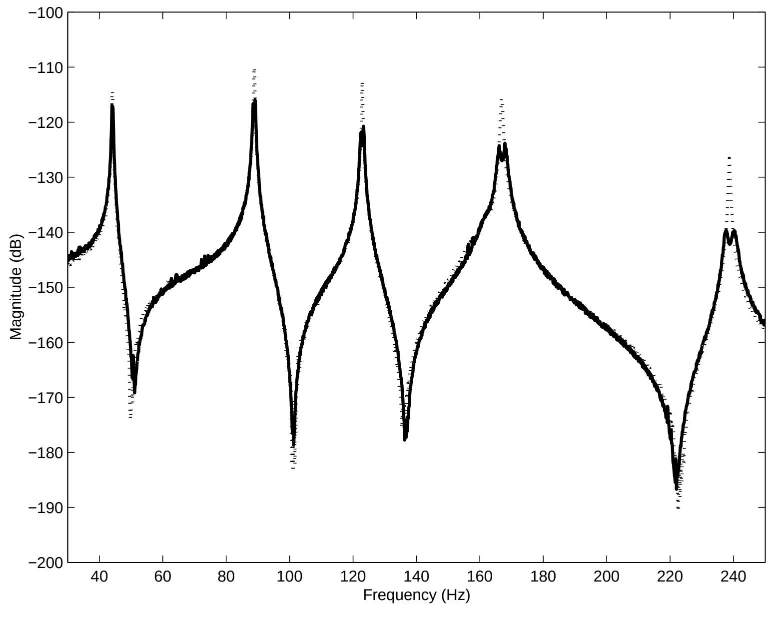

Figure 2.24: Experimental plate frequency response. $|G_{ad}(s)|$ undamped response $(\cdots)$ and $\left|\tilde{G}_{ad}(s)\right|$ damped response (—).

Mode	Simulated (dB)	Experimental (dB)
1	3.2	3.8
2	10.9	10.1
3	13.2	12.8
5	13.9	13.2
6	15.8	14.7

Table 2.12: Amplitude reduction for the plate bounded structure.

Series-Parallel Shunt Controller

A series-parallel impedance structure was designed to damp the $1st$, $2nd$ and $3rd$ modes of the experimental cantilever apparatus, as described in Section 2.6.1, that is the 7.769, 60.14 and 181.3 Hz respectively. A summary of the circuit parameters is provided in Table 2.13. In order to determine the appropriate resistance R_n, the $\mathcal{H}_2$ norm of the $\tilde{G}_{ad}(s)$ could be minimized [12]. Using the optimisation strategy, as suggested by Behrens *et al.* [12], the optimal resistor values were found to be as tabulated in Table 2.13.

To implement the required shunt impedance, the synthetic impedance circuit (2.27), as explained in Section 2.3, was used. The open-loop $G_{ad}(s)$ and closed-loop $\tilde{G}_{ad}(s)$ transfer functions, shown in Figures 2.25 and 2.26 respectively, were measured to gauge vibration damping performance. A good correlation was observed between simulated and experimental results. Peak amplitudes reduction of the $1st$, $2nd$ and $3rd$ modes are summarised in Table 2.14. Therefore, the proposed piezoelectric shunt is an acceptable method for increasing mechanical damping of highly resonant structures.

Resonant Shunt Controllers

In this section, resonant shunt controllers will be applied to two flexible structures; the piezoelectric laminate beam and the piezoelectric laminate plate, as described in Section 2.6.1.

Symbol	Unit (H)	Symbol	Unit (μF)	Symbol	Unit $(k\Omega)$
L_1	246.29	C_1	1.6	R_1	800
L_2	4.11	C_2	1.6	R_2	150
L_3	0.45	C_3	1.6	R_3	36

Table 2.13: Series-parallel shunt circuit parameters.

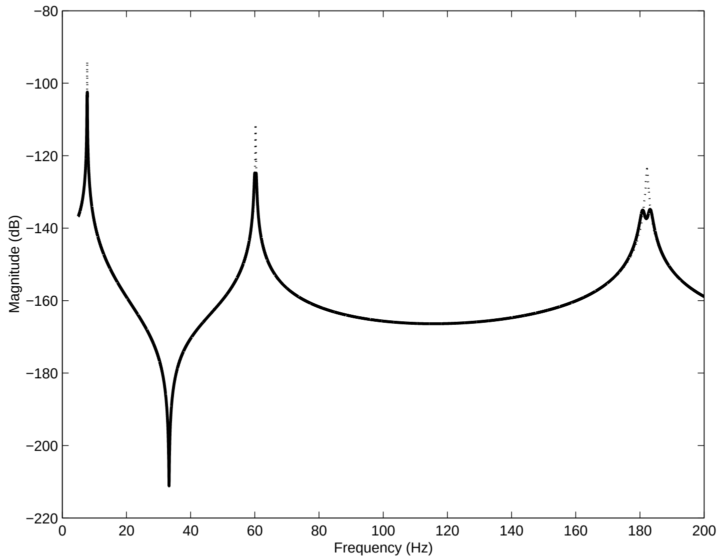

Figure 2.25: Simulated frequency response of $|G_{ad}(s)|$ as $(\cdots)$ and $\left|\tilde{G}_{ad}(s)\right|$ as (—).

Mode	Simulation (dB)	Experimental (dB)
1	8.1	10.2
2	13.2	11.3
3	11.2	13.1

Table 2.14: Amplitude reduction for the cantilever structure.

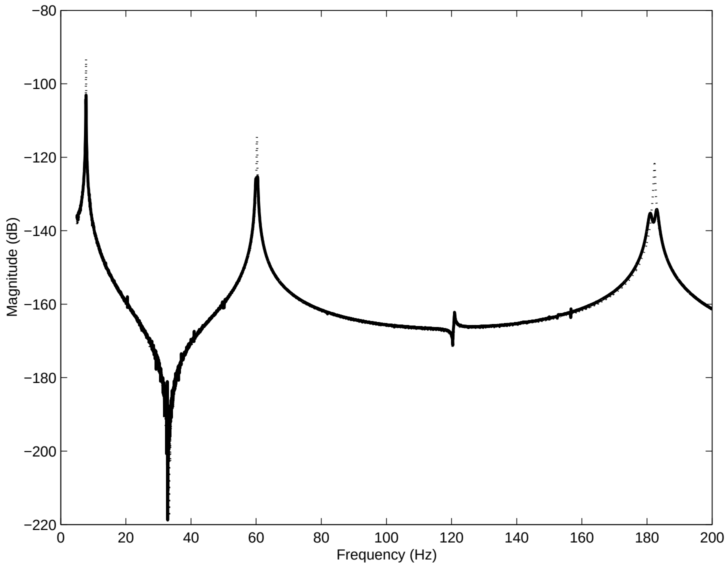

Figure 2.26: Experimental frequency response of $|G_{ad}(s)|$ as $(\cdots)$ and $\left|\tilde{G}_{ad}(s)\right|$ as (—).

The first four modes of the beam and the first six modes of the plate are to be controlled by a shunt impedance $Y(s)$ given in Equation (2.30). Using the procedure explained in Section 2.5.3, and the identified models, an optimal set of damping ratios for $Y(s)$ was determined for each structure. The admittances were digitally implemented using the synthetic admittance circuit described in Section 2.3 and then applied to the shunt transducers. A comparison of the experimental undamped and damped experimental responses for $|G_{ad}(s)|$ are shown in Figures 2.27 and 2.29. The experimental resonance magnitudes were successfully reduced, as summarised in Table 2.15. Figure 2.28 shows the simulated closed-loop and open-loop poles. Figure 2.28 shows that the closed-loop poles have been pushed further to the left on the real-imaginary plane.

Robust Passive Shunt Controller

In the following section, both a single mode and multiple mode robust shunt controller are considered. Simulations are carried out for both cases. Each is then verified experimentally on the piezoelectric laminated plate, as described in Section 2.6.1.

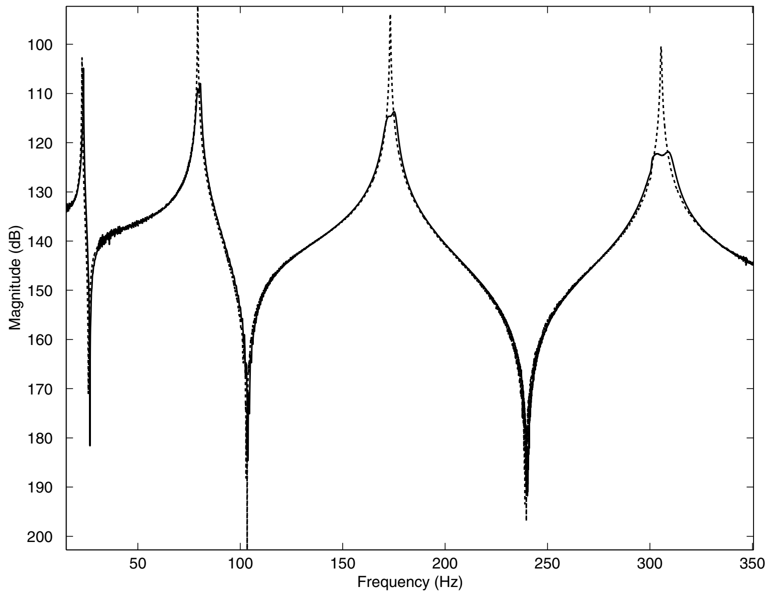

Figure 2.27: Experimental beam undamped $|G_{ad}(s)|$ as $(\cdots)$ and damped $\left|\tilde{G}_{ad}(s)\right|$ as (—) magnitude response.

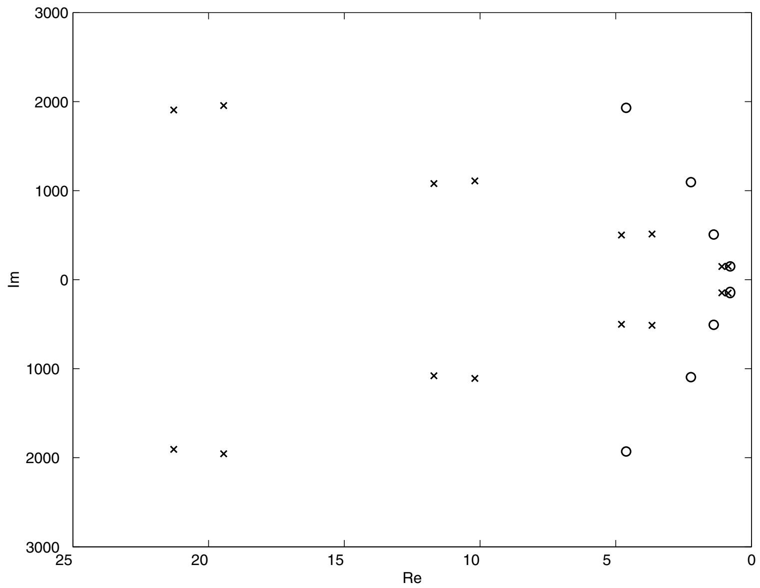

Figure 2.28: Simulated open-loop ($\bigcirc$) and closed-loop ($\times$) poles of the piezoelectric laminated beam.

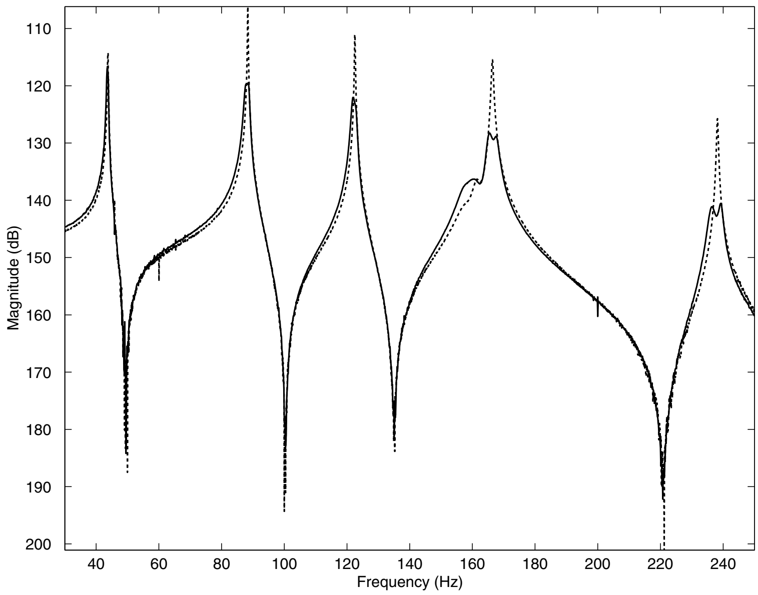

Figure 2.29: Experimental plate undamped $|G_{ad}(s)|$ as $(\cdots)$ and damped $\left|\tilde{G}_{ad}(s)\right|$ as (—) magnitude response.

Mode	**Beam** (dB)	**Plate** (dB)
1	2.0	2.5
2	16.2	13.5
3	19.9	11.0
4	24.1	–
5	–	12.9
6	–	14.8

Table 2.15: Summary of experimental amplitude reduction for both beam and plate structures.

Single Mode Robust Shunt Controller For the single mode case, damping the second mode of the piezoelectric laminated plate structure is considered. In Figure 2.30 (a), a single mode controller is applied to ω_2, or alternatively $\hat{\omega}_{2,0}$, as described in Moheimani *et al.* [84]. Next, two additional controllers are applied to the side lobes $\hat{\omega}_{2,-1}$ and $\hat{\omega}_{2,1}$, as shown in Figures 2.30 (b) and (c). The impedance required to damp the second mode is

$$Z_1(s) = \frac{1-\beta_2}{C_p s \beta_2}, \tag{2.51}$$

where

$$\beta_2 = \frac{\alpha_{2,-1}\hat{\omega}_{2,-1}^2}{s^2 + 2\hat{d}_{2,-1}\hat{\omega}_{2,-1}s + \hat{\omega}_{2,-1}^2} + \frac{\alpha_{2,0}\hat{\omega}_{2,0}^2}{s^2 + 2\hat{d}_{2,0}\hat{\omega}_{2,0}s + \hat{\omega}_{2,0}^2} + \frac{\alpha_{2,1}\hat{\omega}_{2,1}^2}{s^2 + 2\hat{d}_{2,1}\hat{\omega}_{2,1}s + \hat{\omega}_{2,1}^2}.$$

Note that $\alpha_{2,-1} = \alpha_{2,0} = \alpha_{2,1} = \frac{1}{3}$ and the chosen circuit parameters are tabulated in Table 2.16.

In order to achieve the desired performance, appropriate values for the damping parameters $\hat{d}_{2,-1}$, $\hat{d}_{2,0}$ and $\hat{d}_{2,1}$ need to be determined. The following optimization problem for the damped system can be solved:

$$D^* = \arg\min_{D>0} \left\| \tilde{G}_{ad}(s) \right\|_2, \tag{2.52}$$

where $D^* = \{\hat{d}_{2,-1}, \hat{d}_{2,0}, \hat{d}_{2,1}\}$. The above optimisation problem minimises the $\mathcal{H}_2$ norm of the damped transfer function from input disturbance voltage $V_a(s)$, to the displacement at a point on the structure $d(s)$. The optimisation problem was solved from a number of initial guesses, and a solution was found; $\hat{d}_{2,-1} = 0.0110$, $\hat{d}_{2,0} = 0.0101$ and $\hat{d}_{2,1} = 0.0098$.

Simulated results for $|G_{ad}(s)|$ and $\left|\tilde{G}_{ad}(s)\right|$ show that the peak amplitude has been considerably reduced, as shown in Figure 2.30 (c).

To validate the proposed multiple mode robust shunt controller, the above impedance (2.51) and parameters listed in Table 2.16 were applied to the plate structure using the synthetic impedance as described in Section 2.3. When fine-tuning the proposed impedance parameters, they were found to be very sensitive, making the tuning process very time-consuming.

From Figure 2.31, the proposed single mode robust shunt controller experimentally agrees with simulated results.

Aside, it should be noted that the proposed robust shunt controller can be immune to variations in structural dynamics. This contrasts to previous *passive* shunt techniques [48, 50,

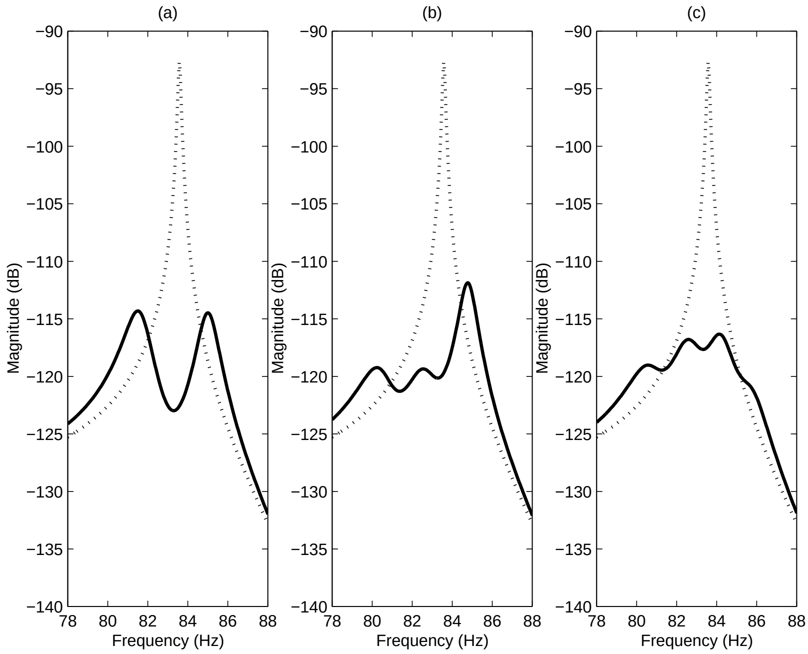

Figure 2.30: Simulated undamped $|G_{ad}(s)|$ ($\cdots$) and damped response $\left|\tilde{G}_{ad}(s)\right|$ (—). Subfigure (a) original single mode controller is applied to $\hat{\omega}_{2,0}$, (b) second controller is applied to $\hat{\omega}_{2,-1}$ and (c) third controller is applied to $\hat{\omega}_{2,1}$.

112, 113] which are generally sensitive to variations in the structural frequencies as verified by shifting the simulated resonance frequencies $\pm 1\ Hz$ from their original values. Simulated results in Figure 2.32, employing the impedance (2.51), show that the performance of the system is not severely deteriorated by disturbing the resonance frequencies.

Multiple Mode Robust Shunt Controller For the multiple mode case, damping the 2^{nd} and 3^{rd} structural modes are considered, i.e. $\omega_2 = 83.68\ Hz$ and $\omega_3 = 118.4\ Hz$. Using the same procedure as suggested in Section 2.6.2, three additional controllers will be applied to the 3^{rd} mode. The the following impedance is required:

$$Z_1(s) = \frac{1-\beta_{23}}{C_p s \beta_{23}}, \tag{2.53}$$

where

$$\beta_{23} = \frac{\alpha_{2,-1}\hat{\omega}_{2,-1}^2}{s^2 + 2\hat{d}_{2,-1}\hat{\omega}_{2,-1}s + \hat{\omega}_{2,-1}^2} + \frac{\alpha_{2,0}\hat{\omega}_{2,0}^2}{s^2 + 2\hat{d}_{2,0}\hat{\omega}_{2,0}s + \hat{\omega}_{2,0}^2} + \frac{\alpha_{2,1}\hat{\omega}_{2,1}^2}{s^2 + 2\hat{d}_{2,1}\hat{\omega}_{2,1}s + \hat{\omega}_{2,1}^2} + \cdots$$
$$\frac{\alpha_{3,-1}\hat{\omega}_{3,-1}^2}{s^2 + 2\hat{d}_{3,-1}\hat{\omega}_{3,-1}s + \hat{\omega}_{3,-1}^2} + \frac{\alpha_{3,0}\hat{\omega}_{3,0}^2}{s^2 + 2\hat{d}_{3,0}\hat{\omega}_{3,0}s + \hat{\omega}_{3,0}^2} + \frac{\alpha_{3,1}\hat{\omega}_{3,1}^2}{s^2 + 2\hat{d}_{3,1}\hat{\omega}_{3,1}s + \hat{\omega}_{3,1}^2}.$$

Parameters	Simulated Unit (Hz)	Experimental Unit (Hz)
$\hat{\omega}_{2,-1}$	82.28	82.92
$\hat{\omega}_{2,0}$	83.68	83.58
$\hat{\omega}_{2,1}$	85.21	85.51

Parameters	Simulated Unit	Experimental Unit
$\hat{d}_{2,-1}$	0.0110	0.0150
$\hat{d}_{2,0}$	0.0101	0.00564
$\hat{d}_{2,1}$	0.0098	0.00245

Table 2.16: Single mode circuit parameters for the plate bounded structure.

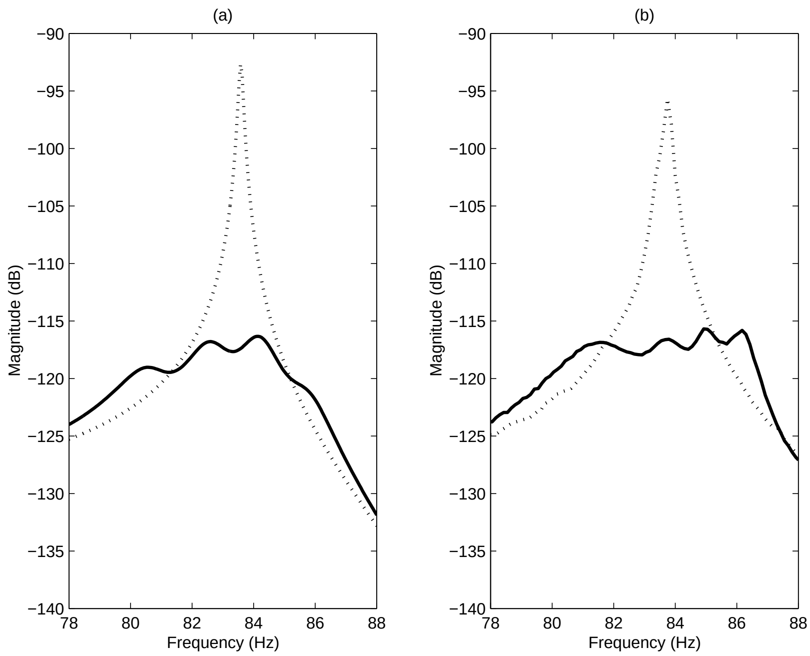

Figure 2.31: Subfigure simulated results (a) and experimental results (b). Undamped $|G_{ad}(s)|$ $(\cdots)$ and damped response $\left|\tilde{G}_{ad}(s)\right|$ (—).

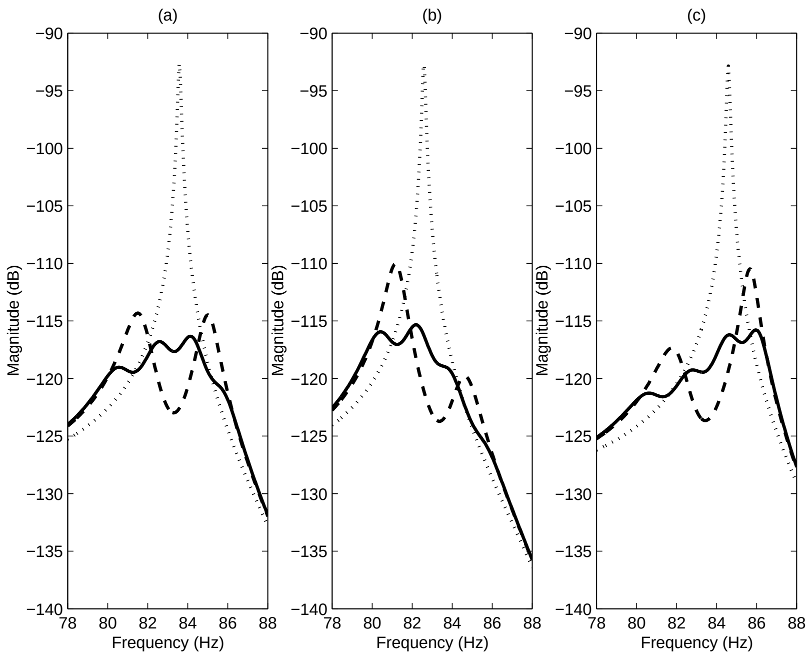

Figure 2.32: Simulated response original system (a), poles moved $-1\ Hz$ from the original system (b), and poles moved $+1\ Hz$ from the original system (c). Undamped system $|G_{ad}(s)|$ ($\cdots$) from the original single mode controller as described in Moheimani *et al.* [84] (- - -) and proposed robust shunt controller (—).

Parameters	Simulated Unit (Hz)	Experimental Unit (Hz)
$\hat{\omega}_{2,-1}$	82.2	81.95
$\hat{\omega}_{2,0}$	83.4	83.27
$\hat{\omega}_{2,1}$	84.6	84.09
$\hat{\omega}_{3,-1}$	117.0	116.12
$\hat{\omega}_{3,0}$	118.4	118.03
$\hat{\omega}_{3,1}$	119.6	119.55

Parameters	Simulated Unit	Experimental Unit
$\hat{d}_{2,-1}$	0.0091	0.00458
$\hat{d}_{2,0}$	0.0084	0.00374
$\hat{d}_{2,1}$	0.0079	0.00123
$\hat{d}_{3,-1}$	0.0074	0.00515
$\hat{d}_{3,0}$	0.0069	0.00864
$\hat{d}_{3,1}$	0.0062	0.00451

Table 2.17: Multiple mode circuit parameters for the plate bounded structure.

Note $\sum_{i=2}^{3}\sum_{i=-3}^{3}\alpha_{i,j}=1$ for $\alpha_{i,j}>0$, and $\alpha_{2,-1}=\alpha_{2,0}=\alpha_{2,1}=\alpha_{3,-1}=\alpha_{3,0}=\alpha_{3,1}=\frac{1}{6}$.

Simulated results for the multiple mode robust shunt controller, undamped $|G_{ad}(s)|$ and damped $\left|\tilde{G}_{ad}(s)\right|$ response, show that the structural amplitude has been considerably reduced, as shown in Figure 2.33. For this case, three individual controllers were applied to the 2^{nd} and 3^{rd} modes. Note that more then three additional controllers were applied to each individual mode.

Using the synthetic impedance, as described in Section 2.3, and the circuit parameters listed in Table 2.17, the impedance (2.53) was applied experimentally to the plate structure. From Figure 2.34, an amplitude reduction of approximately 16 dB for the 2^{nd} and 3^{rd} modes was observed.

From simulated and experimental results, the proposed multiple mode robust shunt controller was developed as an effective method for shunt damping.

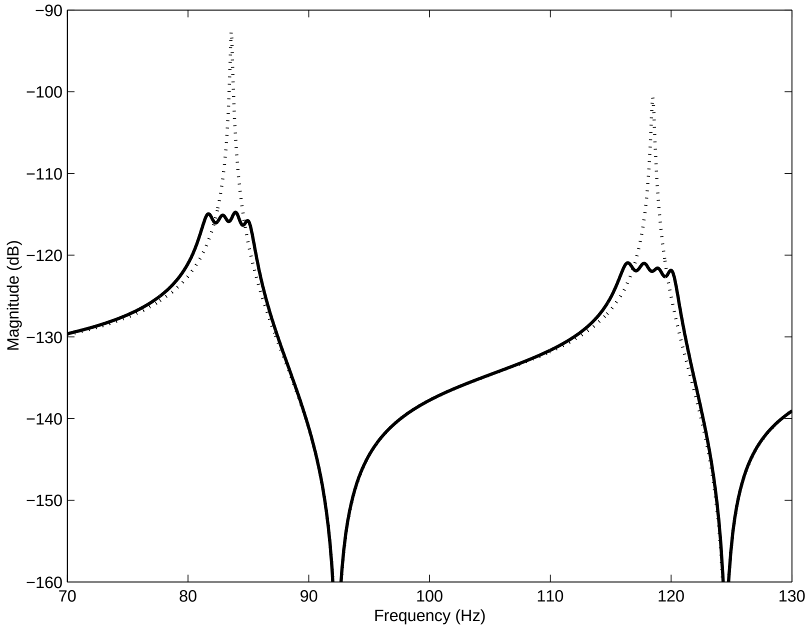

Figure 2.33: Simulated multiple mode robust shunt damping. Undamped $|G_{ad}(s)|$ $(\cdots)$ and damped $\left|\hat{G}_{ad}(s)\right|$ (—) response.

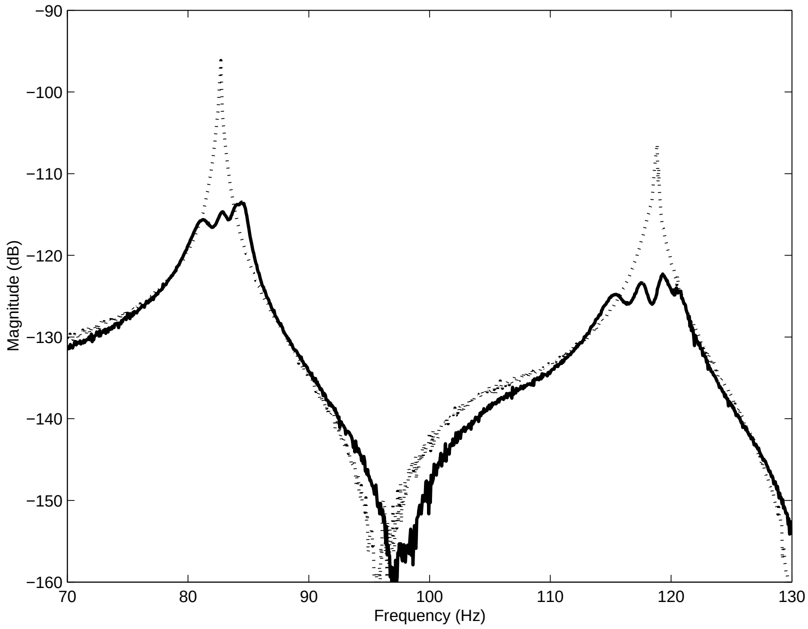

Figure 2.34: Experimental multiple mode robust shunt damping. Undamped $|G_{ad}(s)|$ $(\cdots)$ and damped $\left|\hat{G}_{ad}(s)\right|$ (—) response.

2.7 Discussions

At the beginning of the chapter, the present piezoelectric shunt damping techniques are briefly reviewed. This includes linear and non-linear techniques, and the associated problems with these techniques. Passive piezoelectric shunt damping circuits provide guaranteed stability, reasonable performance and are simple to design. However, dealing with low frequency modes or transducers with small capacitance, shunt impedances may require inductance values of greater than 100 Henrys which is physically impossible to build. To overcome these physical limitations, virtual inductors [93] were considered but made the design too complex when numerous inductors were required, as in multi-mode shunt impedances. The synthetic admittance circuit [36] or CCVS/VCCS [40] was reviewed as a method for implementing an arbitrary shunt impedance circuit [37].

After the reviewing the present shunt damping research, four novel shunt controllers were developed, examined and verified. They were the current-flowing shunt controller, series-parallel shunt controller, resonant shunt controllers and robust passive shunt controller.

The current-flowing shunt controller has been introduced as an alternative method for reducing structural vibrations. While achieving similar damping performance, it has a number of advantages compared to other passive shunt circuits [56, 113, 114]. It is simple (requires less resistors, capacitors and inductors or virtual inductors [93]), mode dominant (capable of damping more dominate or neglecting less dominant modes), multi-mode (can damp multiple modes using a single piezoelectric transducer) and passive (dissipative and guaranteed to be stable). The current-flowing controller has been theoretically and experimentally verified. Overall, the proposed theoretical predictions agree with experimental results.

The series-parallel shunt controller has been introduced as an alternative piezoelectric shunt damping technique for reducing the vibration of multiple structural modes. While achieving comparable performance to other multiple-mode shunting schemes [14, 56, 113, 114], the series-parallel impedance structure has one major advantage; smaller inductor values. The concept presented has been experimentally verified with promising results. In general, theoretical predictions have agreed with experimental results.

Resonant shunt controllers view piezoelectric shunt damping as a feedback control problem where the effective controller is parameterised by the impedance. In this section, a new field of shunt controllers was introduced which can be easily tuned to the resonate frequency of the structure. Additionally, these controllers were found to be passive and robust. The proposed controllers were applied to two experimental apparatuses. From observations of the theoretical and experimental data, the proposed controller was successful.

The robust passive shunt controller was then introduced as a variation of the previous technique to overcome the problems associated with environment changes of the resonate peak. Again, the effect of the robust passive shunt controller was studied theoretically and experimentally on a piezoelectric laminated plate structure. While achieving comparable performance to other passive control schemes [56, 113, 114], the proposed robust passive shunt controller has one major advantage. It is broadband over a desired bandwidth. Preliminary results show that the proposed technique is less susceptible to environmental changes when compared to other techniques. While it may be more difficult to initially tune the controller parameters, it is a valuable method for damping structural modes.

From experimental observation, as shown in Figure 2.29, the proposed impedances are very effective in reducing vibration of the structures. However, the performance for the first mode is very limited, and can be attributed to the location of the piezoelectric shunt transducers on the beam and plate structures. Determining the appropriate transducer location depends on the maximum mode strain for the structure. This requires theoretical modelling and practical experience to determine the position. Therefore, selection of the optimal location for the transducers should improve the damping performance. Refer to reference [52] for more detail.

All of the proposed shunt controllers provided comparable levels of induced damping, both theoretically and experimentally. The robust passive shunt controller is considered to be least preferred due to the difficulty in tuning the controller parameters. The current-flowing and series-parallel shunt controllers provide easier tuning than the previous techniques and perform equally as well because of their circuit duality, i.e. Norton's and Thevenin's equivalence [59]. The resonant shunt controller proved to be the most favourable due to the ease of tuning controller parameters.

The proceeding controllers are demonstrated on experimentally ideal structures which are highly resonant and have ideal boundary conditions. The experimentally ideal structures were chosen for ease of modelling and controller design. In most practical applications, the highly resonant modes will be naturally damped attributed to their irregular shape and diverse boundary conditions. Applying the proposed controllers to more realistic structures would provide a proper evaluation of their damping potential.

Another important issue not raised is this chapter is performance sensitivity. Passive shunt control performance is sensitive to structural resonance frequency and transducer dynamic changes, which is due to operating and environmental conditions. One method to overcome this sensitivity is to adaptive the shunt controllers to the changing conditions. Such adaptive techniques have proven to be very successful and can be found in references [38, 57, 89].

Overall, this chapter has been successful because four new shunt controllers were evaluated and provided outcomes that expand opportunities for further research and development.

Chapter 3

Multivariable Piezoelectric Shunt Control

This chapter is concerned with the problem of multi-mode shunt damping of structural vibrations using several piezoelectric transducers. It will show that there is a multivariable feedback control problem in the impedance, or alternatively the admittance of the electrical shunt, which constitutes the feedback controller.

3.1 Dynamics of a Multivariable System

Consider a flexible structure with m piezoelectric patches bonded to either side in a collocated pattern. Assume that the piezoelectric transducers on one side are used to disturb the structure, while those on the other side of the structure are shunted to an impedance. The impedance is to be designed in a way that the unwanted structural vibrations are minimised. The disturbances acting on the structure can take different forms. Nevertheless, the methodology developed below is general enough to apply to other cases. This point will be further clarified in later sections.

In Figure 3.1, a schematic of this system is depicted and the equivalent electrical circuit of the shunted piezoelectric transducers. In this section the dynamics of the multivariable shunted system is derived.

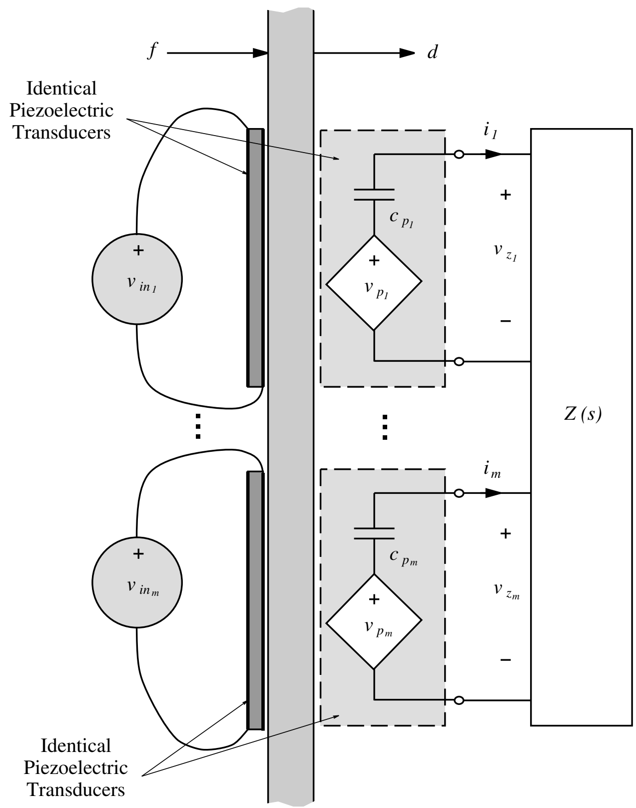

Figure 3.1: Piezoelectric laminate structure with m shunted piezoelectric patches and electrical equivalences.

If

$$V_z(s) = \begin{bmatrix} v_{z_1}(s) \\ v_{z_2}(s) \\ \vdots \\ v_{z_m}(s) \end{bmatrix} \quad V_p(s) = \begin{bmatrix} v_{p_1}(s) \\ v_{p_2}(s) \\ \vdots \\ v_{p_m}(s) \end{bmatrix} \quad V_{in}(s) = \begin{bmatrix} v_{in_1}(s) \\ v_{in_2}(s) \\ \vdots \\ v_{in_m}(s) \end{bmatrix} \quad I_z(s) = \begin{bmatrix} i_1(s) \\ i_2(s) \\ \vdots \\ i_m(s) \end{bmatrix},$$

then

$$V_z(s) = Z(s)I_z(s). \tag{3.1}$$

Furthermore, writing Kirchhoff's voltage law around the k^{th} loop obtains

$$v_{z_k} = v_{p_k} - \frac{1}{c_{p_k}s}i_k,$$

which implies

$$V_z(s) = V_p(s) - \frac{1}{s}\Lambda I_z(s), \tag{3.2}$$

where

$$\Lambda = \text{diag}\left(\frac{1}{c_{p_1}}, \frac{1}{c_{p_2}}, \ldots, \frac{1}{c_{p_m}}\right) \tag{3.3}$$

and $\text{diag}(\alpha_1, \alpha_2, \ldots, \alpha_m)$ represents a matrix with diagonal entries $\alpha_1, \alpha_2, \ldots, \alpha_m$ and all other entries are zeros.

To capture the total effect of the disturbance voltages as well as the effect of the electric shunt on the structure, this may be written as, [48],

$$V_p(s) = G_{vv}(s)V_{in}(s) - G_{vv}(s)V_z(s). \tag{3.4}$$

Here $G_{vv}(s)$ is the multivariable collocated transfer function matrix of the system, i.e.

$$G_{vv}(s) = \sum_{k=1}^{M} \frac{\Psi_k}{s^2 + 2\zeta_k\omega_k s + \omega_k^2}, \tag{3.5}$$

where resonance frequencies are ordered such that $\omega_1 \leq \omega_2 \leq \ldots \leq \omega_M$ and M can be an arbitrarily large number. Furthermore, due to the fact that $G_{vv}(s)$ is a collocated transfer function matrix, the $m \times m$ matrix Ψ_k must be a positive semi-definite matrix [52]. That is

$$\Psi_k = \Psi_k' \geq 0 \quad \text{for all} \quad k. \tag{3.6}$$

It should be pointed out that if the Equation (3.5) is obtained by employing a procedure such as modal analysis [82], it would be expected to have $M \longrightarrow \infty$. However, choosing a very large number for M is quite acceptable, as pointed out in [60] allows the use of finite-dimensional techniques in analysing the dynamics of the system. Models of the form (3.5)

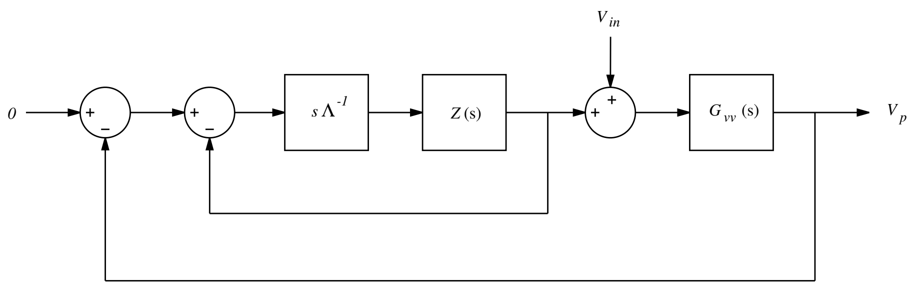

Figure 3.2: Feedback structure associated with the piezoelectric shunt damping problem.

can be obtained using a variety of techniques; modal analysis if the system is simple with well defined boundary conditions or finite element modelling for more complicated structures. An alternative approach is to employ frequency domain identification techniques [81] to identify a model for the system. Frequency domain subspace identification has proved to be an efficient method for identifying highly resonant systems of high orders [80].

Next, Equations (3.1), (3.2) and (3.4) are combined to obtain

$$V_p(s) = \left[I + G_{vv}(s)Z(s)\left(Z(s) + \frac{1}{s}\Lambda\right)^{-1}\right]^{-1} G_{vv}(s)V_{in}(s). \tag{3.7}$$

From Equation (3.7), it can be inferred that the transfer function matrix relating $V_{in}(s)$ to $V_p(s)$ is the feedback connection of $G_{vv}(s)$ with

$$K(s) = Z(s)\left(Z(s) + \frac{1}{s}\Lambda\right)^{-1}. \tag{3.8}$$

This is an interesting observation as it is then possible to employ systems theoretic tools in analysing dynamics and stability of multivariable shunt-damped systems. The feedback control problem associated with (3.7) is depicted in Figure 3.2. Note that the inner feedback loop represents the effective controller $K(s)$ in Equation (3.8). Observe that the purpose of the system is to regulate v_p in the presence of disturbance V_{in}. The signal V_p, however, is not directly measurable. Therefore, notice that this is a very sophisticated form of a cascade feedback control structure, as shown in Section 6.4 of [86].

The above system is mainly used in laboratory experiments. Experimental results in this chapter are obtained from a simply supported beam with two pairs of collocated piezoelectric transducers, as shown below in Section 3.4. In a more realistic setting, the disturbances acting on the structure have a different nature. For example, they may be point forces, moments or

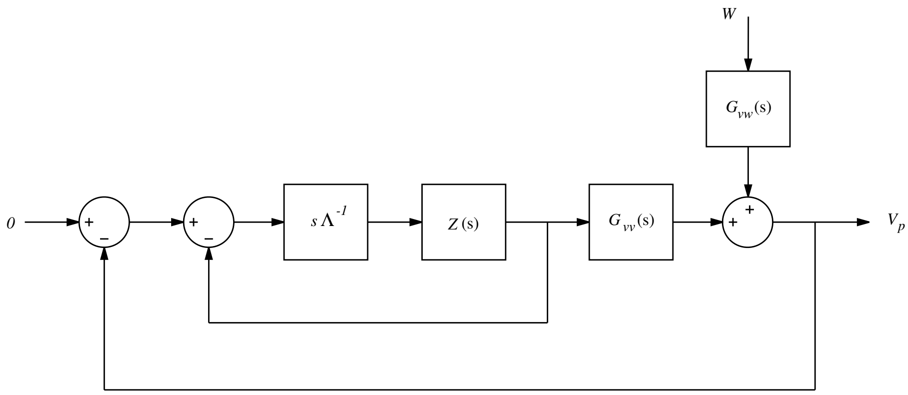

Figure 3.3: The feedback structure associated with the modified piezoelectric shunt damping problem.

a distributed force. In this situation Equation (3.7) can be modified to

$$V_p(s) = G_{vv}(s)V_{in}(s) - G_{vw}(s)W(s), \tag{3.9}$$

where $G_{vw}(s)$ is the unshunted transfer function from the disturbance vector, $W(s)$ to $V_p(s)$. An implication of Equation (3.9) is that the shunted structural dynamics will have to be revised as

$$V_p(s) = \left[I + G_{vv}(s)Z(s)\left(Z(s) + \frac{1}{s}\Lambda\right)^{-1}\right]^{-1} G_{vw}(s)W(s), \tag{3.10}$$

where $G_{vw}(s)$ is the unshunted transfer function from the disturbance vector, $W(s)$ to $V_p(s)$. The transfer function $G_{vw}(s)$ depends solely on the nature as well as the spatial coordinates of the disturbance signal w. Nonetheless, due to the common pole property of flexible structures, $G_{vw}(s)$ and $G_{vv}(s)$ will have identical poles. The zeros of the two transfer functions, however, could be quite different.

Observe that although the nature of the disturbance has changed, stability of the shunted system is still dictated by the feedback connection of $G_{vv}(s)$ and $K(s)$ in (3.8). Furthermore, it is noted that under these circumstances the regulator problem depicted in Figure 3.2 should be modified to that shown in Figure 3.3.

3.2 Stability of the Multivariable Shunted System

A set of conditions regarding the guaranteed stability of the closed-loop system is depicted in Figure 3.3 and derived in this section [85]. Instead of considering the shunting impedance

$Z(s)$ as the controller, the closed-loop stability of the system is studied in terms of the shunted admittance $Y(s) = Z(s)^{-1}$, noting that the closed-loop transfer function in (3.10) can be rewritten as

$$V_p(s) = \left[I + G_{vv}(s) \left(I + \frac{1}{s} \Lambda Y(s) \right)^{-1} \right]^{-1} G_{vw}(s)\ W(s). \tag{3.11}$$

The regulator problem associated with this system is depicted in Figure 3.4. A parameterisation of stabilising controllers for the system in (3.11) is introduced next.

Considering the structure of the feedback system, the Youla parameterisation of all stabilising controllers for the inner feedback loop can be written as

$$Y(s) = (I - Q(s)\Lambda/s)^{-1}\, Q(s).$$

Although the inner loop contains an integrator, the parameterisation for a stable plant can be used as long as $Q(s)$ satisfies a number of conditions. $Q(s)$ must be stable, proper and have a transmission zero at the origin. Furthermore, $I - Q(s)\Lambda/s$ must have a transmission zero at $s = 0$. These conditions can be enforced by choosing

$$Q(s) = H(s)\Lambda^{-1}s,$$

where $H(s)$ is stable, strictly proper and $I - H(s)$ has a zero at the origin, i.e.

$$I - H(s) = sJ(s).$$

This choice for $Q(s)$ results in a closed-loop system with the transfer function matrix

$$[I + s\ G_{vv}(s)J(s)]\, G_{vw}(s). \tag{3.12}$$

It is now possible to find closed-loop stability conditions in terms of $J(s)$ as the stability of (3.12) is equivalent to that of the system depicted in Figure 3.5.

Next, proof is given that the closed-loop system will be stable as long as $J(s)$ is a strictly positive real (SPR) transfer function matrix. The following two definitions and the subsequent theorem due to reference [66] are needed in the proof.

Definition 1 *A $m \times m$ rational matrix $G(s)$ is said to be positive real (PR) if*

1. *All elements of $G(s)$ are analytic in* $\mathrm{Re}(s) > 0$.
2. *$G(s) + G^*(s) \geq 0$ in* $\mathrm{Re}(s) > 0$ *or equivalently*

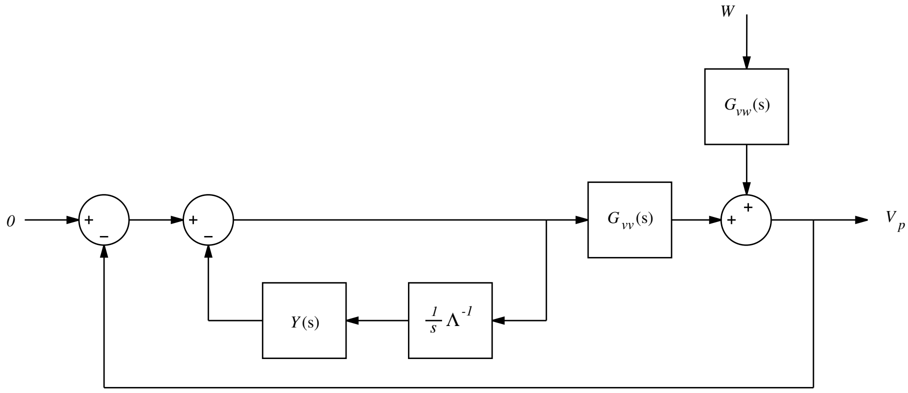

Figure 3.4: Feedback structure associated with the piezoelectric shunt damping problem with admittance as the control variable.

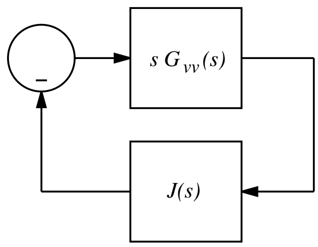

Figure 3.5: Feedback connection of $sG_{vv}(s)$ with $J(s)$.

(a) Poles on the imaginary axis are simple and have nonnegative residues, and

(b) $G(j\omega) + G^*(j\omega) \geq 0$ *for* $\omega \in (-\infty, \infty)$.

Definition 2 *A* $m \times m$ *stable rational matrix* $G(s)$ *is said to be strictly positive real in the weak sense (WSPR) if*

$$G(j\omega) + G^*(j\omega) > 0 \quad \text{for} \quad \omega \in (-\infty, \infty).$$

The following theorem is Corollary 1.1 of [66]:

Theorem 3 *The negative feedback connection of a PR system with a WSPR controller is stable.*

It should be pointed out that there are a number of definitions in the literature for strictly positive real (SPR) systems. For a review of this, refer to references [66, 109]. For almost all such definitions, a similar result to that of Theorem 3 would be expected, i.e. the negative feedback connection of a PR system with a SPR controller is stable. For the problem at hand, Definition 2 is the most relevant.

Now, assuming

$$\tilde{G}_{vv}(s) = s \; G_{vv}(s) \tag{3.13}$$

is a positive real transfer function matrix, it can be noticed from (3.13) and (3.5) that all of the poles of $\tilde{G}_{vv}(s)$ are in the left half of the complex plane, hence the system is stable. Furthermore, the system has no poles on the $j\omega$ axis. To prove positive realness of $\tilde{G}_{vv}(s)$, establish that $\tilde{G}_{vv}(j\omega) + \tilde{G}^*_{vv}(j\omega) \geq 0$ is needed for all $\omega \in (-\infty, \infty)$ [85], that is

$$\begin{aligned}
\tilde{G}_{vv}(j\omega) + \tilde{G}^*_{vv}(j\omega) &= \sum_{k=1}^{N} \left\{ \frac{j\omega\Psi_k}{\omega_k^2 - \omega^2 + j2\zeta_k\omega_k\omega} + \frac{-j\omega\Psi_k}{\omega_k^2 - \omega^2 + -j2\zeta_k\omega_k\omega} \right\} \\
&= \sum_{k=1}^{N} \frac{4\zeta_k\omega_k\omega^2\Psi_k}{(\omega_k^2 - \omega^2)^2 + (2\zeta_k\omega_k\omega)^2} \\
&\geq 0 \qquad \text{for all} \;\; \omega \in (-\infty, \infty),
\end{aligned}$$

where the last inequality follows from Equation (3.6).

An implication of the above analysis is that to guarantee the closed-loop stability of the system, it would sufficient to choose an admittance

$$Y(s) = J(s)^{-1} \left(I - s \; J(s) \right) \Lambda^{-1}$$

with $J(s)$ a WSPR and strictly proper transfer function matrix.

3.3 Propose Decentralised Shunt Controllers

The observation made in the previous section prepares for the design impedance structures that guarantee closed-loop stability of the shunted system. This section introduces two specific decentralised structures that enforce the above conditions. Furthermore, these decentralised impedances result in effective wideband reduction of vibrations of the base structure.

These admittances, from Section 2.5.3, are constructed starting from

$$J_a(s) = \sum_{i=1}^{N} \mathrm{diag}\left(\frac{\alpha_{1i}(s+2d_{1i}\omega_i)}{s^2+2d_{1i}\omega_i s+\omega_i^2} \; , \; \frac{\alpha_{2i}(s+2d_{2i}\omega_i)}{s^2+2d_{2i}\omega_i s+\omega_i^2} \; , \; \dots , \frac{\alpha_{mi}(s+2d_{mi}\omega_i)}{s^2+2d_{mi}\omega_i s+\omega_i^2} \right) \tag{3.14}$$

and

$$J_b(s) = \sum_{i=1}^{N} \mathrm{diag}\left(\frac{\alpha_{1i} s}{s^2+2d_{1i}\omega_i s+\omega_i^2} \; , \; \frac{\alpha_{2i} s}{s^2+2d_{2i}\omega_i s+\omega_i^2} \; , \; \dots , \frac{\alpha_{mi} s}{s^2+2d_{mi}\omega_i s+\omega_i^2} \right), \tag{3.15}$$

where, in both cases,

$$\alpha_{qi} \geq 0, \quad i = 1, 2 \dots, N \quad q = 1, 2, \dots, m \tag{3.16}$$

and

$$\sum_{i=1}^{N} \alpha_{qi} = 1, \quad q = 1, 2, \dots, m. \tag{3.17}$$

It can be verified that both $J_a(s)$ and $J_b(s)$ are strictly proper WSPR systems. Hence, the resulting admittances will guarantee closed-loop stability of the system.

Corresponding to $J_a(s)$ and $J_b(s)$, the expressions for $Y_a(s)$ and $Y_b(s)$ can be determined as

$$Y_a(s) = \mathrm{diag}\left(\frac{\sum_{i=1}^{N} \frac{\alpha_{1i}\omega_i^2}{s^2+2d_{1i}\omega_i s+\omega_i^2}}{1-\sum_{i=1}^{N} \frac{\alpha_{1i}\omega_i^2}{s^2+2d_{1i}\omega_i s+\omega_i^2}} \; , \; \dots \; , \; \frac{\sum_{i=1}^{N} \frac{\alpha_{mi}\omega_i^2}{s^2+2d_{mi}\omega_i s+\omega_i^2}}{1-\sum_{i=1}^{N} \frac{\alpha_{mi}\omega_i^2}{s^2+2d_{mi}\omega_i s+\omega_i^2}} \right) \Lambda^{-1} s \tag{3.18}$$

and

$$Y_b(s) = \mathrm{diag}\left(\frac{\sum_{i=1}^{N} \frac{\alpha_{1i}(2d_{1i}\omega_i s+\omega_i^2)}{s^2+2d_{1i}\omega_i s+\omega_i^2}}{1-\sum_{i=1}^{N} \frac{\alpha_{1i}(2d_{1i}\omega_i s+\omega_i^2)}{s^2+2d_{1i}\omega_i s+\omega_i^2}} \; , \; \dots \; , \; \frac{\sum_{i=1}^{N} \frac{\alpha_{mi}(2d_{mi}\omega_i s+\omega_i^2)}{s^2+2d_{mi}\omega_i s+\omega_i^2}}{1-\sum_{i=1}^{N} \frac{\alpha_{mi}(2d_{mi}\omega_i s+\omega_i^2)}{s^2+2d_{mi}\omega_i s+\omega_i^2}} \right) \Lambda^{-1} s. \tag{3.19}$$

One of the interesting properties of the above admittance transfer functions is that in a specific bandwidth, the option of choosing to control only those modes that are of importance is available. This is reflected in the constraint on parameters α_{qi} in (3.16). This is in contrast to the other control design such as LQG and $\mathcal{H}_\infty$, where the controller tends to have equal dimensions to that of the system that is being controlled.

A further property of the controllers Y_a and Y_b is that in the presence of out of bandwidth modes of the base structure, they do not cause instabilities. The spill-over effect [8, 9] is a serious cause of concern in control design for flexible structures. Often a feedback controller is designed using a model of the structure that contains a limited number of modes. Once the controller is implemented on the full order system, the presence of uncontrolled high frequency modes may destabilise the closed-loop system or severely deteriorate the performance. Considering the discussion in Section 3.2, note that such a problem can not happen here.

Now it is straightforward but tedious, to verify that both $Y_a(s)$ and $Y_b(s)$ are strictly positive real transfer functions. They can be realised by passive circuit components, i.e. resistors, inductors and capacitors. Given that both $Y_a(s)$ and $Y_b(s)$ have decentralised structures, effectively each piezoelectric transducer is shunted by an independent admittance. However, it is not clear how such a network may be obtained as standard synthesis techniques result in realisations that require Gyrators [93] and opamps. Even if passive realisations for (3.18) and (3.19) are found, in practice, such an implementation is likely to be impractical. Given that often low frequency modes of a structure are targeted for shunt damping, the required inductors may be excessively large, i.e. 100 to 1000 Henries. A practical way of implementing Y_a or Y_b is to use the synthetic admittance circuit as described in [36], or the alternative and more effective method explained below in Section 3.4.

3.4 Experimental Verification

To validate the proposed concepts, experiments were carried out on a piezoelectric laminated beam as shown in 3.6

3.4.1 Multivariable Experimental Apparatus

The test structure was a uniform aluminium beam with rectangular cross section and experimentally pinned boundary conditions. Two pairs of collocated piezoelectric transducers were attached symmetrically to either side of the structure, as shown in Figures 3.6 and 3.7. The reason for placing the patches in a collocated fashion here, and throughout the Thesis, is the ease of direct measurement of the transfer function $G_{vv}(s)$, i.e. the transfer function between

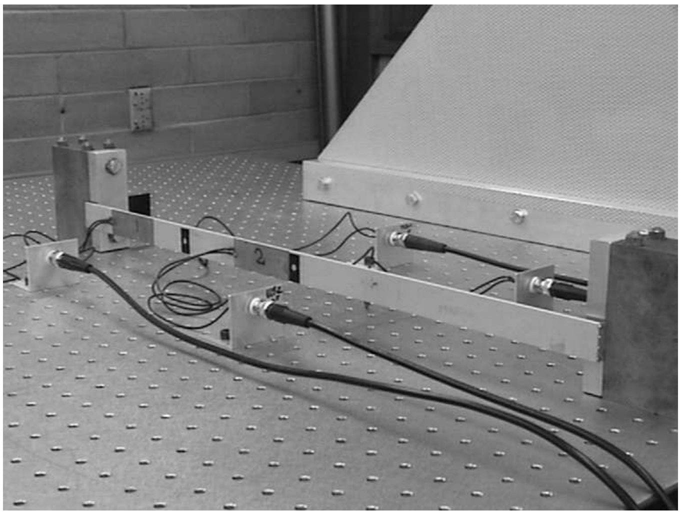

Figure 3.6: Experimental beam apparatus [85].

Parameter	**Symbol**	**Unit**
Length	L	0.6 m
Width	w	0.025 m
Thickness	h	0.004 m
Young's modulus	E	65×10^9 N/m^2
Poisson's ratio	ν	0.3
Mass / unit area	ρ	10.6 Kg/m^2

Table 3.1: Parameters of the simply supported beam.

the $V_z(s)$ to $V_p(s)$. Piezoelectric transducers used in these experiments were PIC151[1] piezoelectric patches. Details of the beam and PIC151 piezoelectric patches are listed in Tables 3.1 and 3.2.

3.4.2 Model Identification for Multivariable System

The first step in the analysis involved procuring a model for the transfer function matrix $G_{vv}(s)$ to simulate the effect of an attached piezoelectric shunt on the transfer function from the applied actuator voltages $V_{in}(s)$ to the generated piezoelectric shunt layer voltages $V_p(s)$.

[1]These patches are manufactured by Polytec PI Ceramics.

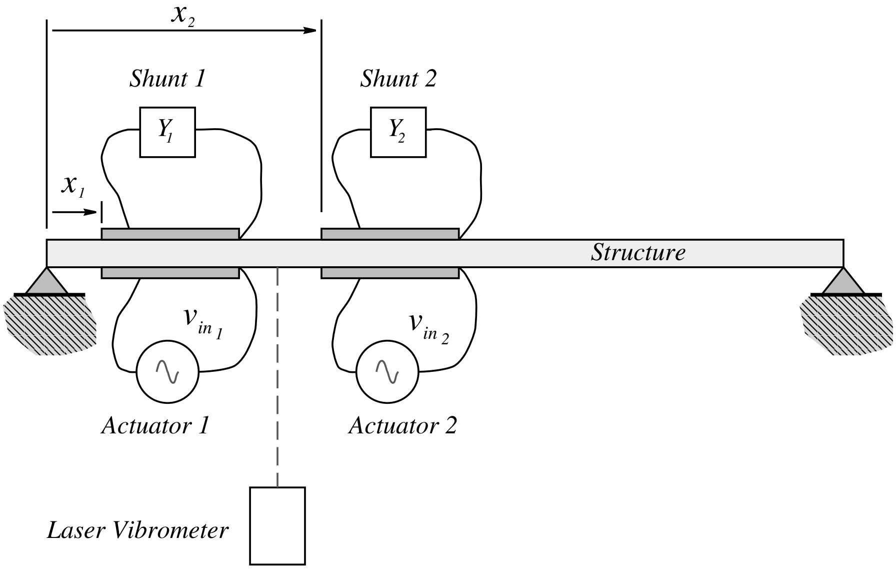

Figure 3.7: Simply supported beam apparatus.

Parameter	Symbol	Unit
Location x-direction	x_1	$0.050\ m$
Location x-direction	x_2	$0.240\ m$
Length	L_p	$0.0724\ m$
Thickness	h_p	$0.00191\ m$
Width	w_p	$0.025\ m$
Capacitance	C_p	$471 \times 10^{-9}\ F$
Young's modulus	E_p	$62 \times 10^{9}\ N/m^2$
Poisson's ratio	ν_p	0.3
Strain constant	d_{31}	$-320 \times 10^{-12}\ m/V$
Electromechanical coupling factor	k_{31}	0.44
Stress constant / voltage coefficient	g_{31}	$-9.5 \times 10^{-3}\ V\ m/N$

Table 3.2: PIC151 piezoelectric parameters.

These variables were internal and can not be measured directly whilst an impedance was attached to the shunting layer. The transfer function from the applied actuator voltages $V_{in}(s)$ to the structural deflection at a point $D(x,s)$ was considered. In the case where there were two actuators and two sensors, a model with two inputs and three outputs was required:

$$\begin{bmatrix} V_p(s) \\ D(x,s) \end{bmatrix} = G_p(s)\ V_{in}(s), \tag{3.20}$$

where $G_p(j\omega) \in \mathbb{C}^{3\times 2}$ is the open-loop plant transfer function matrix.

As discussed earlier in Section 3.1, modelling of piezoelectric laminate structures is spatially distributed problem and generally solved by means of a system identification technique. For this case the Van Overschee and De Moor [105] algorithm will be used to identify a model for the SIMO system.

Experiments were performed to obtain a state-space representation of $G_p(s)$. Referring to Figure 3.7, a pre-filtered periodic chirp was applied to each actuating layer in succession. The resulting open-circuit piezoelectric voltages and displacements were recorded using a dSpace ds1103 rapid prototype system. The chirp pre-filtering was performed by an *FIR* filter designed to reduce the power of the excitation in bands enclosing the resonance frequencies of the structure. This reduces the dynamic range and 'flattened out' the power spectral density and signal-to-noise-ratio versus frequency at the outputs. An estimate for $G_p(j\omega)$ was then obtained using the empirical transfer function estimate [77]. The magnitude frequency response of $G_p(j\omega)$ is plotted in Figure 3.8. 340 frequency samples from 0 to 200 Hz were used to identify a 6 state model for $G_p(s)$. The magnitude frequency response of the model is overlaid on the experimental data in Figure 3.8.

The system identification model matches the experimental data, as verified in Figure 3.8. Results shown in this section and in Section 3.1 authenticate the system identification technique.

3.4.3 Implementation of a Multiport Synthetic Admittance

As introduced in Section 2.3, the synthetic admittance or voltage-control-current-source [35, 36] is used as a means for implementation of piezoelectric shunt damping circuits. Referring back to Figure 2.2, i_z is set as the output of a transfer function and input is the voltage v_z measured across the terminals, i.e. $I_z(s) = Y(s)V_z(s)$. The resulting impedance seen from the terminals is $\frac{1}{Y(s)}$. As in reference [35], an analogue filter or DSP system is used

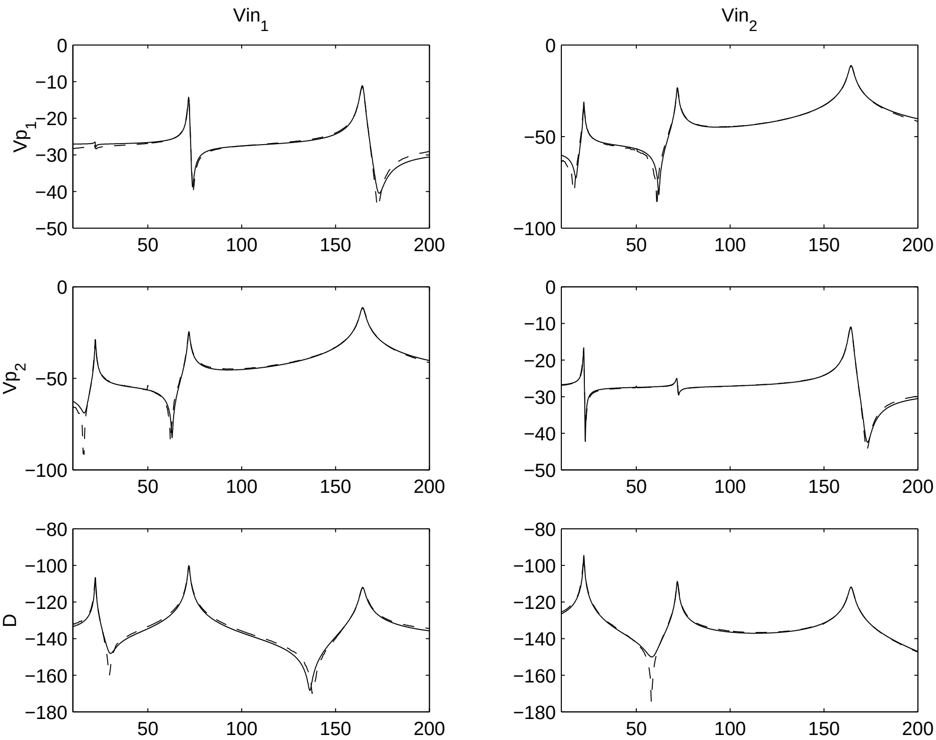

Figure 3.8: Magnitude frequency response of $G_p(s)$. Experimental data ($\cdots$) and identified model (—).

to implement the admittance transfer function. This controls the relationship between the measured terminal voltage and applied current.

To implement the desired multiport synthetic admittance, two identical voltage-control-current-sources were designed and built. Using a single dSpace DSP system two filters were needed to simulate the required admittance transfer functions i.e. the controllers.

Implementing the Admittance Transfer Functions

On first inspection, the admittance structures (3.18) and (3.19) may appear difficult to implement by means of either analog or digital signal processing. In fact the reverse is true, the transfer function can be represented as a simple block diagram composed of second order subsystems. Consider the admittance required for a single piezoelectric transducer using the controller,

$$Y_a(s) = \frac{\sum_{i=1}^{N} \frac{\alpha_i \omega_i^2}{s^2+2d_i\omega_i s+\omega_i^2}}{1-\sum_{i=1}^{N} \frac{\alpha_i \omega_i^2}{s^2+2d_i\omega_i s+\omega_i^2}} C_p s. \tag{3.21}$$

The structure (3.21) is shown diagrammatically in Figure 3.9. Each subsystem $Y_i(s, \alpha_i, d_i, \omega_i)$, parameterised for ease of online tuning, can be implemented by an analogue state variable filter [59] or internally in a DSP algorithm. For digital implementation, each subsystem is most easily parameterised in state-space form. For example,

$$Y_i(s, \alpha_i, d_i, \omega_i) = \frac{y_i}{u} = \frac{\alpha_i \omega_i^2 s}{s^2 + 2d_i\omega_i s + \omega_i^2}, \tag{3.22}$$

where

$$\begin{aligned} \dot{x} &= \begin{bmatrix} 0 & 1 \\ -\omega_i^2 & -2d_i\omega_i^2 \end{bmatrix} x + \begin{bmatrix} 0 \\ 1 \end{bmatrix} u \\ y_i &= \begin{bmatrix} 0 & \alpha_i\omega_i^2 \end{bmatrix} x. \end{aligned} \tag{3.23}$$

3.4.4 Experimental Verification

In the experiments, one of the actuating piezoelectric transducers was used to disturb the structure. The two transducers on opposite sides of the beam were shunted with resonant impedances to attenuate the vibrations generated in the beam. Using the structure $Y_a(s)$ in

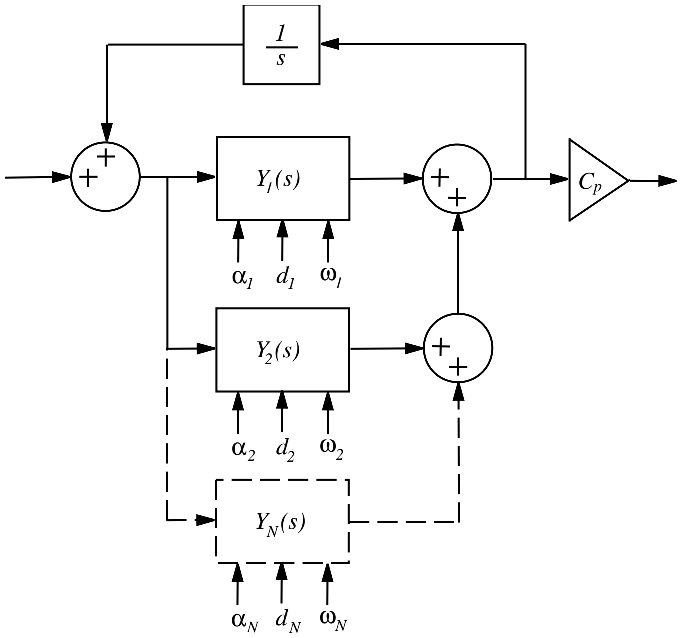

Figure 3.9: System diagram of Equation (3.18) or (3.19).

Equation (3.18), shunt circuits were applied to both of the piezoelectric laminates. Specifically, $Y_1(s)$ was shunted to the first piezoelectric transducer and tuned to control the $2nd$ and $3rd$ modes, and $Y_2(s)$ was shunted to the second piezoelectric transducer and tuned to control the $1st$ and $3rd$ modes. Admittance parameters are shown in Table 3.3. The admittance has a diagonal structure

$$Y_a(s) = \operatorname{diag}\left(Y_1(s)\ ,\ Y_2(s)\right), \tag{3.24}$$

where

$$Y_1(s) = \frac{\left(\frac{\alpha_{1,2}\omega_{1,2}^2}{s^2+2d_{1,2}\omega_{1,2}s+\omega_{1,2}^2} + \frac{\alpha_{1,3}\omega_{1,3}^2}{s^2+2d_{1,3}\omega_{1,3}s+\omega_{1,3}^2}\right)}{1-\left(\frac{\alpha_{1,2}\omega_{1,2}^2}{s^2+2d_{1,2}\omega_{1,2}s+\omega_{1,2}^2} + \frac{\alpha_{1,3}\omega_{1,3}^2}{s^2+2d_{1,3}\omega_{1,3}s+\omega_{1,3}^2}\right)} C_p s \tag{3.25}$$

and

$$Y_2(s) = \frac{\left(\frac{\alpha_{2,1}\omega_{1,1}^2}{s^2+2d_{2,1}\omega_{1,1}s+\omega_{1,1}^2} + \frac{\alpha_{2,3}\omega_{1,3}^2}{s^2+2d_{2,3}\omega_{1,3}s+\omega_{1,3}^2}\right)}{1-\left(\frac{\alpha_{2,1}\omega_{1,1}^2}{s^2+2d_{2,1}\omega_{1,1}s+\omega_{1,1}^2} + \frac{\alpha_{2,3}\omega_{1,3}^2}{s^2+2d_{2,3}\omega_{1,3}s+\omega_{1,3}^2}\right)} C_p s. \tag{3.26}$$

Figure 3.10 compares the simulated frequency response of the unshunted system with that of the shunted system. This figure is associated with a 2×3 system with inputs are the voltages applied to the two actuating piezoelectric patches, with outputs that are the induced piezoelectric voltages and the displacement measurement at $x = 0.17\ m$. The displacement measurements were obtained using a Polytec PSV-300 laser scanning vibrometer.

Figure 3.11 demonstrates the effect of the proposed admittance structure. Observe that by shunting the two piezoelectric patches with the proposed admittances, the closed-loop poles of the system have been pushed further into the left half of the complex plane. Notice that both transducers are used to dampen the third mode, while the first two modes are damped using the second and first transducers respectively. This is due to the location of which the two patches that are mounted on the beam. The first patch offers little authority over the first mode of the beam, while the second patch displays a similar lack of authority over the second mode. Both transducers, however, are effectively reducing vibration corresponding to the third mode of the structure.

In these experiments, variables internal to the piezoelectric transducers were not directly measurable. Therefore, it was not possible to generate experimental results corresponding to all entries of the transfer function matrix displayed in Figure 3.10. However, as the displacement could be measured, results were obtained by applying a disturbance voltage to the first piezoelectric transducer and measuring the resulting displacement. The corresponding transfer functions are plotted in Figure 3.12. Observe that the experimental results closely match the simulation.

Experimental results show a considerable attenuation of the resonant peaks; 5 dB for the $1st$ mode, 10.5 dB for the $2nd$ mode and 14.4 dB for the $3rd$ mode.

To examine the time domain performance of the damped system, a 200 Hz low pass filtered step was applied to V_{in_1}. The simulated and experimental displacement responses measured at $x = 0.17\ m$ are plotted in Figure 3.13. Note that the response is dominated by the first mode of vibration. This is a result of the lower damping achieved for this mode and the comparatively greater low frequency components contained in a step function.

3.5 Discussion

This chapter demonstrates that the problem of piezoelectric shunt damping with several piezoelectric transducers and a multiple impedance is equivalent to a multiple-input-multiple-output feedback control problem parameterised by a multi-input impedance. The multi-input impedance was shown to be inside an inner multi-feedback loop.

Parameter	Unit (Hz)
$\omega_{1,2}$	71.7
$\omega_{1,3}$	161.6
$\omega_{2,1}$	22.14
$\omega_{2,3}$	167.9

Parameter	Unit
$d_{1,2}$	0.021
$d_{1,3}$	0.024
$d_{2,1}$	0.025
$d_{2,3}$	0.023

Parameter	Unit
$\alpha_{1,2}$	0.5
$\alpha_{1,3}$	0.5
$\alpha_{2,1}$	0.5
$\alpha_{2,3}$	0.5

Table 3.3: Admittance parameters.

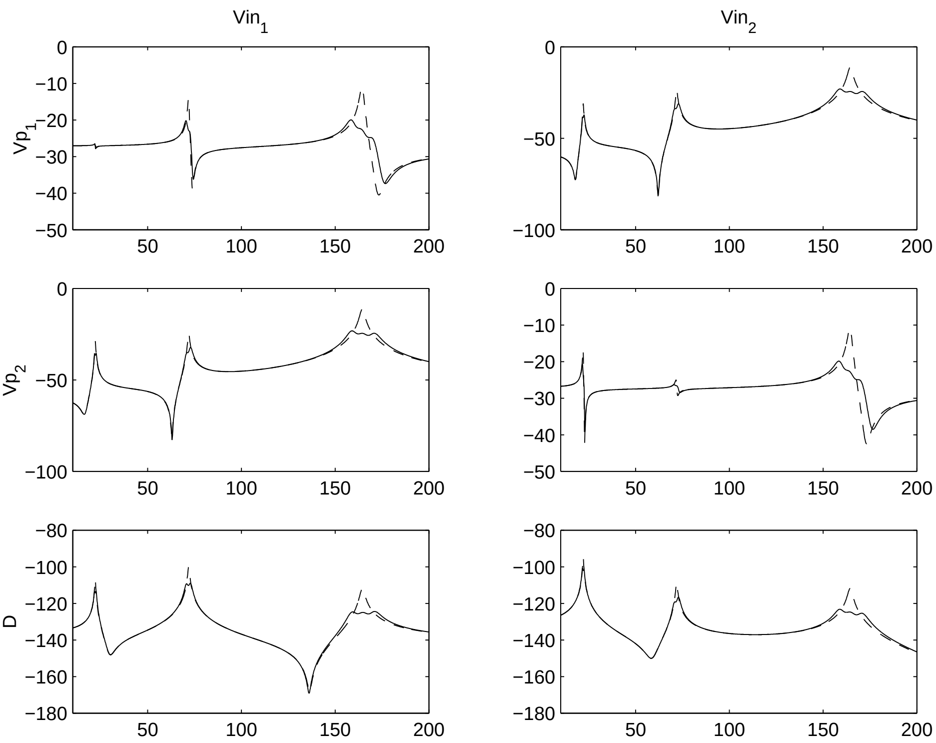

Figure 3.10: Simulated open-loop (−−) and closed-loop (—) magnitude frequency response.

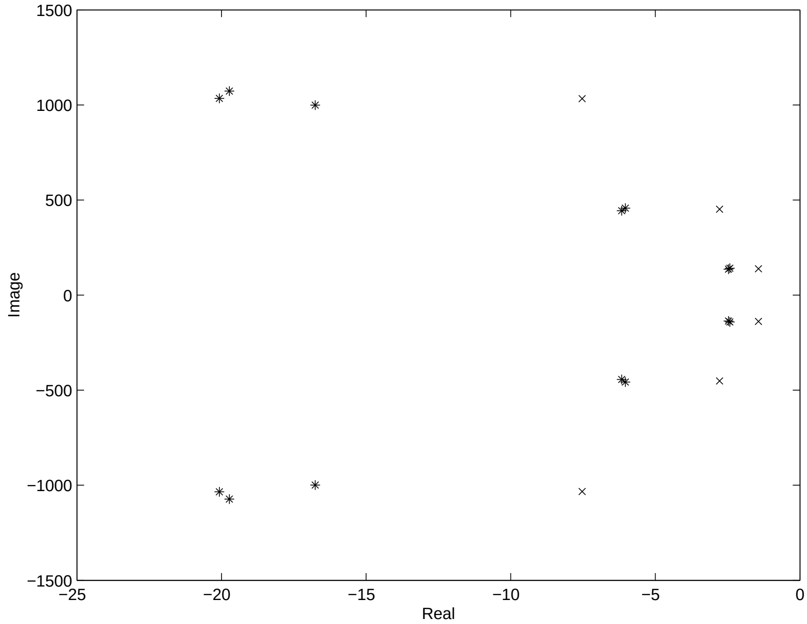

Figure 3.11: Simulated open-loop ($\times$) and closed-loop ($*$) pole locations.

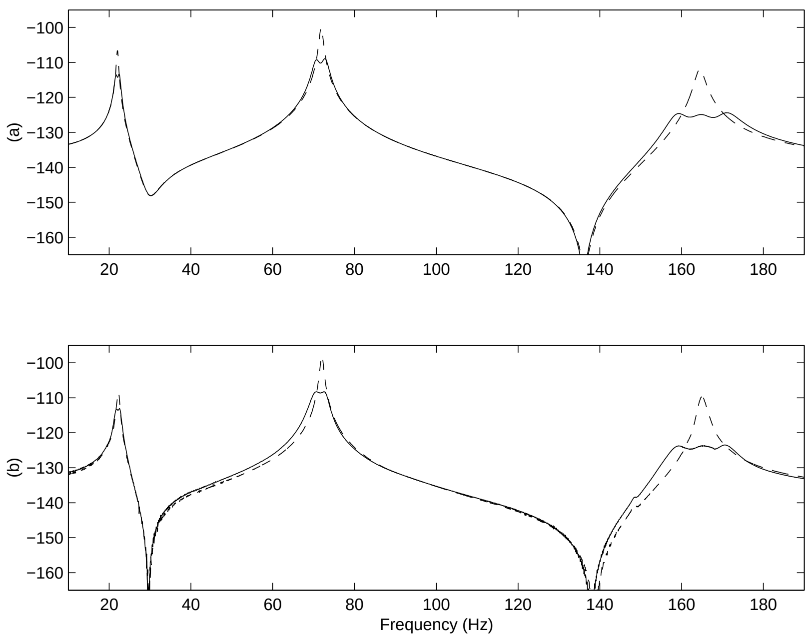

Figure 3.12: Simulated (a) and experimental (b) frequency response from V_{in_1} to the displacement measured at $x = 0.17\ m$. open-loop ($--$) and closed-loop (—).

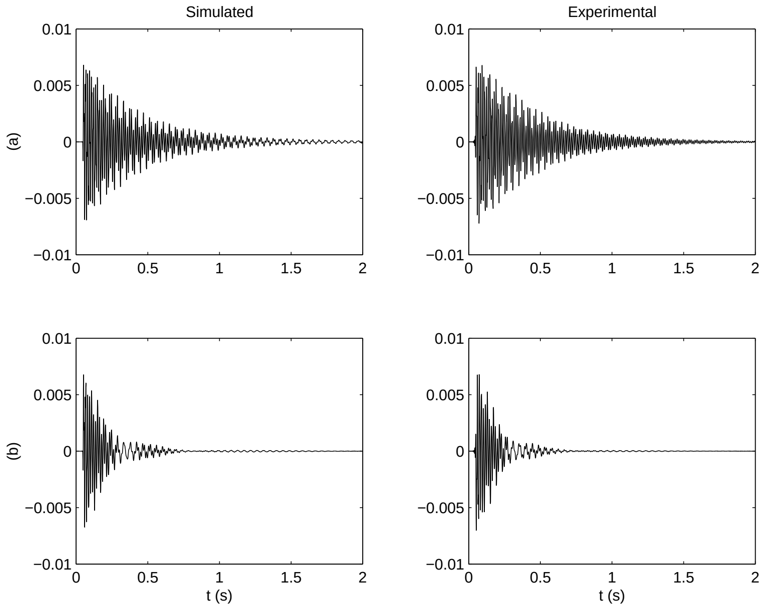

Figure 3.13: Open-loop (a) and closed-loop (b) displacement response at $x = 0.17\ m$ to a low-pass filtered step response applied to V_{in_1}.

Two decentralised shunt impedances/controllers were introduced with favourable stability and robustness properties. The proposed theoretical controllers were validated experimentally on a multivariable experimental apparatus. damping performance was found to match the theroretical and experimental results. However, damping results were slightly disconcerting, since it was anticipated that using multiple shunts should provide increased damping i.e. more control. Unfortunately this was not the case, compared to results found in Chapter 2 and can be attributed to the experimental apparatus configuration. This apparatus had more damped resonate peaks compared to the apparatus found in Chapter 2, and can be attributed to a more durable configuration i.e. thicker electrical wire. This durable configuration can be seen in Figure 3.6 when compared to Figure 2.14.

Overall, this chapter confirms the potential of multivariable shunt control methodologies and paves the way for further research with more realistic applications.

Part II

Electromagnetic Shunt Control

Chapter 4

Electromagnetic Shunt Damping

Part II lays the foundation for an innovative technique for the control of vibration; electromagnetic shunt control. In comparison to previous concepts presented in this work, as illustrated in Section 2.1, electromagnetic shunt control can be designed to minimise vibration without the need of an additional feedback sensor.

In Chapter 2 a technique is presented for the implementation of piezoelectric shunt damping. In this chapter, a new type of shunt damping is proposed: electromagnetic shunt damping. The proposed technique is similar to piezoelectric shunt damping where an appropriately designed impedance is attached to the terminals of an electromagnetic transducer. This provides additional damping to the mechanical structure and eliminates the need for an external sensor, therefore possibly reducing the cost, complexity and sensitivity to transducer failure. Theoretical and experimental results will be presented for a simple electromagnetic shunt damped system.

4.1 Background

Piezoelectric transducers [43] have similar electromechanical properties compared to electromagnetic transducers but exhibit higher mechanical impedance properties. Electromagnetic transducers have considerably different characteristics to piezoelectric transducers. They; have a much greater stroke (usually within the millimeter range as opposed to the micrometer range of piezoelectric transducers), are more physically robust and can be manufactured to any dimensional scale (micro devices [6] to large electrodynamic shakers [32]). Electromagnetic transducers can be found in acoustic speakers [55], active car suspension systems [73], instrument isolation platforms [95], magnetic levitation [19, 108] and magnetic bearings [87].

A new research field called electromagnetic self-sensing, which is similar to the piezoelectric self-sensing technique [7, 31], has recently evolved [19, 53, 74, 87, 108]. A good example of this can be found in reference [21], where the coil current and/or driving voltage can be measured to estimate the relative velocity of the coil (for this case, a speaker coil).

4.2 Electromagnetic Transducers

A Danish scientist, Hans Christian Oersted, established the relationship between electricity and magnetism in 1819. During a lecture he demonstrated that a current carrying wire deflected a nearby compass needle. His discovery, linking magnetic fields with an electric current, was the origin of magnetism.

During the same period, a leading French scientist, Andre-Marie Ampere, is credited for the discovery of electromagnetism - the relationship between electric current and magnetic fields. His work was heavily influenced by the findings of Hans Christian Oersted. Ampere presented a series of papers expounding the theory and basic laws of electromagnetism, which he later called electrodynamics.

Another influential scientist from the same era includes Michael Faraday. He is recognised for combining Oersted's and Ampere's earlier works into somewhat more practical applications. He founded electromagnetic induction which is commonly referred to as Faraday's Law. His contribution involved the invention of the electric motor and generator, which established the first known electromagnetic transducers.

Electromagnetic transducers exhibit similar electromechanical properties as piezoelectric actuators and they can be used as actuators, sensors or both [53, 83, 91]. Piezoelectric transducers take advantage of an electromechanical union between the terminal voltage and developed strain within the transducer, as described in Section 2.1. Correspondingly, electromagnetic transducers take advantage of the union between coil current and induced force. Alternatively, when an electromagnetic transducer experiences a velocity, a voltage is generated across the terminals of the transducer. These transducers are suitable for in-plane force control, have large stroke, physical robustness, high bandwidth, and are low cost which renders them useful in a wide range of applications.

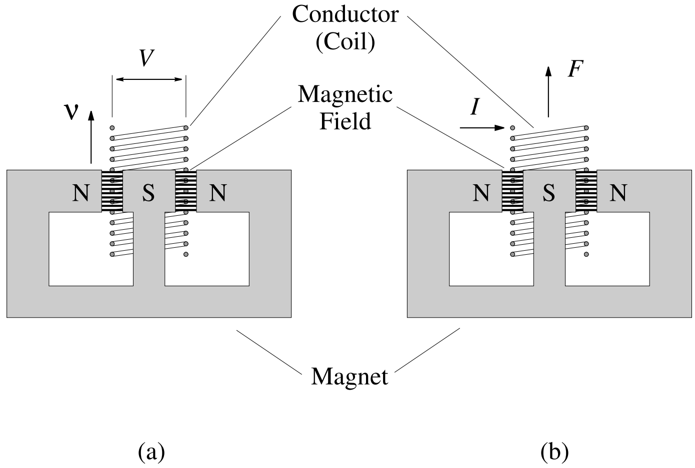

Figure 4.1: Sensing (a) and actuating (b) electromagnetic transducer.

4.2.1 Modelling

An electrical conductor, in the form of a coil moves in a fixed magnetic field which generates voltage V across the terminals of the coil and is proportional to the relative velocity ν, as shown in Figure 4.1 (a). That is, $V \propto \nu$ [91]. Alternatively,

$$V = Bl\nu, \tag{4.1}$$

where B is the magnetic flux (in *teslas* or Wb/m^2) and l is the coil conductor length (in *metres*). Usually the magnetic field is generated by a permanent magnet or a secondary energised coil conductor. Conversely, the coil can be stationary while the magnetic field, normally a permanent magnet, is made to move.

As illustrated in Figure 4.1 (b), when a current I (in *amperes*) is applied to the coil, a force F (in *newtons*) is generated and can be written as

$$F = BlI. \tag{4.2}$$

Therefore, Equation (4.1) and (4.2) can be rewritten [91] as

$$\frac{V}{\nu} = \frac{F}{I} = Bl = C_i, \tag{4.3}$$

where C_i is the ideal electromechanical coupling coefficient.

An electromagnetic transducer can be electrically modelled as an inductor L_e, resistor R_e and a velocity dependent voltage source V_e [53], as shown in Figure 4.2. When the electromagnetic

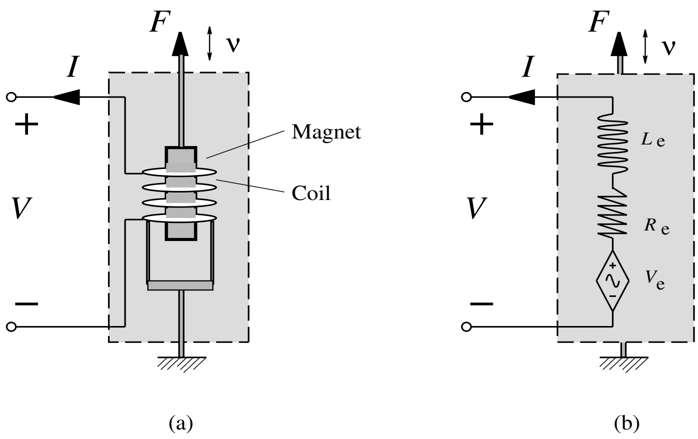

Figure 4.2: Electromagnetic transducer mechanical (a) and electrical (b) equivalent models.

transducer is coupled to a mechanically resonate system, an electro-motive-force (emf) is generated and hence the mechanical velocity can be determined from the terminal voltage. However, more complex forms of the internal impedance can be modeled such as hysteresis, saturation, eddy currents and stray capacitance. For illustration purposes, a nonlinear model is shown in Figure 4.3.

4.3 Modelling a Mechanical System

For most applications where mechanical vibration becomes a problem, the mechanical system can be modelled as a simple mass-spring-damper, as shown in Figure 4.4 (a). The equivalent mass m (in kg), spring constant k (in N/m) and damping constant d (in Ns/m) can be easily determined. The equation of motion for this forced system is given by

$$m\ddot{x}(t) + d\dot{x}(t) + kx(t) = F_d(t), \tag{4.4}$$

where $\ddot{x}(t)$, $\dot{x}(t)$ and $x(t)$ is the acceleration, velocity and displacement of the mass respectively, and $F_d(t)$ is the applied disturbance force. Equation (4.4) can be in the dimensionless form as

$$\ddot{x}(t) + 2\zeta_n\omega_n\dot{x}(t) + \omega_n^2 x(t) = f_d(t), \tag{4.5}$$

where ω_n is the natural frequency $\left(\text{i.e. } \omega_n = \sqrt{\frac{k}{m}}\right)$, ζ_n is the damping coefficient $\left(\zeta_n = \frac{d}{\sqrt{4mk}}\right)$ and the scaled disturbance force $f_d(t) = \frac{F_d(t)}{m}$.

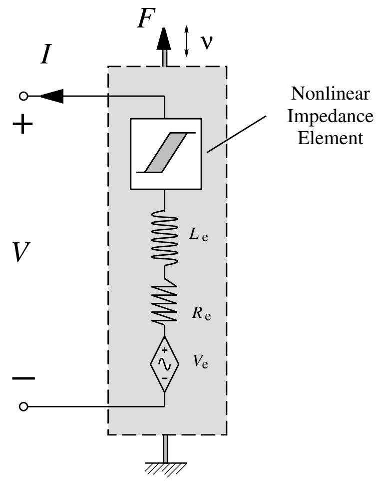

Figure 4.3: Electrically equivalent nonlinear model.

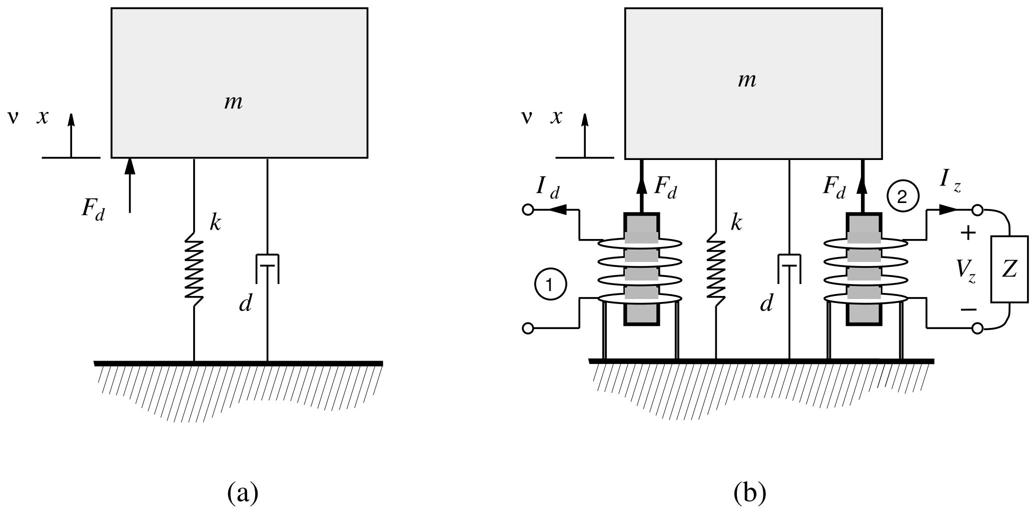

Figure 4.4: Mass-spring-damper system (a) coupled to two identical electromagnetic transducers (b).

Consider Figure 4.4 (b) where an electromagnetic transducer (coil 1) is attached to the mass. If a disturbance current $I_d(t)$ is applied to a linear electromagnetic transducer, a disturbance force $F_d(t)$ is induced, such that

$$F_d(t) = C_1 I_d(t), \tag{4.6}$$

where C_1 is the electromechanical coupling coefficient relating the applied current to a resulting force in coil 1. Using the equation of motion, the disturbed system has the following relationship:

$$m\ddot{x}(t) + d\dot{x}(t) + kx(t) = C_1 I_d(t). \tag{4.7}$$

By taking the Laplace transform, the transfer functions relating the current $I_d(s)$ to displacement $x(s)$ and the current $I_d(s)$ to velocity $\nu(s)$ are

$$G_{ix}(s) \triangleq \frac{x(s)}{I_d(s)} = \frac{C_1}{ms^2 + ds + k} \tag{4.8}$$

and

$$G_{i\nu}(s) \triangleq \frac{\nu(s)}{I_d(s)} = \frac{C_1 s}{ms^2 + ds + k}, \tag{4.9}$$

where the mass velocity $\nu(s)$ is equivalent to $\nu(s) = sx(s)$. Referring to Figure 4.4 (b), note that these two equations are valid when coil 2 is held in open-circuit, i.e. $Z(s) = \infty$.

4.3.1 Shunted Composite Electromechanical System

For an electromagnetic shunted composite system, as shown in Figure 4.4 (b), an impedance $Z(s)$ is attached to coil 2. Therefore the following relationship is

$$m\ddot{x}(t) + d\dot{x}(t) + kx(t) = F_d(t) - F_e(t), \tag{4.10}$$

where $F_e(t)$ is the opposing force due to the impedance $Z(s)$ attached to the terminals of the electromagnetic transducer 2 or coil 2. In the Laplace domain, the following relationship is

$$\nu(s) = \frac{C_1 s}{ms^2 + ds + k} I_d(s) - \frac{s}{ms^2 + ds + k} F_e(s), \tag{4.11}$$

where $I_d(s)$ and $F_e(s)$ are the inputs to the system. That is, $I_d(s)$ is the input current disturbance applied to coil 1 and $F_e(s)$ is the opposing force due to the shunt electromagnetic transducer coil 2.

To determine the opposing force $F_e(s)$, consider the simplified electrical model of the electromagnetic shunt, as shown in Figure 4.5. Ohm's law states that

$$V_z(s) = I_z(s) Z(s), \tag{4.12}$$

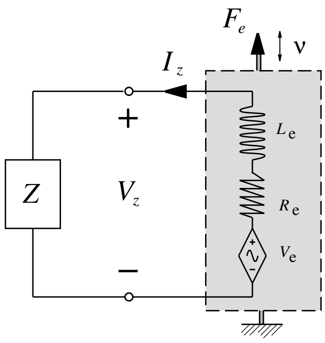

Figure 4.5: Simplified model of the electromagnetic shunt.

where $V_z(s)$ is the voltage across the terminals of the shunt impedance $Z(s)$ and $I_z(s)$ is the corresponding current. From the Kirchhoff's voltage law, the following relationship between $V_e(s)$ and $V_z(s)$ is obtained as

$$V_z(s) = V_e(s) - (L_e s + R_e) I_z(s), \tag{4.13}$$

which implies

$$V_z(s) = \frac{Z(s)}{L_e s + R_e + Z(s)} V_e(s). \tag{4.14}$$

As shown in Equation (4.1), the following linear relationship is

$$V_e(s) = C_4 \nu(s), \tag{4.15}$$

where C_4 is the electromechanical coefficient relating $\nu(s)$ to $V_e(s)$. Since the shunted electromagnetic transducer is attached to the mass m, $\nu(s)$ is equivalent to $sx(s)$.

By substituting (4.15) into (4.14), the results are

$$V_z(s) = \frac{Z(s)}{L_e s + R_e + Z(s)} C_4 \nu(s). \tag{4.16}$$

Alternatively, the current flowing through the shunt $I_z(s)$ is

$$I_z(s) = \frac{V_z(s)}{Z(s)} = \frac{1}{L_e s + R_e + Z(s)} C_4 \nu(s) \tag{4.17}$$

and the opposing shunt force $F_e(s) = C_3 I_z(s)$. Assuming there is a linear electromagnetic transducer, the results are

$$F_e(s) = \frac{C_3 C_4}{L_e s + R_e + Z(s)} \nu(s) = K(s) \nu(s), \tag{4.18}$$

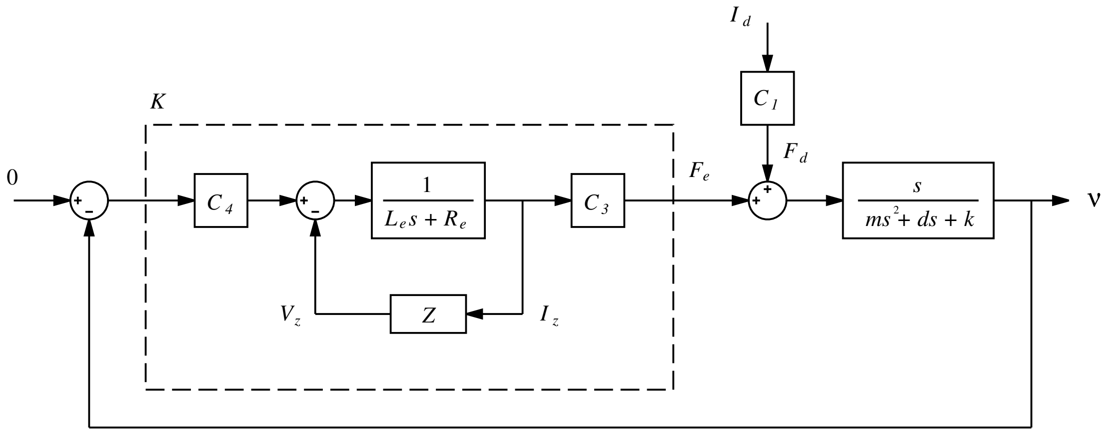

Figure 4.6: Mass-spring-damper feedback control problem where the effective controller $K(s)$ is parameterised by the impedence $Z(s)$. Note this system is equivilent to a velocity $\nu(s)$ feedback control problem.

where the effective controller for the system is

$$K(s) = \frac{C_3 C_4}{L_e s + R_e + Z(s)}. \tag{4.19}$$

By substituting (4.18) into (4.11), the composite system transfer function relating $I_d(s)$ to $\nu(s)$ is

$$\tilde{G}_{i\nu}(s) \triangleq \frac{\nu(s)}{I_d(s)} = \frac{C_1 s}{ms^2 + \left(d + \frac{C_3 C_4}{L_e s + R_e + Z(s)}\right) s + k}, \tag{4.20}$$

as shown in Figure 4.6. The damped system transfer function $\tilde{G}_{i\nu}(s)$ is in the form of a regulator feedback control problem where the velocity $\nu(s)$ is to be regulated to zero. Also, the effective controller $K(s)$ is parameterised by the impedance $Z(s)$, as shown in Figure 4.6.

4.3.2 State-space Shunted Composite Electromechanical System

Figure 4.7 shows a general mechanical plant model P where the inputs to the plant are electromagnetic transducer force F_e and disturbance w. A typical disturbance scenario w could include displacement, velocity, acceleration and/or force disturbances. For this system, the general plant has only a single output; velocity ν. Referring to the simple mass-spring-damper system, as shown in Figure 4.4 (a), the transfer function $G_{F\nu}(s)$ from an applied

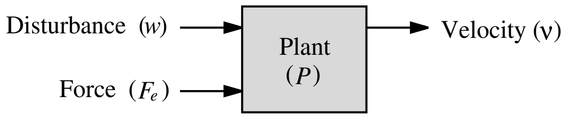

Figure 4.7: General mechanical plant P model.

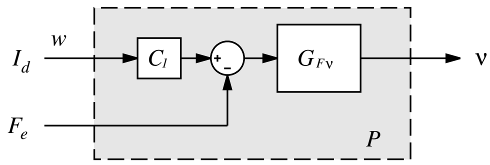

Figure 4.8: Mechanical plant P with disturbance current I_d and control force F_e.

force F_d to the resulting velocity ν is

$$G_{F\nu}(s) = \frac{\nu(s)}{F_d(s)} = \frac{s}{ms^2 + ds + k}. \tag{4.21}$$

Alternatively, the state-space model for $G_{F\nu}(s)$ can be written as

$$\begin{aligned} \dot{\mathbf{x}}_p(t) &= \mathbf{A}_p \mathbf{x}_p(t) + \mathbf{B}_p F_d(t) \\ \nu(t) &= \mathbf{C}_p \mathbf{x}_p(t) \end{aligned} \tag{4.22}$$

where the states of the system are represented by $\mathbf{x}_p(t)$.

Consider Figure 4.4 (b) where a simple mass-spring-damper is coupled by two electromagnetic transducers; transducer 1 and 2. A disturbance force F_d is generated by transducer 1 (or coil 1), while an opposing control force F_e is generated by transducer 2 (or coil 2), as shown in Figure 4.8. The electromechanical coupling coefficients C_1 through C_4 are as

$$C_1 = \tfrac{F_d}{I_d} \quad C_2 = \tfrac{V_{e_1}}{\nu} \quad C_3 = \tfrac{F_e}{I_z} \quad C_4 = \tfrac{V_{e_2}}{\nu}. \tag{4.23}$$

Since transducers (or coils) are not perfectly matched, the force-current or velocity-voltage coupling coefficients will not be identical.

Using the electromechanical coupling coefficients, defined in Equation (4.23), as well as Equations (4.16) and (4.17), the electromagnetic system E for transducer 2 can be modelled, shown in Figure 4.9. Note Figure 4.9 defines the voltage and current driven transducer for transducer 2.

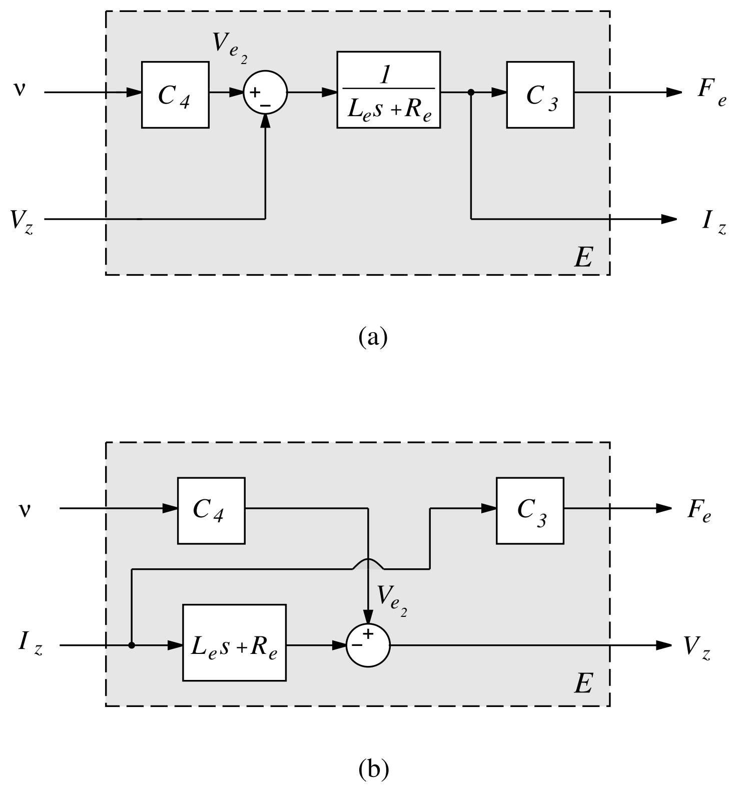

Figure 4.9: Electromagnetic transducer block diagram for representation of a voltage (a) and current (b) driven.

Considering the mechanical plant P and shunted electromagnetic transducer E, as shown in Figures 4.8 and 4.9 the composite system G can be constructed, as shown in Figures 4.10 (a) and 4.11 (a), where $Y(s)$ is the admittance and $Z(s)$ is the impedance.

The admittance $Y(s)$, shown in Figure 4.10 (a), is the transfer function between the transducer terminal voltage and current. By joining the mechanical system P and electromagnetic system E, as shown in Figure 4.10 (b), the composite system G can be cast as a regular feedback control problem where the controller is the admittance $Y(s)$. Therefore, the composite closed-loop transfer function from an applied disturbance current $I_d(s)$ to the resulting plunger velocity $\nu(s)$ is

$$\tilde{G}_{i\nu}(s) \triangleq \frac{\nu(s)}{I_d(s)} = \frac{G_{F\nu}(s)C_1}{1+K(s)G_{F\nu}(s)}, \tag{4.24}$$

where the effective feedback controller is $K(s)$. That is

$$K(s) = \frac{C_3C_4Y(s)}{1+(L_es+R_e)Y(s)}. \tag{4.25}$$

Similar results can be achieved for the impedance $Z(s)$, as shown in Figure 4.11, where the equivalent feedback controller is

$$K(s) = \frac{C_3C_4\frac{1}{L_es+R_e}}{1+\frac{1}{L_es+R_e}Z(s)}. \tag{4.26}$$

4.4 Proposed Shunt Controllers

As illustrated previously in Figures 4.10 and 4.11, and in Equation (4.24), the impedance or admittance can be parameterised as a feedback control problem for the mechanical system $G_{F\nu}(s)$. In the following subsections, a number of novel impedance and/or admittance controllers will be developed to dampen structural vibration.

4.4.1 Capacitor-Resistor Controller

As shown in Section 2.2, authors Forward [41] and Hagood *et al.* [48] suggested that a series inductor-resistor shunt circuit attached across the conducting surfaces of a piezoelectric transducer can be tuned to dissipate the mechanical energy of a host structure. They demonstrated the effectiveness of this technique by tuning the resulting inductor-resistor ($L-R$) circuit and inherent capacitance of the piezoelectric transducer to a specific resonance frequency of the host structure.

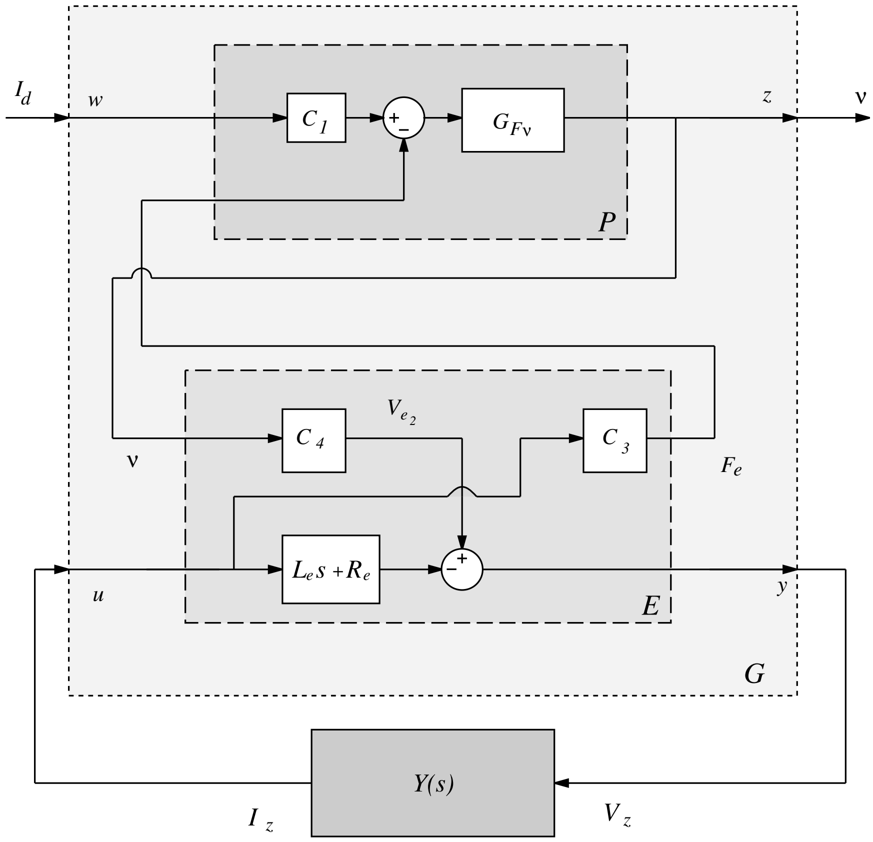

Figure 4.10: Shunt admitance Y controlled electromechanical system G. Note mechanical plant P and electromagnetic transducer system E.

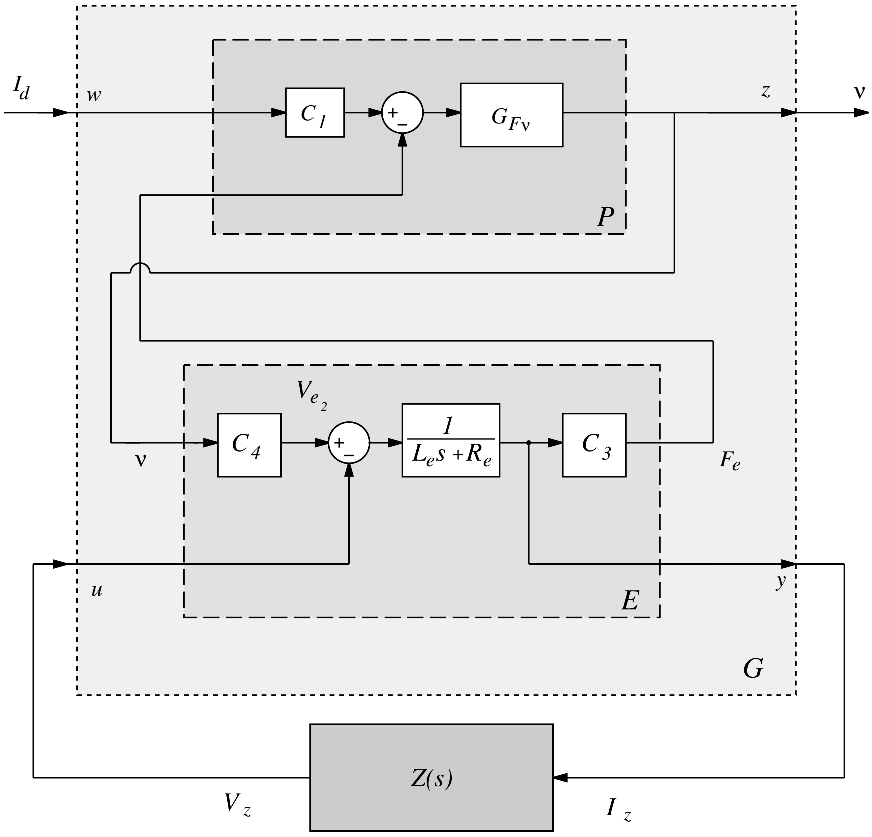

Figure 4.11: Shunt impedance Z controlled electromechanical system G. Note mechanical plant P and electromagnetic transducer system E.

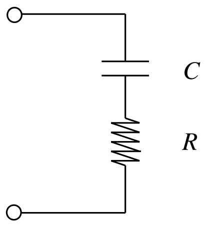

Figure 4.12: Capacitor-resister shunt circuit for an electromagnetic transducer.

Similar to the piezoelectric analogy, a resonant shunt circuit could be used to provide mechanical damping. For this scenario, though, a capacitor-resistor ($C - R$) circuit, as shown in Figure 4.12, needs to be applied to the terminals of the electromagnetic transducer. That is

$$\begin{aligned} Z(s) &= \frac{1}{Cs} + R \\ &= \frac{CRs + 1}{Cs}, \end{aligned} \tag{4.27}$$

where the capacitance value is governed by $\omega_n^2 = \frac{1}{CL_e}$. L_e denotes the inherent inductance of the electromagnetic transducer to be shunted and ω_n is the resonance frequency of the mechanical structure to be controlled.

For example, for a simple mass-spring-damper system, as shown in Figure 4.4 (b), the capacitance is $C = \frac{1}{\omega_n^2 L_e} = \frac{1}{\frac{k}{m} L_e}$. That is $\omega_n = \sqrt{\frac{k}{m}}$, as in Equation (4.5), where k is the spring constant and m the mass of the mechanical system.

For the shunted electromagnetic transducer, $\nu(s)$ is related to F_e via $F_e(s) = K(s)\nu(s)$, where the effective controller is

$$K(s) = \frac{C_3 C_4 \frac{1}{L_e}}{s^2 + \frac{R_t}{L_e} s + \frac{1}{CL_e}}. \tag{4.28}$$

It should be noted that the controller has a resonant structure, thus $R_t = (R_e + R)$ determines the controller damping.

In order to determine an appropriate value for the total shunt resistance R_t, an optimisation approach can be used to minimise the $\mathcal{H}_2$ norm of the closed-loop system $\tilde{G}_{i\nu}(s)$ in references [12, 35]. This required a solution to the following optimisation problem

$$R_t^* = \begin{matrix} \arg\min \\ R_t > 0 \end{matrix} \left\| \tilde{G}_{i\nu}(s) \right\|_2. \tag{4.29}$$

4.4.2 Ideal Negative Inductor-Resistor Controller

Consider a standard velocity feedback regulator problem, as shown in Figure 4.13, where the velocity $\nu(s)$ is sensed and an opposing control force $F_e(s)$ is applied to the mechanical structure. That is $F_e(s) = K(s)\nu(s)$, where $K(s)$ is the control gain. From Figures 4.6 and 4.13, there is a similar feedback control structure where the control force is

$$F_e(s) = \frac{C_3 C_4}{L_e s + R_e + Z(s)} \nu(s) = K(s)\nu(s). \tag{4.30}$$

Therefore, the effective controller $K(s)$ is equivalent to

$$K(s) \triangleq \frac{C_3 C_4}{L_e s + R_e + Z(s)}. \tag{4.31}$$

Now, by simple manipulation of Equations (4.26) and (4.24), the closed-loop system can be obtained as

$$\begin{aligned}\tilde{G}_{i\nu}(s) \triangleq \frac{\nu(s)}{I_d(s)} &= \frac{G_{F\nu}(s)C_1}{1 + \frac{C_3 C_4}{L_e s + R_e + Z(s)} G_{F\nu}(s)} \\ &= \frac{G_{F\nu}(s)C_1 \left(L_e s + R_e + Z(s)\right)}{L_e s + R_e + Z(s) + C_3 C_4 G_{F\nu}(s)}.\end{aligned} \tag{4.32}$$

Note that in the transfer function, Equation (4.32), the numerator is $L_e s + R_e + Z(s)$. Ideally, by setting $L_e s + R_e + Z(s)$ to zero, the closed-loop system $\tilde{G}_{i\nu}(s)$ will be zero. Likewise, by selecting

$$Z_i(s) = -\left(L_e s + R_e\right) \tag{4.33}$$

or

$$Y_i(s) = -\frac{1}{L_e s + R_e}, \tag{4.34}$$

there will be little or no effect by the disturbance on the mechanical system. By implementing Equations (4.34) or (4.33), the effective controller is simply a proportional feedback loop of infinite gain, that is $K(s) = \infty$. A similar result can be found by assuming the composite system $\tilde{G}_{i\nu}(s)$, Equation (4.20), has infinite damping, i.e. $\left(d + \frac{C_3 C_4}{Z(s) + L_e s + R_e}\right) = \infty$.

For the ideal impedance $Z_i(s)$, or $Y_i(s)$ the shunt control scheme is virtually immune to variations in structural dynamics, since the control only depends on the dynamics of the electromagnetic transducer. Also, the composite system will be stable if the controller is less than or equal to the inductance-resistance of the electromagnetic transducer.

In practice the equivalent electrical model of the electromagnetic transducer does not fully describe the internal dynamics, in particular the electromechanical coupling. To deal with uncertainty in the transducer dynamics impedance $Y(s)$ is chosen conservatively, such that

$$Y(s) = -\frac{1}{\varepsilon(L_e s + R_e)}, \tag{4.35}$$

where ε is an uncertainty gain $\varepsilon < 1$. A similar result exists for piezoelectric transducers and can be found in references [10, 11, 116].

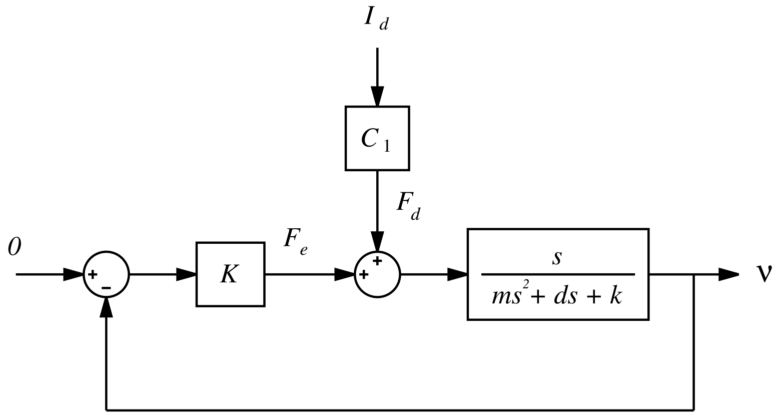

Figure 4.13: Standard velocity feedback regulator problem.

4.4.3 Impedance Synthesis

As discussed earlier in Section 4.3.2, the closed-loop mechanical system $\tilde{G}_{i\nu}(s)$ can be parameterised by a feedback controller impedance $Z(s)$, as shown in Figure 4.11, and in the Equation (4.24). Note an input disturbance I_d results in an output velocity ν.

By applying LQR synthesis control techniques [68], a state-space model is required for the composite system G. Therefore, the state-space model form the electromagnetic transducer coil admittance, i.e. $\frac{1}{L_e s+R_e}$, that is

$$\begin{aligned} \dot{x}_y(t) &= \mathbf{A}_y x_y(t) + \mathbf{B}_y V(t) \\ I_z(t) &= \mathbf{C}_y x_y(t), \end{aligned} \tag{4.36}$$

where

$$\mathbf{A}_y = \left[-\frac{R_e}{L_e} \right] \qquad \mathbf{B}_y = [1] \qquad \mathbf{C}_y = \left[\frac{1}{L_e} \right]$$

and the states of the admittance is represented by $x_y(t)$.

Now the composite system G can be represented as a state-space model as

$$\begin{aligned} \dot{\mathbf{x}}_g(t) &= \mathbf{A}_g \mathbf{x}_g(t) + \mathbf{B}_g \begin{bmatrix} I_d(t) \\ V_z(t) \end{bmatrix} \\ \begin{bmatrix} \nu(t) \\ I_z(t) \end{bmatrix} &= \mathbf{C}_g \mathbf{x}_g(t), \end{aligned} \tag{4.37}$$

where the concatenated matrices $\mathbf{x}_g(t)$, $\mathbf{A}_g$, $\mathbf{B}_g$ and $\mathbf{C}_g$ as

$$\mathbf{x}_g(t) = \begin{bmatrix} \mathbf{x}_p(t) \\ x_y(t) \end{bmatrix}, \qquad \mathbf{B}_g = \begin{bmatrix} \mathbf{B}_p C_1 C_4 & \mathbf{0} \\ \mathbf{0} & -\mathbf{B}_y \end{bmatrix} \tag{4.38}$$

and

$$\mathbf{A}_g = \begin{bmatrix} \mathbf{A}_p & \mathbf{B}_p \mathbf{C}_y C_3 C_4 \\ \mathbf{B}_y \mathbf{C}_p & \mathbf{A}_y \end{bmatrix}, \quad \mathbf{C}_g = \begin{bmatrix} \frac{1}{C_4}\mathbf{C}_p & \mathbf{0} \\ \mathbf{0} & \mathbf{C}_y \end{bmatrix}. \tag{4.39}$$

For this case, the LQR controller design objective is to minimise the velocity $\nu(t)$ while constraining the amplitude of the voltage control signal $V_z(t)$. Therefore, the linear quadratic objective is to minimise

$$J = \int_{-\infty}^{\infty} \left\{ \nu^2(t) + (k_u V_z(t))^2 \right\} \, dt, \tag{4.40}$$

where the voltage control signal $V_z(t)$ has a weighting k_u. Or, in the standard LQR control framework,

$$J = \int_{-\infty}^{\infty} \left\{ \mathbf{x}_g^{'}(t) Q \mathbf{x}_g(t) + u^{'}(t) R u(t) \right\} \, dt, \tag{4.41}$$

where $Q = \begin{bmatrix} \frac{1}{C_4}\mathbf{C}_p & \mathbf{0} \end{bmatrix}^{'} \begin{bmatrix} \frac{1}{C_4}\mathbf{C}_p & \mathbf{0} \end{bmatrix}$ and $R = k_u^2$.

Alternatively, by minimising the $\mathcal{H}_2$ control objective of the weighed sum of the velocity ν and control voltage signal V_z in presence of a disturbance I_d, the following H_2 control objective can be defined as

$$J = \left\| \frac{\nu(s) + k_u V_z(s)}{I_d(s)} \right\|_2 . \tag{4.42}$$

For the augmented plant $\tilde{G}$, as shown in Figure 4.14, G includes the weighting k_u for the voltage control signal V_z, in Equation (4.42) now minimising

$$J = \left\| \frac{z(s)}{w(s)} \right\|_2 , \tag{4.43}$$

where Equation (4.37) has a non-zero D matrix,

$$\tilde{\mathbf{D}}_g = \begin{bmatrix} \mathbf{0} & k_u \\ \mathbf{0} & \mathbf{0} \end{bmatrix}. \tag{4.44}$$

4.5 Experimental Verification

In order to verify the modelling and proposed controller designs presented in the previous sections, each will be applied to an experimental electromagnetic apparatus.

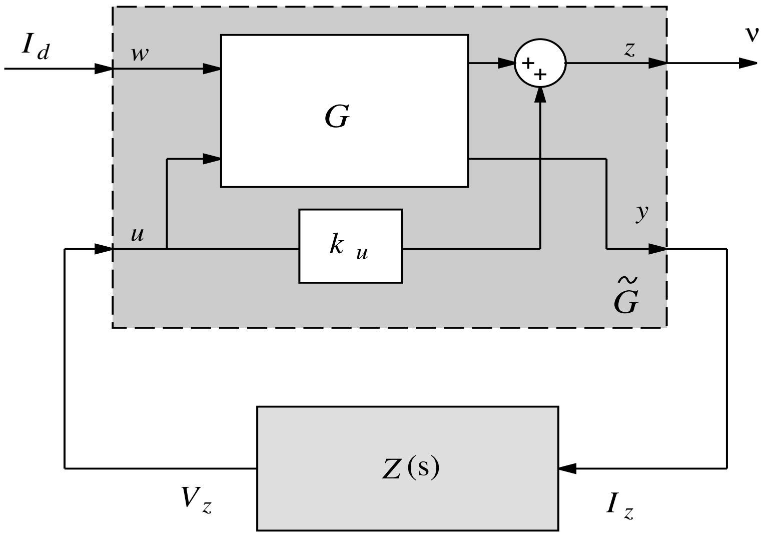

Figure 4.14: Modified system $\tilde{G}$ required for $\mathcal{H}_2$ impedance.

4.5.1 Electromagnetic Apparatus

The electromagnetic apparatus consists of a rigid support, flexible supports, mounting plate and coils as pictured in Figure 4.15. The experimental apparatus essentially consists of two identical electromagnetic transduces (or coils) and a magnetic plunger which is supported by two flexible disks. A sectional view of the experimental apparatus is shown in Figure 4.16. The transducer coils consists of 0.25 mm diameter enamel coated copper wire with an electrical resistance of $R_e = 3.3\ \Omega$ and $L_e = 1\ mH$ inductance. The magnetic plunger consists of three Neodymium-Iron-Boron magnets with opposing poles that meet at the center of each electrical coil. Note the a strong magnetic field exits at right angles to the magnetic plunger. When the magnetic plunger is in travel, a magnetic field intersects through the coil and hence a voltage is generate at the transducer terminals. The physical parameters of the experimental electromagnetic apparatus is summarised in Table 4.1. To prevent distorting the magnetic field, non-magnetic materials such as aluminum and copper were chosen for the construction of the electromagnetic apparatus.

By applying a disturbance current I_d to transducer 1 and measuring the plunger velocity with a PSV-300 Polytec vibrometer, the experimental open-loop ($G_{i\nu}$) and closed-loop ($\tilde{G}_{i\nu}$) transfer functions can be measured.

Parameter	Symbol	Unit
Spring coefficient	k	$56\ kNm^{-1}$
Damping coefficient	d	$2.667\ Nsm^{-1}$
Mass or magnetic plunger mass	m	$0.150\ Kg$
Coupling (current-to-force for transducer 1)	$C_1 = \frac{F_d}{I_d}$	3.55
Coupling (velocity-to-voltage for transducer 1)	$C_2 = \frac{V_{e_1}}{\nu}$	4.06
Coupling (current-to-force for transducer 2)	$C_3 = \frac{F_e}{I_z}$	3.55
Coupling (velocity-to-voltage for transducer 2)	$C_4 = \frac{V_{e_2}}{\nu}$	4.06
Transducer 2 coil inductance	L_e	$1\ mH$
Transducer 2 coil resistance	R_e	$3.3\ \Omega$

Table 4.1: Experimental electromagnetic apparatus parameters.

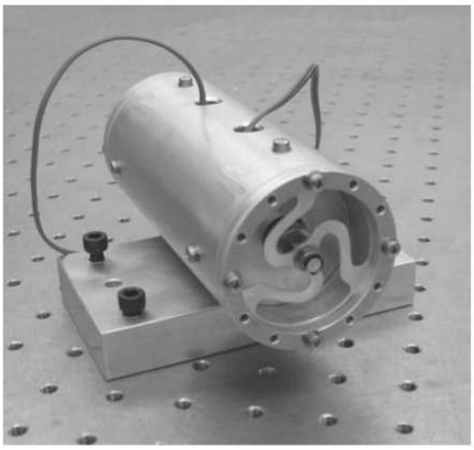

Figure 4.15: Experimental electromagnetic apparatus.

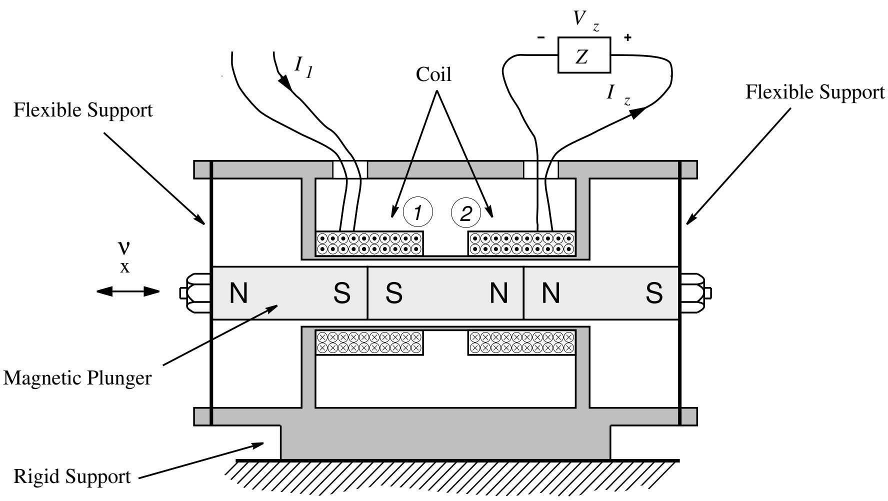

Figure 4.16: Section view of experimental electromagnetic apparatus.

4.5.2 Implementing Electromagnetic Shunt Controllers

As discussed earlier in the thesis in Section 2.3, a current-controlled-voltage-source (CCVS) or a voltage-controlled-current-source (VCCS) was used to implement the desired shunt impedances or admittances. However, the CCVS and VCCS sensing differential amplifiers were reconfigured to operate at lower voltages and higher currents to match the dynamics of the electromagnetic transducer.

4.5.3 Shunt Controllers

In this section, three electromagnetic shunt damping controllers will be examined.

Capacitor-Resistor Controller

The electromechanical model was first determined by measuring the frequency response from an applied current I_d to the resulting plunger velocity $\nu(s)$, that is $G_{i\nu}(s)$, as shown in Figure 4.17. Observe that the model is an accurate representation of the physical system $G_{i\nu}(s)$.

Since damping the fundamental frequency of the mass-spring-damper system is desired, i.e. $\omega_n = 97.3\ Hz$, the required shunt capacitance value is $C = 2.7\ mF$. Using the proposed

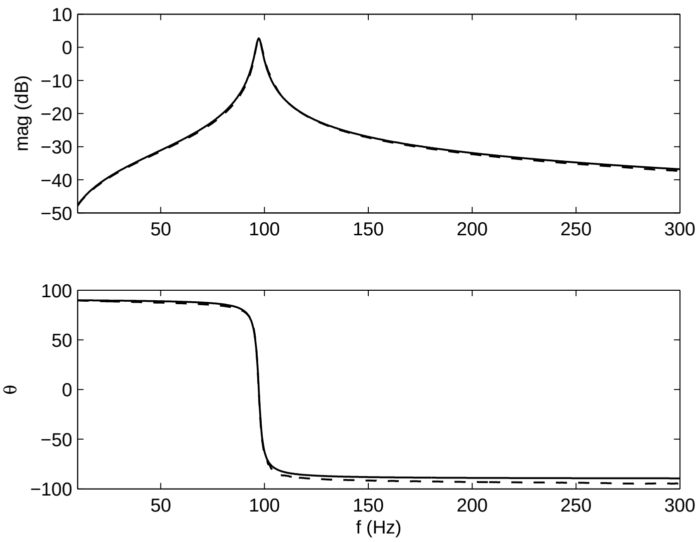

Figure 4.17: Open-loop frequency response from an applied actuator current to plunger velocity, i.e. $G_{i\nu}(s)$, model (—) and measured results (−−).

optimisation strategy the required optimal shunt resistance $R_t^* = 0.29\ \Omega$ was determined. Alternatively, R_t^* can be found by plotting $\mathcal{H}_2$ norm against R_t, as shown in Figure 4.18.

With the aim of damping the system, a total series resistance $R_t = R_e + R = 0.29\ \Omega$ and a capacitance 2.7 mF were applied to the second winding using the CCVS apparatus, explained in Section 4.5.2. Therefore, the required impedance $Z(s)$ is

$$Z(s) = \frac{1}{Cs} + R = \frac{1}{0.0027s} - 3.01. \tag{4.45}$$

The pole-zero map and the frequency response for the passive controller are shown in Figures 4.19 and 4.20 respectively. After examining the open-loop and closed-loop pole locations shown in Figure 4.21, it can be appreciated that the controller is clearly acting to increase the system damping.

The measured open-loop simulated damped $\tilde{G}_{i\nu}(s)$ and measured damped frequency responses are shown in Figure 4.22. A significant reduction of 21.8 dB in the magnitude of the electromechanical system is observed. The effect of such reduction greatly decreases the settling time of the system. Figure 4.23 shows the undamped response of the system to a 1 Amp 300 Hz low-pass filtered step in actuator current. In comparison, the damped response shown in Figure 4.23 settles in less than one tenth of the time taken by the undamped system.

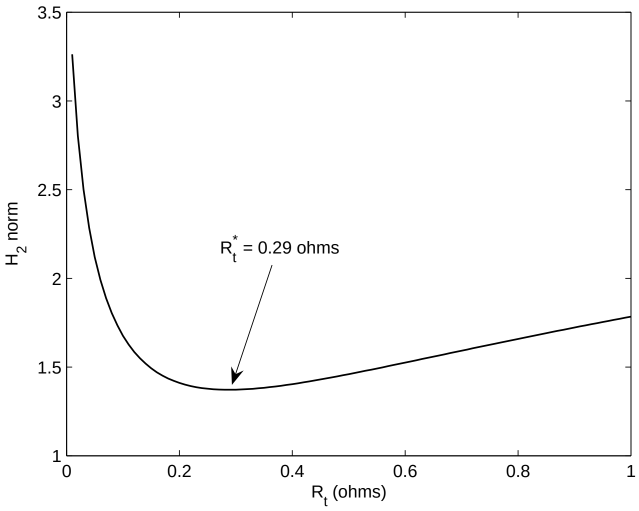

Figure 4.18: $\left\|\tilde{G}_{i\nu}(s)\right\|_2$ against R_t (Ω).

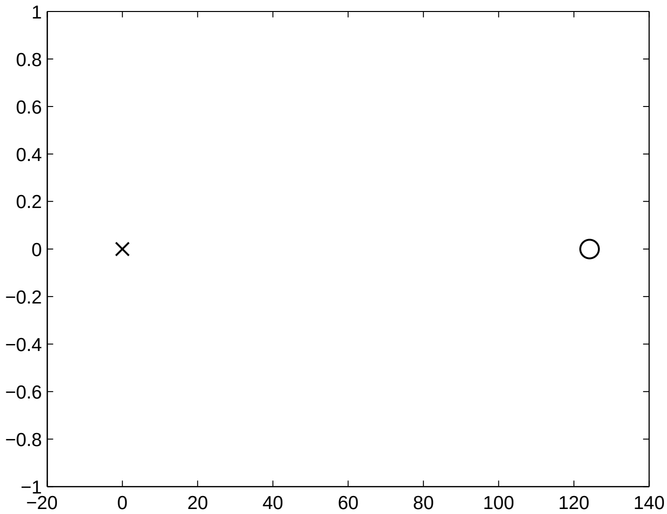

Figure 4.19: Poles ($\times$) and zeros ($\bigcirc$) of the capacitor-resistor impedance.

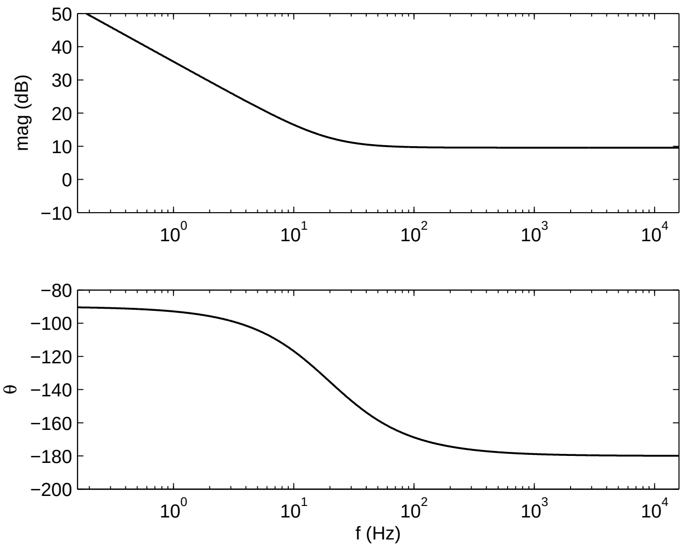

Figure 4.20: Magnitude and phase response for capacitor-resistor controller.

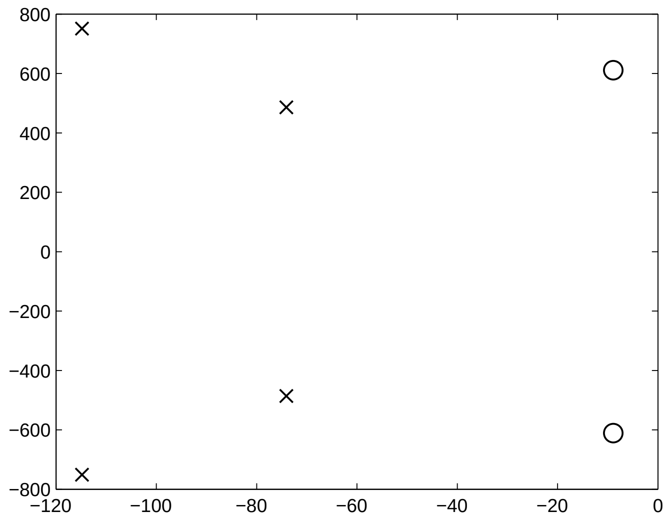

Figure 4.21: Open-loop ($\times$) and closed-loop ($*$) pole locations for the capacitor-resistor shunted system.

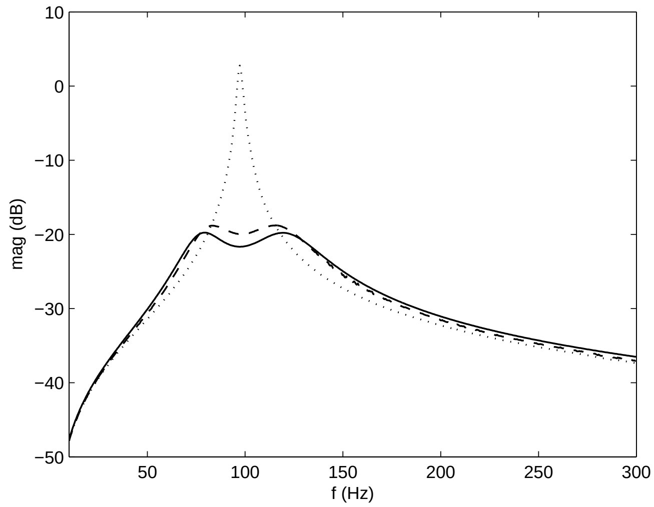

Figure 4.22: Open-loop $(\cdots)$, theoretically predicted damped (—) and measured damped $(--)$ frequency responses from an applied current to resulting plunger velocity.

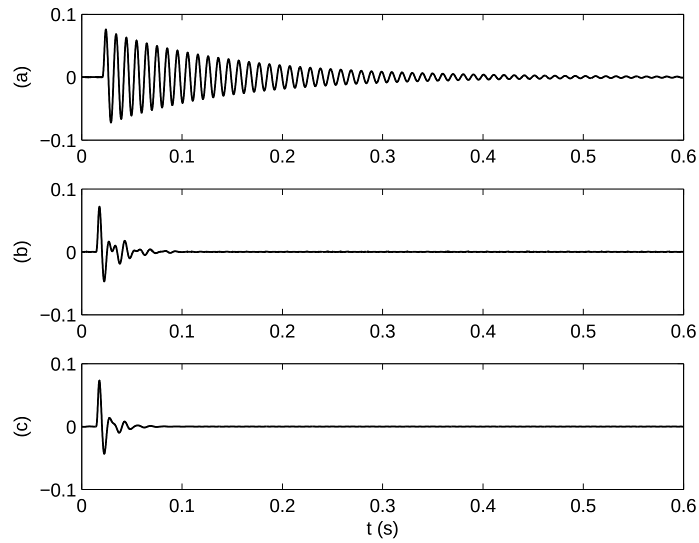

Figure 4.23: Velocity response $\nu(s)$ (in m/s) of the capacitor-resistor controlled system to a $1\ Amp\ 300\ Hz$ low-pass filtered step disturbance current $I_d(s)$; experimental open-loop (a), experimental closed-loop (b), and simulated closed-loop(c).

Ideal Negative Inductor-Resistor Controller

There are two possible ways to implement the proposed negative inductor-resistor controller: (1) negative-impedance-converter (NIC) [59] or (2) voltage-controlled-current-source (VCCS). For the purpose of the proposed work, only the use of the voltage-controlled-current-source is considered, as illustrated in Figure 2.3 (b).

Experiments were carried out on the experimental apparatus, as described above, using the proposed negative inductor-resistor admittance controller $Y(s)$. Assuming $Y(s) = -\frac{1}{\varepsilon(L_e s+R_e)}$, where $\varepsilon = 0.94$ as synthesized by VCCS, coil 2 is employed to damp translational vibrations resulting from an applied disturbance current I_d to coil 1. To remove discrepancies in C_3 and C_4 at high frequencies, the experimental admittance is low-pass filtered at $\approx 1\ kHz$.

The simulated frequency response for the negative inductor-resistor controller is shown in Figure 4.24. Examining the open-loop and closed-loop pole locations, as shown in Figure 4.25, note that the controller is clearly acting to increase the internal damping of the mechanical system.

The measured open-loop simulated damped $\tilde{G}_{i\nu}(s)$ and measured damped frequency responses are shown in Figure 4.26. A significant reduction of 28.2 dB in the magnitude of the electromechanical system is observed. The effect of such reduction greatly decreases the settling time of the system. Figure 4.27 shows the undamped response of the system to a 300 Hz low-pass filtered step in actuator disturbance current. In comparison, the damped response shown in Figure 4.27 settles in approximately less than one twentieth of the time taken by the undamped system.

Impedance Synthesis

For the impedance synthesis, the electromechanical system will be treated as a plant, therefore, sensing and actuation gains will be factored into the system as shown in Figure 4.28. Figure 4.28 shows the sensing and actuator gains where voltages V_1 through V_4 represent the signals applied to, or sensed from, a synthetic impedance, as described in Section 4.5.2. Gains for a_1, a_2, a_3 and a_4 can be found in Table 4.2. The desired electrical shut impedance seen by the transducer is related by the controller $K(s)$, and the gains a_3 and a_4. That is

$$Z_c(s) = \frac{V_z(s)}{I_z(s)} = a_3 K(s) a_4. \tag{4.46}$$

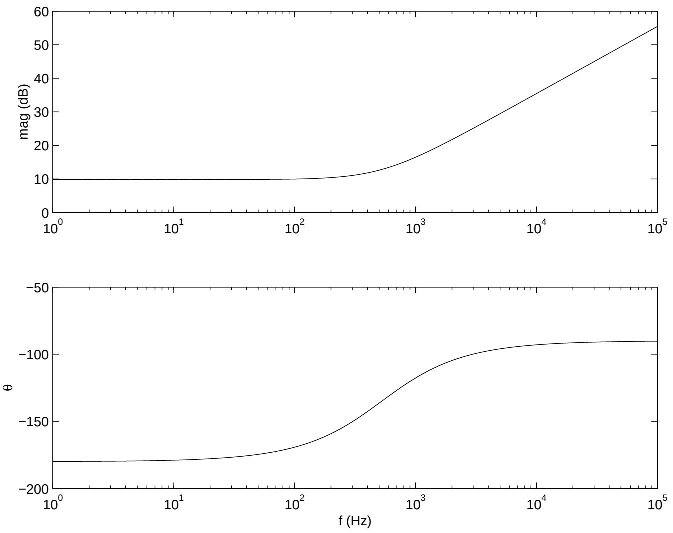

Figure 4.24: Magnitude and phase response for negative inductor-resistor controller.

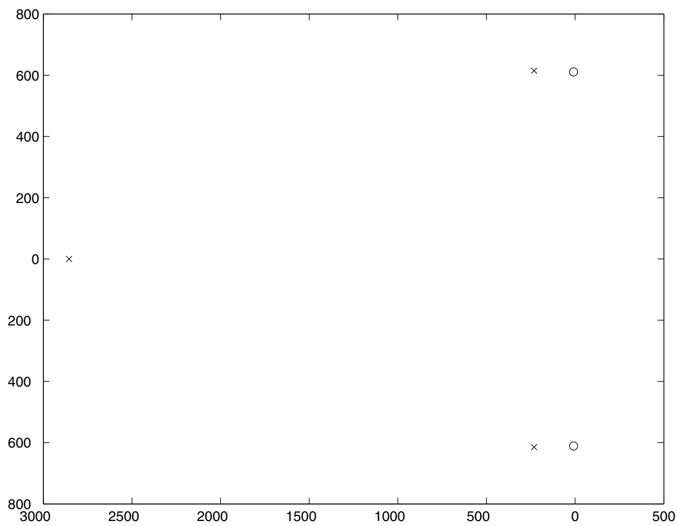

Figure 4.25: Open-loop (◯) and closed-loop (×) pole locations.

Gain	**Unit**
a_1	$1\ A/V$
a_2	$40\ V/ms^{-1}$
a_3	$-4\ V/V$
a_4	$10\ V/A$

Table 4.2: Shunt voltage controlled electromagnetic system external gains.

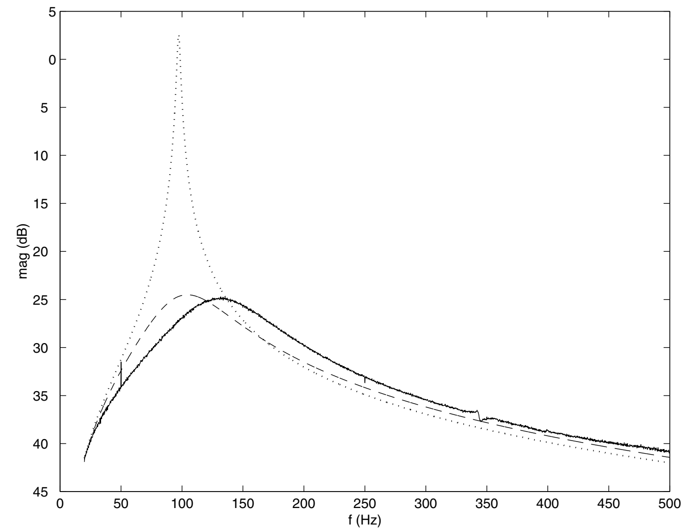

Figure 4.26: Open-loop $(\cdots)$ theoretically predicted damped $(--)$ and measured damped (—) frequency responses from an applied current to the resulting plunger velocity.

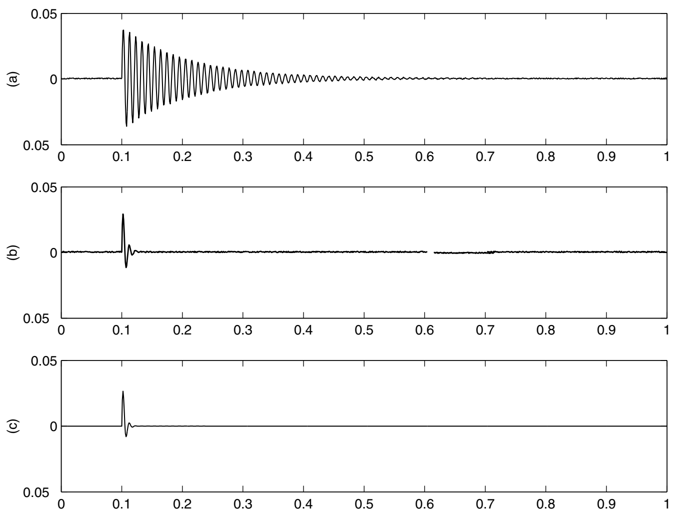

Figure 4.27: Velocity response $\nu(s)$ (in m/s) of the negative inductor-resistor controlled system to a step disturbance current $I_d(s)$; experimental open-loop (a) , experimental closed-loop (b), and simulated closed-loop (c).

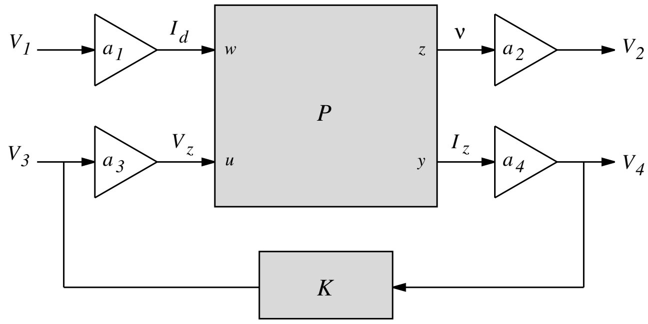

Figure 4.28: Shunt voltage controlled electromagnetic system with external gains and controller.

To evaluate the theoretical model, as discussed in Section 4.24, the experimental multivariable frequency response was measured consecutively from each input to output pair. The residual input was set to zero while measuring the component SISO frequency responses. The theoretical and experimental, magnitude and phase responses for the plant P are shown in Figures 4.29 and 4.30. A good correlation between the theoretical and experimental responses can be observed and, therefore positively validating the proposed theoretical model.

***LQR* Impedance Synthesis** Outlined in Section 4.4.3, a LQR can be designed to command V_z with the objective of regulating the performance signal of the weighted sum of ν and V_z. The measured shunt current I_z is used to estimate the states of the system through an observer [68]. By designing a LQR gain matrix and combining it with an observer, a desired active shunt impedance can be found and then applied to the electromagnetic transducer to dampen structural vibration.

Based on the previously validated theoretical model, a LQR gain matrix was designed to minimise the following objective

$$J = \int_{-\infty}^{\infty} \left\{ a_2 \nu^2(t) + \frac{7}{a_3} V_z^2(t) \right\} \, dt, \tag{4.47}$$

where 7 is the relative control weight. An observer was designed by using standard pole placement whereby the desired closed-loop poles were chosen to be 2 times that of the real component for the open loop poles. As in standard LQR controller designs [68], the control signal weighting and observer pole locations were determined experimentally to provide a

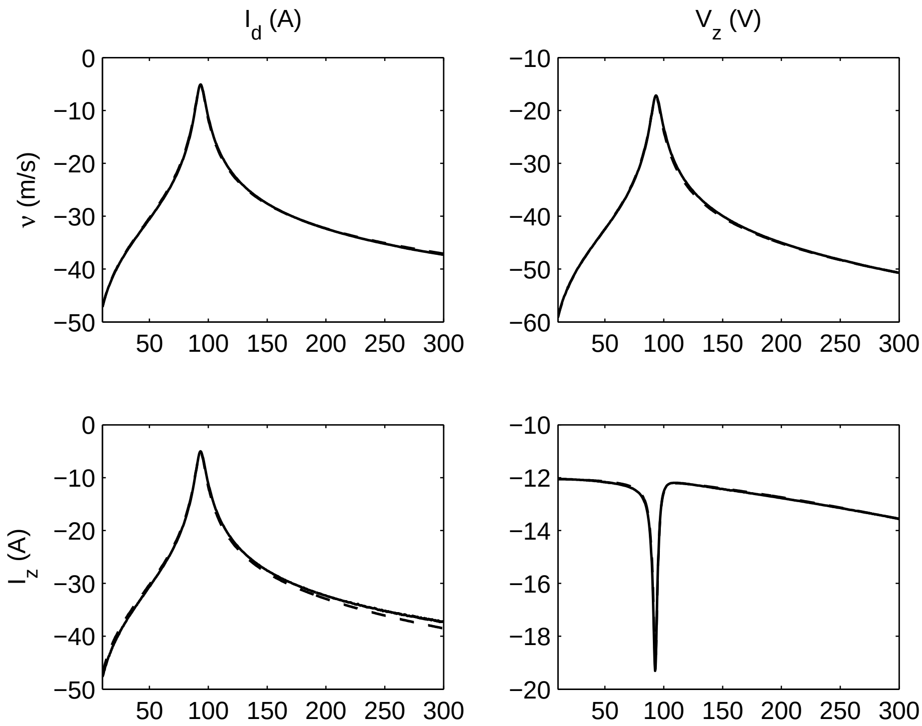

Figure 4.29: Shunt voltage controlled electromagnetic system. Theoretical (—) and experimental (− −) magnitude frequency response (in dB).

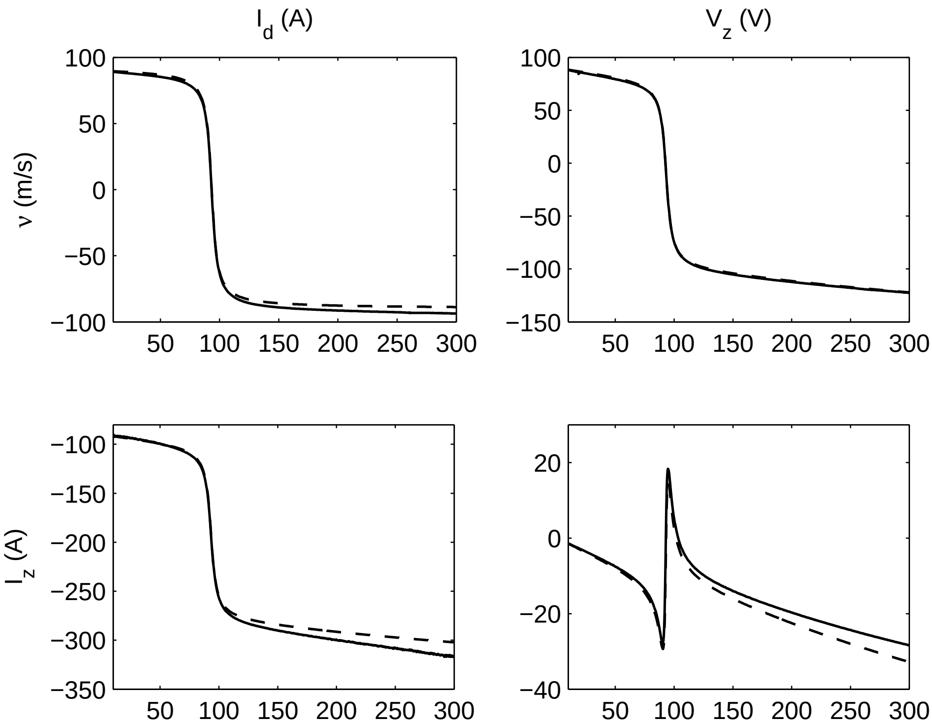

Figure 4.30: Shunt voltage controlled electromagnetic system. Theoretical (—) and experimental (− −) phase frequency response (in degrees).

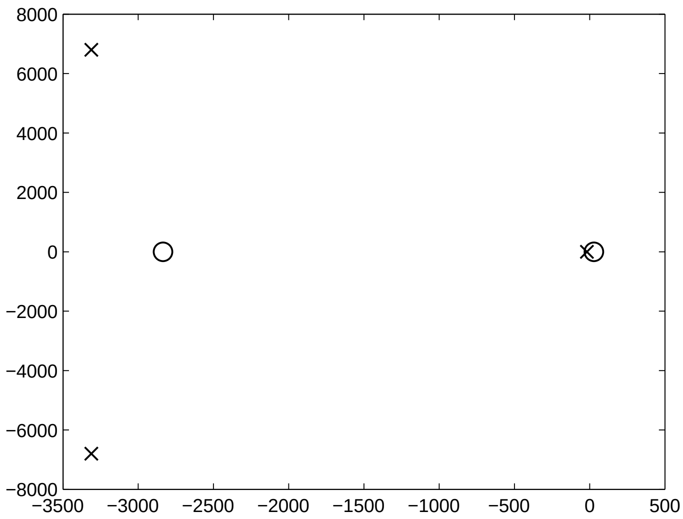

Figure 4.31: Poles ($\times$) and zeros ($\bigcirc$) of the *LQR* impedance.

reasonable a trade-off between control performance, robustness and the control signal amplitude.

The complex impedance frequency responses are shown in Figure 4.32. Frequency and time domains were used to assess the damping performance of the LQR controller. By applying a disturbance current I_d, the theoretical and experimental open-loop and closed-loop frequency responses are shown in Figure 4.34. From Figure 4.34 note that the designed controller damped the resonate peak by 19.4 dB. By applying a disturbance current I_d step change, which was filtered by a 300 Hz low-pass filter, the open-loop and closed-loop time domain velocity response was obtained, as shown in Figure 4.35.

The theoretical closed-loop time response was determined by measuring the filtered step response and applying it to the closed-loop theoretical model.

$\mathcal{H}_2$ Impedance Synthesis In the analogy to Section 4.5.3, an active shunt impedance was designed to minimise the $\mathcal{H}_2$ norm of the transfer function between a disturbance current I_d and a performance signal $z = \nu + k_u V_z$. That is,

$$J = \left\| \frac{a_2 \nu(s) + \frac{k_u}{a_3} V_z(s)}{\frac{I_d(s)}{a_1}} \right\|_2 . \tag{4.48}$$

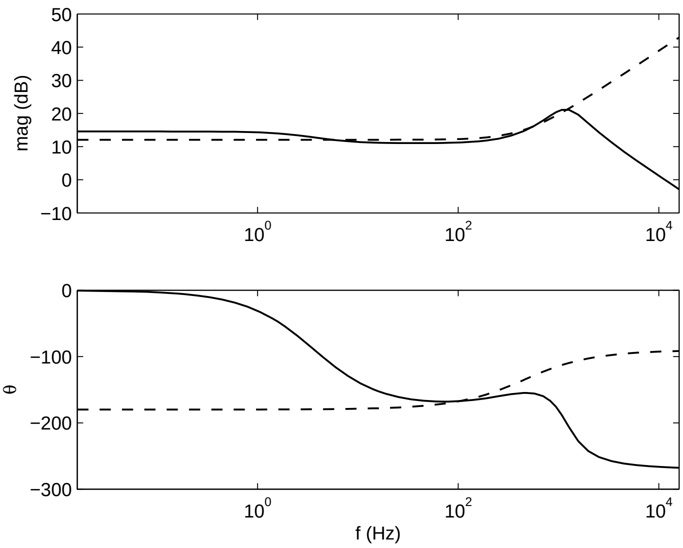

Figure 4.32: *LQR* impedance (—) and ideal negative inductor-resistor controller (- -).

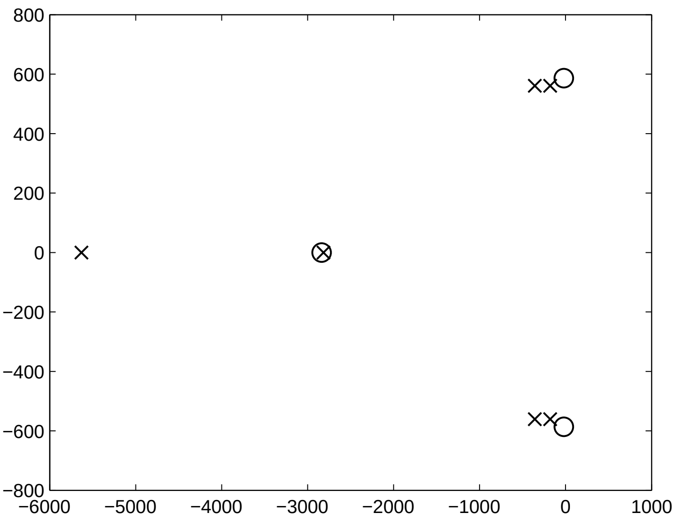

Figure 4.33: Open-loop (◯) and closed-loop (×) pole locations of the *LQR* impedance.

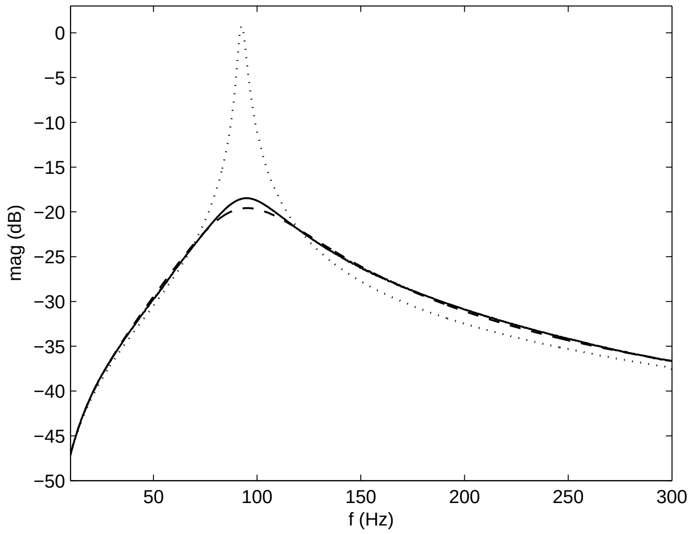

Figure 4.34: Open-loop ($\cdots$), theoretically predicted damped (—), and measured damped ($--$) frequency responses from an applied current $I_d(s)$ to the resulting plunger velocity $\nu(s)$.

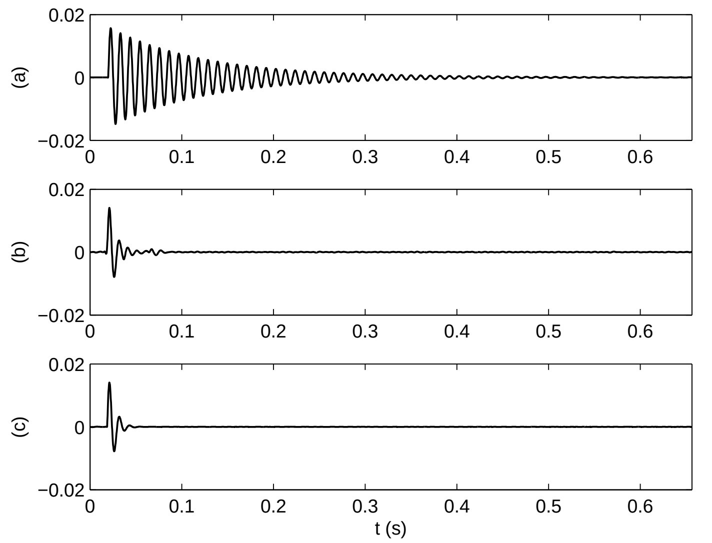

Figure 4.35: Step disturbance current $I_d(s)$ to velocity $\nu(s)$ of the *LQR* impedance controlled system; experimental open-loop (a), closed-loop (b) and simulated closed-loop (c).

The $\mathcal{H}_2$ problem is well defined and feasible for the system under consideration. All the $\mathcal{H}_2$ control conditions are satisfied, that is, the plant is minimal, proper, controllable, observable, and finite. Using the existing tools, the algebraic Riccati solution implemented by the μ-Synthesis Toolbox for Matlab to find a solution, some additional conditions must be meet. In particularly, the full rank condition on the plant matrices D_{21} and D_{12} i.e. the feed-through term from w to y and u to z is non-zero. The only condition not met is D_{21}, as the performance signal z already contains a weighting k_u on the control signal V_z. To overcome this problem an artificial feed-through term was added to D_{21}. Now, there are two design parameters, k_u and D_{21} and were chosen to be 0.1 and 1 respectively. Observations found that by decreasing either of the parameters k_u and D_{21}, the controller bandwidth and closed-loop damping increases.

Under the same test conditions, as discussed in Section 4.5.3, the damping performance for the $\mathcal{H}_2$ controller was 19.25 dB which is comparable to that of the LQR controller.

4.6 Discussions

The aim of this chapter was to develop a new shunt damping technique, electromagnetic shunt damping. This technique was found to have a similar feedback structure to that of piezoelectric shunt damping, as presented earlier in Chapter 2. In addition, this vibration control strategy also eliminated the need for any external sensor.

Like the piezoelectric analogy, as shown in Chapter 2, a resonant shunt circuit capacitor-resistor controller can be used to compensate for the reactive source impedance over a small frequency band. The circuit in Figure 4.12 was shown to significantly attenuate a lightly damped mechanical system. The circuit requires a negative resistance to cancel the natural resistance of the coil. Capacitor-resistor controller or resonant shunt circuits provide a fixed performance objective. They introduce additional dynamics to effectively damp a highly resonant structural mode. Although this is desirable in piezoelectric applications, the same objective is unlikely to arise in electromagnetic applications. For example, most mechanical system are likely to contain a high degree of natural damping. Resonant shunt circuits provide no additional performance in such cases. Overall, the capacitor-resistor controller is a very simple, yet a very effective controller for lightly damped mechanical systems.

The ideal negative inductor-resistor controller, as might be expected, a 'miracle' controller has limited practical uses. By implementing (4.34) or (4.33), the effective controller is simply a proportional feedback loop of infinite gain, as shown in Figure 4.13. Besides the magnitude of control energy required, the stability and performance is extremely sensitive to small changes in the transducer dynamics. Changes in transducer dynamics can be attributed to environmental conditions, such as the temperature of the windings, and magnetic losses. Including additional transducer dynamics into the model may improve system stability and is open to further investigation. In practice, by tuning the magnitudes of the negative inductor-resistor controller, the control effort can be toned down. Due to the *ad hoc* nature of this approach, it is difficult to accurately manipulate the trade-off between control effort and damping performance. For example, using a negative inductor-resistor controller, it is impossible to distribute, concentrate or mitigate the control energy associated with individual structural modes. It is also impossible to minimise a specific performance function not proportionally related to the plunger velocity. In cases where the goal is not simply to reduce the magnitude of plunger velocity, such as in acoustic, isolation and suspension systems, the negative inductor controller is of little use. In spite of the associated problems, this technique warrants mention due to its inherent simplicity and utility in gaining an intuitive understanding of the abstract controllers generated from an automated synthesis process such as LQR or $\mathcal{H}_2$.

For the impedance synthesis technique, the connection of an electrical impedance to the terminals of an electromagnetic coil is equivalent to implementing a standard feedback controller around the mechanical system. By revealing the underlying feedback structure and casting it as a typical control problem, an impedance can be found that minimises some arbitrary performance objectives. The presented techniques are successfully applied to the design and implementation of an LQR and $\mathcal{H}_2$ based active impedance controller. Without the need for any external sensors, the resonant peak of an experimental single-degree-of freedom system was substantially reduced in magnitude by up to 19.4 dB.

Three electromagnetic shunt controllers were successfully applied to an experimental single mass-spring-damper system. The proposed theoretical controllers were found to agree with the experimental data and verified the proposed technique. It was found that the proposed controllers produced similar experimental outcomes, i.e. peak attenuation. However, the capacitor-resistor controller was considered to be the more favourable due to its simplicity and durability.

Current and future work involves both the exploration of additional applications and development of the control theory associated with the synthesis step, as described in Section 4.4.3 and to develop similar control strategies, as proposed in Section 2.2 i.e. to apply multiple mode shunt or switched shunt controllers to more complex electromechanical systems.

Overall, this chapter confirms, through theoretical and experimental verification, the potential of the electromagnetic shunt damping technique.

Chapter 5

Electromagnetic Shunt Isolation

In Chapter 4, electromagnetic shunt damping was presented. In this chapter, electromagnetic shunting control will be applied to a simple isolation system. This technique will be referred to as electromagnetic shunt isolation. The effect of electromagnetic shunt controllers is studied theoretically and then validated experimentally on a simple electromagnetic isolation apparatus.

5.1 Background

The objectives of *damping* and *isolation* of vibration are sometimes confused. In a few words, damping is regarded as the reduction of amplitude of the mechanical system within a limited bandwidth near the resonance frequency. Isolation, however, is defined as supporting a load within a particular bandwidth ω_c, and attenuation of high frequency components above ω_c as shown in Figure 5.1.

Vibration isolation problems can be classed in two different groups. The groups are: (1) an isolated mass may be subjected to a disturbance (normally a force) which propagates into the base structure, and (2) a disturbance generated by the base structure which propagating into the isolated mass. The second case is more commonly found in practice, therefore, this chapter will solely focus on this scenario.

A key example of an isolation system is active suspension control for automobiles [20, 42, 47, 61, 65, 99, 100]. Normally an accelerometer, or force transducer, is used as a sensor while an electromagnetic transducer is used as an actuator. With electromagnetic shunt control,

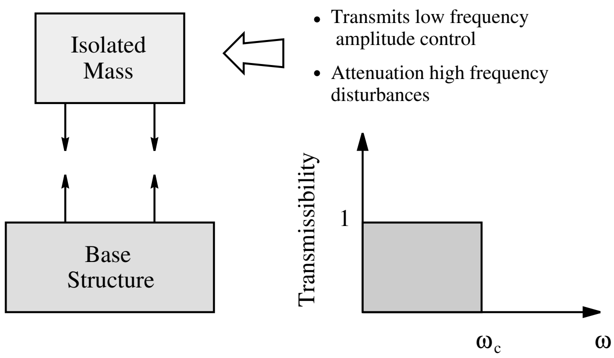

Figure 5.1: Principle of an isolation system and isolation objectives.

both the sensor and actuator are combined together, as explained in Section 1.1, eliminating the need for the sensor. From a theoretical point of view , the proposed control scheme is considered to be perfectly *collocated* [78],which improves the stability and robustness of the closed-loop system. For isolation applications, shunt control could minimise weight, and thus be cost-effective.

5.2 Modelling

Consider the simple isolation system shown in Figure 5.2 (a). The isolation system consists of a linear spring in parallel with a passive damper, where m is the mass, k and d are the stiffness and damping coefficients respectively. The equation of motion is defined as

$$m\ddot{x}(t) + d\dot{x}(t) + kx(t) = d\dot{y}(t) + ky(t), \tag{5.1}$$

where $(\ddot{\cdot})$ and $(\dot{\cdot})$ denote the acceleration and velocity of $x(t)$ and $y(t)$. The resonance frequency of the mechanical system is $\omega_n = \sqrt{\frac{k}{m}}$ and the amount of damping is defined by the damping ratio ζ, where $\zeta = \frac{d}{\sqrt{4mk}}$. The transfer function between the disturbance displacement y and the mass displacement x is given by

$$T(s) \triangleq G_{yx}(s) = \frac{ds + k}{ms^2 + ds + k} = \frac{\frac{2\zeta s}{\omega_n} + 1}{\frac{s^2}{\omega_n^2} + \frac{2\zeta s}{\omega_n} + 1}. \tag{5.2}$$

Equation (5.2) is commonly referred to as the *transmissibility ratio* $T(s)$. $T(s)$ can be plotted against normalised frequency $\frac{\omega}{\omega_n}$ for various values of damping ratio ζ, as shown in Figure 5.3. Many interesting observations can be learned from Figure 5.3. They are:

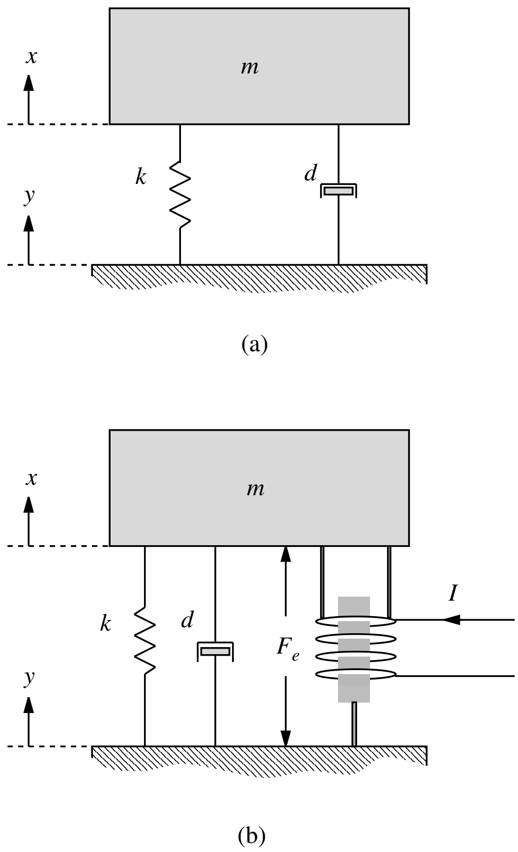

Figure 5.2: Simple mass-spring-damper isolation systems: unforced (a) and forced systems (b).

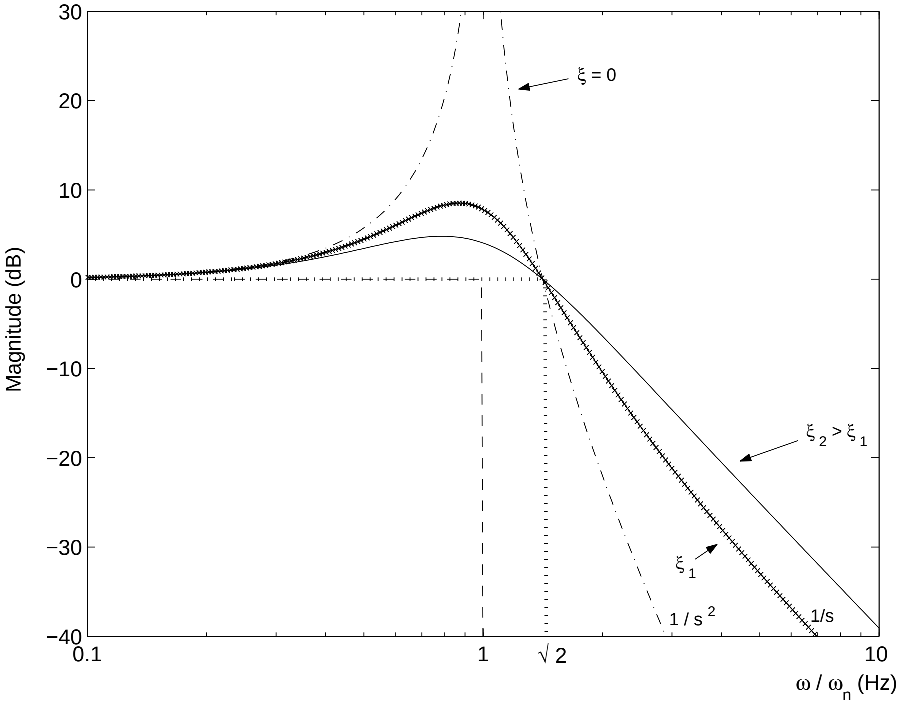

Figure 5.3: Normalised transmissibility ratio $T(s)$ of a passive damper for various values of damping ratio ζ.

1. When the disturbing frequency coincides with the natural frequency of the system ω_n, the system vibrates at the frequency with larger amplitudes.

2. The frequency where the curve crosses over the 0 dB, the disturbed frequency is equal to $\omega_c = \sqrt{2}\omega_n$. This is commonly referred to as the critical frequency ω_c and is the point where the influence of high frequency attenuation begins.

3. At low frequencies, below the resonance of the system ω_n, the displacement of the mass x follows the displacement of the base y as if the isolator was infinitely rigid. However, at higher frequencies greater than the resonance of the system ω_n, the relative displacement of the mass gradually diminishes.

4. By increasing the damping ratio ζ of the system, the resonance that appears at the natural frequency decreases but, unfortunately, the gradient of the high frequency roll-off also decreases.

5. To maintain reasonable roll-off at high frequencies, while decreasing the peak amplitude at the resonance, a control algorithm is needed.

Observe in Figure 5.3 that when $\zeta = 0$, the high frequency roll-off is $1/s^2$ (-40 dB/decade) while a very large amplitude is seen near the natural frequency ω_n. On the other hand, when the damping ratio ζ is increased, the amplitude at the resonance is reduced and the roll-off to $1/s$ (-20 dB/decade) is also reduced. As a result, the design of a passive mechanical damper involves the compromise between the resonance and the high frequency attenuation.

5.2.1 Shunted Composite Electromechanical System

Consider the simple isolation system, as shown in Figure 5.2 (a). By taking the Laplace of Equation (5.1), the following transfer function relating the applied base velocity $\varpi(s)$ and isolated mass velocity $\nu(s)$ is

$$T(s) \triangleq G_{\varpi\nu}(s) = \frac{\nu(s)}{\varpi(s)} = \frac{ds + k}{ms^2 + ds + k}, \tag{5.3}$$

where $\nu(s) = sx(s)$ and $\varpi(s) = sy(s)$. It should be noted that $G_{\varpi\nu}(s)$ is also referred to as the transmissibility ratio $T(s)$.

For the forced isolation problem, as shown in Figure 5.2 (b), a control force $F_e(t)$ is placed between the mass and the base. For this system, the equation of motion is

$$m\ddot{x}(t) + d\dot{x}(t) + kx(t) + F_e(t) = d\dot{y}(t) + ky(t). \tag{5.4}$$

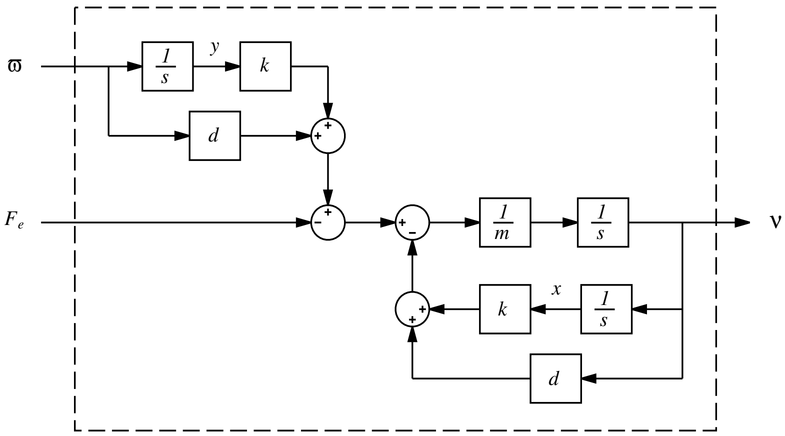

Figure 5.4: Isolation system structure.

By taking the Laplace of Equation (5.4), the following relationship can be found

$$\nu(s) = \frac{ds + k}{ms^2 + ds + k}\varpi(s) - \frac{s}{ms^2 + ds + k}F_e(s), \tag{5.5}$$

where $\varpi(s)$ and $F_e(s)$ are the inputs to the system, as shown in Figure 5.4.

Now, consider a shunted electromagnetic transducer, as shown in Figure 5.5. To determine the opposing force $F_e(s)$, the simplified electrical model of the shunted electromagnetic transducer needs to be considered. Ohm's law states that

$$V_z(s) = I_z(s)Z(s), \tag{5.6}$$

where $V_z(s)$ is the voltage across the terminals of the shunt impedance $Z(s)$ and $I_z(s)$ is the corresponding current. According to Kirchhoff's voltage law, the following relationship between $V_e(s)$ and $V_z(s)$, is

$$V_z(s) = V_e(s) - (L_e s + R_e)V_z(s), \tag{5.7}$$

which implies

$$V_z(s) = \frac{Z(s)}{Z(s) + L_e s + R_e}V_e(s). \tag{5.8}$$

For an ideal electromagnetic transducer, the voltage V_e is proportional to the relative velocity, that is

$$V_e(s) = c_{\nu v}\left(\nu(s) - \varpi(s)\right), \tag{5.9}$$

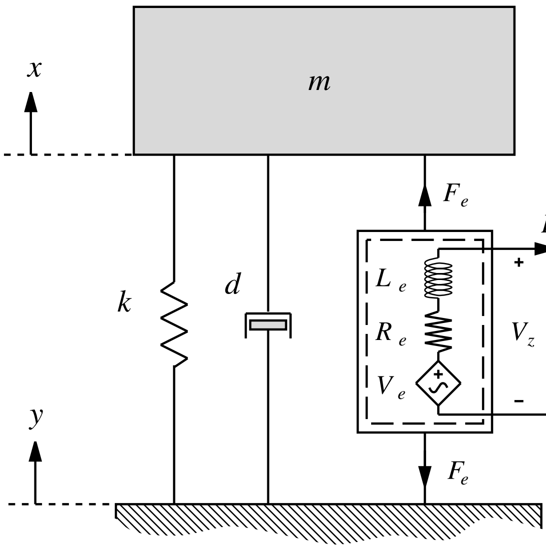

Figure 5.5: Electromagnetic closed-loop isolation system.

where $c_{\nu v}$ is the electromechanical coefficient relating relative velocity to voltage. By substituting Equations (5.9) into (5.8), the following correlation can be found, that is

$$V_z(s) = \frac{Z(s)}{Z(s) + L_e s + R_e} c_{\nu v} \left(\nu(s) - \varpi(s) \right). \tag{5.10}$$

Alternatively, the current-flowing through the shunt $I_z(s)$ is

$$I_z(s) = \frac{V_z(s)}{Z(s)} = \frac{c_{\nu v}}{Z(s) + L_e s + R_e} \left(\nu(s) - \varpi(s) \right) \tag{5.11}$$

and the opposing shunt force $F_e(s) = c_{if} I_z(s)$, assuming a linear electromagnetic transducer $F_e(s)$ is

$$\begin{aligned} F_e(s) &= \frac{c_{\nu v} c_{if}}{L_e s + R_e + Z(s)} \left(\nu(s) - \varpi(s) \right) \\ &= K(s) \left(\nu(s) - \varpi(s) \right). \end{aligned} \tag{5.12}$$

Substituting (5.12) into (5.5), the electromagnetic shunt isolation system $\varpi(s)$ to $\nu(s)$ is

$$\tilde{T}(s) \triangleq \tilde{G}_{\varpi \nu}(s) = \frac{(d + \frac{c_{\nu v} c_{if}}{L_e s + R_e + Z(s)}) s + k}{m s^2 + (d + \frac{c_{\nu v} c_{if}}{L_e s + R_e + Z(s)}) s + k}, \tag{5.13}$$

as shown in Figure 5.6. The closed-loop transmissibility ratio transfer function $\tilde{T}(s)$ is in the form of a regulator feedback control problem where the relative velocity $\nu(s) - \varpi(s)$ is to be regulated to zero for low frequencies. Also, the effective controller $K(s)$ is parameterised by the impedance $Z(s)$, as shown in Figure 5.6.

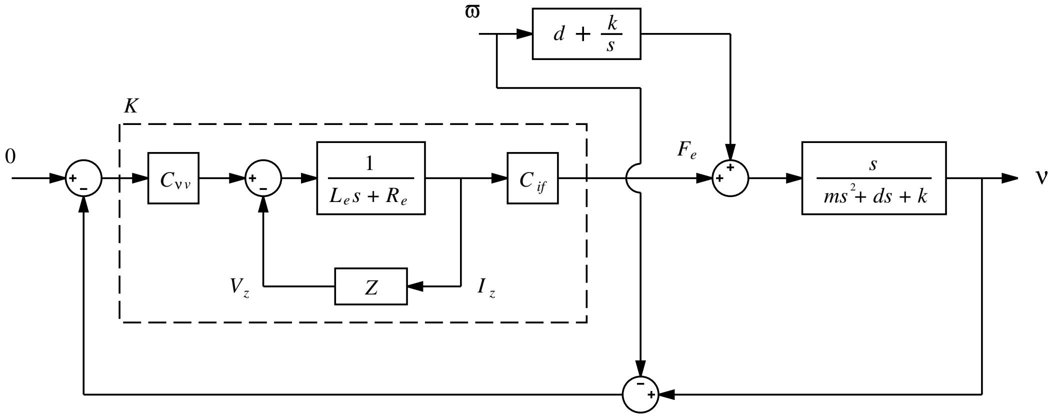

Figure 5.6: Relative velocity regulator feedback problem with filtered input disturbance. Note the effective control K is shown.

5.2.2 State-space Shunted Composite Electromechanical System

The general input-output model of the isolation system is shown in Figure 5.7, where the disturbance velocity is $\varpi(t)$ and control signal is $F_e(t)$. The outputs of the plant are mass velocity $\nu(t)$ velocity of the base and mass $\nu(t) - \varpi(t)$. That is,

$$\begin{bmatrix} \dot{\nu}(t) \\ \nu(t) - \varpi(t) \end{bmatrix} = \begin{bmatrix} -\frac{d}{m} & -\frac{k}{m} \\ 1 & 0 \end{bmatrix} \begin{bmatrix} \nu(t) \\ x(t) - y(t) \end{bmatrix} + \begin{bmatrix} \frac{d}{m} & \frac{1}{m} \\ -1 & 0 \end{bmatrix} \begin{bmatrix} \varpi(t) \\ F_e(t) \end{bmatrix}$$
$$\begin{bmatrix} \nu(t) \\ \nu(t) - \varpi(t) \end{bmatrix} = \begin{bmatrix} 1 & 0 \\ 1 & 0 \end{bmatrix} \begin{bmatrix} \nu(t) \\ x(t) - y(t) \end{bmatrix} + \begin{bmatrix} 0 & 0 \\ -1 & 0 \end{bmatrix} \begin{bmatrix} \varpi(t) \\ F_e(t) \end{bmatrix},$$

where the states of the plant are $\begin{bmatrix} \nu(t) & x(t) - y(t) \end{bmatrix}$.

From the Section 4.3.2, the electromagnetic transducer system E was seen as having the following two-input-two-output system:

$$\dot{x}_e = \left[\frac{-R_e}{L_e}\right] x_e + \begin{bmatrix} c_{\nu v} & -1 \end{bmatrix} \begin{bmatrix} \nu(t) - \varpi(t) \\ V_z(t) \end{bmatrix}$$
$$\begin{bmatrix} F_e(t) \\ I_z(t) \end{bmatrix} = \begin{bmatrix} -\frac{c_{if}}{L_e} \\ \frac{1}{L_e} \end{bmatrix} x_e, \tag{5.14}$$

where the above Equation (5.14) can be represented in diagram form, as shown in Figure (5.8).

For the electromagnetic isolation system, systems P and E can be combined to obtain the

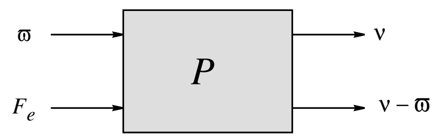

Figure 5.7: Isolation system plant model.

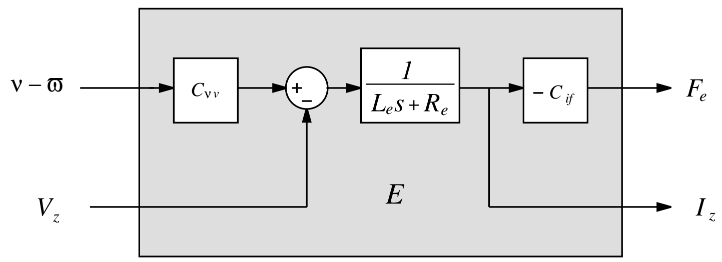

Figure 5.8: Electromagnetic shunt transducer model. Note the −'ve sign for the regulator feedback structure has been included into the c_{if} for simplicity, i.e. $-c_{if}$.

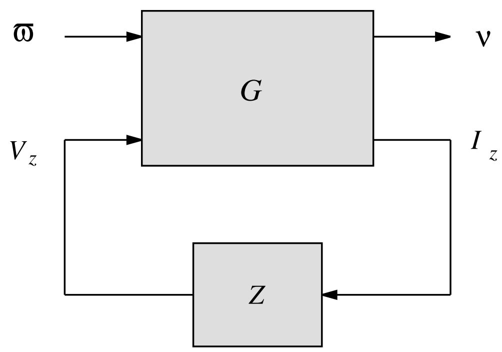

Figure 5.9: Shunt impedance controlled electromechanical isolation system.

following composite system G, where the dynamics of the transducer are introduced to the plant, as shown in Figure 5.9. The state-space representation of G is

$$\begin{bmatrix} \dot{\nu}(t) \\ \nu(t) - \varpi(t) \\ \dot{x}_e(t) \end{bmatrix} = \begin{bmatrix} -\frac{d}{m} & -\frac{k}{m} & -\frac{1}{m}\frac{c_{if}}{L_e} \\ 1 & 0 & 0 \\ c_{\nu v} & 0 & -\frac{R_e}{L_e} \end{bmatrix} \begin{bmatrix} \nu(t) \\ x(t) - y(t) \\ x_e(t) \end{bmatrix} + \begin{bmatrix} \frac{d}{m} & 0 \\ -1 & 0 \\ -c_{\nu v} & -1 \end{bmatrix} \begin{bmatrix} \varpi(t) \\ V_z(t) \end{bmatrix}$$

$$\begin{bmatrix} \nu(t) \\ I_z(t) \end{bmatrix} = \begin{bmatrix} 1 & 0 & 0 \\ 0 & 0 & \frac{1}{L_e} \end{bmatrix} \begin{bmatrix} \nu(t) \\ x(t) - y(t) \\ x_e(t) \end{bmatrix}. \tag{5.15}$$

Alternatively, the system G can be written as

$$\begin{aligned} \dot{\mathbf{x}}_g(t) &= \mathbf{A}\mathbf{x}_g(t) + \mathbf{B_1}\varpi(t) + \mathbf{B_2}V_z(t) \\ \nu(t) &= \mathbf{C}_1\mathbf{x}_g(t) \\ I_z(t) &= \mathbf{C}_2\mathbf{x}_g(t), \end{aligned} \tag{5.16}$$

where

$$\mathbf{A} = \begin{bmatrix} -\frac{d}{m} & -\frac{k}{m} & -\frac{1}{m}\frac{c_{if}}{L_e} \\ 1 & 0 & 0 \\ c_{\nu v} & 0 & -\frac{R_e}{L_e} \end{bmatrix} \qquad \mathbf{x}_g(t) = \begin{bmatrix} \nu(t) \\ x(t) - y(t) \\ x_e(t) \end{bmatrix}$$

$$\mathbf{B}_1 = \begin{bmatrix} \frac{d}{m} \\ -1 \\ -c_{\nu v} \end{bmatrix} \qquad \mathbf{B}_2 = \begin{bmatrix} 0 \\ 0 \\ -1 \end{bmatrix}$$

$$\mathbf{C}_1 = \begin{bmatrix} 1 & 0 & 0 \end{bmatrix} \qquad \mathbf{C}_2 = \begin{bmatrix} 0 & 0 & \frac{1}{L_e} \end{bmatrix}.$$

5.3 Proposed Shunt Controllers

The following subsections introduce a number of techniques for the design of impedance or admittance, controllers to provide damping and high frequency attenuation for a simple mass-spring-damper isolation system. The first approach considers a passive capacitor-resistor impedance as developed in Section 4.4.1. The second technique develops a controller from some of the fundamental elements of the electromechanical system. Finally, an impedance is constructed by parameterising the system as a standard pole placement feedback control problem. All controllers developed are validated on an isolation apparatus.

5.3.1 Capacitor-Resistor Controller

In the previous section, Section 4.4.1, one possible shunting technique that could be considered is shunting the terminals of an electromagnetic transducer with a series capacitor-resistor $(C - R)$, as shown in Figure 4.12. The shunt impedance is

$$Z(s) = \frac{1}{Cs} + R, \tag{5.17}$$

where C is tuned to the resonance frequency of the isolation system, i.e.

$$C = \frac{1}{\omega_n^2 L_e} = \frac{1}{\left(\frac{k}{m}\right) L_e}$$

and R is tuned for the required damping.

The electromagnetic shunt force is equivalent to

$$\begin{aligned} F_e(s) &= \frac{c_{\nu v} c_{if}}{L_e s + R_e + Z(s)} \left(\nu(s) - \varpi(s)\right) \\ &= \frac{c_{\nu v} c_{if} k L_e s}{k L_e^2 s^2 + k L_e \left(R_e + R\right) s + m} \left(\nu(s) - \varpi(s)\right) \end{aligned} \tag{5.18}$$

and the equivalent closed-loop transmissibility ratio is

$$\begin{aligned} \tilde{T}(s) &\triangleq \frac{(d + \frac{c_{\nu v} c_{if}}{L_e s + R_e + Z(s)})s + k}{ms^2 + (d + \frac{c_{\nu v} c_{if}}{L_e s + R_e + Z(s)})s + k} \\ &= \frac{(d + \frac{c_{\nu v} c_{if} k L_e s}{k L_e^2 s^2 + k L_e (R_e + R) s + m})s + k}{ms^2 + (d + \frac{c_{\nu v} c_{if} k L_e s}{k L_e^2 s^2 + k L_e (R_e + R) s + m})s + k}. \end{aligned} \tag{5.19}$$

Note the effective controller $K(s)$ is equivalent to

$$K(s) = \frac{c_{\nu v} c_{if} k L_e s}{k L_e^2 s^2 + k L_e \left(R_e + R\right) s + m}.$$

In order to determine an optimal value for the shunt resistance R, an optimisation approach could be considered. By minimising the $\mathcal{H}_2$ norm of the closed-loop system $\tilde{T}(s)$, or $\tilde{G}_{\varpi\nu}(s)$, the appropriate resistance value R can be determined. This technique is very similar to the technique proposed in Section 4.4.1. This required a solution to the following optimisation problem to be found

$$R_t^* = \begin{matrix} \arg\min \\ R_t > 0 \end{matrix} \left\| \tilde{T}(s) \right\|_2 \tag{5.20}$$

$$= \begin{matrix} \arg\min \\ R_t > 0 \end{matrix} \left\| \frac{(d + \frac{c_{\nu v} c_{if} k L_e s}{k L_e^2 s^2 + k L_e R_t s + m})s + k}{ms^2 + (d + \frac{c_{\nu v} c_{if} k L_e s}{k L_e^2 s^2 + k L_e R_t s + m})s + k} \right\|_2, \tag{5.21}$$

where the total resistance R_t is equivalent to $R_t = R_e + R$.

5.3.2 Ideal Controller

The shunt impedance $Z(s)$ is designed such that the shunted system $\tilde{T}(s)$ is equivalent to $\frac{ds+k}{ms^2+(d+\beta)s+k}$, where β effectively adds damping to the system. That is

$$\tilde{T}(s) \triangleq \frac{(d+\frac{c_{\nu v}c_{if}}{L_e s+R_e+Z(s)})s+k}{ms^2+(d+\frac{c_{\nu v}c_{if}}{L_e s+R_e+Z(s)})s+k} \equiv \frac{ds+k}{ms^2+(d+\beta)s+k}. \tag{5.22}$$

Then, the ideal control impedance $Z(s)$ is

$$Z(s) = -\frac{c_{\nu v}c_{if}ms^2}{\beta(ds+k)} - \frac{c_{\nu v}c_{if}s}{(ds+k)} - L_e s - R_e. \tag{5.23}$$

Similarly, the strictly proper admittance $Y(s)$ is

$$Y(s) = -\frac{\beta\,(ds+k)}{(L_e\beta d+c_{\nu v}c_{if}m)\,s^2+(R_e\beta d+L_e\beta k+c_{\nu v}c_{if}\beta)\,s+R_e\beta k}. \tag{5.24}$$

By substituting Equation (5.23) into (5.12), the force generated is determined by the electromagnetic shunt as

$$F_e(s) = -\frac{\beta(ds+k)}{s(\beta+ms)}\,(\nu(s)-\varpi(s)) \tag{5.25}$$

and, therefore, the effective controller is equivalent to

$$K(s) = -\frac{\beta(ds+k)}{s(\beta+ms)}. \tag{5.26}$$

5.3.3 Impedance Synthesis

The purpose of the controller will be to move specific poles of the system further into the left-half plane without affecting the zeros of the system. To achieve this, a controller needs to be designed that effectively adds mechanical damping to the electromechanical system. This is achieved by allowing the damping term d of the open-loop matrix $\mathbf{A}$ to become $\tilde{d} = d+\alpha$, where α is some positive gain. That is, the effective closed-loop matrix $\tilde{\mathbf{A}}$ becomes

$$\tilde{\mathbf{A}} = \begin{bmatrix} \frac{-\tilde{d}}{m} & \frac{-k}{m} & \frac{-c_{if}}{mL_e} \\ 1 & 0 & 0 \\ c_{\nu v} & 0 & \frac{-R_e}{L_e} \end{bmatrix}. \tag{5.27}$$

therefore the desired closed-loop poles p are the eigenvalues of $\tilde{\mathbf{A}}$.

Now, given the system

$$\dot{\mathbf{x}}_g(t) = \mathbf{A}\mathbf{x}_g(t) + \mathbf{B_2}V_z(t) \tag{5.28}$$

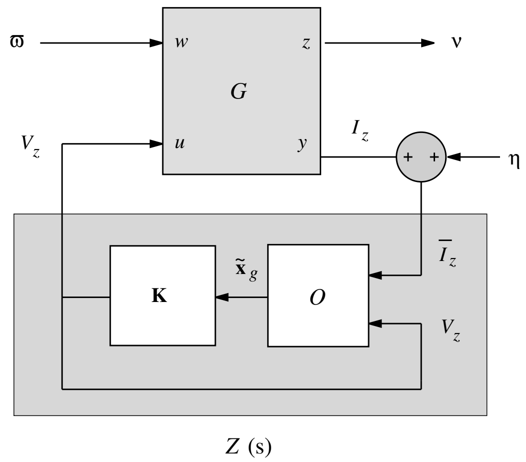

Figure 5.10: Composite plant G controlled by $Z(s)$, an impedance consisting of the state-feedback controller K and Kalman filter O.

and p of desired closed-loop pole locations, Ackermann's formula [68] can be used to calculate a gain vector K such that the state-feedback $V_z(t) = -K\mathbf{x}_g(t)$ places the closed-loop poles at the locations p. In other words, the eigenvalues of $\mathbf{A} - \mathbf{B_2}K$ match the entries of p.

As state-feedback $V_z(t) = -K\mathbf{x}_g(t)$ is not implementable without full state measurement, a linear observer is required, as shown in Figure 5.10. It is possible, however, to derive a state estimate $\tilde{\mathbf{x}}_g(t)$ such that $V_z(t) = -K\tilde{\mathbf{x}}_g(t)$ remains optimal for the output-feedback problem. This state estimate is generated by the Kalman filter [68]

$$\frac{d}{dt}\dot{\tilde{\mathbf{x}}}_g(t) = \mathbf{A}\tilde{\mathbf{x}}_g(t) + \mathbf{B}_2 V_z(t) + \mathbf{L}(\bar{I}_z(t) - \mathbf{C}_2\tilde{\mathbf{x}}_g(t))$$

with inputs $V_z(t)$ (control) and $\bar{I}_z(t)$ (measurement). With the inclusion of measurement noise η, as shown in Figure 5.10, the system representation (5.16) becomes

$$\begin{aligned}
\dot{\mathbf{x}}_g(t) &= \mathbf{A}_g\mathbf{x}_g(t) + \mathbf{B_1}\varpi(t) + \mathbf{B_2}V_z(t) \\
\nu(t) &= \mathbf{C}_1\mathbf{x}_g(t) \\
I_z(t) &= \mathbf{C}_2\mathbf{x}_g(t) + \eta.
\end{aligned}$$

The noise covariance data

$$E\left\{\varpi\varpi'\right\} = \mathbf{Q}_n \quad E\left\{\eta\eta'\right\} = \mathbf{R}_n$$

determines the Kalman gain $\mathbf{L}$ through an algebraic Riccati equation [98].

The Kalman filter is an optimal estimator when dealing with Gaussian white noise η [17]. Specifically, it minimises the asymptotic covariance [68]

$$\lim_{t\to\infty} E\left\{[\mathbf{x}_g(t) - \tilde{\mathbf{x}}_g(t)]\,[\mathbf{x}_g(t) - \tilde{\mathbf{x}}_g(t)]'\right\}, \tag{5.29}$$

of the estimation error $\mathbf{x}_g(t) - \tilde{\mathbf{x}}_g(t)$.

Based on $\mathbf{Q}_n$ and $\mathbf{R}_n$, a Kalman observer [68] that minimises (5.29) can be found through the solution of an algebraic Ricatti equation [98]. The ratio of $\mathbf{Q}_n$ to $\mathbf{R}_n$ essentially represents the confidence in the measured variable $I_z(t)$ and model G. In this work, $\mathbf{Q}_n$ and $\mathbf{R}_n$ are not quantified and simply treated as design parameters influencing the closed-loop pole locations, damping performance and closed-loop stability.

5.4 Experimental Verification

To verify the proposed shunt controller designs, each technique will be applied to an experimental electromechanical isolation apparatus.

5.4.1 Electromagnetic Isolation Apparatus

To support the proposed electromagnetic shunt isolation technique, experiments were carried out on a simple electromagnetic isolation apparatus, as shown in Figure 5.11. The apparatus consists of five identical Jaycar Electronics[1] subsonic transducers Cat. XC-1008. Each transducer consists of a permanent toroid magnet coil, supporting frame, magnetic circuit and flexible supports, as shown in Figure 5.12. Each transducer is mechanically equivalent to the electromagnetic mass-spring-damper, as shown in Figure 5.12.

By connecting electromagnetic transducers together, as shown in Figure 5.13, when the isolation transducer is the isolated mass-spring-damper system and the base transducers as the base disturbance, a simple experimental isolation system is obtained. Note that base transducers are bolted to the ground. For this work a Newport RS 3000 optical table was utilised.

Now a disturbance current $I_d(s)$ is applied to the base transducer to simulate a base disturbance so the transmissibility ratio $T(s)$ of the isolated mass can be measured. To measure the transmissibility ratio, two B&K accelerometers were used to measure the applied base

[1] http://www.jaycar.com.au

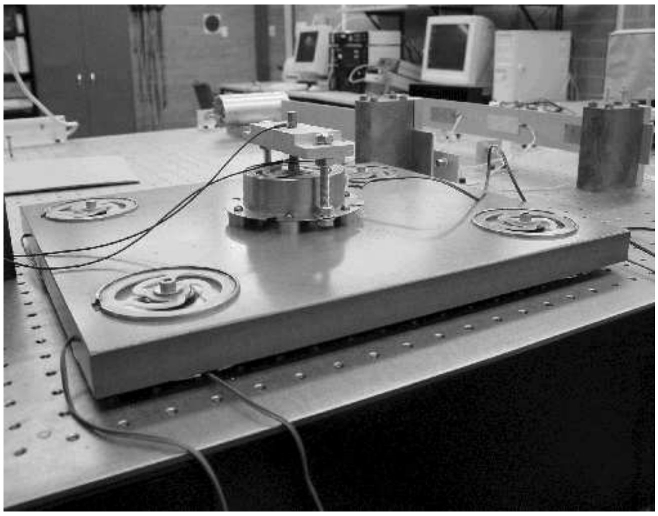

Figure 5.11: Isolation experimental apparatus.

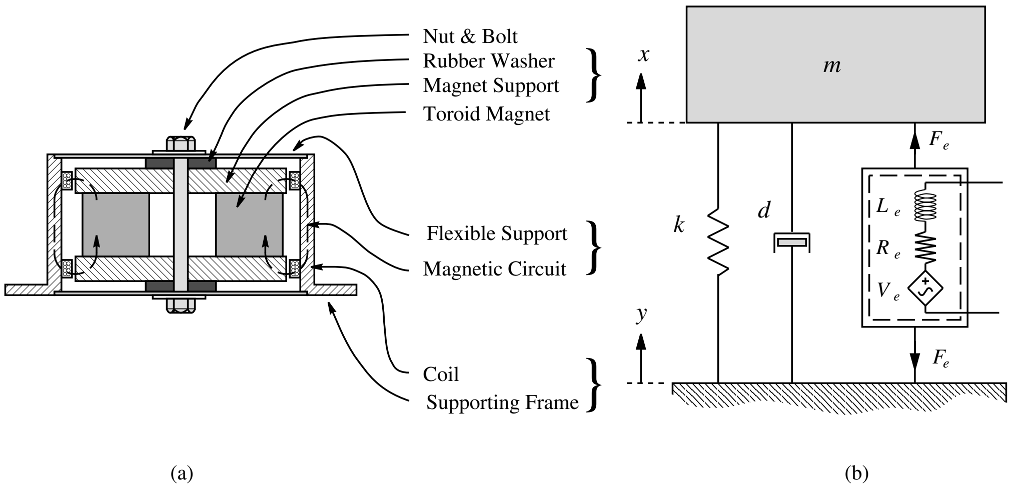

Figure 5.12: Electromagnetic transducer cross section (a) and mechanical equivalent (b).

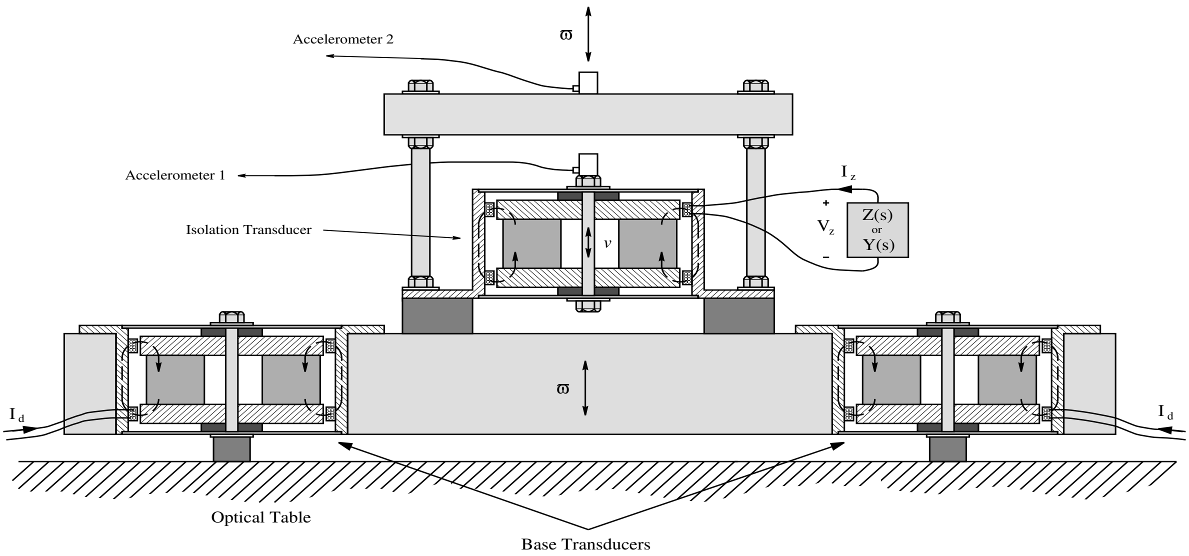

Figure 5.13: Sideview of the experimental isolation apparatus. Isolation transducer is shunted by electrical impedance or admittance while applying a base disturbance current $I_d(s)$ to base transducers.

velocity $\varpi(s)$ (accelerometer 2), and the isolated mass velocity $\nu(s)$ (accelerometer 1), as shown in Figure 5.13. An experimental magnitude frequency response was obtained for the transmissibility ratio, i.e. $T(s) \triangleq G_{\varpi\nu}(s)$, as illustrated in Figure 5.14.

To model the experimental isolated apparatus; the isolated mass m, the damping constant d, the spring constant k, the coil inductance L_e and the coil resistance R_e, the electromechanical coefficients $c_{\nu v}$ and c_{if} need to be determined. The isolated mass, coil inductance and resistances can all be measured directly, while the damping and spring constant can be observed by using the resonance frequency data, i.e. ω_n can be determined from Figure 5.14, $d = 2\zeta\omega_n m$ and $k = \omega_n^2 m$. To determine the electromechanical coefficients $c_{\nu v}$ and c_{if}, a disturbance current $I_d(s)$ is applied to the base transducers. Assuming the transducer 1 is linear, isolation transducer voltage and relative velocity of the isolation mass $\nu(s) - \varpi(s)$ can be measured, i.e. $\frac{V_e(s)}{\nu(s)-\varpi(s)} = c_{\nu v} \approx c_{if}$. Therefore, the experimental parameters for the isolated apparatus are as listed in Table 5.1.

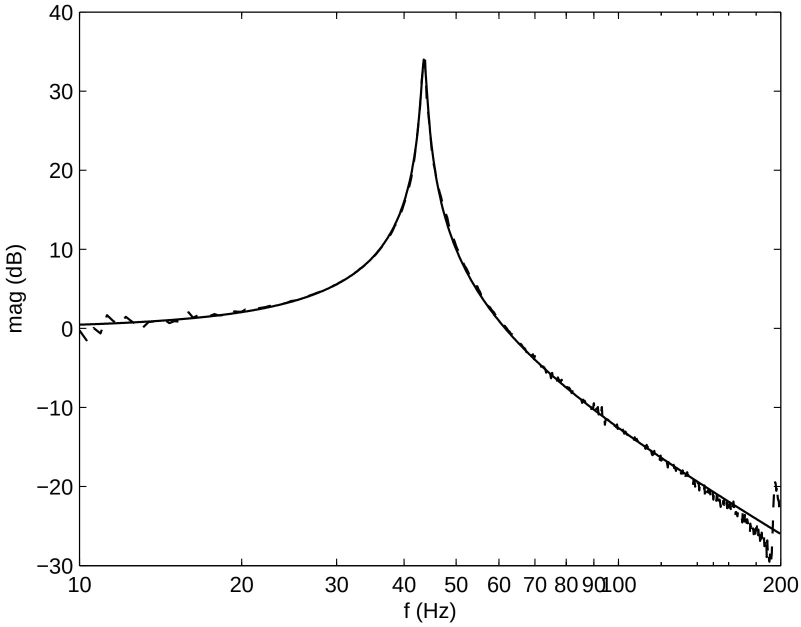

Figure 5.14: Experimental (−−) and simulated (—) transmissibility ratio $T(s)$.

Parameter	**Symbol**	**Unit**
Isolated mass	m	$0.4\ Kg$
Damping constant	d	$2.18\ Nsm^{-1}$
Spring constant	k	$29.4\ kNm^{-1}$
Electromagnetic coupling	$c_{\nu v}$	3.65
Electromagnetic coupling	c_{if}	3.6
Coil inductance	L_e	$0.320\ mH$
Coil resistance	R_e	$4.0\ \Omega$

Table 5.1: Electromagnetic transducer parameters.

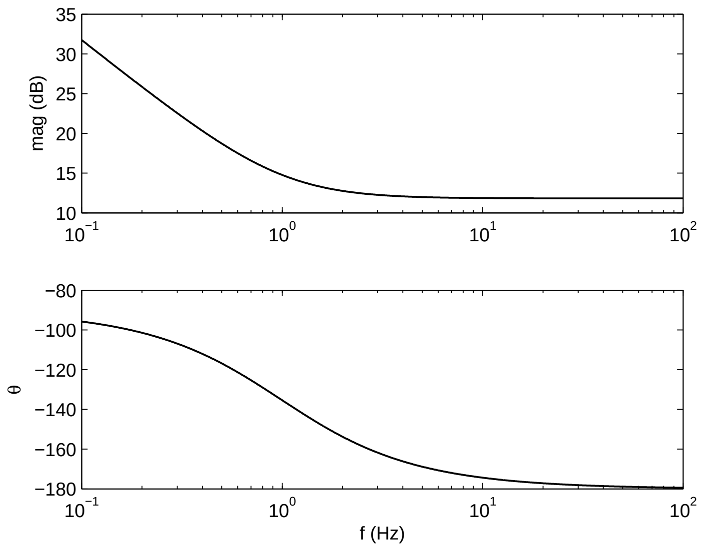

Figure 5.15: Magnitude and phase response for the capacitor-resistor controller.

5.4.2 Shunt Controllers

Capacitor-Resistor Controller

Using the equations described in Section 5.4.1, $C = 0.0414\ F$ and $R = -3.9\ \Omega$ can be derived. For the passive impedance, magnitude-phase for the controller can be plotted, as shown in Figure 5.15.

For the shunt controller design, the desired open-loop and closed-loop pole locations for the shunted system are shown in Figure 5.16. The open-loop and closed-loop transmissibility ratio response for the system can be plotted, as shown in Figure 5.17.

Experiments were performed on the experimental apparatus using the current-controlled-voltage-source (CCVS), as described in Section 4.5.2. Experimental results for transmissibility ratio are shown in Figure 5.17.

From simulation and experimentation, as shown in Figure 5.17, the passive controller has considerably damped the resonance by 28.3 dB, but unfortunately it has also decreased the high frequency attenuation.

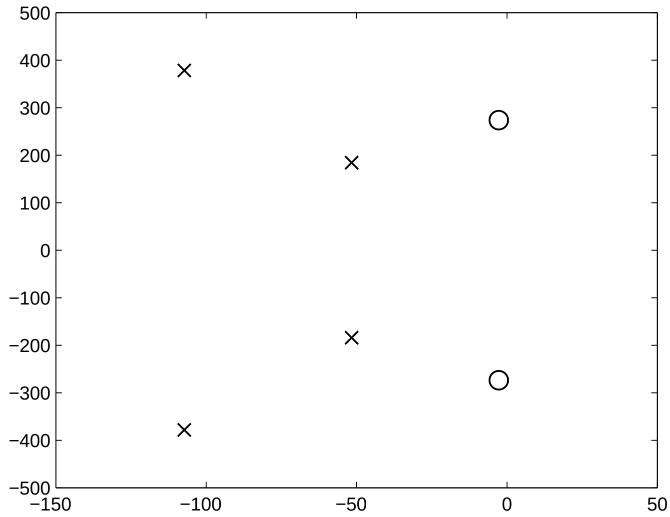

Figure 5.16: Open-loop (◯) and closed-loop ($\times$) poles for the isolation system.

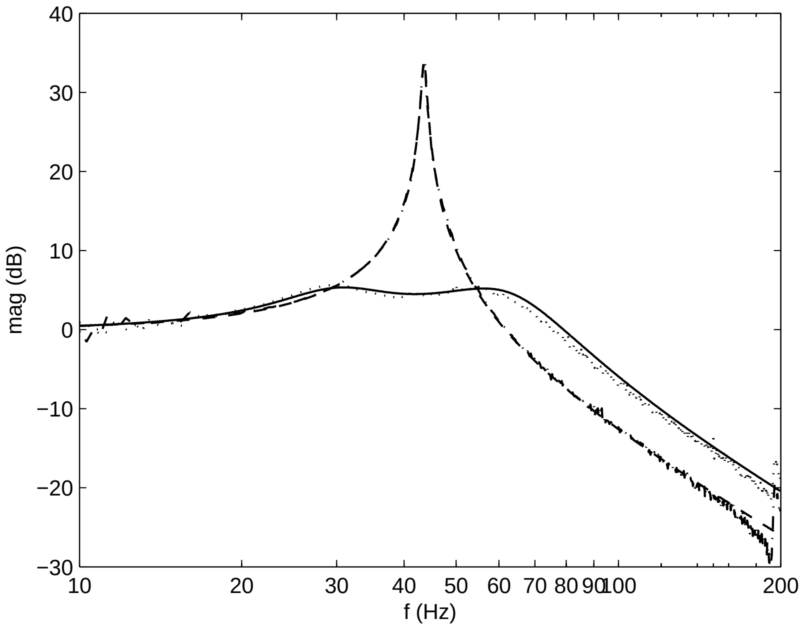

Figure 5.17: Magnitude $T(s)$ response for the capacitor-resistor controller. Simulated open-loop ($--$) and closed-loop (—), and experimental open-loop ($-\cdot-$) and closed-loop ($\cdots$).

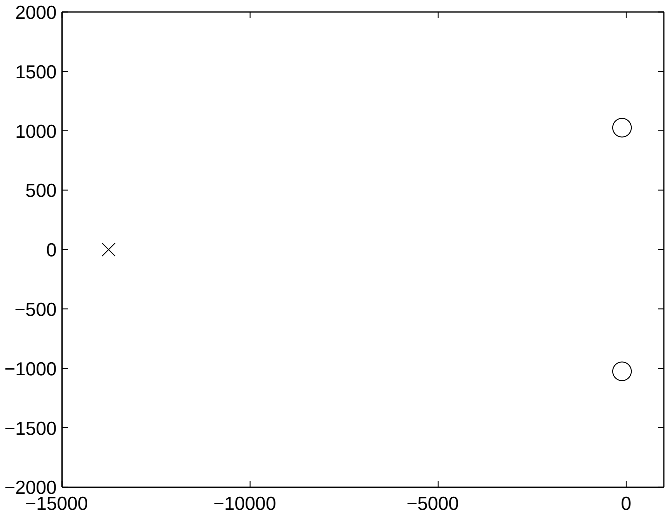

Figure 5.18: Poles ($\times$) and zeros ($\bigcirc$) of the ideal impedance.

Ideal Controller

Assuming $\beta = 24.7$, the poles and zeros for the ideal controller (5.23) can be determined, as shown in Figure 5.18. In Figure 5.19, the ideal impedance of the resulting $Z(s)$ is plotted together with that of the negative coil impedance i.e. $-(L_e s + R_e)$. Note at low frequencies the ideal controller looks very similar to that of the negative coil impedance i.e. $-(L_e s + R_e)$.

To validate the proposed impedance $Z(s)$, the open-loop and closed-loop pole locations for the isolation system can be simulated, as shown in Figure 5.20. Simulated open-loop and closed-loop transmissibility ratio response is also shown in Figure 5.21.

By applying the proposed admittance (5.24) to the isolation apparatus using voltage-controlled-current-source, described in Section 4.5.2, the experimental open-loop and close-loop responses can be measured. These are plotted in Figure 5.21. From Figure 5.21, it can be observed that both resonant peak reduction of 21.6 dB and high frequency attenuation have been achieved.

The proposed $Z(s)$ can be presented as some type of an impedance network consisting of capacitors, inductors and resistors. From observation, it was noted that the impedance network consists of two reactive and two real elements. These impedances could consist of both passive and/or active circuit elements. After an exhaustive search, the following

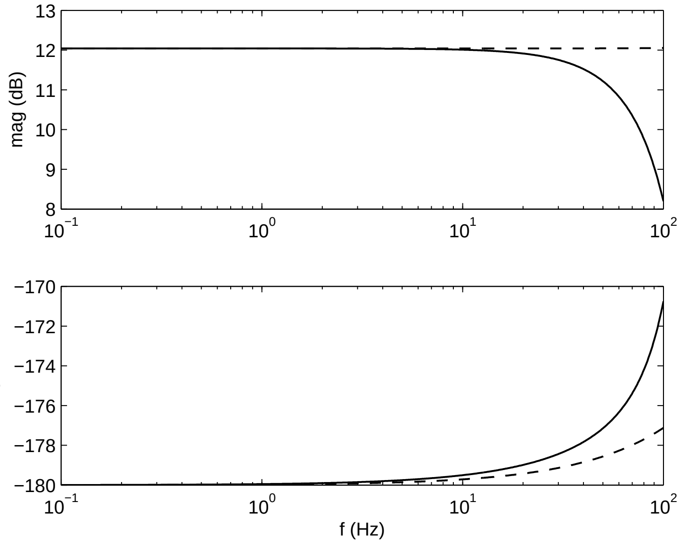

Figure 5.19: Magnitude and phase response for the ideal controller (—) and negative coil impedance (−−).

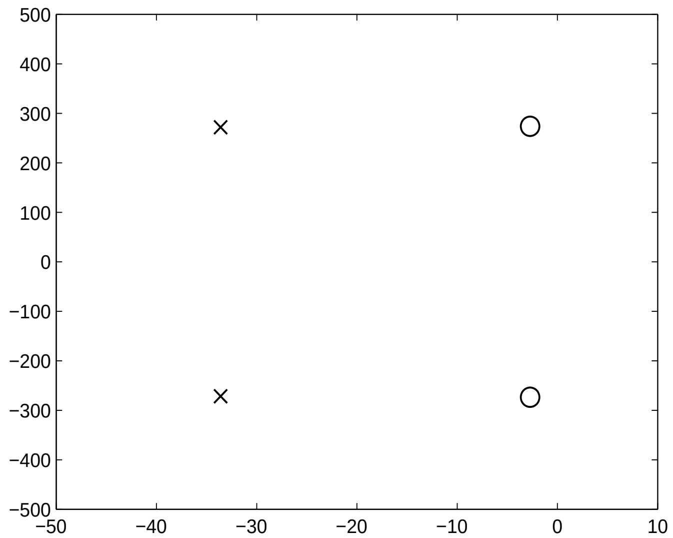

Figure 5.20: Open-loop (◯) and closed-loop (×) poles for the isolation system. Note some high frequency poles are not shown.

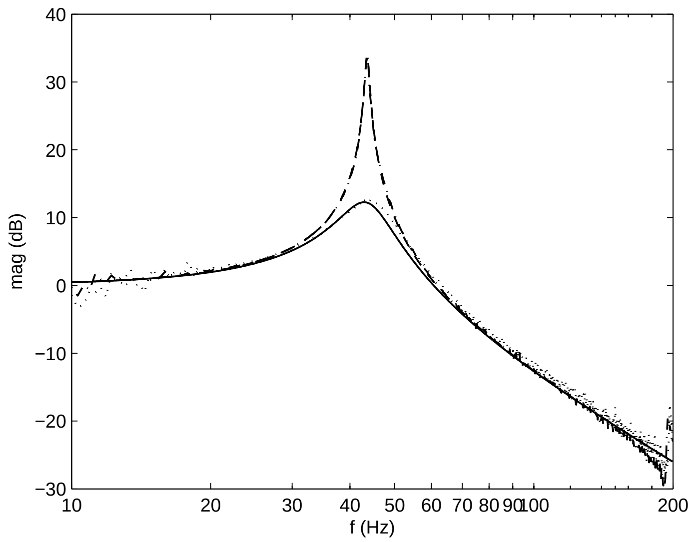

Figure 5.21: Magnitude $T(s)$ response for the ideal controller. Simulated open-loop ($--$) and closed-loop (—), and experimental open-loop ($-\cdot-$) and closed-loop ($\cdots$).

impedance network, as shown in Figure 5.22, was considered. That is

$$Z_\beta(s) = \frac{1}{C_\beta s + \frac{1}{R_{\beta_2}}} + L_\beta s + R_{\beta_1}, \tag{5.30}$$

where the inductor L_β, capacitor C_β, and resistors $R_{\beta_1}$and R_{β_2} are

$$\begin{aligned} L_\beta &= -\left(\frac{c_{\nu v} c_{if} m}{\beta d} + L_e\right) \\ C_\beta &= \left(\frac{\beta d^2}{c_{\nu v} c_{if} k\left(\beta d - km\right)}\right) \\ R_{\beta_1} &= -\left(\frac{c_{\nu v} c_{if}\left(\beta d - km\right)}{\beta d^2} + R_e\right) \\ R_{\beta_2} &= \left(\frac{c_{\nu v} c_{if}\left(\beta d - km\right)}{\beta d^2}\right). \end{aligned}$$

Since $Z(s)$ is known, the required parameters for $Z_\beta(s)$ can be determined using Equation (5.30) that is listed in Table 5.2.

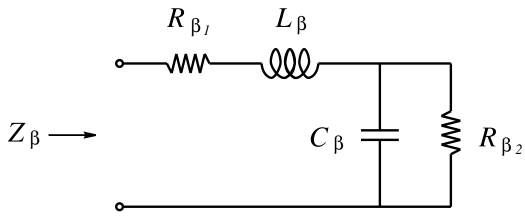

Figure 5.22: Impedance network for $Z_\beta(s)$.

Symbol	Unit
L_β	$-0.0517\ H$
C_β	$-1.0323 \times 10^{-7}\ F$
R_{β_1}	$699.94\ \Omega$
R_{β_2}	$-703.93\ \Omega$

Table 5.2: $Z_\beta(s)$ parameters.

Impedance Synthesis

Similar to the procedure presented in Section 4.5.3, Figure 5.23 shows the gains in Table 5.3. The voltages V_1 through V_4 represent the signals applied to, or sensed from, the current-controlled-voltage-source (CCVS), as described in Section 4.5.2. The required shunt impedance applied to the electromechanical system is

$$Z_c(s) = \frac{V_z(s)}{I_z(s)} = a_3 C(s) a_4. \tag{5.31}$$

Gain	Unit
a_1	$1.0\ ms^{-1}/V$
a_2	$1.0\ V/ms^{-1}$
a_3	$1.0\ V/V$
a_4	$1.0\ V/A$

Table 5.3: External gains associated with the experimental system.

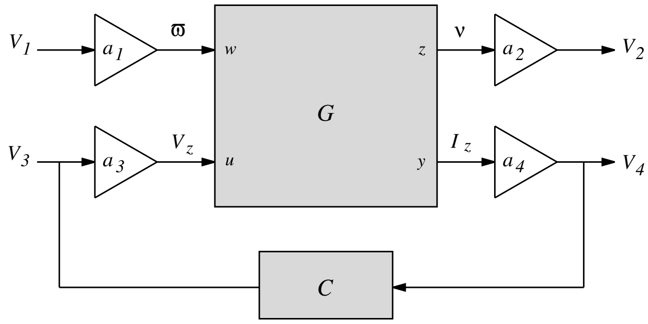

Figure 5.23: External gains associated with the electromechanical system.

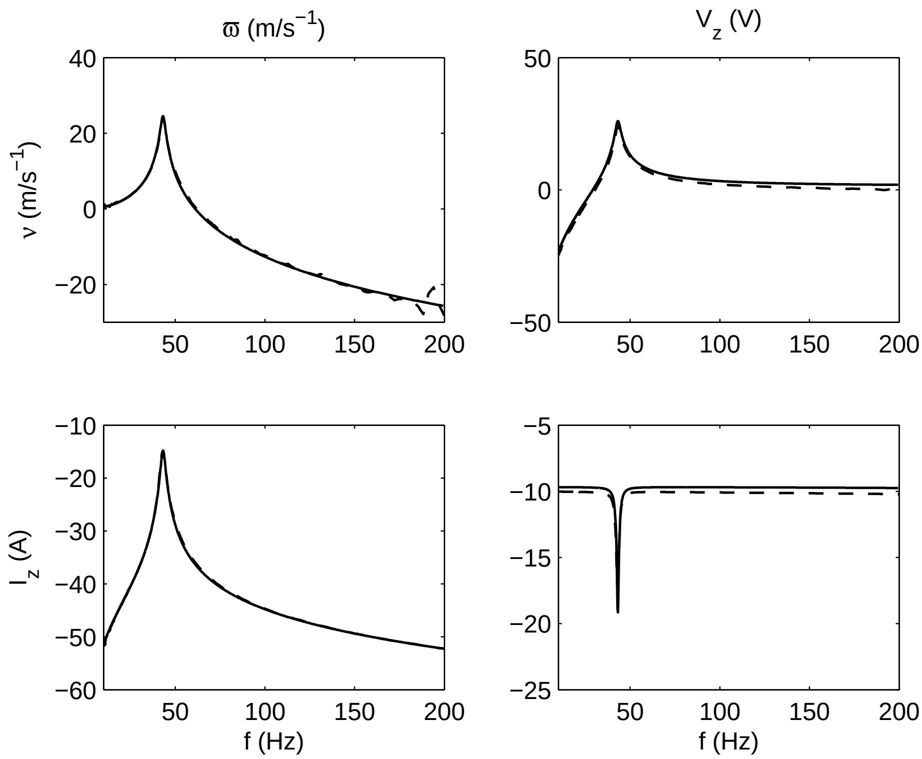

Figure 5.24: Simulated (—) and experimental (−−) magnitude frequency responses (in dB).

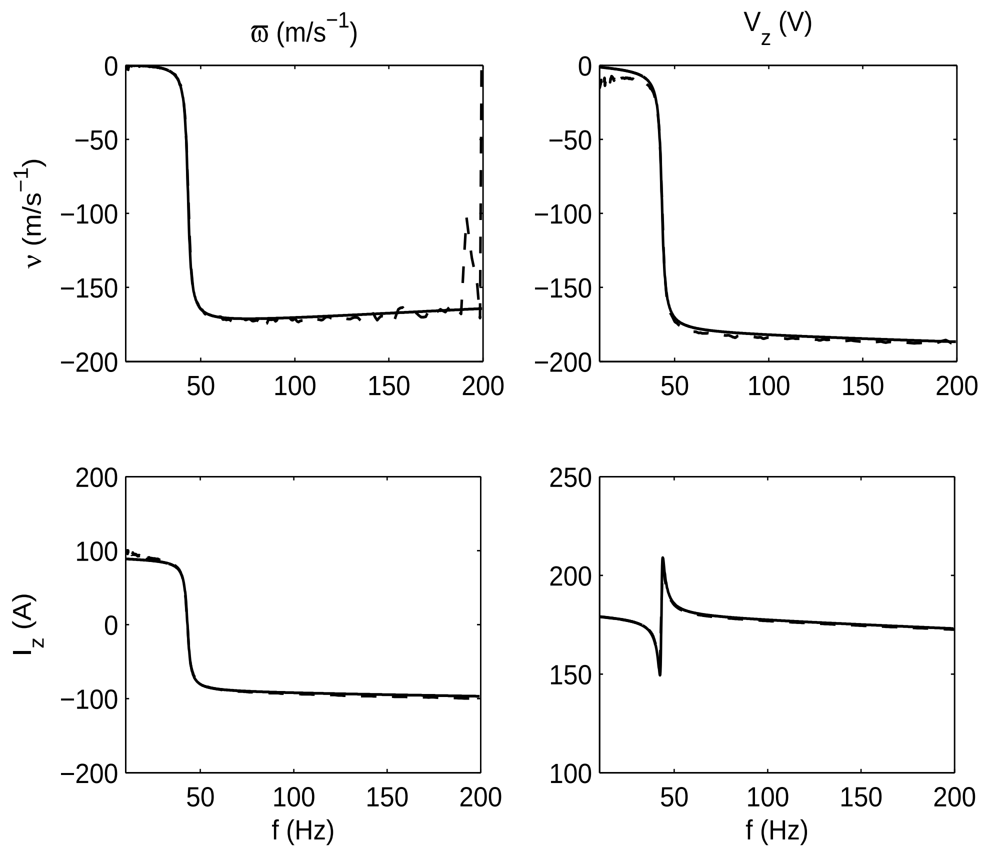

Figure 5.25: Simulated (—) and experimental (−−) phase frequency responses (in degrees).

To validate the proposed model for the electromechanical isolation system, experimental frequency response data was obtained using the same procedure as in Section 4.5.3. The magnitude and phase frequency responses are shown in Figures 5.24 and 5.25. From the previous figures a satisfactory correlation between the theoretical model and experimental data was obtained, validating the proposed model of the electromagnetic isolation apparatus.

As discussed in Section 5.3.3, the Matlab place command can be used to design the state-feedback controller $\mathbf{K}$. Assuming $\alpha = 46$, the state-feedback controller K is

$$\mathbf{K} = \begin{bmatrix} 38.9 & -300.5 & -115.0 \end{bmatrix}.$$

An observer is required to estimate the system state from the measured shunt current I_z. A Kalman observer was designed to estimate the system state $\tilde{\mathbf{x}}_g(t)$ utilising the measured shunt transducer current I_z and control signal V_z. Referring to Section 5.3.3, the disturbance and output noise process covariance matrices $\mathbf{Q}_n$ and $\mathbf{R}_n$ were chosen to be 3 and 0.1 respectively. Such a weighting, although not quantitative, expresses moderate confidence in the fidelity of the measured variable I_z.

By concatenating the K gain matrix and the Kalman observer, and compensating for the system gains a_3 and a_4, the actual impedance presented to the shunt transducer can be determined as

$$Z_c(s) = \frac{-2.448 \times 10^4 s^2 - 2.193 \times 10^8 s + 1.308 \times 10^{11}}{s^3 + 6.345 \times 10^4 s^2 + 9.247 \times 10^7 s - 4.219 \times 10^{10}}. \tag{5.32}$$

In Figure 5.26, the complex impedance of the resulting controller is plotted together with that of the negative coil impedance, i.e. $-(L_e s + R_e)$. A negative coil impedance connected to the true coil impedance effectively removes the source impedance from the transducer. One impedance has a tendency to mimic the other impedance over a certain frequency range. The pole-zero map of the controller is shown in Figure 5.27.

After examining the open-loop and closed-loop pole locations in Figure 5.28, it can be appreciated that the controller is clearly acting to increase the system damping while retaining high frequency attenuation. Corresponding mitigation of the transfer function from an applied disturbance to the measured vibration can be seen in the frequency domain, Figure 5.29. The resonant peak has been experimentally damped by 26.2 dB.

The proposed $Z_c(s)$ can be presented as some type of impedance network consisting of capacitors and resistors. To determine the impedance network structure, $Z_c(s)$ can be broken

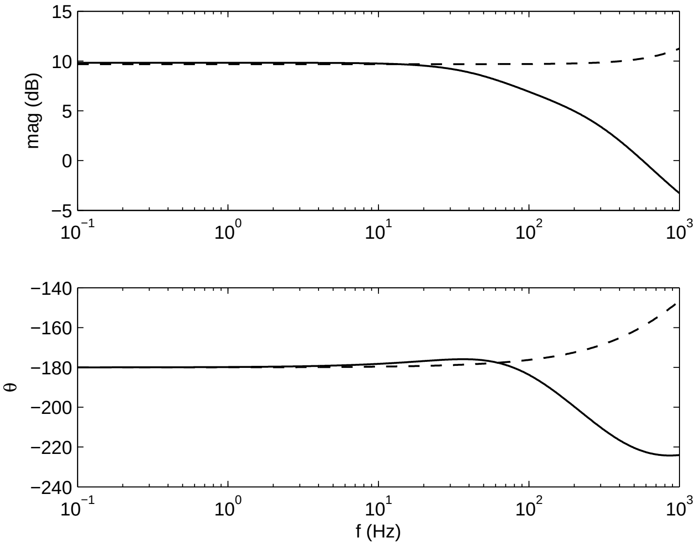

Figure 5.26: Magnitude and phase response of the impedance synthesis controller (—) and negative coil impedance (−−).

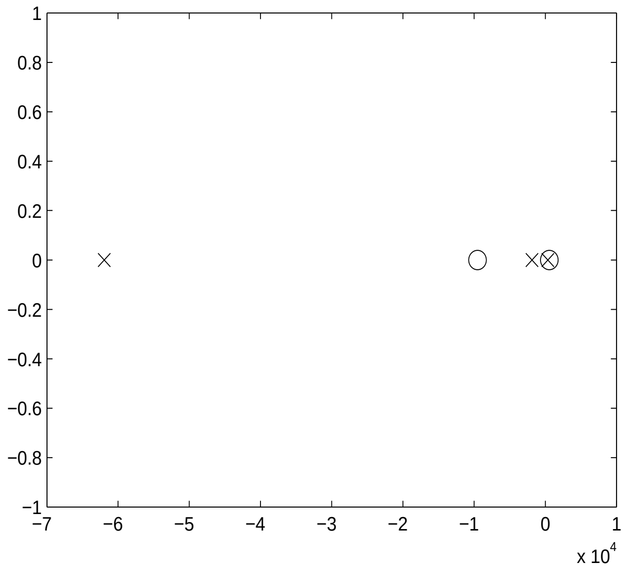

Figure 5.27: Poles (×) and zeros (◯) of the impedance synthesis controller.

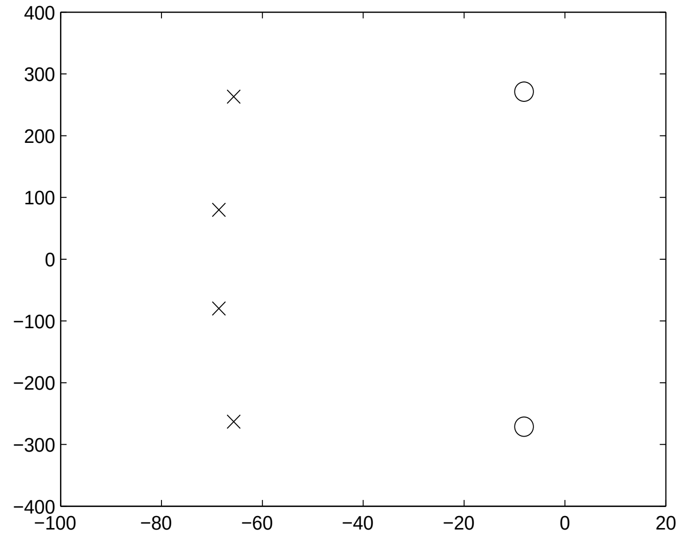

Figure 5.28: Open-loop (◯) and closed-loop ($\times$) pole locations. Note a pair of high-frequency observer poles are not visible within the scope of this plot.

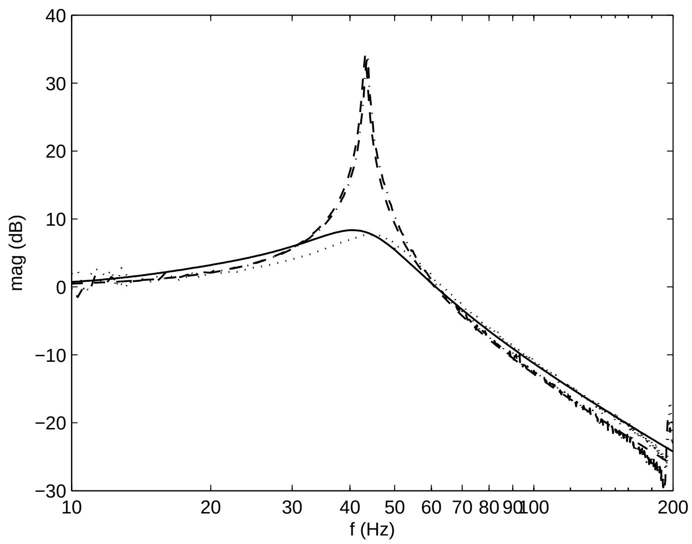

Figure 5.29: Magnitude $T(s)$ response to the ideal controller. Simulated open-loop ($--$) and closed-loop (—), and experimental open-loop ($- \cdot -$) and closed-loop ($\cdots$).

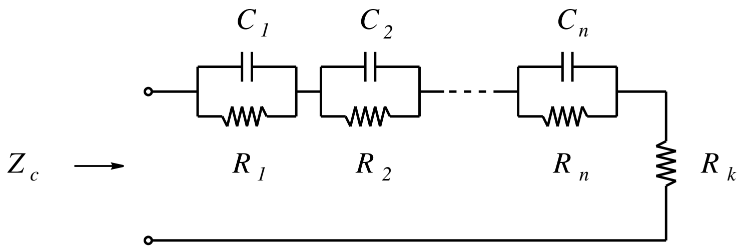

Figure 5.30: Impedance network for Equation (5.33).

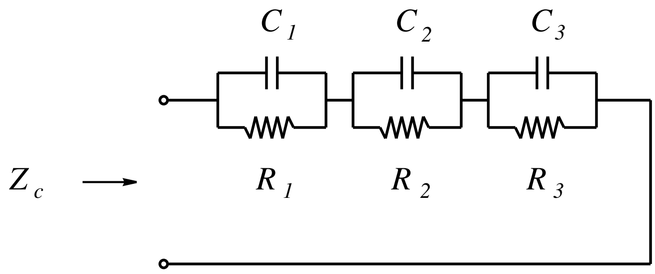

Figure 5.31: Impedance network for $Z_c(s)$.

into its first-order elements by taking a partial-fraction expansion. Assuming

$$\begin{aligned} Z_c(s) &= \frac{r_1}{s-p_1} + \frac{r_2}{s-p_2} + \ldots + \frac{r_n}{s-p_n} + k \\ &= \frac{1}{\frac{1}{r_1}s - \frac{p_1}{r_1}} + \frac{1}{\frac{1}{r_2}s - \frac{p_2}{r_2}} + \ldots + \frac{1}{\frac{1}{r_n}s - \frac{p_n}{r_n}} + k \\ &= \frac{1}{C_1 s + \frac{1}{R_1}} + \frac{1}{C_2 s + \frac{1}{R_2}} + \ldots + \frac{1}{C_n s + \frac{1}{R_n}} + R_k, \end{aligned} \tag{5.33}$$

where $\left\{C_1 = \frac{1}{r_1}, C_2 = \frac{1}{r_2}, \ldots, C_n = \frac{1}{r_n}\right\}$, $\left\{R_1 = -\frac{r_1}{p_1}, R_2 = -\frac{r_2}{p_2}, \ldots, R_n = -\frac{r_n}{p_n}\right\}$ and $R_k = k$, are the impedance network structure for Equation (5.33) as shown in Figure 5.30.

Performing the partial-fraction expansion on Equation (5.33), the network parameters for Figure 5.30 are listed in Table 5.4. Therefore, for the isolation system, the following impedance network is shown in Figure 5.31.

Symbol	Unit
C_1	$-4.6666 \times 10^{-5}\ F$
C_2	$-2.9476 \times 10^{-4}\ F$
C_3	$2.9218 \times 10^{-3}\ F$
R_1	$-0.34595\ \Omega$
R_2	$-1.8159\ \Omega$
R_3	$-0.93883\ \Omega$

Table 5.4: $Z_c(s)$ parameters.

5.5 Discussions

In this chapter, the objective was to apply electromagnetic shunt control to a simple mechanical isolation system which has been defined as electromagnetic shunt isolation. The plant for the isolation system was found to be more complicated compared to the electromagnetic shunt damping system described in Chapter 4. This complexity can be attributed to the isolation system being modelled as a regulator feedback control problem with filtered input disturbance.

Three electromagnetic shunt controllers were developed and applied to a simple experimental isolation apparatus. All control strategies were designed to achieve resonant peak reduction and high frequency attenuation, both theoretically and experimentally.

The first proposed controller, capacitor-resistor controller, technique is very effective around the resonance, but offers limited attenuation at higher frequencies, shown in Figure 5.17. As a result, the design of a passive shunt involves a trade-off between the resonance peak damping and the high frequency attenuation. In spite of the associated problems, this technique warrants mention due to its inherent simplicity.

The second proposed controller, ideal impedance, has two key features. They are: (1) the impedance has a very similar structure to the negative inductor-resistor, as proposed in Section 4.4.2, but contains two additional terms, i.e. $-\frac{c_{\nu v} c_{if} m s^2}{\beta(ds+k)} - \frac{c_{\nu v} c_{if} s}{(ds+k)}$, and (2) the impedance contains negative or active elements. Through simulation and experimentation on the simple isolation system, the proposed controller achieved both peak damping and high frequency attenuation. Although some associated problems were encountered during experimentation, it requires an accurate measurement of system parameters. That is, the ideal impedance relies solely on estimates/measurements of m, d, k, L_e, R_e, $c_{\nu v}$ and c_{if}. Therefore, the proposed impedance is extremely difficult to experimentally tune because of the discrepancies in system parameters.

Impedance synthesis, the third proposed controller, showed that connecting an electrical impedance to the terminals of an electromagnetic isolation system is equivalent to implementing a standard feedback control problem. A method using pole placement and a Kalman observer were used to design an appropriate impedance. While designing the impedance synthesis controller, two important objectives were considered; resonant peak damping and high frequency attenuation. Both of these objectives were achieved through simulation and experimentation on a simple isolation system. Once constructed, the proposed impedance controller can then be broken into first-order elements, capacitors and resistors. Then an impedance network can be constructed using the first-order elements. Unfortunately, this impedance network consists of both passive and active circuit elements. Therefore, the synthetic impedance, as described in Section 4.5.2, is recommended for practical implementation instead of using passive elements (resistors and capacitors) and negative impedance converters [59] (negative resistors and negative capacitors).

From observation, the impedance synthesis technique was considered to be less sensitive to small changes in transducer dynamics and was considered to be more robust compared to the ideal controller. The impedance synthesis technique outperformed the other control strategies by maintaining peak reduction and high frequency attenuation. While the capacitor-resistor controller did provide peak attenuation, it did not provide high frequency attenuation. The ideal controller maintained both peak and high frequency attenuation but proved to be difficult to tune the experimental parameters. Therefore, the author suggests the impedance synthesis technique would be the more preferred method for electromagnetic shunt isolation.

Current and future work will involve both the exploration of the control theory associated with the synthesis step and inclusion of uncertainty in the plant model to guarantee robustness and stability.

Chapter 6

Proof-Mass Inertial Vibration Control

In this chapter, vibration reduction using an electromagnetically actuated inertial drive will be discussed. Both passive and active drive dynamics are considered when constructing a model of the mated mechanical and inertial drive systems. In doing so, the performance of a passive absorber can be augmented with an active feedback system. A method is presented for the modelling, design and implementation of a shunt controlled electromagnetic inertial drive for vibration suppression. By viewing the coil current and voltage as system inputs and outputs, the task of impedance synthesis can be cast as a standard feedback design problem. Arbitrarily objectives such as LQR, LQG, or $\mathcal{H}_2$ goals are easily specified. In this work, displacement is minimised subject to a penalty on the inertial mass travel and applied terminal voltage. Using this technique, the need for external sensors is eliminated, significantly reducing the cost, complexity and sensitivity to transducer failure that in many applications may preclude the use of an active control system.

6.1 Background

Tuned mass dampers, or inertial drives, are commonly used for mechanical vibration control [51, 91]. Tuned mass absorbers utilise an inertial mass and tuned support to introduce additional dynamics and mitigate vibration over a certain frequency range. Active vibration control systems employ inertial drives to regulate the signal from an accelerometer or related performance signal. Active feedback systems are known to provide better performance than

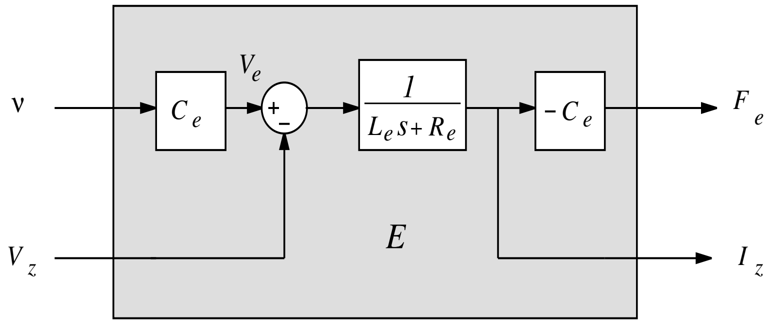

Figure 6.1: Electrical and mechanical dynamics of an electromagnetic transducer.

tuned passive systems.

Although ideal inertial drives develop a pure reaction force in response to a driving current, the flexures used to support the inertial mass effectively filter the applied force and introduce additional passive dynamics, as shown in Chapter 5.

In Chapters 4 and 5, it has been seen that by connecting an electrical impedance to the terminals of an electromagnetic coil, the relative mechanical velocity between the coil and magnet can be reduced. A technique for the synthesis of active shunt impedances was presented in Section 4.4.3. Using active synthesis, performance objectives other than minimisation of the relative velocity are possible. Active electromagnetic shunt control is potentially applicable to vibration damping, isolation systems and suspension systems.

Experiments are performed on a simple single-mode host structure with integrated electromagnetic transducer and suspended absorber mass. The combination of passive and active control results in significant vibration suppression.

6.2 Modelling

In this section, the dynamics of an electromagnetic and mechanical system are studied independently, then combined to reveal the dynamics of a shunted electromagnetic inertial actuator.

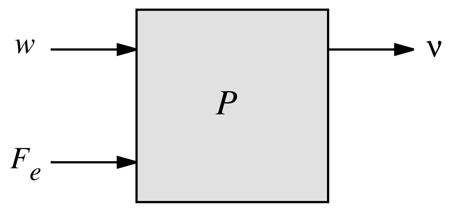

Figure 6.2: General mechanical system suitable for coupling to an electromagnetic transducer. In addition to disturbance input w, the model also includes force input F_e and relative velocity output ν.

6.2.1 Electromagnetic Transducer Dynamics

The electrical and mechanical transducer dynamics are summarised in Figure 6.1. In response to relative velocity ν and terminal voltage V_z, the transducer E develops a force F_e and current I_z. When short-circuited, i.e. when $V_z = 0$, the transducer develops a force opposite in direction to the relative coil velocity ν.

The following state-space representation of the coil admittance $Y_c(s) = \frac{1}{L_e s + R_e}$ will be required as

$$\begin{aligned} \dot{x}_y(t) &= A_y x_y(t) + B_y V_z(t) \\ I_z(t) &= C_y x_y(t), \end{aligned} \tag{6.1}$$

where

$$A_y = \left[\frac{-R_e}{L_e}\right], \qquad B_y = [1], \qquad C_y = [\frac{1}{L_e}]. \tag{6.2}$$

6.2.2 Mechanical System

The general model of a mechanical system is shown in Figure 6.2. In addition to various application specific inputs and outputs to couple the system to an electromagnetic actuator, the model requires a force input F_e and a relative velocity output ν. In a typical scenario, the model would also describe the influence of a specific disturbance input w.

A single degree-of-freedom tuned-mass or inertial vibration control system is shown in Figure 6.3. The reaction force F_e generated by an electromagnetic actuator is employed to minimise the vibration x_2 resulting from a disturbance force F_d. The quantities denoted m, k, d, and

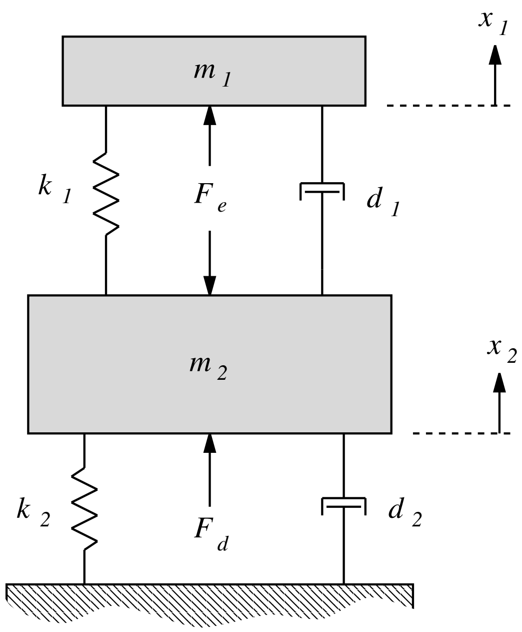

Figure 6.3: Suspended mass m_2 disturbed by force F_d. Absorber mass m_1 is manoeuvred by reaction force F_e to reduce displacement x_2.

x represent the mass (in Kg), the spring constant (in Nm^{-1}), the damping coefficient (in Nsm^{-1}) and the displacement (in $meters$) respectively. The symbols $\dot{\nu}$ and ν will also be used to represent acceleration and velocity.

The equations of motion governing the system can be written as

$$\begin{aligned} m_1\dot{\nu}_1(t) &= -d_1\left(\nu_1(t)-\nu_2(t)\right)-k_1\left(x_1(t)-x_2(t)\right)+F_e(t) \\ m_2\dot{\nu}_2(t) &= d_1\left(\nu_1(t)-\nu_2(t)\right)+k_1\left(x_1(t)-x_2(t)\right)-d_2\nu_2(t)-k_2x_2(t)-F_e(t)+F_d(t). \end{aligned} \tag{6.3}$$

By choosing the state variables ν_1, x_1, ν_2 and x_2, that is $\mathbf{x}_p(t)=[\nu_1(t)\ x_1(t)\ \nu_2(t)\ x_2(t)]'$, the system can be cast in the following state-space form:

$$\begin{aligned} \dot{\mathbf{x}}_p(t) &= \mathbf{A}_p\mathbf{x}_p(t)+\mathbf{B}_p\begin{bmatrix} F_d(t) \\ F_e(t) \end{bmatrix} \\ \begin{bmatrix} x_2(t) \\ \nu_1(t)-\nu_2(t) \end{bmatrix} &= \mathbf{C}_p\mathbf{x}_p(t), \end{aligned} \tag{6.4}$$

where the subscript P denotes the mechanical plant and the output $\nu_1-\nu_2$ represents the relative velocity between the two masses. The system matrices are

$$\mathbf{x}_p(t)=\begin{bmatrix} \nu_1(t) \\ x_1(t) \\ \nu_2(t) \\ x_2(t) \end{bmatrix} \qquad \mathbf{B}_p=\begin{bmatrix} \mathbf{B}_{p1} & \mathbf{B}_{p2} \end{bmatrix}=\begin{bmatrix} 0 & \frac{1}{m_1} \\ 0 & 0 \\ \frac{-1}{m_2} & \frac{1}{m_2} \\ 0 & 0 \end{bmatrix} \tag{6.5}$$

and

$$\mathbf{A}_p=\begin{bmatrix} \frac{-d_1}{m_1} & \frac{-k_1}{m_1} & \frac{d_1}{m_1} & \frac{k_1}{m_1} \\ 1 & 0 & 0 & 0 \\ \frac{d_1}{m_2} & \frac{k_1}{m_2} & \frac{-(d_1+d_2)}{m_2} & \frac{-(k_1+k_2)}{m_2} \\ 0 & 0 & 1 & 0 \end{bmatrix} \qquad \mathbf{C}_p=\begin{bmatrix} \mathbf{C}_{p1} \\ \mathbf{C}_{p2} \end{bmatrix}=\begin{bmatrix} 0 & 0 & 0 & 1 \\ 1 & 0 & -1 & 0 \end{bmatrix}. \tag{6.6}$$

A block diagram of the mechanical system (6.4) is shown in Figure 6.4. As the system includes a control force input F_e and a relative velocity output ν, the model is easily coupled to that of an electromagnetic transducer.

6.2.3 Shunted Composite Electromechanical System

As shown in Figure 6.5, a mechanical system P coupled to an impedance shunted electromagnetic transducer is considered. The force disturbance F_d is realised with the use of an

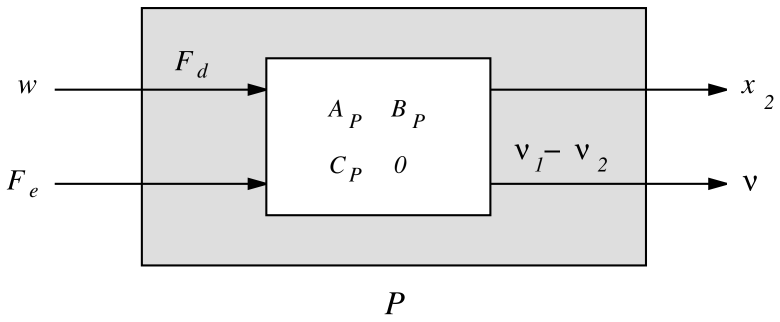

Figure 6.4: Mechanical system (6.4) shown with force disturbance F_d and control inputs F_e and a performance output x_2 and the relative velocity output ν.

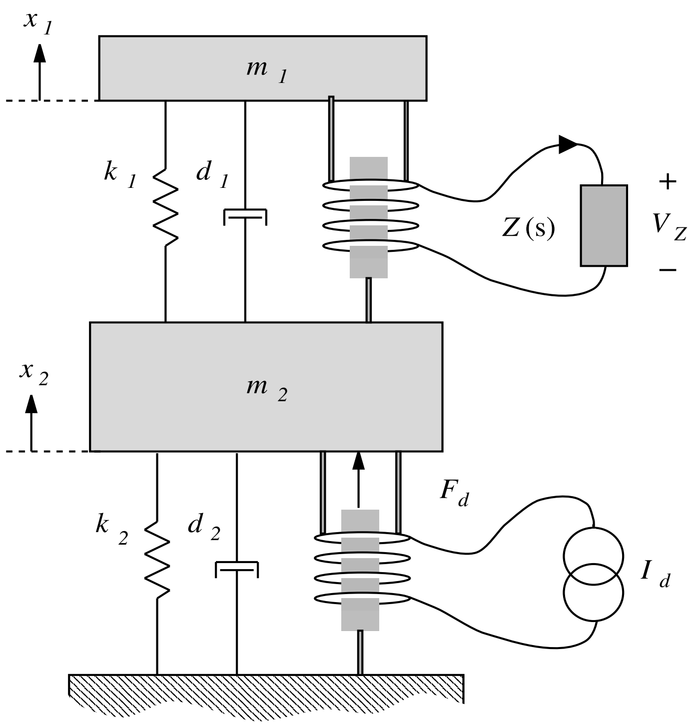

Figure 6.5: Two-mass systems with electromagnetic transducers to realise the disturbance force F_d and control force F_e.

auxiliary transducer and current source, e.g.

$$F_d(t) = C_d I_d(t). \tag{6.7}$$

Within the modelling framework introduced in the previous two subsections, i.e. by treating the mechanical plant and shunted electromagnetic coil as shown in Figures 6.1 and 6.4, the composite plant is easily constructed and demonstrated in Figure 6.6.

In Figure 6.6, the impedance $Z(s)$ is interpreted simply as the transfer function relating coil current to terminal voltage, appears analogous to a feedback controller for the electromechanical system. By concatenating the mechanical and electromagnetic systems P and E, as shown in Figure 6.7, the composite system is cast as a typical regulation problem for the abstracted system G. The state equation of the electrical (6.2) and mechanical (6.4) systems can be collected to describe the system G, therefore

$$\begin{aligned} \dot{\mathbf{x}}_g(t) &= \mathbf{A}_g \mathbf{x}_g(t) + \mathbf{B}_g \begin{bmatrix} I_d(t) \\ V_z(t) \end{bmatrix} \\ \begin{bmatrix} x_2(t) \\ I_z(t) \end{bmatrix} &= \mathbf{C}_g \mathbf{x}_g(t), \end{aligned} \tag{6.8}$$

where

$$\mathbf{x}_g(t) = \begin{bmatrix} \mathbf{x}_p(t) \\ x_y(t) \end{bmatrix}, \qquad \mathbf{A}_g = \begin{bmatrix} \mathbf{A}_p & -C_e \mathbf{B}_{p2} \mathbf{C}_y \\ B_y \mathbf{C}_{p2} C_e & A_y \end{bmatrix} \tag{6.9}$$

and

$$\mathbf{B}_g = \begin{bmatrix} \mathbf{B}_{p1} C_d & 0 \\ 0 & -B_y \end{bmatrix}, \qquad \mathbf{C}_g = \begin{bmatrix} \mathbf{C}_{p1} & 0 \\ 0 & C_y \end{bmatrix}. \tag{6.10}$$

6.3 Impedance Synthesis Controller Design

As shown in Figure 6.6, an impedance connected to a mechanically coupled electromagnetic transducer can be viewed as parameterising a velocity feedback controller for the mechanical system P. The following section introduces a technique for the synthesis of active impedance controllers designed to minimise structural vibration.

The design objective is to minimise the displacement x_2 whilst restraining both the magnitude of control voltage V_z and the absorber mass travel $x_1 - x_2$. As the reaction force F_e results in an acceleration of the absorber, at low frequencies the magnitude of available force is

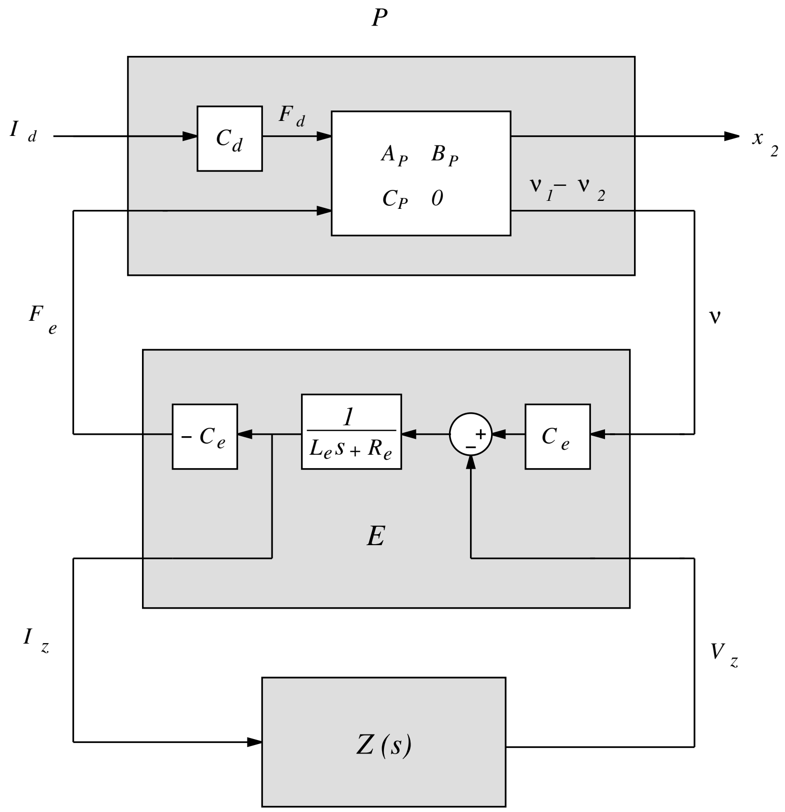

Figure 6.6: Mechanical system P coupled to an impedance shunted electromagnetic transducer E.

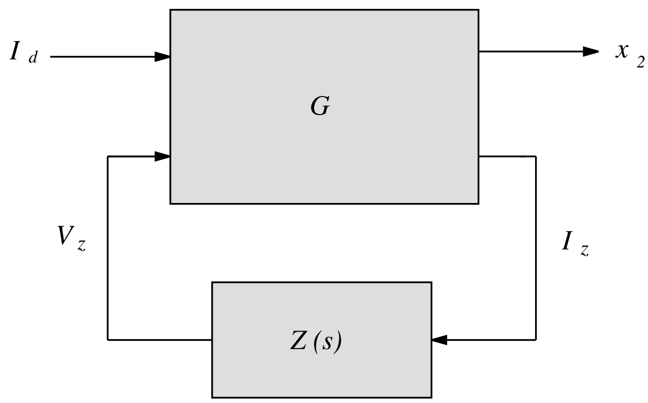

Figure 6.7: Composite system G comprising the mechanical and electromagnetic sub-systems.

strictly limited by the maximum travel $x_1 - x_2$. In a linear quadratic sense, the objective is to minimise

$$J = \int_0^\infty \left\{ x_2^2(t) + k_v V_z^2(t) + k_d \left(x_1(t) - x_2(t)\right)^2 \right\} \, dt, \tag{6.11}$$

where k_v and k_d represent weightings on the applied shunt voltage V_z and the absorber mass travel $x_1 - x_2$. By substituting the state solutions into $x_1(t)$ and $x_2(t)$, the following is obtained

$$J = \int_0^\infty \left\{ \mathbf{x}_p(t)' \mathbf{C}_{p1}' \mathbf{C}_{p1} \mathbf{x}_p(t) + V_z(t)' k_v V_z(t) + \mathbf{x}_p(t)' \mathbf{C}_{p3}' k_d \mathbf{C}_{p3} \mathbf{x}_p(t) \right\} \, dt, \tag{6.12}$$

where $d_1(t) - d_2(t) = \mathbf{C}_{p3} x_p(t)$ and $\mathbf{C}_{p3} = \begin{bmatrix} 0 & -1 & 0 & 1 \end{bmatrix}$. Restated in the standard LQR context,

$$J = \int_0^\infty \left\{ \mathbf{x}_g(t)' \mathbf{Q} \mathbf{x}_g(t) + \mathbf{u}(t)' \mathbf{R} \mathbf{u}(t) \right\} \, dt, \tag{6.13}$$

where

$$\mathbf{Q} = \begin{bmatrix} \mathbf{C}_{p1} & 0 \end{bmatrix}' \begin{bmatrix} \mathbf{C}_{p1} & 0 \end{bmatrix} + k_d \begin{bmatrix} \mathbf{C}_{p3} & 0 \end{bmatrix}' \begin{bmatrix} \mathbf{C}_{p3} & 0 \end{bmatrix} \tag{6.14}$$

and

$$\mathbf{R} = k_v. \tag{6.15}$$

Through the solution of an algebraic Ricatti equation [98], a state feedback matrix K can be found that minimises the objective function J.

6.3.1 Observer Design

As the state variables of the system $\mathbf{x}_g(t)$ are not directly available, a linear observer is required.

For impedance design, the *ad hoc* pole-placement approach to linear observer design becomes difficult. Although an LQR state-feedback regulator is guaranteed (if $\mathbf{R}$ is the chosen diagonal) to result in a phase margin of at least 60 degrees at each plant input channel [69, 94], it is well known that considerable degradation of the stability-margins is to be expected after inclusion of the observer dynamics.

A more automated choice in observer design is the Kalman filter [17, 68]. Here, as shown in Figure 6.8, the controller $K(s)$ consists of an optimal state-feedback regulator K and Kalman observer O. By the Certainty Equivalence Principle or Separation Theorem [98], the two entities can be designed independently. After first finding K to minimise (6.13), a

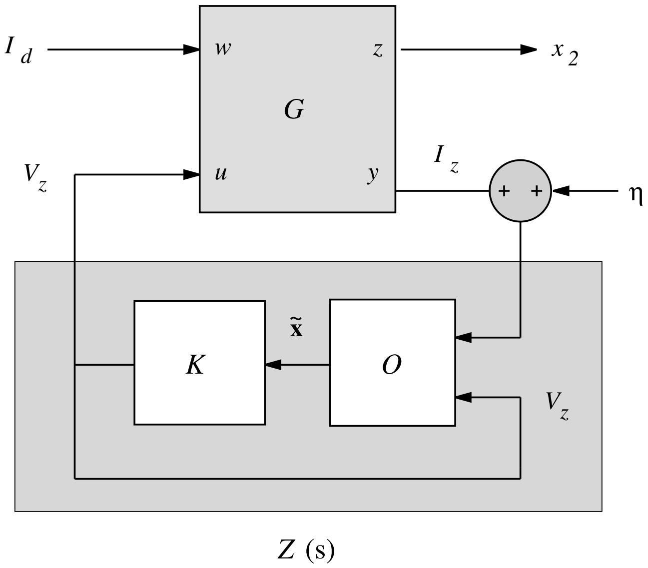

Figure 6.8: Composite plant G controlled by $Z(s)$ with an impedance consisting of the optimal state-feedback regulator K and Kalman filter O.

Kalman filter is then designed to minimize

$$J_k = \lim_{t\to\infty} E\left\{[\mathbf{x}(t) - \tilde{\mathbf{x}}(t)]\,[\mathbf{x}(t) - \tilde{\mathbf{x}}(t)]'\right\}. \tag{6.16}$$

By the Certainty Equivalence Principle, the optimal K and O also result in minimisation of the stochastic performance objective

$$J = E\left\{\lim_{T\to\infty} \frac{1}{T}\int_0^T \left\{\mathbf{x}'(t)\mathbf{Q}\mathbf{x}(t) + \mathbf{u}(t)'\mathbf{R}\mathbf{u}(t)\right\}\, dt\right\}. \tag{6.17}$$

In this scenario, the original state-space system (6.8) is referred to with zero-mean uncorrelated Gaussian process models for the disturbance I_d and additive measurement noise η. With the inclusion of measurement noise, the system representation (6.8) becomes

$$\begin{aligned} \dot{\mathbf{x}}_g(t) &= \mathbf{A}_g\mathbf{x}_g(t) + \mathbf{B}_g \begin{bmatrix} I_d(t) \\ V_z(t) \end{bmatrix} \\ \begin{bmatrix} x_2(t) \\ I_z(t) \end{bmatrix} &= \mathbf{C}_g\mathbf{x}_g(t) + \begin{bmatrix} 0 \\ \eta \end{bmatrix}, \end{aligned} \tag{6.18}$$

where I_d and η satisfy

$$\begin{aligned} E\left\{I_d I_d'\right\} &= \mathbf{Q}_n \\ E\left\{\eta\eta'\right\} &= \mathbf{R}_n. \end{aligned} \tag{6.19}$$

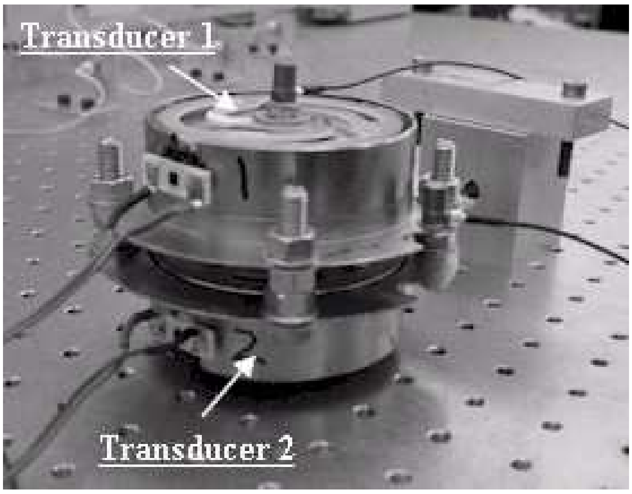

Figure 6.9: Proof-mass experimental apparatus.

Based on $\mathbf{Q}_n$ and $\mathbf{R}_n$, a Kalman observer that minimises (6.16) can be found through the solution of an algebraic Ricatti equation [98]. The ratio of $\mathbf{Q}_n$ to $\mathbf{R}_n$ essentially represents the confidence in the measured variable I_z and plant model G. In this work, $\mathbf{Q}_n$, $\mathbf{R}_n$ and $\mathbf{k}_u$ are not quantified and simply treated as design parameters influencing the closed-loop pole locations, damping performance and closed-loop stability.

6.4 Experimental Verification

To verify the modelling and design techniques presented in the preceding sections, each method has been applied to an experimental electromechanical system.

6.4.1 Proof-Mass Inertial Experimental Apparatus

A photograph of the experimental apparatus shows the rigid body, flexible end supports, mounting plate and coils as provided in Figure 6.9. Observe in Figure 6.10 that the apparatus comprises two identical Jaycar Electronics[1] subsonic transducers Cat. XC-1008. While the lower magnet and flexures are fixed, the two connected transducer cases are free to vibrate and represent the mass m_2. The upper magnet forms the absorber mass m_1. The physical parameters of the electromagnetic and mechanical systems are summarised in Table 6.1.

[1] www.jaycar.com.au

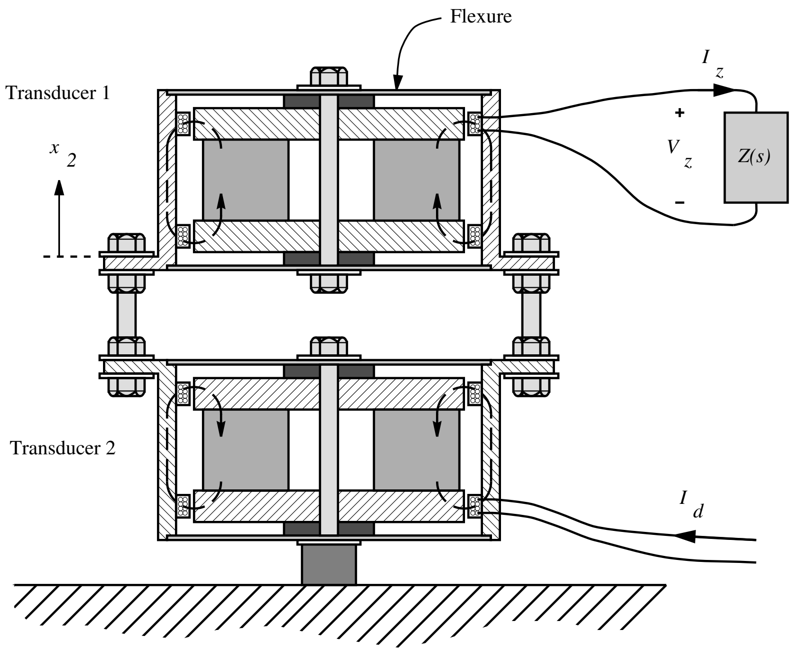

Figure 6.10: Cross-section of the experimental apparatus shown in Figure 6.9.

The main mass displacement x_2 is measured using a PSV-300 Polytec Scanning Laser Vibrometer.

6.4.2 Impedance Synthesis

Using the same procedure, as discussed in Section 4.5.3, the gain associated with Figure 6.11 can be found in Table 6.2. The desired shunt impedance presented to the transducer by the synthetic impedance, described in Section 4.5.2, is

$$Z(s) = \frac{V_z(s)}{I_z(s)} = a_3 C(s) a_4. \tag{6.20}$$

The magnitude and phase frequency responses are shown in Figures 6.12 and 6.13. In the frequency domain there is a good correlation between the model and measured data.

Parameter	Symbol	Unit
Spring constant	k_1	$28.03\ kNm^{-1}$
Damping coefficient	b_1	$1.500\ Nsm^{-1}$
Absorber mass	m_1	$0.340\ Kg$
Spring constant	k_2	$31.14\ kNm^{-1}$
Damping coefficient	b_2	$3.582\ Nsm^{-1}$
Absorber mass	m_2	$0.593\ Kg$
Coil inductance	L_e	$41\ mH$
Coil resistance	R_e	$2.315\ \Omega$
Electromagnetic coupling	C_e	3.408
Electromagnetic coupling	C_d	-6.714

Table 6.1: Electromechanical system parameters.

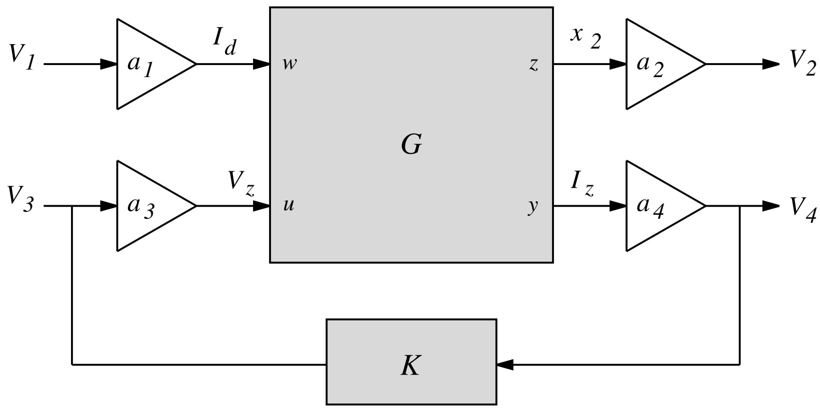

Figure 6.11: External gains associated with the electromechanical system.

Gain	Unit
a_1	$1.006\ A/V$
a_2	$1\ V/m$
a_3	$-1.012\ V/V$
a_4	-10.01 V/A

Table 6.2: External gains associated with the experimental system.

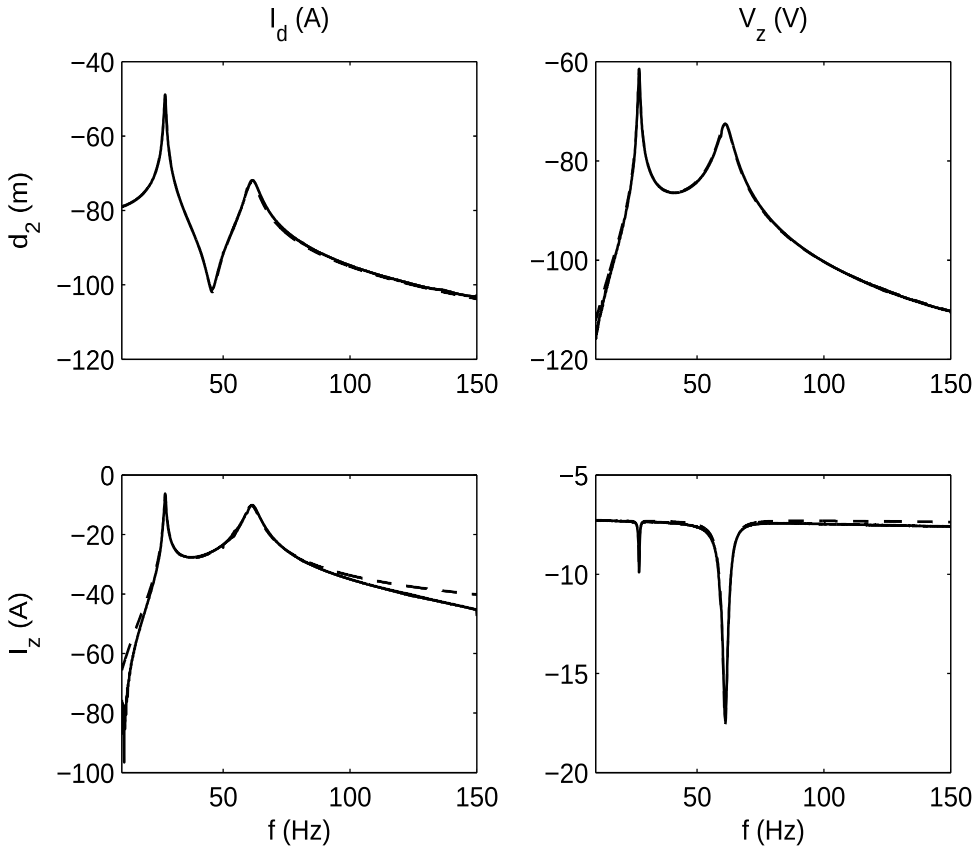

Figure 6.12: Simulated (—) and experimental (− −) magnitude frequency response (in dB).

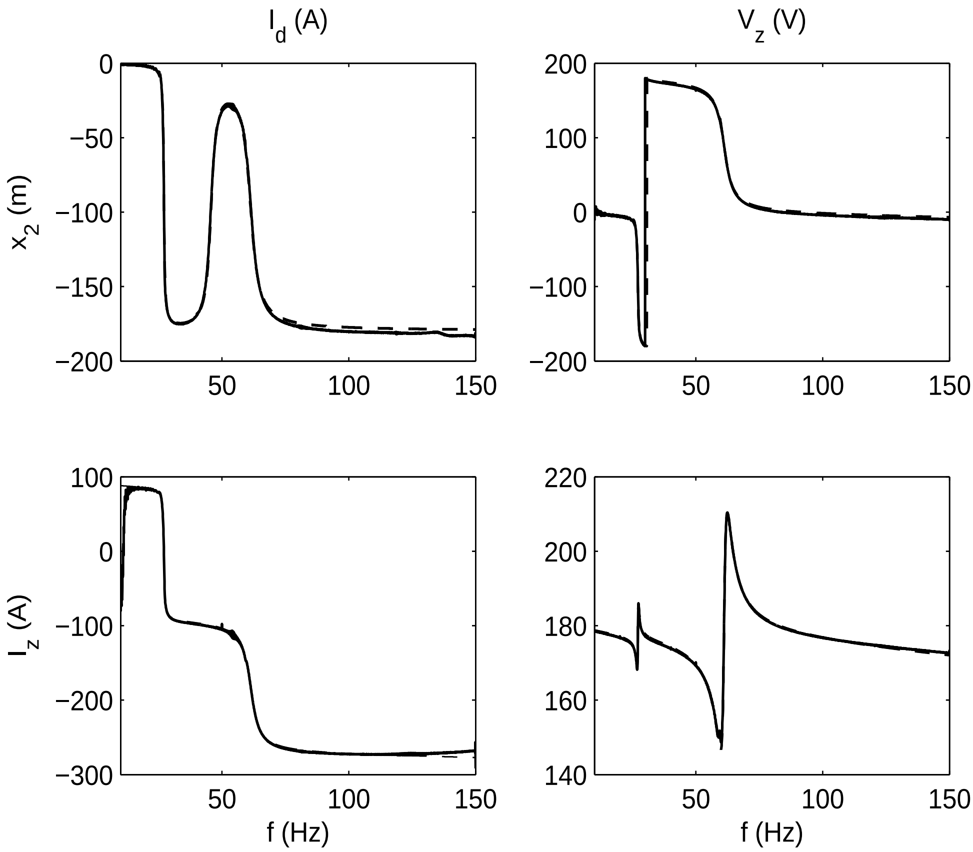

Figure 6.13: Simulated (—) and experimental (− −) phase frequency response (in degrees).

***LQR* Impedance Synthesis**

As discussed previously in Section 6.3, a LQR controller can be designed to command the shunt voltage V_z by minimising vibration x_2. That is, LQR gain matrix was constructed to minimise the following performance function

$$J = \int_{-\infty}^{\infty} \left\{ x_2^2(t) + k_v V_z^2(t) + k_d \left(x_1(t) - x_2(t)\right)^2 \right\} \, dt, \tag{6.21}$$

where the factor $k_d = 1$ and $k_v = 1 \times 10^{-7}$. A Kalman observer was created to estimate the system state $x_g(t)$ utilising the measured shunt transducer current I_z and control signal V_z. Referring to Section 6.3.1, the disturbance and output noise process covariance matrices, $\mathbf{Q}_n$ and $\mathbf{R}_n$ were chosen to be 100 and 0.1 respectively. Such a weighting, although not quantitative, expresses a moderate confidence in the fidelity of the measured variable I_z.

By concatenating the LQR gain matrix and Kalman observer and compensating for the system gains a_3 and a_4, the actual impedance presented to the shunt transducer can be determined. In Figure 6.15, the complex impedance of the resulting controller is plotted together with that of the negative coil impedance i.e. negative inductor-resistor. The LQG impedance has a tendency to mimic this impedance over a certain frequency range. The pole-zero map of the LQG controller is shown in Figure 6.14.

After examining the open-loop and closed-loop pole locations shown in Figure 6.16, it can be appreciated that the controller is clearly acting to increase the system damping. Corresponding mitigation of the transfer function from an applied disturbance to the measured vibration can be seen in both the frequency domain, Figure 6.17, and time domain, Figure 6.18. The action of the additional mass and electromagnetic shunt reduces the single-mass resonant peak by a minimum of 23.2 dB. The shunted electromagnetic transducer reduces the two-mass first and second resonant peaks by 18.7 and 23.6 dB respectively.

Note the additional dynamics at 20 and 60 Hz in Figure 6.17. These dynamics are due to pivot modes of the structure about the base fixture. The stiffening effect of the controller has a tendency to increase the frequency of low-profile pivot and sway modes. Such modes would be absent in a more rigidly supported inertial drive.

6.5 Discussions

A technique has been presented for the control of vibration using an electromagnetically actuated inertial drive. By viewing the coil current and voltage as system inputs and outputs,

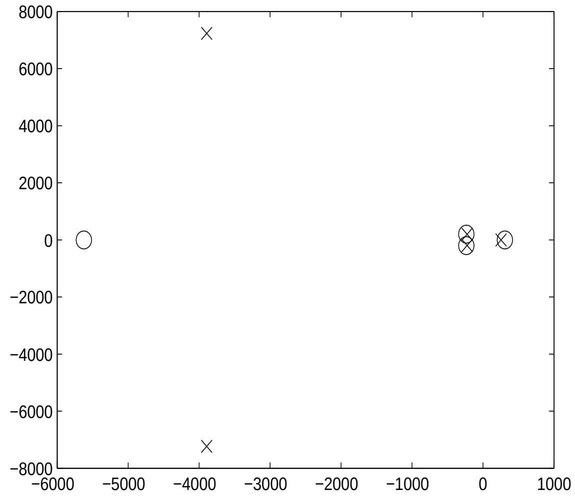

Figure 6.14: Poles ($\times$) and zeros ($\bigcirc$) of the *LQG* impedance.

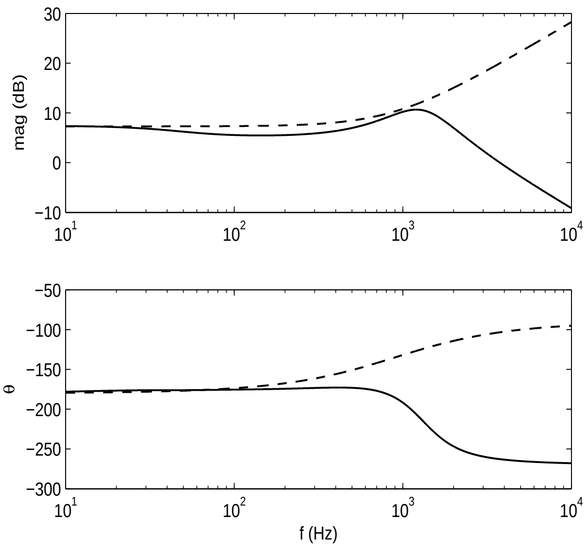

Figure 6.15: Magnitude and phase responses of the *LQG* impedance (—) and negative coil impedance ($--$).

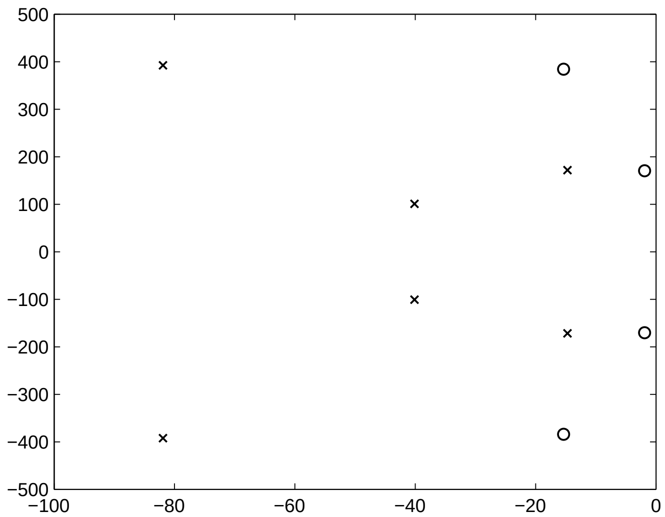

Figure 6.16: Open-loop (◯) and closed-loop (×) pole locations. Note that one pair of high-frequency observer poles are not visible within the scope of this plot.

standard synthesis techniques were applied to minimise displacement subject to a penalty on the inertial mass travel and applied terminal voltage. Electromagnetic shunt control requires no sensors, thus significantly reduces the cost and complexity.

Experiments were performed on a simple apparatus representing a scenario where the vibration experienced by a host structure is controlled with a suspended absorber mass and electromagnetic coil. In practice, the mass of the absorber is usually limited to about one tenth the host structure. In this regard, the experiment is somewhat unrealistic as the mass of the absorber is only slightly less than that of the host mass. The available control authority is directly related to both the size of the mass and the available travel.

After adding the absorber mass, the passive dynamics split the original resonant mode into two lightly damped secondary peaks. By then designing a suitable control impedance and presenting it to the terminals of the electromagnetic coil, further vibration reduction is achieved by augmenting the passive damping of the secondary modes. As the control design penalises the absorber mass travel, which increases at low frequencies, the impedance suppresses higher frequency vibration more heavily. The combination of passive and active dynamics reduces the displacement response to a force input by up to 38 dB at the frequency of the original resonance.

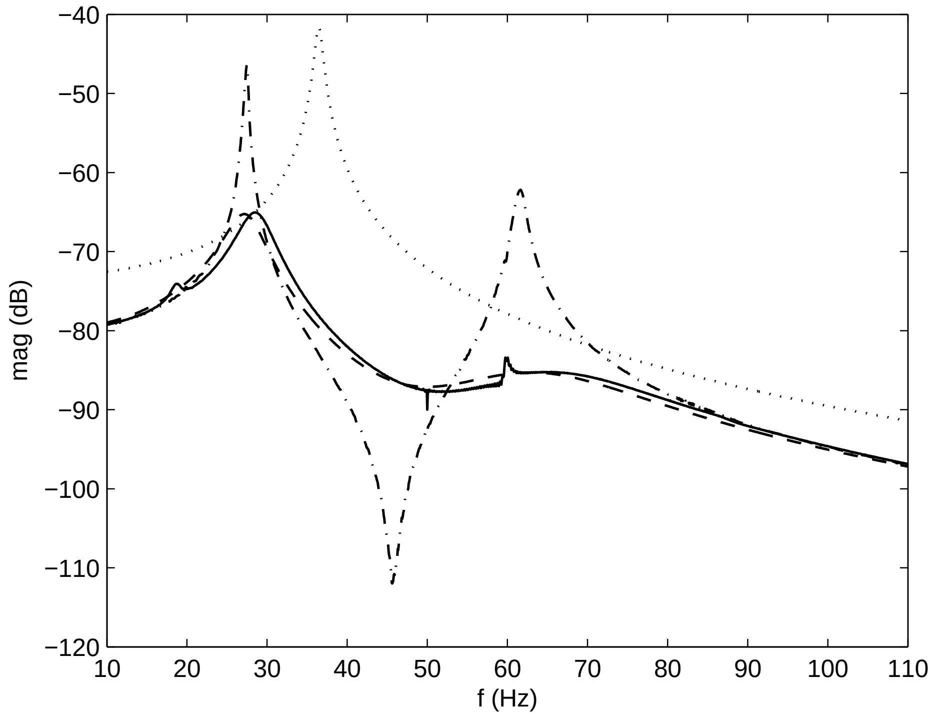

Figure 6.17: Single-mass $(\cdots)$, two-mass $(- \cdot -)$, experimental closed-loop (—), and simulated closed-loop $(--)$ magnitude frequency response $\frac{x_2(s)}{I_d(s)}$.

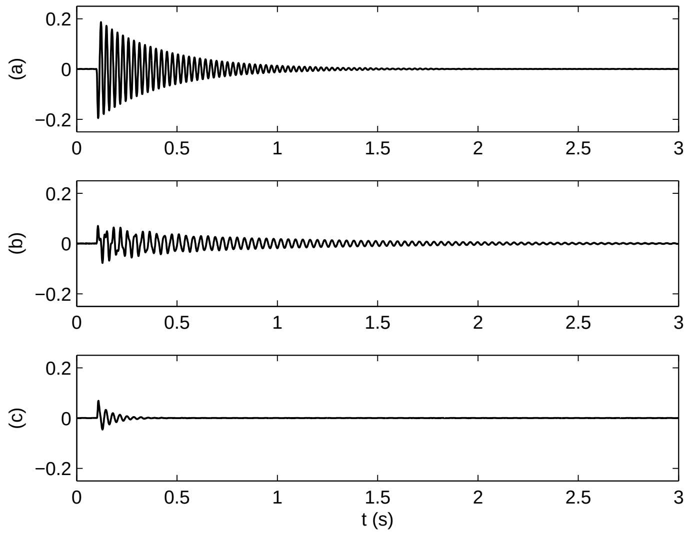

Figure 6.18: Single-mass (a), two-mass (b) and shunted two-mass (c) velocity responses to a 1 Amp step in I_d.

Suggested opportunities includes multi-drive multi-dimensional systems and restricted active controller designs. The active impedance design contains negative reactive components and is unstable in a theoretical control systems sense. Although, the connection of the electromagentic transducer coil and control impedance is stable, an inherently stable effective controller is more desirable. It is presently unclear if an unstable effective controller is necessary to result in useful vibration control.

The overall objectives of this chapter were successfully fulfilled through theoretical and experimental verification.

Chapter 7

Conclusions

The goal of this thesis was to develop new vibration control strategies by improving upon existing techniques. This goal was achieved by the development of new piezoelectric shunt controllers. Additionally, a new class of electromagnetic shunt controllers were also developed.

The following summarises the presented work, chapter by chapter, and gives suggestions for future research opportunities. Detailed discussions can be found at the end of each chapter.

Part I of the thesis focused on piezoelectric shunt control and consists of two unique chapters, Chapters 2 and 3. Electromagnetic shunt control was presented in Part II and consists of three chapters, Chapters 4, 5 and 6.

Chapter 2 introduces the piezoelectric effect, and a method for modelling the dynamics of a piezoelectric transducer and piezoelectric shunted damped system. A review of current piezoelectric shunt damping techniques and their associated limitations were then discussed. The synthetic impedance was reiterated as a solution to overcoming these limitations. Using the synthetic impedance and developed models, four distinct piezoelectric shunt controllers were proposed and validated on three different experimental apparatuses.

Chapter 3 was concerned with the problem of multi-mode shunt damping of structural vibrations using several piezoelectric transducers. Knowledge gained from Chapter 2, showed that the problem can be cast as a multivariable feedback control problem whereby the effective controller was parameterised by multi-port impedance. Multi-port impedance was then developed and validated on a piezoelectric laminated structure using multiple synthetic impedances.

Chapter 4 introduced electromagnetic transducers and a method for modelling the dynamics of the transducer. Through experience gained in Part I, by attaching an electromagnetic transducer to a mechanical structure and shunting the transducer with electrical impedance, vibration could be controlled. This new vibration control technique was referred to as electromagnetic shunt damping. Although the underlying dynamics of this technique was different, compared to that of the piezoelectric shunt damping, the resulting feedback control structure or model was found to remarkably similar. Using the developed feedback model three novel controllers were developed; capacitor-resistor, negative inductor-resistor and impedance synthesis. The proposed controllers and feedback model were then validated experimentally on a simple electromagnetic mass-spring-damper apparatus.

Chapter 5 extends concepts developed in Chapter 4 to a more complicated system: electromagnetic shunt control. A model was developed for the electromagnetic shunt control system and three controllers were designed to satisfy two performance objectives. The first performance objective was to provide damping at the resonance and the second was to maintain high frequency attenuation. The proposed controllers were successfully applied theoretically and experimentally to an isolation apparatus. Controllers included capacitor-resister, ideal (derivative of a negative inductor-resistor) and impedance synthesis.

Chapter 6 combined the mechanical systems, damped and isolation, and knowledge gained from Chapters 4 and 5; the proof-mass inertial vibration control was developed. A model was then derived and validated for the experimental proof-mass inertial apparatus. Using the model an impedance synthesis controller was then developed and verified experimentally to satisfy the required performance objectives.

The knowledge gained from the above chapters, has lead to many open-ended questions. When confronted with the two various shunt control strategies, that is, piezoelectric or electromagnetic shunt control, the obvious question comes to mind: "Should piezoelectric or electromagnetic shunt control be used?" The answer to this question depends on the application. For example, a car suspension system requires relatively large displacements, say in the order of ± 100 mm, then an electromagnetic shunt control is chosen due to the stroke of the electromagnetic transducer. On the other hand, a nano-positioning system requires ± 10 μm displacements, and then a piezoelectric shunt control is chosen.

Other questions that may also arise: "Which is the easiest shunt controller to implement?" and "Which shunt controller provides the best performance?" Although, there is of course no fundamental answer to either of these questions, some important observations were found throughout the thesis. For instance, all of the shunt controllers tend to resemble the complex impedance of an ideal negative transducer dynamics over some frequency band. Correspondingly, the impedance synthesis controllers tend to be of a higher bandwidth, and therefore, more difficult to implement. It is recommended using synthetic impedance, to synthesise the required controllers.

Suggested work for shunt control involves both the exploration of more advanced applications and development of the control theory associated with the synthesis techniques, i.e. LQG, $\mathcal{H}_2$, or $\mathcal{H}_\infty$. Additionally, the author stresses a high priority for the inclusion of model uncertainty in the mechanical plant when considering shunt controllers to achieve improved robustness and stability while maintaining acceptable performance objectives.

Bibliography

[1] *IEEE Standard on Piezoelectricity.* ANSI/IEEE standard 176-1987, 1987.

[2] S. Acrabelli and A. Tonoli. System properties of flexible structures with self-sensing piezoelectric transducers. *Journal of Sound and Vibration*, 235(1):1–23, 2000.

[3] H. J. M. T. A. Adriaens, W. L. de Koning and R. Banning. Modelling piezoelectric actuators. *IEEE/ASME Transactions on Mechatronics*, 5(4):331–341, December 2000.

[4] T. E. Alberts and J. A. Colvin. Observations on the nature of transfer functions for control of piezoelectric laminates. *Journal of Intelligent Material Systems and Structures*, 8(5):605–611, 1991.

[5] J. B. Aldrich, N. W. Hagood, A. von Flotow and D. W. Vos. Design of passive piezoelectric shunt damping for space structures. In *Proc. SPIE Conference of Smart Structures and Intelligent Systems, SPIE Vol. 1917*, pages 629–705, 1993.

[6] R. Amirtharajah and A. P. Chandrakasan. Self-powered signal processing using vibration-based power generation. *IEEE Journal of Solid-State Circuits*, 33(5):687–695, May 1998.

[7] E. H. Anderson, N. W. Hagood and J. M. Goodliffe. Self-sensing piezoelectric actuation: Analysis and application to controlled structures. In *Proc. AIAA/ASME/ASCE/AHS/ASC Structures, Structural Dynamics and Materials*, pages 2141–2155, 1992.

[8] M. J. Balas. Active control of flexible systems. *Journal of Optimization Theory and Applications*, 25(3):415–436, 1978.

[9] M. J. Balas. Feedback control of flexible systems. *IEEE Transactions on Automatic Control*, AC-23(4), 1978.

[10] S. Behrens. Passive and semi-active control of piezoelectric laminates. Master's thesis, Department of Electrical and Computer Engineering, The University of Newcastle, Australia, 2000.

[11] S. Behrens, A. J. Fleming and S. O. R. Moheimani. A broadband controller for piezoelectric shunt damping of structural vibration. *IOP Smart Materials and Structures*, 12:18–28, January 2003.

[12] S. Behrens and S. O. R. Moheimani. Optimal resistive elements for multiple mode shunt-damping of a piezoelectric laminated beam. In *Proc. IEEE Conference on Decision and Control*, pages 4018–4023, Sydney, Australia, December 2001.

[13] S. Behrens, A. J. Fleming and S. O. R. Moheimani. Series-parallel Impedance Structure for Piezoelectric Vibration Damping. In *Proc. SPIE Smart Materials II: Nano-, and Micro Smart Systems, Volume No. 4934*, pages 12–22, Melbourne, Victoria, Australia, December 2002.

[14] S. Behrens, S. O. R. Moheimani and A. J. Fleming. Multiple mode current flowing passive piezoelectric shunt controller. *Journal of Sound and Vibration*, 266(5):929–942, October 2003.

[15] S. Behrens, S. O. R. Moheimani and A. J. Fleming. Multiple mode passive piezoelectric shunt dampener. In *Proc. IFAC Mechatronics 2002*, Berkerley, California, USA, December 2002.

[16] E. Bianchini, R. Spangler and C. Andrus. The use of piezoelectric devices to control snowboard vibrations. In *Proc. SPIE Smart Structures and Materials: Smart Structures and Integrated Systems, SPIE Vol. 3329*, pages 106–114, 1998.

[17] R. G. Brown and P.Y.C. Hwang. *Introduction to Random Signals and Applied Kalman Filtering*. John Wiley and Sons Inc., 1997.

[18] J. R. Carstens. *Electrical Sensors and Transducers*. Prentice-Hall, 1993.

[19] C. Choi and K. Park. Self-sensing magnetic levitation using LC resonant circuits. *Sensors and Actuators*, pages 1276–1281, 1999.

[20] J. W. Choi, Y. B. Seo, W. S. Yoo and M. H. Lee, "LQR approach using eignstructure assignment with an active suspension control application," in *Proc. IEEE International Conference on Control Applications*, pages 1235–1239, Trieste, Italy, September 1998.

[21] R. L. Clark and K. D. Frampton. Phase compensation for feedback control of enclosed sound fields. *Journal of Sound and Vibration*, 195(5):701–718, 1996.

[22] R. L. Clark, W. R. Saunders and G. P. Gibbs. *Adaptive Structures: Dynamics and Control*. John Wiley and Sons Inc., 1998.

[23] W. W. Clark. Vibration control with state-switched piezoelectric materials. *Journal of Intelligent Material Systems and Structures*, 11:263–271, April 2000.

[24] D. G. Cole and R. L. Clark. Adaptive compensation of piezoelectric sensori-actuators. *Journal of Intelligent Material Systems and Structures*, 5:665–672, 1994.

[25] R. D. Cook. *Finite Element Modelling for Stress Analysis*. John Wiley and Sons Inc., 1995.

[26] L. R. Corr and W. W. Clark. Comparison of low-frequency piezoelectric switching shunt techniques for structural damping. *IOP Smart Materials and Structures*, 11:370–376, 2002.

[27] D. Croft, G. Shedd and S. Devasia. Creep, hysteresis and vibration compensation for piezoactuators: Atomic force microscopy application. In *Proc. American Control Conference*, pages 2123–2128, Chicago, Illinois, USA, June 2000.

[28] CSA Engineering Inc., *http://www.csaengineering.com*, 2003.

[29] C. L. Davis and G. A. Lesieutre. An actively tuned solid-state vibration absorber using capacitive shunting of piezoelectric stiffness. *Journal of Sound and Vibration*, 232(3):601–617, 2000.

[30] K. K. Denoyer, S. F. Griffin and D. Sciulli. Hybrid structural/acoustic control of a subscale payload fairing. In *Proc. SPIE Smart Structures and Materials: Smart Structures and Integrated Systems, SPIE Vol. 3329*, pages 237–243, 1998.

[31] J. J. Dosch, D. J. Inman and E. Garcia. A self-sensing piezoelectric actuator for collocated control. *Journal of Intelligent Material Systems and Structures*, 3:166–185, January 1992.

[32] *Large Shaker Model No. V53-64/DSA4*. Gearing and Watson Electronics Ltd., http://www.gearing-watson.com.

[33] D. J. Ewins. Modal testing as an aid to vibration analysis. In *Proc. Conference on Mechanical Engineering*, May 1990.

[34] Ronald L. Fante. *Signal Analysis and Estimation. An Introduction.* John Wiley and Sons Inc., 1988.

[35] A. J. Fleming, S. Behrens and S. O. R. Moheimani. Optimization and implementation of multi-mode piezoelectric shunt damping systems. *IEEE/ASME Transactions on Mechatronics*, 7(1):87–94, March 2002.

[36] A. J. Fleming, S. Behrens and S. O. R. Moheimani. Synthetic impedance for implementation of piezoelectric shunt damping circuits. *Electronics Letters*, 36(18):1525–1526, 2000.

[37] A. J. Fleming, S. Behrens and S. O. R. Moheimani. Active LQR and H_2 shunt control of electromagnetic transducers. In *Proc. IEEE Conference on Decision and Control 2003*, Maui, Hawaii, December 2003.

[38] A. J. Fleming and S. O. R. Moheimani. Adaptive piezoelectric shunt damping. *IOP Smart Materials and Structures*, 12:36–48, January 2003.

[39] A. J. Fleming and S. O. R. Moheimani. Control orientated synthesis of high performance piezoelectric shunt impedances for structural vibration control. *IEEE Transactions on Control Systems Technology*, 13(5):98–112, January 2005.

[40] A. J. Fleming and S. O. R. Moheimani. Improved current and charge amplifiers for driving piezoelectric loads, and issues in signal processing design for synthesis of shunt damping circuits. *Journal of Intelligent Material Systems and Structures.*, 15(2):77–92, January 2005.

[41] R. L. Forward. Electronic damping of vibrations in optical structures. *Applied Optics*, 18(5):690–697, March 1979.

[42] T. Fukao, A. Yamawaki and N. Adachi, Nonlinear and $\mathcal{H}_\infty$ control of active suspension systems with hydraulic actuators. In *Proc. IEEE Conference on Decision and Control*, pages 5125–5128, Phoenix, Arizona, USA, December 1999.

[43] C. R. Fuller, S. J. Elliott and P. A. Nelson. *Active Control of Vibration.* Academic Press, 1996.

[44] P. Gao, Y. Lou and K. Okada. Detection and suppression for mechanical resonance in hard disk drives with built-in piezoelectric sensors. In *Proc. SPIE Smart Structures and Materials: Smart Sensor Technology and Measurement Systems, SPIE Vol. 4694*, pages 78–85, 2002.

[45] E. Garcia, J. D. Dosch and D. J. Inman. Vibration attenuation in an active antenna structure. In *Proc. Conference on Recent Advances in Active Control of Sound and Vibration*, pages S35–S42, Virginia Polytechnique Institute and State University, Blacksburg, VA USA, April 15-17 1991.

[46] E. Garcia, D. J. Inman and J. D. Dosch. Vibration suppression using smart structures. In *Proc. SPIE Smart Structures and Materials*, pages 167–172, 1991.

[47] T. D. Gillespie, *Fundamentals of Vehicle Dynamics.* Society of Automotive Engineers, 1992.

[48] N. W. Hagood and A. Von Flotow. Damping of structural vibrations with piezoelectric materials and passive electrical networks. *Journal of Sound and Vibration*, 146(2):243–268, 1991.

[49] N. W. Hagood, W. H. Chung and A. von Flotow. Modelling of piezoelectric actuator dynamics for active structural control. *Journal of Intelligent Material Systems and Structures*, 1:327–354, 1990.

[50] N. W. Hagood and E. F. Crawley. Experimental investigation of passive enhancement of damping for space structures. *Journal of Guidance, Control and Dynamics*, 14(6):1100–1109, 1991.

[51] D. J. Inman. *Engineering Vibrations.* Prentice Hall, 2nd edition, 2000. ISBN: 013726142X.

[52] D. Halim and S. O. R. Moheimani. Spatial resonant control of flexible structures - application to a piezoelectric laminate beam. *IEEE Transactions on Control Systems Technology*, 9(1):37–53, January 2001.

[53] B. M. Hanson, M. D. Brown and J. Fisher. Self sensing; closed-loop estimation for a linear electromagnetic actuator. In *Proc. IEEE American Control Conference*, pages 1650–1655, Arlington, VA USA, June 2001.

[54] Head Inc., *http://www.head.com*, 2003.

[55] J. Heng, J. C. Akers, R. Venugopal, M. Lee, A. G. Sparks, P. D. Washabaugh and D. Bernstien. Modelling, identification, and feedback control of noise in an acoustic duct. *IEEE Transactions on Control Systems Technology*, 4(3):283–291, 1996.

[56] J. J. Hollkamp. Multimodal passive vibration suppression with piezoelectric materials and resonant shunts. *Journal of Intelligent Materials Systems and Structures*, 5:49–56, 1994.

[57] J. J. Hollkamp and T. F. Jr. Starchville. A self-tuning piezoelectric vibration absorber. *Journal of Intelligent Materials Systems and Structures*, 5:559–65, 1994.

[58] M. A. Hopkins, D. A. Henderson, R. W. Moses, T. Ryall, D. G. Zimcik and R. L. Spangler. Active vibration-suppression systems applied to twin-tail buffeting. In *Proc. SPIE Smart Structures and Materials: Industrial and Commercial Applications of Smart Structures Technologies, SPIE Vol. 3326*, pages 27–33, 1998.

[59] P. Horowitz and W. Hill. *The Art of Electronics.* Cambridge University Press, 1980.

[60] P. C. Hughes. Space structure vibration modes: how many exist? Which ones are important? *IEEE Control Systems Magazine*, pages 22–28, February 1987.

[61] S. Ikenaga, F. L. Lewis, J. Campos and L. Davis, Active suspension conrol of ground vehicle based on a full-vehicle model. In *Proc. IEEE American Control Conference*, pages 4019–4024, Chicago, Illinois, USA, June 2000.

[62] B. Jaffe, W. R. Cook and H. Jaffe. *Piezoelectric Ceramics.* Academic Press, 1971.

[63] H. Janocha. Actuators in adaptronics. In B. Clephas, editor, *Adaptronics and Smart Structures*, Chapter 6. Springer, 1999.

[64] H. Janocha. *Adaptronics and Smart Structures - Basics, Material, Design, and Applications.* Springer, 1999.

[65] D. S. Joo, N. Al-Holou, J. M. Weaver, Lahdhiri and F. Al-Abbas, Nonlinear modelling of vehicle suspenesion systems. In *Proc. IEEE American Control Conference*, pages 115–118, Chicago, Illinois, USA, June 2000.

[66] S. M. Joshi and S. Gupta. On a class of marginally stable positive-real systems. *IEEE Transactions on Automatic Control*, 41(1):152–155, January 1996.

[67] K2 Inc., *http://www.k2inc.net*, 2003.

[68] T. Kailath. *Linear Systems.* Prentice-Hall, Upper Saddle River, NJ USA, 1980.

[69] R. Kalman. When is a linear control system optimal. *Journal of Basic Engineering - Transaction on ASME - Series D*, 86:51–60, 1964.

[70] H. K. Khalil. *Nonlinear Systems* 2nd Edition. Printice-Hall, Englewood Cliffs NJ, 1996.

[71] J. Kim, J. Choi and R. H. Cabell. Noise reduction performance of smart panels incorporating piezoelectric shunt damping. In *Proc. SPIE Smart Structures and Materials: Industrial and Commercial Applications of Smart Structures Technologies, SPIE Vol. 4698*, pages 143–149, 2002.

[72] S. Kim, C. Han and C. Yun. Improvement of aeroelastic stability of hingeless helicopter rotor blade by passive piezoelectric damping. In *Proc. SPIE Smart Structures and Materials: Passive Damping and Isolation, SPIE Vol 3672*, pages 131–141, Newport Beach, California, USA, March 1999.

[73] Y. B. Kim, W. G. Hwang, C. D. Kee and H. B. Yi. Active vibration control of suspension system using an electromagnetic damper. In *Proc. Of the Int. MECH Eng. Part D Journal of Automoblie Engineering,* Professional Engineering Publishing, Vol. 8, pages 865–873, 2001.

[74] S. A. Lane and R. L. Clark. Improving loudspeaker performance for active noise control. *Journal of the Audio Engineering Society*, 46(6):508–519, June 1998.

[75] K. B. Lazarus and E. F. Crawley. Multivariable active lifting surface control using strain actuation: analytical and experimental results. In *Proc. 3rd International Conference on Adaptive Structures*, pages 87–101, San Diego, California USA, 1992.

[76] Y. Lim, V. V. Varadan and V. K. Varadan. Closed-loop finite element modelling of active/passive damping in structural vibration control. In *Proc. SPIE Smart Materials and Structures 1997: Mathematics and Control in Smart Structures, SPIE Vol. 3039*, San Diego, California, USA, March 1997.

[77] L. Ljung. *System Identification: Theory for the User.* Prentice Hall, 1999.

[78] D. G. MacMartin. Collocated structural control: motivation and methodology. In *Proc. IEEE International Conference on Control Applications*, pages 1092–1097, Albany, New York, USA, September 1995.

[79] T. McKelvey, H. Akcay and L. Ljung. Subspace based multivariable system identification from frequency response data. *IEEE Transactions on Automatic Control*, 41(7):960–978, July 1996.

[80] T. McKelvey, A. J. Fleming and S. O. R. Moheimani. Subspace based system identification for an acoustic enclosure. *ASME Journal of Vibration and Acoustics*, 124(3):414–419, July 2002.

[81] T. McKelvy and L. Ljung. Frequency domain maximum likelihood identification. In *Proc. IFAC Symposium on System Identification*, pages 1741–1746, Fukuoda, Japan, July 1997.

[82] L. Meirovitch. *Elements of Vibration Analysis*, 2nd edition. McGraw-Hill, Sydney, Australia, 1996.

[83] S. Mirzaei, S. M. Saghaiannejad, V. Tahani and M. Moallem. Electromagnetic shock absorber. In *IEEE International Conference on Electric Machines and Drives Conference IEMDC 2001*, pages 760–764, 2001.

[84] S. O. R. Moheimani, A. J. Fleming, and S. Behrens. On the feedback structure of wideband piezoelectric shunt damping systems. *IOP Smart Materials and Structures*, 12:49–56, January 2003.

[85] S. O. R. Moheimani, S. Behrens and A. J. Fleming. Dynamics and stability of wideband vibration absorbers with multiple piezoelectric transducers. In *IFAC Mechatronics*, Berkeley, California, USA, December 9-11, 2002.

[86] M. Morari and E. Zafiriou. *Robust Process Control*. Prentice Hall, 1989.

[87] N. Morse, R. Smith, B. Paden and J. Antaki. Position sensed and self-sensing magnetic bearing configuations and associated robustness limitations. In *Proc. IEEE Conference on Decision and Control*, pages 2599–2604, Tampa, Florida, USA, December 1998.

[88] A. J. Moulson and J. M. Herbert. *Electroceramics: Materials, Properties, Applications*. London: Chapman and Hall, 1990.

[89] D. Niederberger, M. Morari and S. Pietrsko. Adaptive resonant shunted piezoelectric devices for vibration supression. In *Proc. SPIE Smart Structures and Materials - Damping and Isolation*, San Diego, California, USA, March 2003.

[90] C. Niezrecki and H. H. Cudney. Feasibility to control launch vehicle internal acoustics using piezoelectric actuators. *Journal of Intelligent Material Systems and Structures*, 12:647–660, September 2001.

[91] S. S. Rao. *Mechanical Vibrations*. Addison-Wesley Publishing Company, 3rd edition, 1995.

[92] C. Richard, D. Guyomar, D. Audigier and H. Bassaler. Enhanced semi-passive damping using continuous switching of a piezoelectric devices on an inductor. In *Proc. SPIE Smart Structures and Materials, Damping and Isolation, SPIE Vol. 3989*, pages 288–299, Newport Beach, California, USA, March 2000.

[93] R. H. S. Riordan. Simulated inductors using differential amplifiers. *IEE Electronics Letters*, 3(2):50–51, 1967.

[94] M. G. Safonov and M. Athans. Gain and phase margin for multiloop LQG regulators. *IEEE Transactions on Automatic Control*, AC-22(2):173–179, 1977.

[95] J. Shaw. Active vibration isolation by adaptive control. In *Proc. IEEE International Conference on Control Applications*, pages 1509–1514, Hawaii, USA, August 1999.

[96] W. H. Shields, J. Ro and A. M. Baz. Control of sound radiation from a plate into an acoustic cavity using active piezoelectric-damping composites. In *Proc. SPIE Smart Structures and Materials: Mathematics and Control in Smart Structures, SPIE Vol. 3039*, pages 70–90, 1997.

[97] J. Simpson and J. Schweiger. Industrial approach to piezoelectric damping of large fighter aircraft components. In *Proc. SPIE Smart Structures and Materials: Industrial and Commercial Applications of Smart Structures Technologies, SPIE Vol. 3326*, pages 34–46, 1998.

[98] S. Skogestad and I. Postlethwaite. *Multivariable Feedback Control.* John Wiley and Sons, 1996.

[99] M. C. Smith and F. Wang, Controlle parameterization for disturnbance response decoupling: Application to vehicle active suspension control, *IEEE Transactions on Control Systems Technology*, vol. 10, pp. 393–407, May 2002.

[100] H. C. Sohn, K. S. Hong and J. K. Hedrick, Semi-active control of the macpherson supension system: Hardware-in-the-loop simulations. In *Proc. IEEE International Conference on Control Applications*, pages 982–987, Anchorage, Alaska, USA, September 2000.

[101] D. Stansfield. *Underwater Electroacoustic Transducers.* Bath University Press and Institute of Acoustics, Bath, UK, 1991.

[102] O. Thorp, M. Ruzzene and B. Liu. Attenuation and localization of wave propagation in rods with periodic shunted piezoelectric patches. *Smart Materials and Structures*, 10:979–989, 2001.

[103] TRS Ceramics Inc., *http://www.trcceramics.com*, 2003.

[104] P. Vallone. High-performance piezo-based self-sensor for structural vibration control. In *Proc. SPIE Smart Structures and Materials: Smart Structures and Integrated systems, SPIE Vol. 2443*, pages 643–655, 1995.

[105] P. Van Overschee and B. De Moor. Continuous-time frequency domain subspace system identification. *Signal Processing*, 52:179–194, 1996.

[106] M. Viberg. Subspace-based methods for the identification of linear time invariant systems. *Automatica*, 31(12):1835–1851, 1995.

[107] J. S. Vipperman and R. L. Clark. Hybrid analog and digital adaptive compensation of piezoelectric sensoriactuators. In *Proc. AIAA/ASME Adaptive Structures Forum*, pages 2854–2859, New Orleans, Louisiana, USA, 1995.

[108] D. Vischer and H. Bleuler. Self-sensing active magnetic levitation. *IEEE Transactions on Magnetics*, 29(2):169–177, 1993.

[109] J. T. Wen. Time domain and frequency domain conditions for strict positive realness. *IEEE Transactions on Automatic Control*, 33(10):988–992, October 1998.

[110] C. C. Won. Piezoelectric transformer. *Journal of Guidancce, Control, and Dynamics*, 18(1):96–101, 1995.

[111] S. Wu, T. L. Turner and S. A. Rizzi. Piezoelectric shunt vibration damping of an F-15 panel under high-acoustic excitation. In *Proc. SPIE Smart Structures and Materials: Damping and Isolation, SPIE Vol. 3989*, Huntington Beach, California, USA, pages 276–287, 2000.

[112] S. Y. Wu. Piezoelectric shunts with parallel R-L circuit for structural damping and vibration control. In *Proc. SPIE Smart Structures and Materials: Passive Damping and Isolation, SPIE Vol. 2720*, pages 259–269, Huntington Beach, California, USA, March 1996.

[113] S. Y. Wu. Method for multiple mode shunt damping of structural vibration using a single PZT transducer. In *Proc. SPIE Smart Structures and Materials, Smart Structures and Intelligent Systems, SPIE Vol. 3327*, pages 159–168, Huntington Beach, California, USA, March 1998.

[114] S. Y. Wu. Multiple PZT transducers implemented with multiple-mode piezoelectric shunting for passive vibration damping. In *Proc. SPIE Smart Structures and Materials, Passive Damping and Isolation, SPIE Vol. 3672*, pages 112–122, Huntington Beach, California, USA, March 1999.

[115] S. Y. Wu. Broadband piezoelectric shunts for structural vibration control. Patent No. 6,075,309, June 2000.

[116] S. Y. Wu. Broadband piezoelectric shunts for passive structural vibration control. In *Proc. SPIE Smart Structure and Materials 2001: Damping and Isolation, SPIE Vol. 4331*, pages 251–261, Newport Beach, California, USA, March 2001.

[117] S. Y. Wu and A. S. Bicos. Structural vibration damping experiments using improved piezoelectric shunts. In *Proc. SPIE Smart Structures and Materials, Passive Damping and Isolation, SPIE Vol. 3045*, pages 40–50, March 1997.

[118] J. M. Zhang, W. Chang, V. K. Varadan and V. V. Varadan. Passive underwater acoustic damping using shunted piezoelectric coatings. *IOP Journal of Smart Materials and Structures*, 10:414–420, 2001.